Institute of Soil Science and Land Evaluation
University of Hohenheim
Dept. of Soil Chemistry and Pedology
Prof. Dr. Thilo Rennert

Associations of short-range ordered aluminosilicates and organic matter: Formation, properties and stabilization of organic matter

Dissertation
submitted in fulfillment of the regulations to aquire the degree
„Doktor der Agrarwissenschaften“ (Dr.sc.agr. in Agricultural Sciences)
to the
Faculty of Agricultural Sciences

presented by

Katharina Raphaela Lenhardt

from Filderstadt

2023

This thesis was accepted as a doctoral thesis (Dissertation) in fulfillment of the regulations to acquire the doctoral degree "Doktor der Agrarwissenschaften" by the Faculty of Agricultural Sciences at University of Hohenheim on 13 December 2023.

Date of the oral examination: 13 May 2024

Chairperson of the oral examination:	Prof. Dr. Uwe Ludewig
Supervisor, first reviewer, examiner:	Prof. Dr. Thilo Rennert
Second reviewer, examiner:	Prof. Dr. Christian Mikutta
Third reviewer:	Apl. Prof. Dr. Jörg Prietzel
Additional examiner:	Prof. Dr. Ellen Kandeler

Contents

Summary

Short-range ordered aluminosilicates (SROAS) typically form during the weathering of volcanic ejecta by polymerization of released aluminium (Al) and silicon (Si). These minerals exhibit variable chemical composition and crystallinity. Tubular imogolite is a SROAS with long-range order; its locally defined Si configuration occurs also in poorly ordered SROAS. Interactions of SROAS and organic matter (OM) promote carbon (C) accrual by protecting OM from microbial degradation in the long term; however, the fundamental processes are poorly understood. Stable mineral-organic associations may form by adsorption of dissolved OM (DOM) on SROAS surfaces and by co-precipitation of DOM with SROAS during mineral formation. The objective of this study was to elucidate the chemical interactions between DOM and SROAS by both processes, and to assess the stability of OM sorbed by SROAS. Therefore, the impact of SROAS composition on DOM adsorption, partitioning of OM moieties by adsorption and co-precipitation, the structure of co-precipitates, and the degradability of co-precipitated OM was investigated.

A method to synthesize SROAS at ambient conditions was developed to mimic the surface properties of natural weathering products. Characterization of SROAS structure by solid-state ^{27}Al and ^{29}Si nuclear magnetic resonance (NMR) spectroscopy and Fourier transform infrared (FTIR) spectroscopy evinced a close similarity of synthetic SROAS to their natural analogues. Aluminium-rich SROAS (molar Al:Si>2) resembled proto-imogolite, with Al mainly in octahedral coordination and ≥38% of Si nuclei exhibiting an imogolite-like configuration. Silicon-rich SROAS (molar Al:Si = 1.4) contained tetrahedral Al and Si existed largely in ill-defined environments. Analyses of the specific surface area by nitrogen adsorption revealed marked aggregation of Al-rich SROAS, which was less pronounced in Si-rich SROAS. These results show that the poor crystallinity of Al-rich SROAS permits a very dense spatial arrangement of mass at the submicron scale, while Si incorporation restricts aggregation.

Interactions of SROAS and DOM were studied using natural DOM with heterogeneous composition collected *in situ* from a Dystric Cambisol at two depths, and by water extraction of litter. Solid-state ^{13}C-NMR and FTIR spectroscopy revealed a major contribution of oxidized aromatic moieties to soil DOM, likely originating from lignin degradation, while litter DOM was predominantly composed of carbohydrates. Soil DOM adsorption was driven by surface accessibility and was thus larger for Si-rich SROAS than for Al-rich SROAS, showing the importance of SROAS physical properties for OM retention. Aromatic products of lignin degradation preferentially adsorbed on SROAS, inducing relative enrichment of aliphatic substances, particularly carbohydrates, in the residual DOM. Topsoil DOM adsorption depended more strongly on contact time (1–168 h) than subsoil DOM adsorption, possibly due to qualitative differences of the aromatic fraction. Associations formed by co-precipitation contained more C than adsorption complexes. As Al interacted preferentially with oxidized

aromatic compounds, co-precipitation of DOM increased as a function of aromatic C. Nevertheless, marked sorption of carbohydrates from litter DOM evinced possible retention of substances with low affinity for Al by co-precipitation, in contrast to adsorption.

Time-dependent (1–72 h) structural evolution of SROAS in the absence of DOM was examined to resolve the mechanisms of SROAS formation. Irrespective of the initial molar Al:Si ratio, amorphous precursors formed by olation during the first hour. After 72 h, up to 50% of Si nuclei exhibited imogolite-like configuration, showing rapid development of short-range order. Dissolved OM interfered in condensation of Al and Si, causing partial exclusion of Si, and slowed crystallisation of the octahedral Al sheet, promoting ill-defined Si species in the co-precipitates. Hence, DOM likely impedes assembly of precursors into structurally ordered particles, in particular, oxidized aromatic DOM in topsoils.

The binding strength of DOM to SROAS surfaces may be affected by Si incorporation due to structure modifications. Thus, a mechanistic adsorption study was conducted with oxalic, salicylic and octanoic acid as models of functional moieties in DOM. Adsorption of oxalic and salicylic acid was up to 80–90% lower for Si-rich SROAS than for Al-rich SROAS. Rapid (<1 min) release of hydroxyls, indicating ligand exchange, was observed only for oxalic and salicylic acid, suggesting octanoic acid interacted electrostatically with SROAS surfaces. Chelate complexes of oxalic acid and partial inner-sphere binding of salicylic acid on both SROAS were identified by FTIR spectroscopy. Fast adsorption kinetics were retraced by changes in electrical conductivity using a stopped-flow technique. Ligand exchange by oxalate proceeded at a similar rate as complexation of monomeric Al^{3+}, showing its binding to octahedral Al. Hence, the much lower susceptibility of Si-rich SROAS to ligand exchange with carboxyl groups is caused by tetrahedral Al. Consequently, little OM may be stabilized by chemical bonds with Si-rich SROAS.

The degradability of co-precipitated carbohydrates was tested by addition of β-glucosidase, a microbial extracellular enzyme, at optimal concentration and quantification of the reaction product glucose. Glucose release was analysed for initial DOM, co-precipitated OM and for residual DOM to account for compositional changes by co-precipitation. As a result of carbohydrate enrichment in residual DOM, its degradability by β-glucosidase increased. Minor amounts of glucose were released from co-precipitated carbohydrates, showing their restricted accessibility for enzymes due to occlusion.

Formation of SROAS in soils likely induces preferential association of lignin degradation products with the mineral matrix and alters the composition of OM introduced to the subsoil. Otherwise easily degradable OM with low affinity for SROAS surfaces can be effectively protected from mineralization by co-precipitation. As the structure of SROAS reflects formation processes and affects their reactivity, future research characterizing natural SROAS will give mechanistic insights into C sequestration and potentially other vital soil functions.

Zusammenfassung

Schwach kristalline Aluminosilikate (“short-range ordered aluminosilicates”, SROAS) entstehen typischerweise während der Verwitterung von vulkanischem Gestein durch die Polymerisation von Aluminium (Al) und Silizium (Si). Diese Minerale kommen mit variabler Zusammensetzung und Kristallinität vor. Röhrenförmiger Imogolit ist ein SROAS mit Fernordnung, dessen Siliziumkonfiguration auch in SROAS mit geringem Ordnungsgrad auftritt. Wechselwirkungen zwischen SROAS und organischer Bodensubstanz (OBS) hemmen langfristig den mikrobiellen Abbau der OBS und tragen so zur Kohlenstoff(C)-Akkumulation bei, allerdings sind die ursächlichen Prozesse kaum erforscht. Stabile mineral-organische Assoziationen können durch Adsorption von gelöster OBS an die Oberflächen von SROAS und durch Ko-Fällung bei der Bildung von SROAS entstehen. Das Ziel dieser Studie war hinsichtlich beider Prozesse ein tieferes Verständnis der chemischen Interaktionen zwischen SROAS und OBS zu erlangen und die Stabilität sorbierter OBS zu ermitteln. Deshalb wurde der Einfluss der Zusammensetzung von SROAS auf die Adsorption von OBS, die Fraktionierung der OBS bei Adsorption und Ko-Fällung, die Struktur der Ko-Präzipitate, und die Abbaubarkeit von ko-gefällter OBS untersucht.

Es wurde eine Synthesemethode für SROAS bei Raumtemperatur entwickelt. Die Charakterisierung der Struktur der SROAS mittels Festkörper-^{27}Al-, und ^{29}Si-Kernspinresonanz-(NMR)-spektroskopie und Infrarot(IR)-spektroskopie zeigte die Ähnlichkeit der synthetischen SROAS zu natürlichen SROAS. Aluminium-reiche SROAS (Al:Si>2) glichen Proto-Imogolit, da Al vorwiegend in oktaedrischer Koordination und ≥38% der Si-Kerne in Imogolit-Konfiguration vorlagen. Silizium-reiche SROAS (Al:Si = 1.4) enthielten Al in tetraedrischer Koordination und Si befand sich größtenteils in ungeordneter chemischer Umgebung. Die Analyse der spezifischen Oberflächen mittels Stickstoffadsorption zeigte eine starke Aggregierung der Al-reichen SROAS, während diese bei Si-reichen SROAS geringer ausgeprägt war. Diese Ergebnisse zeigen, dass die geringe Kristallinität der Al-reichen SROAS eine sehr dichte Anordnung der Partikel auf der Submikronskala ermöglicht, während der Einbau von Si die Aggregierung beschränkt.

Die Wechselwirkungen von SROAS und OBS wurden mit heterogen zusammengesetzter, gelöster OBS aus einer podsolierten Braunerde (Dystric Cambisol) aus zwei Bodentiefen und mit wasserlöslicher OBS aus Streu untersucht. Mittels Festkörper-^{13}C-NMR-Spektroskopie und IR-Spektroskopie wurde ein hoher Anteil an oxidierten aromatischen Verbindungen aus dem Ligninabbau in der bodenbürtigen OBS nachgewiesen, während die OBS aus Streu hauptsächlich Kohlenhydrate enthielt. Die Adsorption von OBS wurde von der Zugänglichkeit der Mineraloberfläche gesteuert und erreichte deshalb bei Si-reichen SROAS ein größeres Ausmaß als bei Al-reichen SROAS, was die Relevanz der physikalischen Eigenschaften der SROAS für die Bindung von OBS verdeutlicht. Die aromatischen Verbindungen adsorbierten

präferentiell an SROAS, während aliphatische Verbindungen, insbesondere Kohlenhydrate, vorwiegend in der Lösung verblieben. Das Ausmaß der Adsorption von OBS aus dem Oberboden hing stärker von der Kontaktzeit (1–168 h) ab als dasjenige von OBS aus dem Unterboden, was auf die unterschiedliche Zusammensetzung der aromatischen Substanzen zurückgeführt werden konnte. Durch Ko-Fällung wurden größere Mengen an OBS an SROAS gebunden, als durch Adsorption. Aluminium interagierte vorwiegend mit den oxidierten aromatischen Substanzen, deshalb nahm die Ko-Fällung von OBS mit dem Gehalt an aromatischem C zu. Allerdings konnten erhebliche Mengen an gelösten Kohlenhydraten aus Streu ko-gefällt werden, was zeigt, dass insbesondere durch Ko-Fällung Stoffe mit geringer Affinität für Al gebunden werden können.

Die zeitabhängige (1–72 h) Kristallisation von SROAS wurde zunächst in Abwesenheit von OBS untersucht, um die Mechanismen der Fällung von SROAS zu klären. Unabhängig vom initialen Al:Si-Verhältnis bildeten sich innerhalb der ersten Stunde amorphe Spezies durch Olation. Nach 72 h lagen bis zu 50% der Si-Kerne in Imogolitkonfiguration vor, was eine zügige Entstehung von Nahordnung nachweist. Gelöste OBS störte die Kondensation von Al und Si, wodurch Si teilweise in Lösung verblieb, und verlangsamte die Kristallisation der Al-Oktaederschicht, was das Auftreten von ungeordneten Si-Spezies in den Ko-Präzipitaten förderte. Folglich verhindert OBS sehr wahrscheinlich die Bildung von SROAS mit hohem Ordnungsgrad, insbesondere im Oberboden.

Die Bindungsstärke von OBS an die Oberflächen von SROAS könnte durch den Einbau von Si beeinflusst werden, da dies die Struktur von SROAS modifiziert. Deshalb wurde eine mechanistische Studie der Adsorption von organischen Säuren durchgeführt (Oxalsäure, Salicylsäure, Octansäure). Das Ausmaß der Adsorption von Oxal- und Salicylsäure war bei Si-reichen SROAS um 80–90% geringer als bei Al-reichen SROAS. Die schnelle (<1 min) Freisetzung von Hydroxylionen durch Oxal- und Salicylsäure zeigte Ligandenaustausch, während Octansäure elektrostatisch gebunden wurde. Mittels IR-Spektroskopie wurde die Bindung von Oxalsäure über Chelatkomplexe und eine teilweise inner-sphärische Komplexierung von Salicylsäure identifiziert. Die schnelle Kinetik (<1 min) der Adsorption wurde mittels Messungen der elektrischen Leitfähigkeit mit einer Stopped-Flow-Methode untersucht. Der Ligandenaustausch mit Oxalat zeigte eine ähnliche Geschwindigkeitskonstante wie die Komplexierung von gelöstem Al^{3+}, was auf die Bindung an oktaedrisches Al hinweist. Die geringe Reaktivität der Si-reichen SROAS ist demnach durch das tetraedrisch koordinierte Al verursacht. Die Stabilisierung von OBS durch chemische Bindung an Si-reiche SROAS könnte deshalb gering sein.

Die Abbaubarkeit von ko-gefällten Kohlenhydraten wurde durch die Zugabe von β-Glucosidase, einem mikrobiellen extrazellulären Enzym, geprüft. Bei optimaler Enzymkonzentration wurde die Freisetzung von Glucose quantifiziert. Um die Fraktionierung der OBS

bei der Ko-Fällung zu berücksichtigen, wurde die Glucosefreisetzung sowohl für die initiale OBS, als auch für die ko-gefällte OBS und die in Lösung verbliebene OBS bestimmt. Letztere zeigte eine erhöhte Abbaubarkeit durch β-Glucosidase durch die Anreicherung von Kohlenhydraten. Aus ko-gefällten Kohlenhydraten wurde nur eine geringfügige Menge Glucose freigesetzt, was die verringerte Zugänglichkeit des Substrats für das Enzym durch Okklusion zeigt.

Die Entstehung von SROAS kann in Böden zur präferentiellen Assoziation von Produkten des Ligninabbaus mit dem Mineralkörper führen und die Zusammensetzung von OBS, die dem Unterboden zugeführt wird, verändern. Leicht abbaubare OBS mit geringer Affinität für die Oberflächen von SROAS kann durch Ko-Fällung vor der Mineralisierung geschützt werden. Da die Struktur von SROAS deren Bildungsbedingungen widerspiegelt und deren Reaktivität beeinflusst, kann die Charakterisierung natürlicher SROAS das mechanistische Verständnis der C-Sequestrierung und weiterer Bodenfunktionen erweitern.

Chapter 1

Introduction

Soil organic matter (SOM) is a critical component of the earth's carbon (C) cycle. Globally, more C is stored in soils as SOM than in the atmosphere and the terrestrial vegetation combined (~1500 Pg organic C to 1 m depth; Scharlemann et al., 2014). Soil organic matter comprises all biologically derived, non-living organic material residing within the soil matrix and on the soil surface. Plant debris, microbial residues, root exudates and their degradation products thus contribute to SOM (Kögel-Knabner, 2002). Decomposition of SOM is crucial for soil development as it provides vital nutrients and energy for soil organisms, driving alteration of parent rocks towards a liveable base for plants. However, a fraction of SOM escapes mineralization, that is, conversion to carbon dioxide (CO_2), by interaction with minerals, resulting in its long-term preservation (Kögel-Knabner et al., 2008; Kleber et al., 2015). A large portion of SOM is closely associated with minerals, the amount of C contained therein was estimated 899 Pg to a depth of 1 m (Georgiou et al., 2022). Allocation of SOM to the mineral matrix and its subsequent degradability is strongly affected by particle size and surface charge of clay-sized minerals (<2 µm; Bruun et al., 2010; Singh et al., 2017). In soils characterized by silicate weathering, poorly crystalline phases formed by precipitation of released aluminium (Al), iron (Fe) and silicon (Si) may control SOM accrual (Rasmussen et al., 2018), a process particularly pronounced in Andosols developing from volcanic ejecta (e.g., Torn et al., 1997). Andosols are soils having andic properties defined based on bulk density, oxalate-extractable Al and Fe, and phosphate retention, or containing volcanic glasses, according to the World Reference Base for Soil Resources (IUSS Working Group WRB, 2022). Amongst mineral soils, Andosols stand out by containing a disproportionate amount of organic C relative to their spatial distribution (~78 Pg to 1 m depth; Eswaran et al., 1993) and exceptionally old SOM (Mathieu et al., 2015). Short-range ordered aluminosilicates (SROAS) are a major mineral constituent of Andosols promoting immobilization of SOM (Lilienfein et al., 2004). Turnover of SOM in other soils such as Cambisols and Podzols may also be affected by SROAS (e.g., Stahr and Nakai, 1984; Gustafsson et al., 1999). Decomposition of freshly added organic substances is decelerated by SROAS (Zunino et al., 1982; Fujii et al., 2019), possibly by formation of intricate mineral-organic associations at the submicron scale (Basile-Doelsch et al., 2007; Wagai et al., 2018); however, the interactions of SOM and SROAS are poorly understood.

Short-range ordered aluminosilicates

Short-range ordered aluminosilicates are hydrous secondary minerals characterized by varying chemical composition and degree of spatial order. They form by polymerization of Al and Si and exhibit molar Al:Si ratios of about 1–4. Based on these ratios, SROAS are classified as Al-rich (Al:Si≥2) or Si-rich (Al:Si~1; Levard and Basile-Doelsch, 2016). In the following,

SROAS will be used as a generic term to refer to imogolite, allophanes, their precursors, and amorphous aluminosilicates with similar Al:Si ratios.

Imogolite is a tubular mineral with a well-defined structure; its outer surface is composed of a dioctahedral Al sheet with single Si tetrahedra linked to three Al octahedra at the inside (Cradwick et al., 1972). The imogolite-like Si configuration is denoted as Q^0(3Al), indicating the number of bonds with neighbouring Si (0) and Al atoms (3; Smith et al., 1983). The imogolite tubes have a diameter of about 2 nm and can reach lengths of several µm (e.g., Henmi and Wada, 1976). Hence, imogolite can exhibit long-range structural repetition in one dimension, the tube axis. Imogolite was named after a locality in the Kumamoto Prefecture, Japan, that is, 'Imogo soil' (Yoshinaga and Aomine, 1962) and was approved as a mineral species by the International Mineralogical Association (IMA) in 1986 (Bayliss, 1987).

The term 'allophane' was first used by Haussmann and Strohmeyer in 1816 for an inorganic rock isolate (Haussmann and Strohmeyer, 1816). Nowadays, allophane is used as a generic term for diversely structured SROAS less crystalline than imogolite. Allophane is considered a variably composed, grandfathered mineral species by the IMA (IMA, 2023). Visualization of synthesized and naturally formed SROAS at the nanometre scale by transmission electron microscopy (TEM) usually depicts aggregates of globular particles (Henmi and Wada, 1976; Kleber et al., 2004; Iyoda et al., 2012; Huang et al., 2016). Resolving the morphology of Al-rich SROAS at <3 nm by TEM, Wada and Wada (2014) have convincingly shown that the primary particles of Al-rich SROAS can take the shape of hollow spheres with diameters of 3–5 nm. A corresponding structural model has been proposed by Creton et al. (2008). However, assuming a sphere-shaped morphology of poorly characterized SROAS should be avoided because granular shapes were also observed for other poorly ordered phases such as ferrihydrite co-precipitated with organic matter (Eusterhues et al., 2008).

Technical advances of spectroscopic methods revealed that SROAS are usually not amorphous (Mitchell et al., 1964) but contain short-range order. A material is amorphous when the atoms are arranged with variable bond lengths, coordination and geometry so that no spatial order occurs (Harsh, 2011). In contrast, Si in Q^0(3Al) configuration was detected by solid-state ^{29}Si nuclear magnetic resonance (NMR) and infrared spectroscopy in many SROAS isolated from weathered rocks and soils (e.g., Goodman et al., 1985; Basile-Doelsch et al., 2005; Rennert et al., 2014). Signals of Si nuclei in Q^0(3Al) configuration evince ordering of their second coordination sphere, that is, a defined arrangement of Al octahedra with characteristic bond lengths (Cradwick et al., 1972; Barron et al., 1982). A dioctahedral Al ring with one Si tetrahedron in Q^0(3Al) configuration has a diameter of about 0.84 nm (Cradwick et al., 1972). Assembly of these domains may extend over several nanometres, forming curved fragments and ultimately particles with a defined morphology such as spheres or imogolite tubes (Wada and Wada, 2014; Du et al., 2017). Aluminium-rich SROAS, in particular, contain Si in Q^0(3Al)

configuration and dominantly octahedral Al (>80% of Al, Goodman et al., 1985; Ildefonse et al., 1994) and were thus referred to as ‘proto-imogolite’ (Parfitt et al., 1980; Gustafsson et al., 1999). The structure of proto-imogolites may correspond to curved fragments of tube- or sphere-shaped particles (Lowe, 1995).

Abundant silicic acid promotes Si incorporation into SROAS, resulting in molar Al:Si ratios <2 and structural modifications (e.g., Parfitt et al., 1980). A portion of Si nuclei in structurally ill-defined chemical environments arises and the formed SROAS contain Al in tetrahedral coordination (Goodman et al., 1985; Ildefonse et al., 1994). Synthesis at alkaline conditions and high silicic-acid concentration (initial molar Al:Si<1) yielded Si-rich SROAS with >58% of Al in tetrahedral coordination and no Si in Q^0(3Al) configuration (Farmer et al., 1979; Goodman et al., 1985; Doucet et al., 2001). However, in naturally formed Si-rich SROAS more than half of Al nuclei was in octahedral coordination and a small amount of Si in Q^0(3Al) configuration was present (Goodman et al., 1985; Childs et al., 1990; Ildefonse et al., 1994).

Two divergent models for the local structure of the ill-defined Si fraction of Si-rich SROAS have been proposed. A locally layered structure similar to 1:1 phyllosilicate was assumed as spectroscopic characterization evinced condensed Si tetrahedra (Childs et al., 1990; MacKenzie et al., 1991). Childs et al. (1990) postulated curved layers with the external surface built up by the basal oxygens of linked Si tetrahedra and their binding via the apical oxygen to incomplete octahedral Al sheets as a fraction of Al is located in the tetrahedral sheets. In contrast, Farmer et al. (1979) implied a three-dimensional network of Si tetrahedra by using the term ‘hydrous feldspathoid’. The similarity of the chemical environment of tetrahedral Al in SROAS to tetrahedral Al in tectosilicates and glasses supports this view (Ildefonse et al., 1994). Hence, the polymerized Si domains may be linked to fragmented imogolite-like layers in variable proportions (Parfitt et al., 1980; Levard and Basile-Doelsch, 2016).

Previous studies mostly characterized SROAS isolated from weathered rocks or subsoils, while spectroscopic investigations of SROAS formed in soil horizons with substantial organic matter accumulation are scarce (Hiradate et al., 2006; Basile-Doelsch et al., 2007; Rennert et al., 2014). Carboxylic acids and organic matter extracted from soil impeded SROAS crystallization in synthesis experiments (Inoue and Huang, 1990). Nevertheless, Si nuclei in Q^0(3Al) configuration were detected in pedogenic Al-bearing phases showing a strong distortion of the octahedral sheet by organic functional groups (Levard et al., 2012). Hence, SROAS are regarded minerals in this thesis in spite of their equivocal structure and the fact that SROAS are not crystalline according to Nickel (1995). Crystallinity is therein defined by atomic ordering at a scale that can produce an indexable diffraction pattern when exposed to a wave with suitable wave length (Nickel, 1995). Imogolite fulfils this criterion only when the tubes have lengths >100 nm or several tubes are stacked together in bundles (Wada, 1989; Mukherjee et al., 2005; Du et al., 2017). However, given that the structure of Si in Q^0(3Al)

configuration does not occur in other minerals, SROAS are accepted as a distinct mineral species, including the related, possibly amorphous, variants (Nickel, 1995).

Stabilization of SOM by SROAS

Stabilization comprehensively refers to processes that cause protection of SOM from mineralization (von Lützow et al., 2006). Several stabilization mechanisms have been postulated to be actuated by SROAS, including binding of SOM, a reduction of the spatial accessibility of SOM, and negative impacts on the viability and activity of microorganisms (Matus et al., 2014).

Binding of SOM by SROAS reduces the probability of its exposition to extracellular enzymes or its uptake into microbial cells; moreover, conformational changes may inhibit enzymatic cleavage (Chenu and Stotzky, 2002). Allocation of SOM to SROAS may be favoured by a large surface area and formation of chemical bonds with organic functional groups (Parfitt et al., 1977; Singh et al., 2017). In comparison to crystalline clay-sized minerals, SROAS having particle sizes <50 nm exhibit a higher density of reactive surface sites, which enables multiple bond formation with organic molecules (Kaiser and Guggenberger, 2003) and renders SOM very stable against desorption and oxidation (Mikutta and Mikutta, 2006). Furthermore, admixture of SOM and small-sized, poorly ordered SROAS in andic soils suggests that incorporation of SOM into SROAS during their formation contributes to SOM binding (Mikutta et al., 2009; Levard et al., 2012).

Interactions of SROAS particles promote aggregation, that is, the development of soil structure by formation of porous assemblages composed of minerals and SOM. Aggregation results in entrapment of SOM and thus diminishes its accessibility for decomposers (von Lützow et al., 2006). In andic soils containing SROAS, a substantial amount of pore space has diameters too small for colonization by microorganisms (<100 nm; Baldock and Skjemstad, 2000; Chevallier et al., 2010; Calvelo Pereira et al., 2019). Moreover, SOM may be inaccessible for microbial enzymes due to encapsulation between SROAS particles (Huang et al., 2016; Filimonova et al., 2016) as diffusion of enzymes into pores with diameters <10 nm is restricted (Zimmerman et al., 2004a). The high tortuosity of pores in SROAS aggregates strongly decelerates diffusion (Woignier et al., 2019) which may impede release of SOM from aggregates or affect oxygen availability at the aggregate interior. Low oxygen availability at sites with high rainfall limited SOM decomposition in soils developed from volcanic parent material (Schuur and Matson, 2001), possibly by imposing metabolic constraints on SOM mineralization (Keiluweit et al., 2016).

Besides effects on pore morphology, SROAS also enhance aggregate stability. Aggregates from andic soils are very resistant to disruption by ultrasonication and addition of chemical extractants such as hydrogen peroxide (Churchman and Tate, 1986). Aggregation of SROAS

is favoured by alternating water contents as water emission locally concentrates SROAS and causes particle interactions (Kubota, 1972; Wells and Theng, 1988). Drying of SROAS induces irreversible loss of pore volume (Rousseaux and Warkentin, 1976; Chevallier et al., 2008) which may relate to condensation of surface groups (Kubota, 1975). Successive breakdown of aggregates from andic soils revealed that a large fraction of SOM is closely co-localized with SROAS at the submicron scale and has an above-average age, showing that mineral-organic associations are persistent binding agents (Asano and Wagai, 2014; Wagai et al., 2018).

Several effects of SROAS on microorganisms and their enzymes may decelerate the degradation of SOM besides mechanisms affecting its availability. As SOM is largely composed of macromolecules that cannot enter microbial cells, depolymerisation at the exterior by extracellular enzymes is necessary. A reduction of the catalytic potential of several enzymes by SROAS was reported (Kobayashi and Aomine, 1967; Ross, 1983; Shindo et al., 2002; Menezes-Blackburn et al., 2011). Binding of extracellular enzymes by SROAS may block the active site or change the conformation of the molecule (Quiquampoix et al., 2002). Moreover, as phosphorus (P) is an essential element for microorganisms and scarcely contained in plant biomass, the high phosphate retention capacity of SROAS (Theng et al., 1982) may induce P limitation of SOM degradation (Zechmeister-Boltenstern et al., 2015; Matus et al., 2014). Phosphate addition to andic soil material stimulated soil respiration in incubation experiments (Munevar and Wollum, 1977); however, partial displacement of SOM from minerals possibly occurred (Beck et al., 1999; Spohn and Schleuss, 2019). In field experiments, P fertilization of andic soils decreased phosphatase activities, showing the adaptability of the microbial community to P availability by regulation of enzyme exudation (Olander and Vitousek, 2000). The viability of microorganisms may be further compromised by toxic effects of mobilized Al as observed for plant roots growing in andic soil (Nierop et al., 2005; Tonneijck et al., 2010; Takahashi and Dahlgren, 2016). The toxicity of Al is related to the strong binding of dissolved monomeric Al (Al^{3+}) to vital biomolecules, inducing a loss of their function (Piña and Cervantes, 1996; Gensemer and Playle, 1999). In incubation experiments, amorphous Al hydroxide decelerated SOM mineralization more strongly than ferrihydrite although SOM binding was limited by a low surface area (Miltner and Zech, 1998), suggesting that colonization of SROAS may be impeded which was observed for Al-containing glasses (Roberts, 2004).

Associations of SROAS and organic matter

Formation of stable associations by interactions of organic matter and SROAS can be conceptualized by assuming two pathways: (1) Adsorption of organic matter on the surfaces of previously formed SROAS and (2) co-precipitation during formation of SROAS (Kleber et al., 2015).

Adsorption is the enrichment of substances at the interface between a solid and the adjacent aqueous or gaseous phase, a strictly two-dimensional process (Scheidegger and Sparks, 1996). Several adsorption mechanisms possibly occur that differ in the binding strength established between the SROAS surface and SOM. Ligand exchange is the displacement of hydroxyls or water from the first coordination sphere of metals by charged organic functional groups and results in inner-sphere complexes. If one or more water molecules are interposed between the surface and the organic molecule, an outer-sphere complex is formed (Sposito, 2016). Outer-sphere complexes involve binding by electrostatic interactions between charged organic functional groups and charged surface sites, including bridging by protons ('hydrogen bonding'; Sposito, 2016). Uncharged organic molecules may be adsorbed weakly by van der Waals forces (Sposito, 2016). Less energy is released by adsorption due to electrostatic interactions and van der Waals forces than by ligand exchange, indicating a lower stability of outer-sphere complexes (Gu et al., 1994; Arnarson and Keil, 2000).

Co-precipitation is the three-dimensional enrichment of a substance with a newly formed solid. During co-precipitation of organic matter with SROAS, several processes may occur simultaneously: Complexation of ions by organic functional groups, adsorption of organic matter on newly formed particles, entrapment of organic matter by particle interactions ('occlusion'), and flocculation (Eusterhues et al., 2008). Flocculation refers to the process by which colloids, that is, particles unaffected by gravitational settling, coalesce to form larger particles (Gustafsson and Gschwend, 1997; Sposito, 2016). In the following, sorption will be used as a general term for adsorption, co-precipitation, and diffusion of substances into particles (Scheidegger and Sparks, 1996).

Adsorption of SOM may be affected by SROAS composition and structure, as these factors influence surface functional group abundance and surface charge. Singly coordinated aluminol groups are prone to ligand exchange with phosphate and oxalate, while doubly coordinated aluminol groups provided by imogolite are not (Parfitt et al., 1977; Theng et al., 1982). Hence, the reactivity of Al-rich SROAS towards SOM may decrease with extension of short-range order. Incorporation of Si into SROAS reduces the molar Al:Si ratio and adds silanol groups which do not participate in ligand exchange with organic functional groups (Pokrovski and Schott, 1998). This effect may explain a positive correlation between molar Al:Si ratio and adsorption of oxalate and phosphate (Clarke and McBride, 1984; Hanudin et al., 2002). However, as silicic acid impedes crystallization of octahedral Al (Exley et al., 2002), there might be a positive effect of Si incorporation on SROAS reactivity. Silicon incorporation also adds variable charge by silanol groups and permanent negative charge due to formation of tetrahedral Al (Su et al., 1992). Sugars, nitrogenous compounds and benzene derivatives adsorbed by electrostatic interactions on SROAS (Hashizume and Theng, 2007; Nishikiori et al., 2009), indicating the relevance of weak forces for SOM binding. Moreover, nonpolar

siloxane groups provided by condensed Si tetrahedra may be important for retention of aliphatic SOM. Amorphous silica adsorbed amino acids with hydrophobic moieties while binding via charged moieties to silanol groups was negligible (Zimmerman et al., 2004b). Hence, several adsorption mechanisms possibly occur during interactions of SOM and SROAS as a function of SROAS composition. In particular, the effect of Si incorporation on surface reactivity of SROAS needs to be elucidated, as ligand exchange thwarts desorption and mineralization (Gu et al., 1994; Mikutta et al., 2007).

Co-precipitation of SOM may retain more C than adsorption because more Al is available for interaction with SOM while SOM adsorption is limited by the available surface area (Eusterhues et al., 2011; Mikutta et al., 2011; Chen et al., 2014). Complexation of Al and Fe by organic functional groups impedes polymerization of the metals, hampering crystallisation and particle growth (Masion et al., 1994; Eusterhues et al., 2008; Chen et al., 2014). As a result, co-precipitates may exhibit a greater abundance and accessibility of functional groups for reactions with, for example, SOM and pollutants (Liu and Huang, 2003; Mikutta and Kretzschmar, 2008; Mikutta et al., 2014). Acid polysaccharides did not significantly alter the crystallinity of ferrihydrite (Mikutta et al., 2008), whereas water-extractable organic matter from a forest topsoil strongly impeded its structural ordering (Eusterhues et al., 2008), showing the importance of SOM composition for mineral formation. In synthesis experiments at 95 °C, low-molecular-weight organic acids and organic matter extracted from soil perturbed imogolite crystallization as a function of concentration and affinity for Al complexation (Inoue and Huang, 1986, 1990). In contrast, a positive effect of organic matter on the quantity of Si nuclei in Q^0(3Al) configuration in co-precipitates was found at ambient conditions (Rouff et al., 2012). Perturbation of the octahedral Al sheet by organic functional groups was evinced spectroscopically for SROAS formed in andic soils (Basile-Doelsch et al., 2005; Levard et al., 2012), underlining the importance of SOM interference in SROAS formation. Hence, the effects of SOM on the speciation of Al and Si in SROAS should be investigated under realistic conditions.

Organic compounds in the aqueous phase of soils are the primary fraction of SOM interacting with minerals due to their high mobility (Kleber et al., 2015). Dissolved organic matter (DOM) is operationally defined as organic matter that can pass a 0.45 µm filter. The composition of DOM usually varies with soil depth as mainly plant-derived components are mobilized in the upper soil compartments and microbial residues may contribute in the subsoil (Kaiser and Kalbitz, 2012). The interplay of variable surface properties of SROAS and heterogeneously composed DOM may induce fractionation of organic matter. Oxidized aromatic moieties of DOM outcompeted aliphatic substances due to stronger affinity for surface sites of soil minerals (e.g., Kaiser et al., 1997; Chorover and Amistadi, 2001; Schneider et al., 2010). Fractionation may be time-dependent as adsorption kinetics relate to molecular size (Zhou et al., 2001).

Preferential sorption of aromatic compounds mobilised from litter was also found for co-precipitation with Al (Kaiser, 1998; Scheel et al., 2008). Fractionation by co-precipitation may be particularly pronounced for DOM dominated by molecules with high affinity for metal complexation, showing that source DOM composition affects the speciation of retained compounds (Eusterhues et al., 2011). Selective retention of DOM by SROAS may explain accumulation of specific substances in andic soils, for example, carboxylic and aromatic moieties (Kramer et al., 2012). However, preservation of polysaccharides (Parfitt et al., 1999; Nierop et al., 2005; Buurman et al., 2007) and hydrophobic aliphatic compounds from plant cell walls has also been observed (Buurman et al., 2007). Hence, partitioning of organic matter in variably composed DOM by adsorption on and co-precipitation with SROAS should be clarified.

Adsorption of organic matter to SROAS rendered it less biodegradable than organic matter bound to phyllosilicates irrespective of the composition of source DOM because a chemically similar fraction was retained in inner-sphere complexes (Sanderman et al., 2014). In accordance, organic-matter degradability was controlled by chemical binding to other mineral surfaces (Mikutta et al., 2007). In contrast to adsorption, co-precipitation allows for entrapment of SOM between mineral particles, suggesting an additional effect of occlusion on stabilization (Eusterhues et al., 2014). A fraction of SOM at the interior of co-precipitates may be inaccessible for microbial enzymes (Zimmerman et al., 2004a). Co-precipitated organic matter was partially stabilized by Al and Fe forms, but not to a greater extent than adsorbed organic matter (Mikutta et al., 2011; Eusterhues et al., 2014). However, the magnitude of mineralization vastly differed between associations formed from litter-derived organic matter and microbial residues, that is, about 1 up to 57% of sorbed C was mineralized (Eusterhues et al., 2014; Mikutta et al., 2011). Hence, the degradability of variably composed organic matter co-precipitated with SROAS should be investigated complementary to the reactivity of SROAS.

Research objectives

The aim of this study was to clarify interactions of organic matter with SROAS by adsorption and co-precipitation and their consequences for stabilization of organic matter. First, to obtain model adsorbents, a method to synthesize SROAS with structural properties similar to natural, poorly ordered weathering products was developed. Deviating from previously reported protocols (reviewed by Thill, 2016), synthesis was performed at ambient temperature using an inorganic Si source to avoid carryover of C.

Second, interactions of DOM and SROAS by adsorption and co-precipitation were investigated. As the composition of DOM was presumed a major factor influencing sorption processes, soil solutions from a Dystric Cambisol were collected *in situ* at two depths to mimic natural conditions. The impact of DOM composition on co-precipitation was elucidated using

water-extractable organic matter from litter in addition to soil DOM. Adsorption was studied in batch experiments with variable contact time and co-precipitation was examined in titration experiments at a controlled neutralization rate. To gain a mechanistic understanding of DOM interference in SROAS formation, a detailed knowledge of SROAS formation in the absence of DOM was necessary. Hence, prior to experiments with DOM, the time-dependent structural evolution of SROAS in the absence of organic substances was clarified. Partitioning of organic matter and the structure of co-precipitates was uncovered by spectroscopic techniques.

The third objective of this study was to analyse structural impacts on the binding strength of SOM to SROAS surfaces. Oxalic, salicylic and octanoic acid were used as models of functional moieties present in DOM. The adsorption mechanisms were resolved by spectroscopic characterization of the adsorbates and evaluation of the fast adsorption kinetics. Adsorption was monitored at a resolution of milliseconds using a conductivity-based stopped-flow technique.

Finally, the degradability of co-precipitated organic matter was inspected focusing on carbohydrates. Carbohydrates are a preferred substrate of microorganisms and mobilized by exudation of β-glucosidase. Hence, the enzyme was added to co-precipitates from variably composed DOM at optimal concentration and the reaction product glucose was quantified. Taking fractionation into account, glucose release was also measured for initial DOM and DOM remaining in the supernatant after co-precipitation.

Organization of this thesis

The following chapters represent published papers (chapters 2 to 5). Hence, each chapter contains an abstract, an introduction, a method description, results and discussion. The structure and style (e.g., citation style, caption format) correspond to the requirements of the respective journals and thus vary between the chapters. The final chapter (6) presents an overall discussion and suggestions for further research.

References

Arnarson T. S. and Keil R. G. (2000) Mechanisms of pore water organic matter adsorption to montmorillonite. Mar. Chem. 71, 309–320.

Asano M. and Wagai R. (2014) Evidence of aggregate hierarchy at micro- to submicron scales in an allophanic andisol. Geoderma 216, 62–74.

Baldock J. A. and Skjemstad J. O. (2000) Role of the soil matrix and minerals in protecting natural organic materials against biological attack. Org. Geochem. 31, 697–710.

Barron P. F., Wilson M. A., Campbell A. S. and Frost R. L. (1982) Detection of imogolite in soils using solid state ^{29}Si NMR. Nature 299, 616–618.

Basile-Doelsch I., Amundson R., Stone W. E. E., Borschneck D., Bottero J. Y., Moustier S., Masin F. and Colin F. (2007) Mineral control of carbon pools in a volcanic soil horizon. Geoderma 137, 477–489.

Basile-Doelsch I., Amundson R., Stone W. E. E., Masiello C. A., Bottero J. Y., Colin F., Masin F., Borschneck D. and Meunier J. D. (2005) Mineralogical control of organic carbon dynamics in a volcanic ash soil on La Réunion. Eur. J. Soil Sci. 56, 689–703.

Bayliss P. (1987) Mineral nomenclature: imogolite. Mineral. Mag. 51, 327–327.

Beck, M. A., Robarge, W. P. and Buol, S. W. (1999) Phosphorus retention and release of anions and organic carbon by two Andisols. Eur. J. Soil Sci. 50, 157—164.

Bruun T. B., Elberling B. and Christensen B. T. (2010) Lability of soil organic carbon in tropical soils with different clay minerals. Soil Biol. Biochem. 42, 888–895.

Buurman P., Peterse F. and Almendros Martin G. (2007) Soil organic matter chemistry in allophanic soils: A pyrolysis-GC/MS study of a Costa Rican Andosol catena. Eur. J. Soil Sci. 58, 1330–1347.

Calvelo Pereira R., Camps Arbestain M., Kelliher F. M., Theng B. K. G., McNally S. R., Macías F. and Guitián F. (2019) Assessing the pore structure and surface area of allophane-rich and non-allophanic topsoils by supercritical drying and chemical treatment. Geoderma 337, 805–811.

Chen C., Dynes J. J., Wang J. and Sparks D. L. (2014) Properties of Fe-organic matter associations via coprecipitation versus adsorption. Environ. Sci. Technol. 48, 13751–13759.

Chenu, C. and Stotzky, G. (2002) Interactions between microorganisms and soil particles. An overview. In: Interactions Between Soil Particles and Microorganisms (Eds. P. M. Huang, J.-M. Bollag and N. Senesi), pp. 3–39. Wiley-VCH, Weinheim.

Chevallier T., Woignier T., Toucet J. and Blanchart E. (2010) Organic carbon stabilization in the fractal pore structure of Andosols. Geoderma 159, 182–188.

Chevallier T., Woignier T., Toucet J., Blanchart E. and Dieudonné P. (2008) Fractal structure in natural gels: Effect on carbon sequestration in volcanic soils. J. Sol-Gel Sci. Technol. 48, 231–238.

Childs C. W., Parfitt R. L. and Newman R. H. (1990) Structural studies of Silica Springs allophane. Clay Miner. 25, 329–341.

Chorover J. and Amistadi M. K. (2001) Reaction of forest floor organic matter at goethite, birnessite and smectite surfaces. Geochim. Cosmochim. Acta 65, 95–109.

Churchman G. J. and Tate K. R. (1986) Aggregation of clay in six New Zealand soil types as measured by disaggregation procedures. Geoderma 37, 207–220.

Clarke C. J. and McBride M. B. (1984) Cation and anion retention by natural and synthetic allophane and imogolite. Clays Clay Miner. 32, 291–299.

Cradwick P. D. G., Farmer V. C., Russell J. D., Masson C. R., Wada K. and Yoshinaga N. (1972) Imogolite, a hydrated aluminum silicate of tubular structure. Nat Phys Sci 240, 187–189.

Creton B., Bougeard D., Smirnov K. S., Guilment J. and Poncelet O. (2008) Structural model and computer modeling study of allophane. J. Phys. Chem. C 112, 358–364.

Doucet F. J., Schneider C., Bones S. J., Kretchmer A., Moss I., Tekely P. and Exley C. (2001) The formation of hydroxyaluminosilicates of geochemical and biological significance. Geochim. Cosmochim. Acta 65, 2461–2467.

Du P., Yuan P., Thill A., Annabi-Bergaya F., Liu D. and Wang S. (2017) Insights into the formation mechanism of imogolite from a full-range observation of its sol-gel growth. Appl. Clay Sci. 150, 115–124.

Eswaran H., Van Den Berg E. and Reich P. (1993) Organic carbon in soils of the world. Soil Sci. Soc. Am. J. 57, 192–194.

Eusterhues K., Neidhardt J., Hädrich A., Küsel K. and Totsche K. U. (2014) Biodegradation of ferrihydrite-associated organic matter. Biogeochemistry 119, 45–50.

Eusterhues K., Rennert T., Knicker H., Kögel-Knabner I., Totsche K. U. and Schwertmann U. (2011) Fractionation of organic matter due to reaction with ferrihydrite: Coprecipitation versus adsorption. Environ. Sci. Technol. 45, 527–533.

Eusterhues K., Wagner F. E., Häusler W., Hanzlik M., Knicker H., Totsche K. U., Kögel-Knabner I. and Schwertmann U. (2008) Characterization of ferrihydrite-soil organic matter coprecipitates by X-ray diffraction and Mössbauer spectroscopy. Environ. Sci. Technol. 42, 7891–7897.

Exley C., Schneider C. and Doucet F. J. (2002) The reaction of aluminium with silicic acid in acidic solution: An important mechanism in controlling the biological availability of aluminium? Coord. Chem. Rev. 228, 127–135.

Farmer V. C., Fraser A. R. and Tait J. M. (1979) Characterization of the chemical structures of natural and synthetic aluminosilicate gels and sols by infrared spectroscopy. Geochim. Cosmochim. Acta 43, 1417–1420.

Filimonova S., Kaufhold S., Wagner F. E., Häusler W. and Kögel-Knabner I. (2016) The role of allophane nano-structure and Fe oxide speciation for hosting soil organic matter in an allophanic Andosol. Geochim. Cosmochim. Acta 180, 284–302.

Fujii K., Hayakawa C., Inagaki Y. and Ono K. (2019) Sorption reduces the biodegradation rates of multivalent organic acids in volcanic soils rich in short-range order minerals. Geoderma 333, 188–199.

Gensemer R. W. and Playle R. C. (1999) The bioavailability and toxicity of aluminum in aquatic environments. Crit Rev Environ Sci Technol. 29, 315–450.

Georgiou K., Jackson R. B., Vindušková O., Abramoff R. Z., Ahlström A., Feng W., Harden J. W., Pellegrini A. F. A., Polley H. W., Soong J. L., Riley W. J. and Torn M. S. (2022) Global stocks and capacity of mineral-associated soil organic carbon. Nat. Commun. 13:3797.

Goodman B. A., Russell J. D., Montez B., Oldfield E. and Kirkpatrick R. J. (1985) Structural studies of imogolite and allophanes by aluminum-27 and silicon-29 nuclear magnetic resonance spectroscopy. Phys. Chem. Miner. 12, 342–346.

Gu B., Schmitt J., Chen Z., Liang L. and McCarthy J. F. (1994) Adsorption and desorption of natural organic matter on iron oxide: Mechanisms and models. Environ. Sci. Technol. 28, 38–46.

Gustafsson J. P., Bhattacharya P. and Karltun E. (1999) Mineralogy of poorly crystalline aluminium phases in the B horizon of Podzols in southern Sweden. Appl. Geochem. 14, 707–718.

Gustafsson Ö. and Gschwend P. M. (1997) Aquatic colloids: Concepts, definitions, and current challenges. Limnol. Oceanogr. 42, 519–528.

Hanudin E., Matsue N. and Henmi T. (2002) Reactions of some short-range ordered aluminosilicates with selected organic ligands. Dev. Soil Sci. 28, 319–332.

Harsh J. (2011) Poorly Crystalline Aluminosilicate Clay Minerals. In: Handbook of Soil Sciences Properties and Processes (Eds. P. M. Huang, Y. Li, M. E. Sumner), pp. 23:1–13. CRC Press, Boca Raton.

Hashizume H. and Theng B. K. G. (2007) Adenine, adenosine, ribose and 5`-AMP adsorption to allophane. Clays Clay Miner. 55, 599–605.

Hausmann J. F. L. and Strohmeyer F. (1816) [Notification on Silberkupferglanz and Allophan] Göttingische Gelehrte Anzeigen 2, 1251–1253.

Henmi T. and Wada K. (1976) Morphology and composition of allophane. Am. Mineral. 61, 379–390.

Hiradate S., Hirai H. and Hashimoto H. (2006) Characterization of allophanic Andisols by solid-state ^{13}C, ^{27}Al, and ^{29}Si NMR and by C stable isotopic ratio, $\delta^{13}C$. Geoderma 136, 696–707.

Huang Y.-T., Lowe D. J., Churchman G. J., Schipper L. A., Cursons R., Zhang H., Chen T.-Y. and Cooper A. (2016) DNA adsorption by nanocrystalline allophane spherules and nanoaggregates, and implications for carbon sequestration in Andisols. Appl. Clay Sci. 120, 40–50.

Ildefonse P., Kirkpatrick R. J., Montez B., Calas G., Flank A. M. and Lagarde P. (1994) ^{27}Al MAS NMR and aluminum X-ray absorption near edge structure study of imogolite and allophanes. Clays Clay Miner. 42, 276–287.

Inoue K. and Huang P. M. (1986) Influence of selected organic ligands on the formation of allophane and imogolite. Soil Sci. Soc. Am. J. 50, 1623–1633.

Inoue K. and Huang P. M. (1990) Perturbation of imogolite formation by humic substances. Soil Sci. Soc. Am. J. 54, 1490.

International Mineralogical Association (2023) The new IMA list of minerals – A work in progress. Updated: July 2023. Retrieved on 19.7.2023. http://cnmnc.units.it/master_list/IMA_Master_List_%282023-07%29.pdf

IUSS Working Group WRB (2022) World Reference Base for Soil Resources. International soil classification system for naming soils and creating legends for soil maps. 4th edition. International Union of Soil Sciences (IUSS), Vienna.

Iyoda F., Hayashi S., Arakawa S., John B., Okamoto M., Hayashi H. and Yuan G. (2012) Synthesis and adsorption characteristics of hollow spherical allophane nano-particles. Appl. Clay Sci. 56, 77–83.

Kaiser K. (1998) Fractionation of dissolved organic matter affected by polyvalent metal cations. Org. Geochem. 28, 849–854.

Kaiser K. and Guggenberger G. (2003) Mineral surfaces and soil organic matter. Eur. J. Soil Sci. 54, 219–236.

Kaiser K., Guggenberger G., Haumaier L. and Zech W. (1997) Dissolved organic matter sorption on subsoils and minerals studied by ^{13}C-NMR and DRIFT spectroscopy. Eur. J. Soil Sci. 48, 301–310.

Kaiser K. and Kalbitz K. (2012) Cycling downwards - dissolved organic matter in soils. Soil Biol. Biochem. 52, 29–32.

Keiluweit M., Nico P. S., Kleber M. and Fendorf S. (2016) Are oxygen limitations under recognized regulators of organic carbon turnover in upland soils? Biogeochemistry 127, 157–171.

Kleber M., Eusterhues K., Keiluweit M., Mikutta C., Mikutta R. and Nico P. S. (2015) Mineral-Organic Associations: Formation, Properties, and Relevance in Soil Environments. Adv. Agron. 130, 1–140.

Kleber M., Mikutta C. and Jahn R. (2004) Andosols in Germany - Pedogenesis and properties. Catena 56, 67-83-67–83.

Kobayashi Y. and Aomine S. (1967) Mechanism of inhibitory effect of allophane and montmorillonite on some enzymes. Soil Sci. Plant Nutr. 13, 189–194.

Kramer M. G., Sanderman J., Chadwick O. A., Chorover J. and Vitousek P. M. (2012) Long-term carbon storage through retention of dissolved aromatic acids by reactive particles in soil. Glob. Change Biol. 18, 2594–2605.

Kubota T. (1972) Aggregate-formation of allophanic soils: Effect of drying on the dispersion of the soils. Soil Sci. Plant Nutr. 18, 79–97.

Kubota T. (1975) Role of hydroxyaluminium ions in the interparticle bonding of layer-aluminosilicate clays. Soil Sci. Plant Nutr. 21, 1–12.

Kögel-Knabner I. (2002) The macromolecular organic composition of plant and microbial residues as inputs to soil organic matter. Soil Bio. Biochem. 34, 139–162.

Kögel-Knabner I., Guggenberger G., Kleber M., Kandeler E., Kalbitz K., Scheu S., Eusterhues K. and Leinweber P. (2008) Organo-mineral associations in temperate soils: Integrating biology, mineralogy, and organic matter chemistry. J. Plant. Nutr. Soil Sci. 171, 61–82.

Levard C. and Basile-Doelsch I. (2016) Geology and mineralogy of imogolite-type materials. Dev. Clay Sci. 7, 49–65.

Levard C., Doelsch E., Basile-Doelsch I., Abidin Z., Miche H., Masion A., Rose J., Borschneck D. and Bottero J.-Y. (2012) Structure and distribution of allophanes, imogolite and proto-imogolite in volcanic soils. Geoderma 183–184, 100–108.

Lilienfein J., Qualls R. G., Uselman S. M. and Bridgham S. D. (2004) Adsorption of dissolved organic carbon and nitrogen in soils of a weathering chronosequence. Soil Sci. Soc. Am. J. 68, 292.

Liu C. and Huang P. M. (2003) Kinetics of lead adsorption by iron oxides formed under the influence of citrate. Geochim. Cosmochim. Acta 67, 1045–1054.

Lowe D. J. (1995) Teaching clays: From ashes to allophane. In: Clays Controlling the Environment (Eds. G. J. Churchman, R. W. Fitzpatrick, R.A. Eggleton), pp. 19–23. CSIRO Publishing, Melbourne.

von Lützow M. V., Kögel-Knabner I., Ekschmitt K., Matzner E., Guggenberger G., Marschner B. and Flessa H. (2006) Stabilization of organic matter in temperate soils: Mechanisms and their relevance under different soil conditions - A review. Eur. J. Soil Sci. 57, 426–445.

MacKenzie K. J. D., Bowden M. E. and Meinhold R. H. (1991) The structure and thermal transformations of allophanes studied by ^{29}Si and ^{27}Al high resolution solid-state NMR. Clays Clay Miner. 39, 337–346.

Masion A., Thomas F., Bottero J.-Y., Tchoubar D. and Tekely P. (1994) Formation of amorphous precipitates from aluminum-organic ligands solutions: Macroscopic and molecular study. J. Non-Cryst. Solids 171, 191–200.

Mathieu J. A., Hatté C., Balesdent J. and Parent É. (2015) Deep soil carbon dynamics are driven more by soil type than by climate: A worldwide meta-analysis of radiocarbon profiles. Glob. Change Biol. 21, 4278–4292.

Matus F., Rumpel C., Neculman R., Panichini M. and Mora M. L. (2014) Soil carbon storage and stabilisation in andic soils: A review. Catena 120, 102–110.

Menezes-Blackburn D., Jorquera M., Gianfreda L., Rao M., Greiner R., Garrido E. and de la Luz Mora M. (2011) Activity stabilization of *Aspergillus niger* and *Escherichia coli* phytases immobilized on allophanic synthetic compounds and montmorillonite nanoclays. Bioresour. Technol. 102, 9360–9367.

Mikutta C. and Kretzschmar R. (2008) Synthetic coprecipitates of exopolysaccharides and ferrihydrite. Part II: Siderophore-promoted dissolution. Geochim. Cosmochim. Acta 72, 1128–1142.

Mikutta C., Mikutta R., Bonneville S., Wagner F., Voegelin A., Christl I. and Kretzschmar R. (2008) Synthetic coprecipitates of exopolysaccharides and ferrihydrite. Part I: Characterization. Geochim. Cosmochim. Acta 72, 1111–1127.

Mikutta R., Lorenz D., Guggenberger G., Haumaier L. and Freund A. (2014) Properties and reactivity of Fe-organic matter associations formed by coprecipitation versus adsorption: Clues from arsenate batch adsorption. Geochim. Cosmochim. Acta 144, 258–276.

Mikutta R. and Mikutta C. (2006) Stabilization of organic matter at micropores (<2 nm) in acid forest subsoils. Soil Sci. Soc. Am. J. 70, 2049–2056.

Mikutta R., Mikutta C., Kalbitz K., Scheel T., Kaiser K. and Jahn R. (2007) Biodegradation of forest floor organic matter bound to minerals via different binding mechanisms. Geochim. Cosmochim. Acta 71, 2569–2590.

Mikutta R., Schaumann G. E., Gildemeister D., Bonneville S., Kramer M. G., Chorover J., Chadwick O. A. and Guggenberger G. (2009) Biogeochemistry of mineral-organic associations across a long-term mineralogical soil gradient (0.3-4100 kyr), Hawaiian Islands. Geochim. Cosmochim. Acta 73, 2034–2060.

Mikutta R., Zang U., Chorover J., Haumaier L. and Kalbitz K. (2011) Stabilization of extracellular polymeric substances (*Bacillus subtilis*) by adsorption to and coprecipitation with Al forms. Geochim. Cosmochim. Acta 75, 3135–3154.

Miltner A. and Zech W. (1998) Carbohydrate decomposition in beech litter as influenced by aluminium, iron and manganese oxides. Soil Bio. Biochem. 30, 1–7.

Mitchell B. D., Farmer V. C. and McHardy W. J. (1964) Amorphous inorganic materials in soils. Adv. Agron. 16, 327–383.

Mukherjee S., Bartlow V. M. and Nair S. (2005) Phenomenology of the growth of single-walled aluminosilicate and aluminogermanate nanotubes of precise dimensions. Chem. Mater. 17, 4900–4909.

Munevar F. and Wollum A. G. (1977) Effects of the addition of phosphorus and inorganic nitrogen on carbon and nitrogen mineralization in Andepts from Colombia. Soil Sci. Soc. Am. J. 41, 540–545.

Nickel E. H. (1995) The definition of a mineral. Can. Mineral. 33, 689–690.

Nierop K. G. J., Van Bergen P. F., Buurman P. and Van Lagen B. (2005) NaOH and $Na_4P_2O_7$ extractable organic matter in two allophanic volcanic ash soils of the Azores Islands - A pyrolysis GC/MS study. Geoderma 127, 36–51.

Nishikiori H., Shindoh J., Takahashi N., Takagi T., Tanaka N. and Fujii T. (2009) Adsorption of benzene derivatives on allophane. Appl. Clay Sci. 43, 160–163.

Olander L. P. and Vitousek P. M. (2000) Regulation of soil phosphatase and chitinase activity by N and P availability Biogeochemistry 49, 175–190.

Parfitt R. L., Fraser A. R., Russell J. D. and Farmer V. C. (1977) Adsorption on hydrous oxides: II. Oxalate, benzoate and phosphate on gibbsite. J. Soil Sci. 28, 40–47.

Parfitt R. L., Furkert R. J. and Henmi T. (1980) Identification and structure of two types of allophane from volcanic ash soils and tephra. Clays Clay Miner. 28, 328–334.

Parfitt R. L., Yuan G. and Theng B. K. G. (1999) A ^{13}C-NMR study of the interactions of soil organic matter with aluminium and allophane in podzols. Eur. J. Soil Sci. 50, 695–700.

Piña R.G. and Cervantes C. (1996) Microbial interactions with aluminium. BioMetals 9, 311–316.

Pokrovski G. S. and Schott J. (1998) Experimental study of the complexation of silicon and germanium with aqueous organic species: Implications for germanium and silicon transport and Ge/Si ratio in natural waters. Geochim. Cosmochim. Acta 62, 3413–3428.

Quiquampoix H., Servagent-Noinvilee S. and Baron M. (2002) Enzyme adsorption on soil mineral surfaces and consequences for the catalytic activity. In: Enzymes in the Environment - Activity, Ecology and Applications (Eds. R. G. Burns and R. P. Dick), pp. 285–306. Taylor and Francis Group, New York.

Rasmussen C., Heckman K., Wieder W. R., Keiluweit M., Lawrence C. R., Berhe A. A., Blankinship J. C., Crow S. E., Druhan J. L., Pries C. E. H., Marin-Spiotta E., Plante A. F., Schädel C., Schimel J. P., Sierra C. A., Thompson A. and Wagai R. (2018) Beyond clay: Towards an improved set of variables for predicting soil organic matter content. Biogeochemistry 137, 297–306.

Rennert T., Eusterhues K., Hiradate S., Breitzke H., Buntkowsky G., Totsche K. U. and Mansfeldt T. (2014) Characterisation of Andosols from Laacher See tephra by wet-chemical and spectroscopic techniques (FTIR, ^{27}Al-, ^{29}Si-NMR). Chem. Geol. 363, 13–21.

Roberts J. A. (2004) Inhibition and enhancement of microbial surface colonization: The role of silicate composition. Chem. Geol. 212, 313–327.

Ross D. J. (1983) Invertase and amylase activities as influenced by clay minerals, soil-clay fractions and topsoils under grassland. Soil Bio. Biochem. 15, 287–293.

Rouff A. A., Phillips B. L., Cochiara S. G. and Nagy K. L. (2012) The effect of dissolved humic acids on aluminosilicate formation and associated carbon sequestration. Appl. Environ. Soil Sci. 2012.

Rousseaux J. M. and Warkentin B. P. (1976) Surface properties and forces holding water in allophane soils. Soil Sci. Soc. Am. J. 40, 446–451.

Sanderman J., Maddern T. and Baldock J. (2014) Similar composition but differential stability of mineral retained organic matter across four classes of clay minerals. Biogeochemistry 121, 409–424.

Scharlemann J. P., Tanner E. V. Hiederer R. and Kapos V. (2014) Global soil carbon: Understanding and managing the largest terrestrial carbon pool. Carbon Manag. 5, 81–91.

Scheel T., Haumaier L., Ellerbrock R. H., Rühlmann J. and Kalbitz K. (2008) Properties of organic matter precipitated from acidic forest soil solutions. Org. Geochem. 39, 1439–1453.

Scheidegger A. M. and Sparks D. L. (1996) A critical assessment of sorption-desorption mechanisms at the soil mineral/water interface. Soil Sci. 161, 813–831.

Schneider M. P. W., Scheel T., Mikutta R., van Hees P., Kaiser K. and Kalbitz K. (2010) Sorptive stabilization of organic matter by amorphous Al hydroxide. Geochim. Cosmochim. Acta 74, 1606–1619.

Schuur E. A. and Matson P. A. (2001) Net primary productivity and nutrient cycling across a mesic to wet precipitation gradient in Hawaiian montane forest. Oecologia 128, 431–442.

Shindo H., Watanabe D., Onaga T., Urakawa M., Nakahara O. and Huang Q. (2002) Adsorption, activity, and kinetics of acid phosphatase as influenced by selected oxides and clay minerals Soil Sci. Plant Nutr. 48, 763–767.

Singh M., Sarkar B., Hussain S., Ok Y. S., Bolan N. S. and Churchman G. J. (2017) Influence of physico-chemical properties of soil clay fractions on the retention of dissolved organic carbon. Environ. Geochem. Health, 1335–1350.

Smith K. A., Kirkpatrick R. J., Oldfield E. and Henderson D. M. (1983) High-resolution silicon-29 nuclear magnetic resonance spectroscopic study of rock-forming silicates Amer Mineral. 68, 1206–1215.

Spohn M. and Schleuss P.-M. (2019) Addition of inorganic phosphorus to soil leads to desorption of organic compounds and thus to increased soil respiration. Soil Biol. Biochem. 130, 220–226.

Sposito G. (2016) The chemistry of soils. Oxford University Press, New York.

Stahr K. and Nakai M. (1984) Der Nachweis von Imogulit in sauren Braunerden und Podsolen des Südschwarzwaldes und seine Bedeutung für die Bodenentwicklung. Mitteilungen Dtsch. Bodenkd. Ges. 39, 53–58.

Su C., Harsh J. B. and Bertsch P. M. (1992) Sodium and chloride sorption by imogolite and allophanes. Clays Clay Miner. 40, 280–286.

Takahashi T. and Dahlgren R. A. (2016) Nature, properties and function of aluminum-humus complexes in volcanic soils. Geoderma 263, 110–121.

Theng B. K. G., Russell M., Churchman G. J. and Parfitt R. L. (1982) Surface properties of allophane, halloysite, and imogolite. Clays Clay Miner. 30, 143–149.

Thill A. (2016) From Molecular Precursor to Imogolite Nanotubes. Dev. Clay Sci. 7, 429–457.

Tonneijck F. H., Jansen B., Nierop K. G. J., Verstraten J. M., Sevink J. and De Lange L. (2010) Towards understanding of carbon stocks and stabilization in volcanic ash soils in natural Andean ecosystems of northern Ecuador. Eur. J. Soil Sci. 61, 392–405.

Torn M. S., Trumbore S. E., Chadwick O. A., Vitousek P. M. and Hendricks D. M. (1997) Mineral control of soil organic carbon storage and turnover. Nature 389, 170–173.

Wada K., 1989. Allophane and imogolite. In: Minerals in Soil Environments. (Eds. J. B. Dixon and J. B. Weed), pp. 1051–1087. Soil Science Society of America, Madison.

Wada S.-I. and Wada K. (2014) Visualization of the hollowness in unit particles of allophane and imogolite. J. Fac. Agric. Kyushu Univ. 59, 369–372.

Wagai R., Kajiura M., Uchida M. and Asano M. (2018) Distinctive roles of two aggregate binding agents in allophanic andisols: Young carbon and poorly-crystalline metal phases with old carbon. Soil Syst. 2, 1–23.

Wells N. and Theng B. K. G. (1988) The cracking behaviour of allophane- and ferrihydrite-rich materials; Effect of pretreatment and material amendments. Appl. Clay Sci. 3, 237–252.

Woignier T., Rangon L., Clostre F., Mottes C., Cattan P., Primera J. and Jannoyer M. (2019) Physical limitation of pesticides (chlordecone) decontamination in volcanic soils: Fractal approach and numerical simulation. Environ. Sci. Pollut. Res.

Yoshinaga N. and Aomine S. (1962) Imogolite in some ando soils. Soil Sci. Plant Nutr. 8, 22–29.

Zechmeister-Boltenstern S., Keiblinger K. M., Mooshammer M., Peñuelas J., Richter A., Sardans J. and Wanek W. (2015) The application of ecological stoichiometry to plant-microbial-soil organic matter transformations. Ecol Monogr 85, 133–155.

Zhou Q., Maurice P. A. and Cabaniss S. E. (2001) Size fractionation upon adsorption of fulvic acid on goethite: Equilibrium and kinetic studies. Geochim. Cosmochim. Acta 65, 803–812.

Zimmerman A. R., Chorover J., Goyne K. W. and Brantley S. L. (2004a) Protection of mesopore-adsorbed organic matter from enzymatic degradation. Environ. Sci. Technol. 38, 4542–4548.

Zimmerman A. R., Goyne K. W., Chorover J., Komarneni S. and Brantley S. L. (2004b) Mineral mesopore effects on nitrogenous organic matter adsorption. Org. Geochem. 35, 355–375.

Zunino H., Borie F., Aguilera S., Martin J. P. and Haider K. (1982) Decomposition of ^{14}C-labeled glucose, plant and microbial products and phenols in volcanic ash-derived soils of chile. Soil Biol. Biochem. 14, 37–43.

Chapter 2

Synthesis of short-range ordered aluminosilicates at ambient conditions

Coauthors: Hergen Breitzke, Gerd Buntkowsky, Erik Reimhult, Max Willinger, Thilo Rennert

Scientific Reports (2021) 11:4207

https://doi.org/10.1038/s41598-021-83643-w

Abstract

We report here on structure-related aggregation effects of short-range ordered aluminosilicates (SROAS) that have to be considered in the development of synthesis protocols and may be relevant for the properties of SROAS in the environment. We synthesized SROAS of variable composition by neutralizing aqueous aluminium chloride with sodium orthosilicate at ambient temperature and pressure. We determined elemental composition, visualized morphology by microscopic techniques, and resolved mineral structure by solid-state ^{29}Si and ^{27}Al nuclear magnetic resonance and Fourier-transform infrared spectroscopy. Nitrogen sorption revealed substantial surface loss of Al-rich SROAS that resembled proto-imogolite formed in soils and sediments due to aggregation upon freezing. The effect was less pronounced in Si-rich SROAS, indicating a structure-dependent effect on spatial arrangement of mass at the submicron scale. Cryomilling efficiently fractured aggregates but did not change the magnitude of specific surface area. Since accessibility of surface functional groups is a prerequisite for sequestration of substances, elucidating physical and chemical processes of aggregation as a function of composition and crystallinity may improve our understanding of the reactivity of SROAS in the environment.

Introduction

Sufficient release of aluminium (Al) and silicon (Si) by weathering of siliceous parent material facilitates precipitation of hydrous, short-range ordered aluminosilicates (SROAS). Accumulation of these phases results in coatings and alteromorphs in volcanic rocks [1,2], clay-sized particles in andic soils [3–5] or stream deposits from waters passing through extrusive rocks [6,7]. Formation of SROAS is not limited to volcanic parent material, but also takes place along pedogenetic transformation of more crystalline siliceous rocks [8–10]. The presence of SROAS imposes peculiar properties on soil material with respect to retention of plant nutrients [11], pollutants [12] and degradation products of soil organic matter (SOM) [13], which promotes carbon sequestration in andic soils [14]. Efficient sorption of various compounds is ascribed to large surface areas and the microporous nature of SROAS, including the presence of reactive functional groups [15]. To investigate molecular interactions in detail, preparation of mineral analogues by synthesis is a common procedure in environmental research, since physical separation of SROAS from natural samples may not be sufficient with respect to mass or selectivity. For instance, synthetic SROAS were used to study their interactions with extracellular enzymes in soils [16,17], adsorption mechanisms of potentially toxic metals [18,19], and retention of organic and inorganic anions [20].

Surface properties of SROAS are fundamentally related to their structure as it governs the quantity, reactivity and arrangement of functional groups. Microscopic techniques revealed that SROAS can develop distinct morphologies at the nanoscale, such as tubes and hollow spheres [21,22]. Tube-shaped SROAS have a well-defined structure and are termed imogolite [23]. Imogolite occurs as bundles of tubes with external diameters of approximately 2 nm that can reach lengths of several micrometres by anisotropic crystallization [8,21]. Its structure is built up by a dioctahedral Al sheet constituting the outer surface, with single Si tetrahedra linked to three Al octahedra inside the tube [23]. This specific configuration of Si can be detected by solid-state ^{29}Si nuclear magnetic resonance (NMR) spectroscopy, henceforth denoted as $Q^0(3Al)$ [24]. Because of its morphology, imogolite offers porosity provided by pores with diameters < 1 nm [25]. Allophane is a generic term, referring to structurally less defined SROAS with variable chemical compositions that are classified according to their Al:Si ratio in the first instance [26]. Particularly Al-rich compounds (Al:Si ≥ 2) may contain Si in $Q^0(3Al)$ coordination and may be termed proto-imogolite, implying their function as precursors of more ordered phases [26]. As single hydroxyl groups coordinated to Al nuclei at defect sites are more reactive than bridging hydroxyls, adsorption capacity by ligand exchange decreases with crystallinity [27,28]. Given a sufficient Si supply, the Al:Si ratio decreases close to 1, and the atomic arrangement is more similar to tectosilicates, including Al in tetrahedral coordination (Al^{IV}) [29]. As a result, particles exert permanent negative charge and exhibit fewer sites prone to ligand exchange due to a larger contribution of silanol groups [27,30]. Structural models that assume primary particles of

both Al-rich and Si-rich SROAS to be hollow spheres have been proposed [31,32], but have seldom been unambiguously verified in natural and synthetic samples. As crystallisation and assembly of precursors are likely inhibited in soil environments, respective SROAS may rather be perceived as fragments and poorly defined precursors of more ordered varieties [33].

We aimed at synthesizing compounds that mimic pristine surfaces of SROAS forming at the initial stages of weathering. We thus employed ambient temperature and pressure conditions. Since organic species interfere with precipitation processes [34] and may remain in the precipitate, we performed synthesis in aqueous media from inorganic salts of weakly complexing counter ions. We achieved precipitation of SROAS by neutralizing an acid Al chloride solution with an alkaline sodium (Na) orthosilicate solution [35,36]. To obtain precipitates with different Al:Si ratios, we varied the input of Si to give molar concentration ratios of 1, 1.5 and 2. We used a monomeric Si source to favour the formation of Si in Q^0(3Al) coordination and to minimize the inheritance of amorphous silica ($SiO_{2(am)}$), but worked at decimolar concentrations, potentially enabling its formation. We report here on the structure of synthesized SROAS, studied by X-ray diffractrometry (XRD), Fourier-transform infrared (FTIR) and solid-state ^{27}Al and ^{29}Si NMR spectroscopy, and its consequences on specific surface area (SSA) of dry solids because we consider them relevant for future syntheses and possibly the behaviour of similar minerals in soils and sediments. Furthermore, we describe the effects of cryomilling on the physical and structural properties of SROAS.

Results and discussion

Morphology and composition of SROAS

Elemental analysis of SROAS revealed that an increase in Si supply successfully led to advanced Si incorporation into the solids, resulting in Al:Si ratios of 2.6, 2.1 and 1.4 in the precipitates (Table 1). Silicon incorporation into the solid was accompanied by retention of Na, as observed by Na contents of 0.3, 1.8, and 23.1 mg g^{-1} with decreasing Al:Si ratios. This points to different amounts of negatively charged sites to be balanced by Na. In the following, we will refer to SROAS according to the classification in Al-rich (Al:Si ≥ 2) and Si-rich (Al:Si ≤ 2) [26], giving the Al:Si ratio in parentheses to identify an Al-rich compound. All solids exhibited larger Al:Si ratios than those originally employed in synthesis batches, evidencing preferential loss of Si during dialysis. Relative to the amount of Si expected with complete incorporation into the solid and calculated from Al content and initial Al:Si ratios, the amount of Si in the precipitates was lower by 22 to 30%. This corresponds to a portion of 7 to 19 mmol Si l^{-1} in the retentate, which is a cautious estimation under the assumption of no Al loss. This value is well beyond the solubility of $SiO_{2(am)}$ at pH 7 [37]. Provided an excess of Si species was unaffected by the presence of Al, the kinetics of Si polymerization allow formation of $SiO_{2(am)}$ within the timeframe of neutralization [38]. Depolymerization rates of $SiO_{2(am)}$ are also sufficient to consider

its dissolution during dialysis [39]. However, incomplete incorporation of Si into SROAS at ambient synthesis conditions but concentrations below 2 mM Si was reported previously and shown to depend on the Al:Si ratio, indicating Al speciation to be a controlling factor in Si removal [40]. Furthermore, it was shown that Si-rich SROAS are less stable, leading to a structure-dependent preferential mobilisation of Si [41,42]. Overall, it is thus very likely that Si was removed from the retentate both by diffusion of Si species that were not incorporated into the solid during neutralization and by the dissolution of unstable Si species during dialysis.

Table 1: Selected chemical and physical properties of synthesized short-range ordered aluminosilicates. Proportion of Si nuclei in imogolite-like coordination (Q^0(3Al)) and Al nuclei in tedrahedral (Al^{IV}), pentahedral (Al^{V}) and octahedral (Al^{VI}) coordination was quantified by solid-state nuclear magnetic resonance spectroscopy. Specific surface area (SSA), total pore volume (V_T) and pore volume of pores with diameters from 2 to 10 nm (V_{2-10}) and 10 to 50 nm (V_{10-50}) was derived from nitrogen sorption analysis.

Initial Al:Si	**Al:Si**	**Al**	**Si**	**Na**	**Si in Q^0(3Al)**	**Al^{IV}**	**Al^{V}**	**Al^{VI}**	**SSA**	**V_T**	**V_{2-10}**	**V_{10-50}**
			[mg g^{-1}]		[% Si]		[% Al]		[m^2 g^{-1}]		[mm^3 g^{-1}]	
1	1.4	200.9	146.3	23.1	9	29	5	66	295.5			
cryomilled									274.2	943	167	617
1.5	2.1	245.2	122	1.8	38	13	6	80	25.6			
cryomilled									43.2	125	47	32
2	2.6	250.1	100.7	0.3	48	9	6	85	0.7			
cryomilled					44	7	6	87	6.9	58	3	20

Dry SROAS differed markedly in bulk density, whereas Si-rich SROAS occupied a much greater volume per mass than Al-rich SROAS (Supplementary Fig. S1). Visualized by environmental scanning electron microscopy (ESEM), all variants appeared as micrometre-sized angular particles with visible breaking edges (Supplementary Fig. S2). The SEM images show that Al-rich SROAS (2.6) consisted by trend of larger particles than Si-rich SROAS and aggregate surfaces of Si-rich SROAS appeared rougher (Fig. 1). Both Al-rich SROAS appeared to have smoother aggregate surfaces than Si-rich SROAS (Supplementary Fig. S3). Similar composition-dependent morphological differences were previously described as glassy versus granular aggregates and related to the mineral structure of precipitates [43].

Mineral structure of SROAS

All materials showed very broad reflections when exposed to Co Kα radiation indicative of a poorly ordered structure (Fig. 2). Reflections centred at *d*-values of 0.77, 0.33 and 0.22 nm are related to the unit cell of imogolite and were reported in several types of SROAS [23,26]. In Al-rich SROAS, reflections close to 0.77 and 0.22 nm were slightly more pronounced than in Si-rich SROAS (see Supplementary Fig. S4), pointing to a structural similarity to proto-imogolite of the former. Reflections at *d*-values above 0.9 nm were previously shown to be related to the

extent of assembly of imogolite-like precursors [44]. Hence, poor resolution in this range evidences that structural repetition occurred at very narrow distances in the precipitates only.

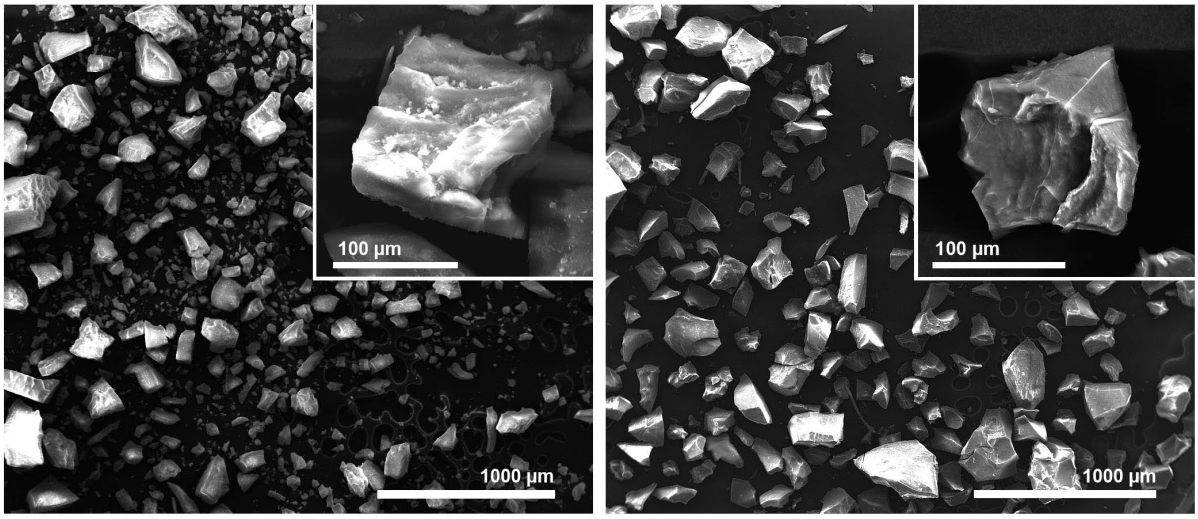

Figure 1: Environmental scanning electron microscopy images of Si-rich (Al:Si 1.4, left) and Al-rich short-range ordered aluminosilicates (Al:Si 2.6, right). The images were taken by Christian Buchmann.

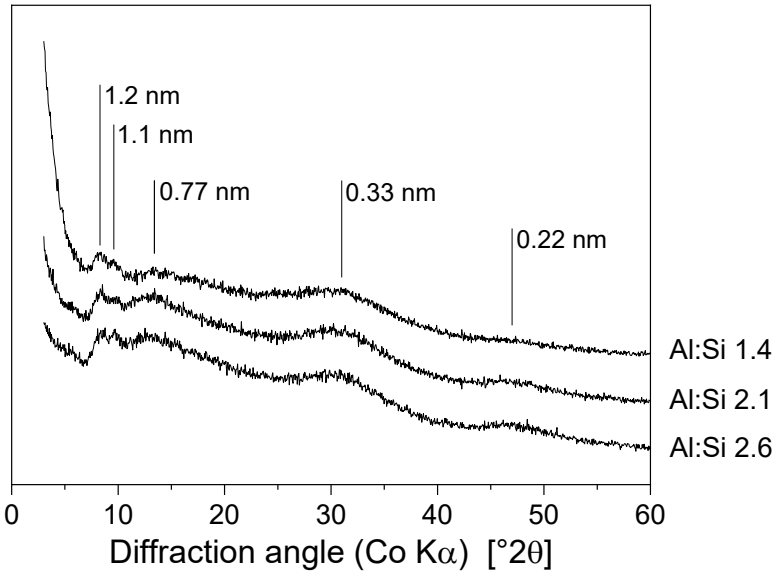

Figure 2: X-ray diffractograms of short-range ordered aluminosilicates. Data is shifted along the y-axis for clarity and given in arbitrary units.

All SROAS caused a symmetric peak centred at around -79 ppm in ^{29}Si-NMR spectra indicative of Si in Q^0(3Al) coordination [24] (Fig. 3A). The proportion of Si nuclei in this chemical environment varied from 9% in Si-rich SROAS to 38% and 48% in Al-rich SROAS with Al:Si ratios of 2.1 and 2.6, respectively (Table 1). The presence of Q^0(3Al) shows that oxolation of Al and Si precursors led to locally defined structural domains, but as the kinetics of this process are poorly resolved, it is not clear whether it occurred during the neutralization step or by structural rearrangement during dialysis. Precipitates that formed within one hour by neutralization at ambient conditions at decimolar concentrations analysed previously

contained Si in Q^0(3Al) coordination together with ill-defined Si environments, indicating that crystallization is initiated rapidly [35,44]. We did not observe any signals at positions above -79 ppm [45], demonstrating that small polynuclear species that may have formed during the initial steps of condensation reactions were consumed prior to structural analysis. At more negative chemical shifts, resonances of ill-defined Si species appeared in the spectra. Condensation of Si tetrahedra causes shielding of Si nuclei and thus upfield chemical shifts, whereas the extent depends on the number of substituted silanol groups [46]. However, the upfield shift is counteracted by reactions with Al, since the deshielding effect of Al leads to a downfield shift with an increasing number of bonds between Al and Si [46]. The intensity distribution between -80 and -110 ppm differed among SROAS, whereas the region at higher chemical shifts was favoured in Al-rich SROAS. This indicates that Si in ill-defined coordination comprised more bonds to Al nuclei on average in Al-rich SROAS. In Si-rich SROAS, bonds between Si tetrahedra contributed, but the amount of Si nuclei bound to four Si tetrahedra was low as indicated by only small spectral intensities at chemical shifts below -95 ppm [46]. Consistent with previous reports, we found that the ratio of Si nuclei in Q^0(3Al) coordination to nuclei in more ill-defined species decreased with Si input [47]. The ill-defined fraction was observed to be lost upon heating, indicating its lower stability and transformation in favour of more ordered phases [35,44,48].

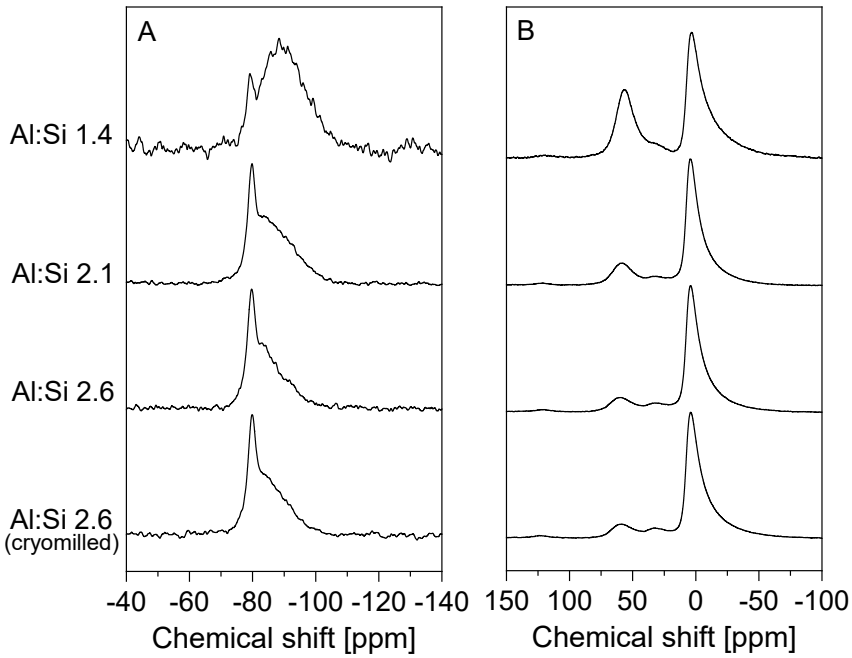

Figure 3: Solid-state nuclear magnetic resonance spectra (A, ^{29}Si; B, ^{27}Al) of short-range ordered aluminosilicates at a line broadening of 50 Hz.

Solid-state ^{27}Al NMR spectra of SROAS exhibited two main peaks attributable to Al^{IV} and Al nuclei in octahedral coordination (Al^{VI}; Fig. 3B) [49]. The latter was detected by an asymmetric peak exhibiting its maximum at 4 ppm in Al-rich SROAS, the intensity of which constituted 80 to 85% of the signal (Table 1). In Si-rich SROAS, this peak was slightly shifted upfield to 3

ppm, and its intensity contribution was lower, amounting to 66%. The chemical shift of Al nuclei is not only affected by the number of adjacent oxygen atoms but also sensitive to the structural arrangement of coordination spheres. This can be exploited to conclude the state of the dioctahedral sheet. Octahedral Al in well-crystallized gibbsite resonates at 9.5 ppm, which is shifted upfield with structural disorder to 8.5 ppm in X-ray amorphous Al hydroxides [50]. Octahedral Al in synthetic imogolite with well-developed tubular morphology exhibits peak maxima at 4 to 6 ppm [44,48]. Both synthetic imogolite precursors and natural samples of proto-imogolite obtained from weathered volcanic ejecta contain Al^{VI} resonating at 4 to 6 ppm [29,33,51]. Low chemical shifts of Al^{VI} nuclei in Al-rich SROAS thus corroborate results derived from XRD. We conclude that assembly of polynuclear species with a local imogolite-like Si environment did not lead to spatially ordered tube- or ball-shaped particles during synthesis, but rather small, likely curved, fragments [44,48].

Both Al- and Si-rich SROAS contained Al^{IV} as observed by peaks centred at 56 to 60 ppm. The contribution of Al^{IV} increased with Si content from 9 to 13% in Al-rich SROAS and a further surge to 29% in Si-rich SROAS (Table 1). Compared with natural samples from altered volcanic ejecta, contents of Al^{IV} in Al-rich SROAS were in the same range, but Si-rich SROAS contained more than natural analogues previously characterized (max. 21%) [29]. A small resonance line at 32 to 34 ppm indicated traces of Al in pentahedral coordination (Al^{V}) [52]. Integration of spectra yielded an area contribution of about 5% for all three SROAS, but quantification is ambiguous due to poor peak separation particularly with Si-rich SROAS [52]. Chemical shifts of Al^{IV} in our precipitates resonated in the same range as observed in natural SROAS samples [29], and its quantity is related to the amount of Si in ill-defined species as observed previously in natural and synthetic samples [47,51]. As Al^{IV} in tectosilicates and glasses resonates in the same range, this points to its incorporation to a network with Si tetrahedra [29]. Besides, transient species that form during neutralization of Al salts and contain Al^{IV} resonating at 62 to 65 ppm can be inherited by a small extent into solid poorly ordered Al phases synthesized at ambient conditions [50,53,54]. Such species may also form during synthesis of SROAS and may be located at the edges of fragments of imogolite precursors [48]. The downfield shift with Al content may thus indicate corresponding structural variations.

Infrared spectra of all SROAS show a broad absorption band centred at 3440 cm^{-1} due to OH stretching in hydroxyl groups and at 1640 cm^{-1} due to OH bending in adsorbed water (Fig. 4A and Supplementary Fig. S5). There was no difference in shape or position between SROAS. An absorption band between 1018 and 975 cm^{-1} is caused by stretching vibrations of oxygen bridges formed by condensation of Si and Al [55]. This band had the highest intensity for all materials. The position of the band shifted to higher wavenumbers with increasing Si content due to its sensitivity to the coordination environment of oxygen atoms [56,57], corroborating the observation by ^{29}Si NMR spectroscopy that the portion of Al-O-Si bonds increased with Al

content relative to the portion of Si-O-Si bonds. All SROAS exhibited an absorption band between 590 and 570 cm^{-1} due to Al-OH bending vibrations [55]. Relative to the intensity of the band in the Si-O-(Al) stretching region, this band decreased in intensity with increasing Si content as observed previously [56]. A shoulder around 870 cm^{-1} may be related to Al-OH bending or Si-OH stretching [23]. Characterization of Si-rich SROAS revealed an absorption maximum at 690 cm^{-1}. Regarding Al-rich SROAS, this band only occurred as a shoulder and its intensity was lower relative to Al-OH bending at 590 to 570 cm^{-1}. This corresponds to a trend previously observed in SROAS with increasing Si content and is caused by differences in coordination environments of OH groups related to Al and Si speciation [56,57]. In contrast to Al-rich (2.6) SROAS, Si-rich SROAS did not cause a distinct band at 348 cm^{-1} indicating that the concentration of Q^0(3Al) was too low to be detected by FTIR (Fig. 4B) [56]. Both phases showed a band at 430 to 440 cm^{-1} related to vibrations of silanol groups, the intensity and frequency of which increased with Si content as observed previously [56].

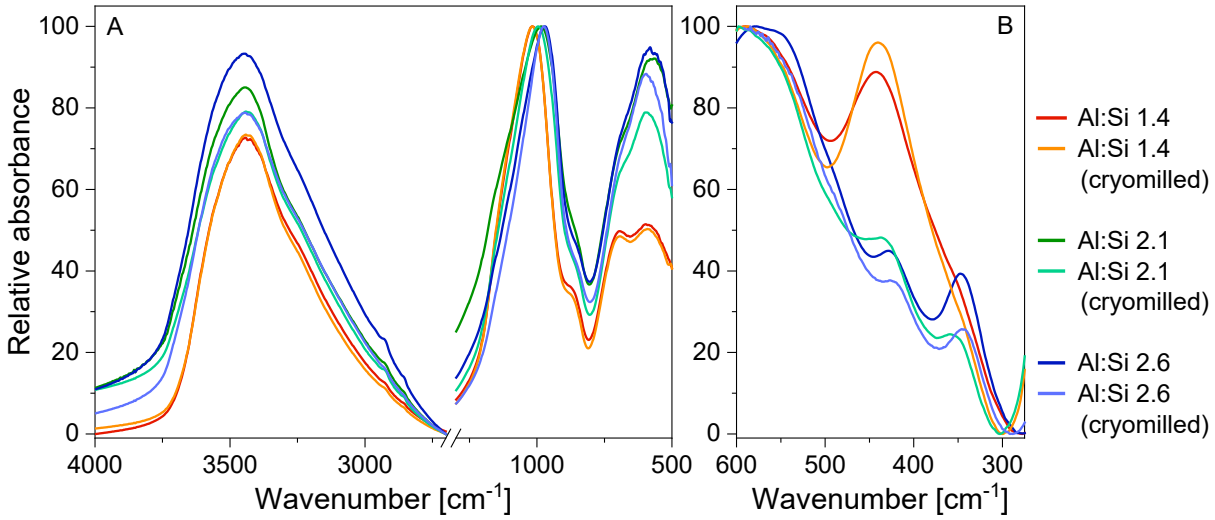

Figure 4: Fourier-transform infrared spectra of short-range ordered aluminosilicates recorded in transmission mode.

Synthesis at high batch volumes and rapid neutralization may favour structural inhomogeneity caused by local pH gradients [45], but we did not observe any indication of Al hydroxides or amorphous silica. Crystalline Al hydroxides are detectable by XRD and FTIR, but we did not observe any distinct corresponding feature [58]. However, since poorly crystalline Al hydroxides may give no reflections in XRD [50,58] and reflections in our diffractograms were poorly resolved, we cannot exclude their formation. Aluminium-rich SROAS did not contain polymerized Si tetrahedra as derived from ^{29}Si NMR spectra, whereas a pure $SiO_{2(am)}$ phase is hardly differentiable from aluminosilicate polymers in Si-rich SROAS.

Physical properties as derived from nitrogen sorption

We studied N_2 sorption to SROAS to derive SSAs by the BET method and found distinct differences between compositional varieties. Nitrogen sorption increased with Si content and

Si-rich SROAS held the greatest SSA of 295.5 $m^2 g^{-1}$ with a C value of 141 (Table 1; Supplementary Table S1). Both parameters decreased in Al-rich (2.1) SROAS to a SSA of 25.6 $m^2 g^{-1}$ and a C value of 110. Nitrogen sorption to Al-rich (2.6) SROAS was surprisingly low. A specific surface area of 0.7 $m^2 g^{-1}$ and a C value < 10 was derived from linear regression of the BET equation but the magnitude of N_2 sorption constrains measurement accuracy [59]. Assuming mineral material to be a monodisperse assemblage of smooth cubic particles, SSA is geometrically related to the edge length by six divided by density [g cm^{-3}] times edge length [µm] [60]. Densities of natural and synthetic SROAS with variable Al:Si ratios have been reported to range between 1.8 and 2.7 g cm^{-3} [61]. It follows that SSA is driven by the mass fraction of particles with an edge length < 1 µm. As assessed from particle visualization by ESEM, the mass fraction of particles < 1 µm was negligible in both Al-rich (2.6) SROAS and minor in Si-rich (1.4) SROAS. Hence, N_2 sorption data of Al-rich (2.6) SROAS corresponded well with microscopic characterization and suggested that the solid consisted of dense aggregates that were not penetrated by N_2 molecules under measurement conditions. On the other hand, particle sizes of Al-rich (2.1) and particularly Si-rich (1.4) SROAS were not sufficient to explain the higher amount of sorbed N_2. This leads to the conclusion that either surface roughness at the submicron scale or intraaggregate porosity advances N_2 sorption to these materials.

Synthetic SROAS can exhibit SSA of up to 700 $m^2 g^{-1}$, but aggregation is a common process restricting surface accessibility of primary particles for N_2 molecules and thus frequently resulting in lower values [36,44,57]. However, very low N_2 sorption with SSA below 5 $m^2 g^{-1}$ is rather rare, but has been previously reported [44,57,62–64]. Notably, and in accordance with our results, such a massive surface reduction did only occur in precipitates with an Al:Si ratio close to 2 and poor spatial order, indicating that this phenomenon is specific of a certain composition. Precipitates synthesized at ambient temperature by Du et al. [44] were structurally very similar to our Al-rich (2.6) SROAS and only developed microporous nature and greater SSA upon assembly to tile- and ultimately tube-shaped particles induced by heating. Crystallization was likely inhibited in synthesis protocols that previously reported exceptionally low SSA [44,57,62–64] either by decimolar concentrations [45], the presence of counter-ions during the heating step [65] or ambient synthesis conditions [44].

As precipitation by neutralization yielded turbid suspensions of small particles, aggregation resulting in micrometre-sized particles was obviously provoked during the dehydration procedure. Drying conditions varied between synthesis protocols that previously observed very low SSA of Al-rich SROAS [44,57,62–64] and included freeze-drying [44,57,64] and drying at 110 °C [63] or were not specified [62]. Outgassing of the samples before N_2 sorption measurements was done at temperatures from 100 to 400 °C, whereas we worked at T = 80 °C, since structural changes were reported at T > 100 °C [66]. Crystallization of poorly ordered Al and iron (Fe) phases is accompanied by a substantial loss of SSA and is possible at T < 100 °C [67,68].

Although SROAS rearranged structurally upon heating to T = 100 < 400 °C, coinciding changes in SSA were small [69,70], indicating that the magnitude of SSA is imposed on the dry solid beforehand. Indeed, we observed that thawing of frozen synthesis batches yielded clear suspensions with rapidly settling particles and thus assumed that aggregation happened primarily during the freezing process. We repeated N_2 sorption analysis of Al-rich (2.6) SROAS obtained by decanting, drying and outgassing at 40 °C. The N_2 sorption capacity of decanted aggregates was not substantially larger (calculated SSA = 1.9 $m^2 g^{-1}$, C < 10, Supplementary Table S1). We thus conclude that processes during freezing determined the physical properties of the dry mineral material.

Formation of dense aggregates from aqueous suspensions of Al and Fe oxides and hydroxides upon freezing was previously observed [71] and can be explained by physical interactions of ice, liquid water and suspended particles [72,73]. As we froze large volumes (400 ml) of suspension at -20 °C, cooling was limited by heat conductance of ice and water and ice formation progressed only slowly from the exterior of the volume inward (ca. 0.6 to 1.4 µm s^{-1}) [71]. At such low freezing rates, particles with a diameter < 1 µm are expelled from the freezing front and transported [72]. This phenomenon is caused by repulsive forces caused by surface tension of a film of liquid water between the freezing front and the particle [72]. The co-occurrence of ice and liquid water induces migration of the latter to the former, usually referred to as cryosuction. When suspensions with sufficient particle concentration are slowly frozen, the combination of particle repulsion and cryosuction leads to a concentrated layer of particles ahead of the freezing front [73,74]. As this layer freezes, colloidal suspensions are segregated on a macroscopic scale into areas with crack-like boundaries between ice and particle enriched zones [73,74]. Similar segregation phenomena are likely responsible for the shape of SROAS aggregates we observed by ESEM as sublimation of ice led to the disintegration of frozen batches. Stress caused by cryosuction and freezing has been observed to be sufficient to overcome electrostatic repulsion between particles and cause particle packing into clusters that do not disintegrate after thawing [71,74,75]. Interfacial effects reducing the mobility of water molecules and inhibiting complete crystallization [76] ultimately limit the dehydration of poorly crystalline solids. Consistently, porosity analysis of Fe (hydr)oxide aggregates indicated that crystallites were separated by a hydration layer [71]. The magnitude of SSA of Al-rich SROAS and the fact that it is not substantially affected by outgassing evidence that inaccessibility of interparticle spaces to N_2 molecules was caused by freezing and homogeneously distributed within the material since otherwise water emission would have created porosity. Small pore sizes and possibly sorbed water likely restricted N_2 diffusion, an effect that is particularly relevant for pores < 1 nm [77]. Taking this effect into account by assuming a maximal pore radius of 2 nm, calculation of the respective particle diameter that is necessary to explain impermeable aggregate surfaces on the basis of cubic close-packing of monodisperse spheres

gives a value of 4.8 nm (see Supplementary information). Considering the hydration layer (0.9 to 2 nm) [71], this calculation illustrates that primary building entities have to be <4 nm as structural analysis already indicated. Consistent with previous reports, we observed an increase in SSA with Si content in poorly ordered SROAS [57,63,78], pointing to a structure-dependent effect on the spatial arrangement of mass at the submicron scale. In summary, increasing incorporation of Si into poorly ordered SROAS or advanced crystallization of Al-rich SROAS seems to cause resistance to compaction and consequently a rise in SSA.

Considering mechanisms and forces responsible for SROAS aggregation, Wells and Childs [79] proposed a model based on the assembly of hollow spheres that recognized the degree of water removal as a measure to quantify the interactions between particles. As long as the hydration layer prevails around particles, van der Waals forces and electrostatic interactions are perceived to be responsible for holding particles together [79], with a possible contribution of aluminol-group condensation [80]. The latter is especially likely during the formation of Al-rich SROAS in our syntheses by concentration of small Al-rich fragments. Our results show that incorporation of Si interferes with aggregation, but the mechanisms are not clear yet. Both the presence of silanol groups and oxygen bridges between Si tetrahedra as well as the formation of Al^{IV} imposes changes on surface properties that may lead to variations in interfacial processes between particles and water dynamics.

Effects of cryomilling on particle size, mineral structure and SSA

We aimed at increasing the yield of particles with diameters <1 µm and greater SSA of mineral material and thus decided to mill SROAS. It was previously shown that SROAS are sensitive to heating and mechanical stress, resulting in structural changes [66,81]. Hence, we employed mechanical treatment of dry material under constant cooling with liquid N_2, i.e. cryomilling. Cryomilling of metallic powders was shown to accelerate fracturing of particles but suppress structural rearrangement [82]. We investigated particle size and morphology in resulting powders by transmission electron microscopy (TEM). We did not find particles with diameters >15 µm, indicating that cryomilling efficiently crushed aggregates already after 2 to 5 min (Supplementary Fig. S6). We found striking differences in particle morphology between Si-rich and Al-rich SROAS (Fig. 5). Both Al-rich SROAS assembled into aggregates of variably sized, dense particles with defined boundaries. On the contrary, Si-rich SROAS appeared as finely differentiated clusters, which could be observed as loose aggregates on the TEM carbon grid but rarely as particles with defined barriers. Many Al-rich SROAS particles with a diameter >300 nm had an angular shape probably retained from disruption of primary material (Supplementary Fig. S7).

Inspection for structural rearrangement by FTIR spectroscopy of cryomilled samples revealed only small changes. Neither spectra showed a shift in the position of stretching vibrations of Si-O-Al bridges (1018 to 975 cm^{-1}), but spectra of both Al-rich SROAS exhibited a small relative

decrease of absorption by Al-OH bending at 595 cm^{-1} (Fig. 4A). At lower wavenumbers, absorption at 348 cm^{-1} in Al-rich SROAS (2.6) decreased, while absorption at 440 cm^{-1} in Si-rich SROAS increased (Fig. 4B). Hence, the spectra point to small changes of Si speciation induced by cryomilling, which led to a particular interest in the behaviour of Si in Q^0(3Al) coordination. We thus repeated solid-state NMR spectroscopic analyses of Al-rich (2.6) SROAS, showing that Si in Q^0(3Al) coordination was largely retained after cryomilling, but small amounts of more ill-defined species were generated by mechanical treatment in spite of low temperatures (Fig. 3A, Table 1). We did not try to resolve such changes in Si-rich SROAS, since ^{29}Si NMR spectroscopy yielded a poor resolution of Si speciation in the primary material.

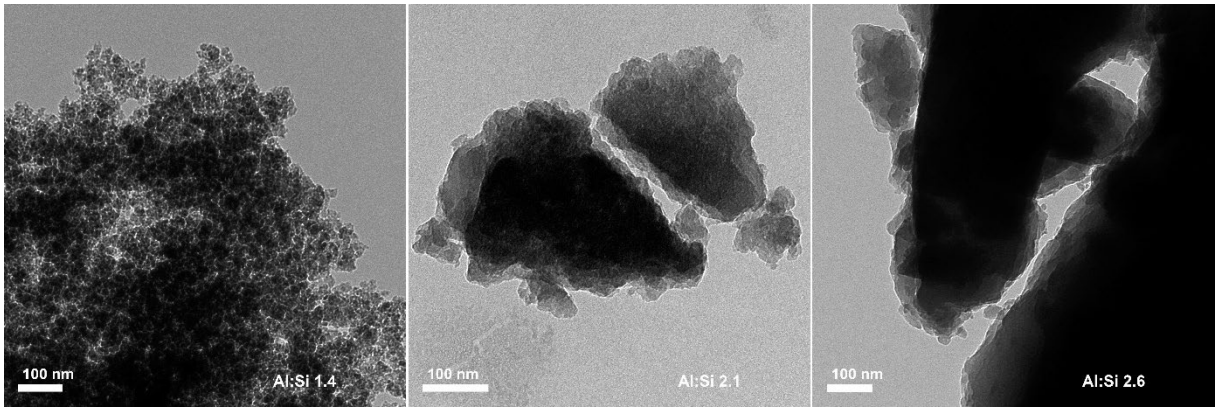

Figure 5: Transmission electron microscopy images of cryomilled Si-rich (Al:Si 1.4, left) and Al-rich (Al:Si 2.1 and 2.6, middle and right, respectively) short-range ordered aluminosilicates.

In addition to particle visualization by TEM, we employed N_2 sorption experiments over the whole range of relative pressure to derive SSA and porosity of cryomilled SROAS. Silicon-rich (1.4) SROAS remained to be the strongest N_2 sorbent after cryomilling. The measured sorption capacity at relative pressures below 0.35 was slightly lower compared to unmilled solid, resulting in a decrease of SSA by 7.2% (Table 1), but effects of this size might be related to measurement inaccuracy. We observed desorption hysteresis at relative pressures above 0.7 (Fig. 6A), indicating the presence of mesopores with diameters from 2 to 50 nm [83]. Evaluation of N_2 sorption data with respect to micropore volume suggested negligible contribution of pores in this size range (< 2 nm) [59]. Nitrogen sorption to Al-rich SROAS increased after cryomilling, causing enhanced SSA (43.2 and 6.9 $m^2\ g^{-1}$ for solids with Al:Si ratios of 2.1 and 2.6, respectively; Table 1). None of the sorption branches exhibited a distinct knee indicating completion of the monolayer and there was thus no evidence of accessible micropores (Figs. 6B, C). For Al-rich (2.1) SROAS, we detected desorption hysteresis between relative pressures of 0.45 and 0.9 evidencing present mesopores to have smaller diameters on average than in Si-rich SROAS. As assessed from the shape of N_2 sorption isotherms (Fig. 6C), Al-rich (2.6) SROAS appeared as a non-porous solid [59]. Nitrogen sorption experiments accorded with TEM observations and confirmed spatial matter segregation in Si-rich SROAS at scales < 100 nm, offering porosity and considerable SSA. On the other hand, Al-rich SROAS consisted of

consolidated particles. Our results demonstrate that nanoscale compaction of synthetic SROAS cannot be reversed by cryomilling as it does not change the magnitude of SSA, limiting the feasibility of a top-down approach to mineral synthesis. Furthermore, structural changes already occurring at short milling durations suggest that prolonged milling is not an option.

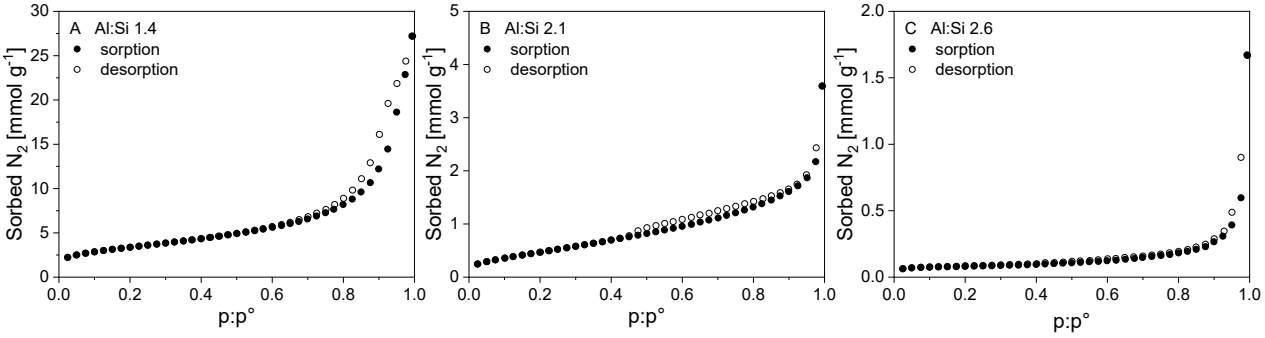

Figure 6: Nitrogen sorption and desorption isotherms at -196 °C of cryomilled short-range ordered aluminosilicates with varying Al:Si ratios (A, 1.4; B, 2.1; C, 2.6).

Implications of structure-related aggregation effects for the reactivity of SROAS in the environment

A comparison of spectroscopic properties of synthesized SROAS with natural analogues supports structural similarity. As assessed from Si speciation and elemental analysis, Al-rich SROAS resembled proto-imogolite phases precipitated from waters percolating shales and volcanic rocks (designated as Derbyshire allophane and Ki-P) [51,84]. Furthermore, FTIR spectra indicated a similar composition to Al-rich (Al:Si > 2.8) samples isolated from Podzols [10]. A Si-rich SROAS separated from andesitic ashes exhibited structural similarity to our synthetic Si-rich SROAS with respect to Al:Si ratio, Si speciation and content of Al^{IV} (designated as Okamoto allophane) [29,51]. Specific surface areas of natural SROAS determined by N_2 sorption ranged from 21 to 478 $m^2\ g^{-1}$ [70,85–87], whereas isotherms indicated the presence of micropores [87]. Values of SSA of naturally precipitated SROAS are thus in the same range as observed for synthetic samples, but as Al:Si ratio and structural properties were scarcely characterized, the relation of composition to SSA in natural samples remains ambiguous.

However, irreversible aggregation is a well-known phenomenon in both bulk soil containing SROAS and particle-size fractions. Andic soil material was irreversibly compacted upon water removal [88] and lost substantial SSA compared to a treatment without capillary stress [89,90]. Freeze-drying of clay fractions from an andic subsoil caused the formation of micrometre-sized aggregates (>20 µm) [91] and aggregation of clay-sized particles was also observed to be caused by air-drying [92]. Saturation deficits at ambient temperature and relative humidity are sufficient to induce a decrease in water retention capacity [93] and sorption capacity of ionic species to SROAS [80,94], evidencing physical reorganization to affect the accessible surface. Both evaporation of water and physical processes occurring during freezing lead to a spatial concentration of mineral mass, which causes particles to interact. The dehydration efficacy

likely depends on the drying method, whereas it may be higher in freezing compared to air-drying at ambient temperatures.

In soils and sediments, the water regime determines the degree of SROAS dehydration. Formation of SROAS requires sufficient silicate weathering that intensifies under a udic moisture regime. However, SROAS aggregation is enhanced by drying so that aggregation is likely most pronounced in soil with fluctuating water contents. Such conditions prevail for example in sandy substrates, where drying can progress into the subsoil. Precipitation of Al-rich SROAS led to induration of subsoil horizons by the formation of continuous coatings of SROAS with Al:Si ratio of about 2 in andesitic deposits [95] and podzolic soils [96,97]. Characterization by FTIR spectroscopy evidenced a coating with Si in Q^0(3Al) conformation [96]. Based on our results, we expect such strongly dehydrated Al-rich precipitates to be relatively unreactive, as aggregation likely decreased accessibility of surface functional groups. Association of SROAS with SOM interferes with physical processes of aggregation and particles assembled less efficiently in topsoils upon drying [92]. SROAS separated from a soil horizon that was characterized by SOM accumulation was structurally different from our precipitates regarding Al speciation, evidencing molecular interactions between SOM and SROAS that affected structure and potentially masked aluminol groups [33]. Besides structure, the water regime and presence of SOM should thus be included in studies on physicochemical mechanisms of SROAS aggregation.

Conclusion

We synthesized SROAS with variable Al:Si ratios that exhibit structural features similar to poorly crystalline phases precipitating in soils and weathered volcanic ejecta. As we employed ambient conditions, precipitates did not develop a ball- or tube-like morphology and thus likely had a functional group distribution similar to natural nanoscale initial weathering products. We propose that aqueous suspensions contained small polynuclear species that resembled precursors of Al- and Si-rich imogolite and allophane. Our results indicate that composition and crystallinity severely alter the accessibility of functional groups due to changes in aggregation mechanisms during dehydration. Incorporation of Si led to an increase in specific surface area, potentially evidencing a physicochemical impact on SROAS reactivity. Studying physical processes causing aggregation of poorly crystalline minerals as a function of structural properties may thus improve our understanding of their adsorption behaviour in the natural environment. Retention of organic substances by SROAS is particularly relevant for carbon sequestration in soils and sorption of nutrients, i.e. phosphate, which affects their bioavailability. With respect to future syntheses, we recommend careful customization of dehydration conditions.

Materials and methods

Precipitation of SROAS

We synthesized SROAS of variable Al:Si ratios at ambient temperature and pressure by neutralizing a 0.2 M aluminium chloride hexahydrate solution ($AlCl_3$; AppliChem GmbH, Darmstadt, Germany) with sodium orthosilicate (Na_4SiO_4; abcr GmbH, Karlsruhe, Germany). Due to the pH conditions of the stock solutions, both reactants were in monomeric form, i.e. Al in hexacoordinated, partially hydrolysed, aquacomplexes (pH < 3) [53] and Si as monomeric silicic acid and dissociated silicate ions [98]. After mixing the stock solutions, the batch volume contained 67 mmol Al and 33, 44 or 67 mmol Si, resulting in molar Al:Si ratios of 1, 1.5 and 2, respectively. Synthesis procedures differed between variants with respect to the course of neutralization. Each synthesis procedure was carried out in triplicate. Titration data is presented in Supplementary Fig. S8. A Si-rich SROAS (Al:Si = 1) was precipitated by mixing 1 l of a 0.2 M $AlCl_3$ solution with 2 l of a 0.1 M Na_4SiO_4 solution under vigorous stirring within approximately 1 min. The $AlCl_3$ solution was acidified with 70 ml of a 1 M HCl solution (Chemsolute, Th. Geyer GmbH & Co. KG, Renningen, Germany) beforehand to keep synthesis pH <7. The final suspension had a pH of 6.6 (± 0.3; glass electrode, InLab Expert Pro, Mettler Toledo, Gießen, Germany) and was stirred for 1 h, during which the pH increased slightly (+ 0.2). An Al-rich SROAS (Al:Si = 2) was synthesized by mixing 1 l of a 0.2 M $AlCl_3$ solution with 1 l deionized H_2O and 1 l of a 0.1 M Na_4SiO_4 solution. The resulting suspension had a pH of 3.8 (± 0.04) and was further neutralized with 234 (± 2) ml of 1 M NaOH (1.17 mol OH^- mol^{-1} Al^{-1}, AppliChem GmbH) within 30 min. Final pH was 6.1 (± 0.1) and stable during a further 30 min of stirring. Another SROAS (Al:Si = 1.5) was precipitated by mixing 1 l of a 0.2 M $AlCl_3$ solution with 2 l of a 0.067 M Na_4SiO_4 solution, resulting in a suspension with pH 4 (± < 0.1) that was neutralized (pH 6.4 ± 0.2) with 131 (± 2) ml 1 M NaOH (0.66 mol OH^- mol^{-1} Al^{-1}). The pH was constant during another 30 min of stirring. Suspensions were subsequently transferred to dialysis membranes with a molecular weight cut-off of 14 kDa (Viskase GmbH, Köln, Germany) and dialysed for one week until the electrical conductivity in the permeate was below 5 µS cm^{-1} for 24 h.

Retrieval and cryomilling of the solids

As separation by centrifugation and filtration was not practicable, we decided to achieve mass retrieval by freeze-drying. After dialysis, about 400 ml of suspension volume were filled into polyethylene bottles and frozen at -20 °C in a conventional freezer. Shortly after complete freezing, the suspensions were freeze-dried and pooled per Al:Si variant. Three bottles of frozen Al-rich SROAS suspensions (initial Al:Si ratio = 2) were excluded from this procedure and thawed at room temperature. Rapidly settling precipitates were decanted, pooled and dried at 40 °C. A portion of each variant of freeze dried material was ground with a ball mill under constant cooling with liquid N_2 (CryoMill, Retsch, Haan, Germany). About 3 g were filled

into the sample chamber, which was then precooled for 3 min and subsequently shaken at a frequency of 30 Hz. Samples did not come into contact with liquid N_2. We chose a shaking time of 2 min for Si-rich SROAS and 5 min for both Al-rich SROAS.

Characterization of unground SROAS

Morphology of the synthesized SROAS was studied by ESEM under low vacuum and acceleration voltage of 30 kV (FEI Quanta 250 ESEM, FEI Company, Hillsboro, United States). Their elemental composition was determined by microwave digestion of 0.1 g in 28 ml deionised water, 2.5 ml 68% HNO_3 and 0.5 ml 40% HF. Aluminium, Si and Na concentrations were quantified by inductively coupled plasma optical emission spectrometry (ICP-OES; Agilent 5110, Agilent Technologies, Waldbronn, Germany). Mineral structure was investigated by XRD, FTIR, ^{27}Al and ^{29}Si NMR spectroscopy. Mineral powders prepared by grinding in a mortar were exposed to Co Kα radiation (λ = 0.179 nm), and diffraction patterns were recorded from 3 to 60 °2θ at a step size of 0.05 °2θ and a counting time of 1.5 s (D500, Siemens, München, Germany). We obtained FTIR spectra at wavenumbers from 4000 to 500 cm^{-1} with the transmission accessory of a LUMOS infrared microscope (Bruker, Ettlingen, Germany). Pellets were prepared from mixtures of 1 mg of ground sample and 200 to 280 mg of KBr. Fifty background spectra were recorded against the atmosphere, and subsequently 100 sample scans accumulated at a resolution of 4 cm^{-1}. Spectra at wavenumbers from 600 to 270 cm^{-1} were measured with a Nicolet 5700 spectrometer accumulating 64 scans at a resolution of 2 cm^{-1} (Thermo Scientific, Darmstadt, Germany). Pellets were prepared at the same mass ratio, but with a hydraulic press. The chemical environment of ^{27}Al and ^{29}Si nuclei was studied by solid-state NMR spectroscopy with direct-polarization (DP) and magic angle spinning (MAS) on a 400 MHz Bruker Avance II+ spectrometer, equipped with a 4 mm H/X MAS probe. Samples were spun in 4 mm zirconia rotors. ^{27}Al NMR spectra were obtained at a resonance frequency of 104.3 MHz and a MAS frequency of 12 kHz. A DP pulse of 22° was applied and relaxation delay was set to 4 s. ^{1}H was decoupled with a tppm20 pulse sequence. Between 64 and 256 scans were accumulated. Chemical shifts are expressed relative to an aqueous solution of $AlCl_3$. ^{29}Si NMR spectra were recorded at a resonance frequency of 79.5 MHz and a MAS frequency of 8 kHz. Decoupling of ^{1}H was achieved with a spinal64 pulse sequence. A number of 2127 to 3072 scans were acquired with DP by a 22° pulse (2 µs) and a delay time of 120 s. ^{29}Si spectra were referenced to tetramethylsilane. All data was collected at an acquisition time of 0.04096 s, 4096 observation points and a spectral width of 50 kHz, giving a resolution of 12.02 Hz. Phase adjustment and baseline correction was conducted with TopSpin 4.0.7 (Bruker). The quantitative contribution of Si nuclei in Q^0(3Al) coordination was derived from fitting Lorentzian functions to spectral data and calculating the proportion of integrals to the total area of the resonance signal (OriginPro 2020, OriginLab Corporation, Northhampton, USA). Spectra were normalized and base line was set to the median of all data

points. The position of the resonance signal of ^{29}Si in $Q^0(3Al)$ coordination was fixed to the maximum of the visible peak at -79 ppm, whereas no specifications were made for other nuclei. Resonance of these ill-defined species was reproduced by 3 to 5 functions with no specification of peak position, height or width (see Supplementary Fig. S9). We first analysed the data at a line broadening >0 Hz to identify positions of local maxima and then repeated the fit with spectra at a line broadening of 0 Hz to obtain integrals. We modelled ^{27}Al NMR spectra at a line broadening of 0 Hz with a combination of Gaussian and Lorentzian functions, whereas neither peak position nor width or height was fixed (see Supplementary Fig. S10). Integrals of functions were ascribed to a coordination of Al according to the chemical shift [49] and summed. We determined the SSA by N_2 sorption to freeze-dried, unground SROAS manometrically at eleven points below a relative pressure of 0.35 with an Autosorb AS 1 at -196 °C (Quantachrome Instruments, Boynton Beach, USA) after degassing the samples at 80 °C until the pressure increase was < 0.067 mbar min^{-1}. Volume was recorded after 5 min of equilibration. Measurements were replicated three times. A sample of Al-rich SROAS obtained by decanting was analysed at 10 points after 2 min equilibration time on a Quantachrome Autosorb iQ (Anton Paar Quanta Tec Inc., USA) after degassing at 40 °C for 24 h [67]. Specific surface area was derived by linear regression with the Brunauer-Emmett-Teller (BET) equation after selecting data points in the range of continuous increase in sorbed N_2 times (p°- p) with p:p° [59].

Characterization of cryomilled SROAS

Structural analysis by FTIR and NMR spectroscopy was conducted as described above. Specific surface area and porosity were analysed by determining both N_2 sorption and desorption isotherms on a Quantachrome Autosorb iQ after degassing at 60 °C for at least 8 h. Specific surface area was calculated as described above. Total pore volume (V_T) was obtained from the volume of sorbed N_2 at p:p° = 0.99. Respective volumes of pores with a diameter in the mesopore range (2-10 nm, 10-50 nm) were derived from the desorption branch according to the Barret-Joyner-Halenda (BJH) method [83]. To visualize particles by TEM, a small portion of mineral material was dispersed in 98% ethanol, deposited on carbon grids and dried protected overnight at room temperature to remove the excess liquid before insertion in the UHV imaging chamber. Images were recorded with a FEI Tecnai G2 (FEI Europe B.V., Biedermannsdorf, Austria) with 160 kV acceleration voltage.

References

1. Gérard, M., Caquineau, S., Pinheiro, J. & Stoops, G. Weathering and allophane neoformation in soils developed on volcanic ash in the Azores. *Eur. J. Soil Sci.* **58**, 496–515 (2007).
2. Jongmans, A. G., Verburg, P., Nieuwenhuyse, A. & van Oort, F. Allophane, imogolite, and gibbsite in coatings in a Costa Rican Andisol. *Geoderma* **64**, 327–342 (1995).

3. Basile-Doelsch, I. *et al.* Mineralogical control of organic carbon dynamics in a volcanic ash soil on La Réunion. *Eur. J. Soil Sci.* **56**, 689–703 (2005).
4. Hiradate, S., Hirai, H. & Hashimoto, H. Characterization of allophanic Andisols by solid-state ^{13}C, ^{27}Al, and ^{29}Si NMR and by C stable isotopic ratio, $\delta^{13}C$. *Geoderma* **136**, 696–707 (2006).
5. Rennert, T. *et al.* Characterisation of Andosols from Laacher See tephra by wet-chemical and spectroscopic techniques (FTIR, ^{27}Al-, ^{29}Si-NMR). *Chem. Geol.* **363**, 13–21 (2014).
6. Henmi, T. The occurrence of allophane in a stream-deposit from Ehime-prefecture, Japan. *Clay Miner.* **14**, 333–338 (1979).
7. Wells, N., Childs, C. W. & Downes, C. J. Silica Springs, Tongariro National Park, New Zealand - analyses of the spring water and characterisation of the alumino-silicate deposit. *Geochim. Cosmochim. Acta* **41**, 1497–1506 (1977).
8. Gustafsson, J. P., Bhattacharya, P. & Karltun, E. Mineralogy of poorly crystalline aluminium phases in the B horizon of Podzols in southern Sweden. *Appl. Geochem.* **14**, 707–718 (1999).
9. Skjemstad, J. O., Fitzpatrick, R. W., Zarcinas, B. A. & Thompson, C. H. Genesis of Podzols on coastal dunes in Southern Queensland. II. Geochemistry and forms of elements as deduced from various soil extraction procedures. *Aust. J. Soil Res.* **30**, 615–644 (1992).
10. Young, A. W., Campbell, A. S. & Walker, T. W. Allophane isolated from a podsol developed on a non-vitric parent material. *Nature* **284**, 46–48 (1980).
11. Parfitt, R. L., Hume, L. J. & Sparling, G. P. Loss of availability of phosphate in New Zealand soils. *J. Soil Sci.* **40**, 371–382 (1989).
12. Woignier, T. *et al.* The pesticide chlordecone is trapped in the tortuous mesoporosity of allophane clays. *Environ. Sci. Pollut. Res.* **25**, 21350–21361 (2018).
13. Kramer, M. G., Sanderman, J., Chadwick, O. A., Chorover, J. & Vitousek, P. M. Long-term carbon storage through retention of dissolved aromatic acids by reactive particles in soil. *Glob. Change Biol.* **18**, 2594–2605 (2012).
14. Basile-Doelsch, I. *et al.* Mineral control of carbon pools in a volcanic soil horizon. *Geoderma* **137**, 477–489 (2007).
15. Filimonova, S., Kaufhold, S., Wagner, F. E., Häusler, W. & Kögel-Knabner, I. The role of allophane nano-structure and Fe oxide speciation for hosting soil organic matter in an allophanic Andosol. *Geochim. Cosmochim. Acta* **180**, 284–302 (2016).
16. Allison, S. D. Soil minerals and humic acids alter enzyme stability: Implications for ecosystem processes. *Biogeochemistry* **81**, 361–373 (2006).
17. Menezes-Blackburn, D. *et al.* Activity stabilization of Aspergillus niger and Escherichia coli phytases immobilized on allophanic synthetic compounds and montmorillonite nanoclays. *Bioresour. Technol.* **102**, 9360–9367 (2011).
18. Baldermann, A. *et al.* Removal of barium, cobalt, strontium, and zinc from solution by natural and synthetic allophane adsorbents. *Geosci. Switz.* **8**, 309 (2018).
19. Clarke, C. J. & McBride, M. B. Chemisorption of Cu(II) and Co(II) on allophane and imogolite. *Clays Clay Miner.* **32**, 300–310 (1984).
20. Jara, A. A., Violante, A., Pigna, M. & de la Luz Mora, M. Mutual interactions of sulfate, oxalate, citrate, and phosphate on synthetic and natural allophanes. *Soil Sci. Soc. Am. J.* **70**, 337 (2006).

21. Henmi, T. & Wada, K. Morphology and composition of allophane. *Am. Mineral.* **61**, 379–390 (1976).
22. Wada, S.-I. & Wada, K. Visualization of the hollowness in unit particles of allophane and imogolite. *J. Fac. Agric. Kyushu Univ.* **59**, 369–372 (2014).
23. Cradwick, P. D. G. *et al.* Imogolite, a hydrated aluminum silicate of tubular structure. *Nat. Phys. Sci.* **240**, 187–189 (1972).
24. Barron, P. F., Wilson, M. A., Campbell, A. S. & Frost, R. L. Detection of imogolite in soils using solid state ^{29}Si NMR. *Nature* **299**, 616–618 (1982).
25. Ackerman, W. C. *et al.* Gas/vapor adsorption in imogolite: A microporous tubular aluminosilicate. *Langmuir* **9**, 1051–1057 (1993).
26. Levard, C. & Basile-Doelsch, I. Geology and Mineralogy of Imogolite-Type Materials. in *Developments in Clay Science* (eds. Yuan, P., Thill, A. & Bergaya, F.) vol. 7 49–65 (Elsevier B.V., 2016).
27. Clarke, C. J. & McBride, M. B. Cation and anion retention by natural and synthetic allophane and imogolite. *Clays Clay Miner.* **32**, 291–299 (1984).
28. Theng, B. K. G., Russell, M., Churchman, G. J. & Parfitt, R. L. Surface properties of allophane, halloysite, and imogolite. *Clays Clay Miner.* **30**, 143–149 (1982).
29. Ildefonse, P. *et al.* ^{27}Al MAS NMR and aluminum X-ray absorption near edge structure study of imogolite and allophanes. *Clays Clay Miner.* **42**, 276–287 (1994).
30. Su, C., Harsh, J. B. & Bertsch, P. M. Sodium and chloride sorption by imogolite and allophanes. *Clays Clay Miner.* **40**, 280–286 (1992).
31. Childs, C. W., Parfitt, R. L. & Newman, R. H. Structural studies of Silica Springs allophane. *Clay Miner.* **25**, 329–341 (1990).
32. Creton, B., Bougeard, D., Smirnov, K. S., Guilment, J. & Poncelet, O. Structural model and computer modeling study of allophane. *J. Phys. Chem. C* **112**, 358–364 (2008).
33. Levard, C. *et al.* Structure and distribution of allophanes, imogolite and proto-imogolite in volcanic soils. *Geoderma* **183–184**, 100–108 (2012).
34. Huang, P. M. Ionic factors affecting the formation of short-range ordered aluminosilicates. *Soil Sci. Soc. Am. J.* **55**, 1172–1180 (1991).
35. Iyoda, F. *et al.* Synthesis and adsorption characteristics of hollow spherical allophane nano-particles. *Appl. Clay Sci.* **56**, 77–83 (2012).
36. Ohashi, F., Wada, S.-I., Suzuki, M., Maeda, M. & Tomura, S. Synthetic allophane from high-concentration solutions: Nanoengineering of the porous solid. *Clay Miner.* **37**, 451–456 (2002).
37. Gunnarsson, I. & Arnórsson, S. Amorphous silica solubility and the thermodynamic properties of H_4SiO_4° in the range of 0° to 350°C at P_{sat}. *Geochim. Cosmochim. Acta* **64**, 2295–2307 (2000).
38. Tobler, D. J., Shaw, S. & Benning, L. G. Quantification of initial steps of nucleation and growth of silica nanoparticles: An in-situ SAXS and DLS study. *Geochim. Cosmochim. Acta* **73**, 5377–5393 (2009).
39. Baumann, H. Polymerisation und Depolymerisation der Kieselsäure unter verschiedenen Bedingungen. *Kolloid-Z.* **162**, 28–35 (1959).
40. Strekopytov, S., Jarry, E. & Exley, C. Further insight into the mechanism of formation of hydroxyaluminosilicates. *Polyhedron* **25**, 3399–3404 (2006).

41. Farmer, V. C., McHardy, W. J., Palmieri, F., Violante, A. & Violante, P. Synthetic allophanes formed in calcareous environments: Nature, conditions of formation, and transformations. *Soil Sci. Soc. Am. J.* **55**, 1162–1166 (1991).
42. Schneider, C., Doucet, F., Strekopytov, S. & Exley, C. The solubility of an hydroxyaluminosilicate. *Polyhedron* **23**, 3185–3191 (2004).
43. Wilson, M. A., McCarthy, S. A. & Fredericks, P. M. Structure of poorly-ordered aluminosilicates. *Clay Miner.* **21**, 879–897 (1986).
44. Du, P. *et al.* Insights into the formation mechanism of imogolite from a full-range observation of its sol-gel growth. *Appl. Clay Sci.* **150**, 115–124 (2017).
45. Thill, A. From Molecular Precursor to Imogolite Nanotubes. in *Developments in Clay Science* (eds. Yuan, P., Thill, A. & Bergaya, F.) vol. 7 429–457 (Elsevier B.V., 2016).
46. Lippmaa, E., Magi, M., Samoson, A., Engelhard, G. & Grimmer, A.-R. Structural studies of silicates by solid-state high-resolution 29Si NMR. *J. Am. Chem. Soc.* **102**, 4889–4893 (1980).
47. Doucet, F. J. *et al.* The formation of hydroxyaluminosilicates of geochemical and biological significance. *Geochim. Cosmochim. Acta* **65**, 2461–2467 (2001).
48. Yucelen, G. I. *et al.* Formation of single-walled aluminosilicate nanotubes from molecular precursors and curved nanoscale intermediates. *J. Am. Chem. Soc.* **133**, 5397–5412 (2011).
49. Hiradate, S. Speciation of aluminum in soil environments: Application of NMR technique. *Soil Sci. Plant Nutr.* **50**, 303–314 (2004).
50. Isobe, T., Watanabe, T., D'Espinose De La Caillerie, J. B., Legrand, A. P. & Massiot, D. Solid-state ^{1}H and ^{27}Al NMR studies of amorphous aluminum hydroxides. *J. Colloid Interface Sci.* **261**, 320–324 (2003).
51. Goodman, B. A., Russell, J. D., Montez, B., Oldfield, E. & Kirkpatrick, R. J. Structural studies of imogolite and allophanes by aluminum-27 and silicon-29 nuclear magnetic resonance spectroscopy. *Phys. Chem. Miner.* **12**, 342–346 (1985).
52. Childs, C. W., Hayashi, S. & Newman, R. H. Five-coordinate aluminum in allophane. *Clays Clay Miner.* **47**, 64–69 (1999).
53. Bi, S., Wang, C., Cao, Q. & Zhang, C. Studies on the mechanism of hydrolysis and polymerization of aluminum salts in aqueous solution: Correlations between the 'Core-links' model and 'Cage-like' Keggin-Al_{13} model. *Coord. Chem. Rev.* **248**, 441–455 (2004).
54. Lukić, M. J., Wiedenbeck, E., Reiner, H. & Gebauer, D. Chemical trigger toward phase separation in the aqueous Al(III) system revealed. *Sci. Adv.* **6**, eaba6878 (2020).
55. Bishop, J. L. *et al.* Spectral and hydration properties of allophane and imogolite. *Clays Clay Miner.* **61**, 57–74 (2013).
56. Farmer, V. C., Fraser, A. R. & Tait, J. M. Characterization of the chemical structures of natural and synthetic aluminosilicate gels and sols by infrared spectroscopy. *Geochim. Cosmochim. Acta* **43**, 1417–1420 (1979).
57. Montarges-Pelletier, E. *et al.* Synthetic allophane-like particles: Textural properties. *Colloids Surf. Physicochem. Eng. Asp.* **255**, 1–10 (2005).
58. Kumara, C. K., Ng, W. J., Bandara, A. & Weerasooriya, R. Nanogibbsite: Synthesis and characterization. *J. Colloid Interface Sci.* **352**, 252–258 (2010).

59. Sing, K. S. W. Assessment of Surface Area by Gas Adsorption. in *Adsorption by Powders and Porous Solids (Second Edition)* (eds. Rouquerol, F., Rouquerol, J., Sing, K. S. W., Llewellyn, P. & Maurin, G.) 237–268 (Academic Press, 2014).
60. Rouquerol, F., Rouquerol, J., Sing, K. S. W., Maurin, G. & Llewellyn, P. Introduction. in *Adsorption by Powders and Porous Solids (Second Edition)* (eds. Rouquerol, F., Rouquerol, J., Sing, K. S. W., Llewellyn, P. & Maurin, G.) 1–24 (Academic Press, 2014).
61. Wada, S.-I. & Wada, K. Density and structure of allophane. *Clay Min.* **12**, 289–298 (1977).
62. Garrido-Ramirez, E. G. *et al.* Catalytic wet peroxide oxidation of phenol over iron or copper oxide-supported allophane clay materials: Influence of catalyst SiO_2/Al_2O_3 ratio. *Microporous Mesoporous Mater.* **162**, 189–198 (2012).
63. Hietala, S. L., Smith, D. M., Golden, J. L. & Brinker, C. J. Anomalously low surface area and density in the silica—alumina gel system. *J. Am. Ceram. Soc.* **72**, 2354–2358 (1989).
64. Nakanishi, R., Wada, S.-I., Suzuki, M. & Maeda, M. Heat-induced gelation of hydroxy-aluminosilicate synthesized by instantaneous mixing of sodium silicate and aluminum chloride. *J. Fac. Agric. Kyushu Univ.* **52**, 147–151 (2007).
65. Abidin, Z., Matsue, N. & Henmi, T. Differential formation of allophane and imogolite: Experimental and molecular orbital study. *J. Comput.-Aided Mater. Des.* **14**, 5–18 (2007).
66. Henmi, T., Tange, K., Minagawa, T. & Yoshinaga, N. Effect of SiO_2/Al_2O_3 ratio on the thermal reactions of allophane. II. Infrared and X-ray powder diffraction data. *Clays Clay Miner.* **29**, 124–128 (1981).
67. Clausen, L. & Fabricius, I. BET measurements: Outgassing of minerals. *J. Colloid Interface Sci.* **227**, 7–15 (2000).
68. Kaiser, K. & Guggenberger, G. Mineral surfaces and soil organic matter. *Eur. J. Soil Sci.* **54**, 219–236 (2003).
69. Du, P. *et al.* Calcination-induced changes in structure, morphology, and porosity of allophane. *Appl. Clay Sci.* **158**, 211–218 (2018).
70. Vandickelen, R., De Roy, G. & Vansant, E. F. New Zealand allophanes: A structural study. *J. Chem. Soc. Faraday Trans. 1 Phys. Chem. Condens. Phases* **76**, 2542–2551 (1980).
71. Hofmann, A. *et al.* Characterization of the pores in hydrous ferric oxide aggregates formed by freezing and thawing. *J. Colloid Interface Sci.* **271**, 163–173 (2004).
72. Asthana, R. & Tewari, S. N. The engulfment of foreign particles by a freezing interface. *J. Mater. Sci.* **28**, 5414–5425 (1993).
73. Peppin, S. S. L., Elliott, J. A. W. & Worster, M. G. Solidification of colloidal suspensions. *J. Fluid Mech.* **554**, 147–166 (2006).
74. Anderson, A. M. & Worster, M. G. Periodic ice banding in freezing colloidal dispersions. *Langmuir* **28**, 16512–16523 (2012).
75. Spannuth, M., Mochrie, S. G. J., Peppin, S. S. L. & Wettlaufer, J. S. Particle-scale structure in frozen colloidal suspensions from small-angle X-ray scattering. *Phys. Rev. E Stat. Nonlinear Soft Matter Phys.* **83**, 021402 (2011).
76. Jähnert, S. *et al.* Melting and freezing of water in cylindrical silica nanopores. *Phys. Chem. Chem. Phys.* **10**, 6039–6051 (2008).

77. Zelenka, T. Adsorption and desorption of nitrogen at 77 K on micro- and meso- porous materials: Study of transport kinetics. *Microporous Mesoporous Mater.* **227**, 202–209 (2016).
78. Pyman, M. A. F. & Posner, A. M. The surface areas of amorphous mixed oxides and their relation to potentiometric titration. *J. Colloid Interface Sci.* **66**, 85–94 (1978).
79. Wells, N. & Childs, C. W. Flow behaviour of allophane and ferrihydrite under shearing forces. *Aust. J. Soil Res.* **26**, 145–152 (1988).
80. Kaufhold, S. *et al.* Allophane compared with other sorbent minerals for the removal of fluoride from water with particular focus on a mineable Ecuadorian allophane. *Appl. Clay Sci.* **50**, 25–33 (2010).
81. Henmi, T., Nakai, M., Seki, T. & Yoshinaga, N. Structural changes of allophanes during dry grinding: dependence on SiO_2/Al_2O_3 ratio. *Clay Miner.* **18**, 101–107 (1983).
82. Katiyar, N. K., Biswas, K. & Tiwary, C. S. Cryomilling as environmentally friendly synthesis route to prepare nanomaterials. *Int. Mater. Rev.* **66**, 493-532 (2020).
83. Sing, K. S. W., Rouquerol, F., Rouquerol, J. & Llewellyn, P. Assessment of Mesoporosity. in *Adsorption by Powders and Porous Solids (Second Edition)* (eds. Rouquerol, F., Rouquerol, J., Sing, K. S. W., Llewellyn, P. & Maurin, G.) 269–302 (Academic Press, 2014).
84. Mackenzie, K. J. D., Bowden, M. E. & Meinhold, R. H. The structure and thermal transformations of allophanes studied by ^{29}Si and ^{27}Al high resolution solid-state NMR. *Clays Clay Miner.* **39**, 337–346 (1991).
85. Aomine, S. & Otsuka, H. Surface of soil allophanic clays. *Trans 9th Int Congr Soil Sci* **1**, 731–737 (1968).
86. Kaufhold, S. *et al.* A new massive deposit of allophane raw material in Ecuador. *Clays Clay Miner.* **57**, 72–81 (2009).
87. Paterson, E. Specific surface area and pore structure of allophanic soil clays. *Clay Miner.* **12**, 1–9 (1977).
88. Chevallier, T., Woignier, T., Toucet, J., Blanchart, E. & Dieudonné, P. Fractal structure in natural gels: Effect on carbon sequestration in volcanic soils. *J. Sol-Gel Sci. Technol.* **48**, 231–238 (2008).
89. Calvelo Pereira, R. *et al.* Assessing the pore structure and surface area of allophane-rich and non-allophanic topsoils by supercritical drying and chemical treatment. *Geoderma* **337**, 805–811 (2019).
90. Woignier, T., Primera, J., Duffours, L., Dieudonné, P. & Raada, A. Preservation of the allophanic soils structure by supercritical drying. *Microporous Mesoporous Mater.* **109**, 370–375 (2008).
91. Inagaki, T. M., Mueller, C. W., Lehmann, J. & Kögel-Knabner, I. Andosol clay re-aggregation observed at the microscale during physical organic matter fractionation. *J. Plant Nutr. Soil Sci.* **182**, 145–148 (2019).
92. Kubota, T. Aggregate-formation of allophanic soils: Effect of drying on the dispersion of the soils. *Soil Sci. Plant Nutr.* **18**, 79–97 (1972).
93. Karube, J. & Abe, Y. Water retention by colloidal allophane and imogolite with different charges. *Clays Clay Miner.* **46**, 322–329 (1998).
94. Rousseaux, J. M. & Warkentin, B. P. Surface properties and forces holding water in allophane soils. *Soil Sci. Soc. Am. J.* **40**, 446–451 (1976).
95. Jongmans, A. G., Denaix, L., Van Oort, F. & Nieuwenhuyse, A. Induration of C horizons by allophane and imogolite in Costa Rican volcanic soils. *Soil Sci. Soc. Am. J.* **64**, 254–262 (2000).

96. Farmer, V. C., Fraser, A. R., Robertson, L. & Sleeman, J. R. Proto-imogolite allophane in podzol concretions in Australia: possible relationship to aluminous ferrallitic (lateritic) cementation. *J. Soil Sci.* **35**, 333–340 (1984).
97. Thompson, C. H., Bridges, E. M. & Jenkins, D. A. Pans in humus podzols (Humods and Aquods) in coastal southern Queensland. *Aust. J. Soil Res.* **34**, 161–182 (1996).
98. Knight, C. T. G. & Kinrade, S. D. A primer on the aqueous chemistry of silicon. in *Silicon in Agriculture* (eds. Datnoff, L. E., Snyder, G. H. & Korndörfer, G. H.) vol. 8 57–84 (Elsevier, 2001).

Acknowledgements

This work was funded by the Deutsche Forschungsgemeinschaft (RE 2251/9-1). We thank Dr. Dörte Diehl and Prof. Gabriele Schaumann (Universität Koblenz-Landau), Mathias Stein (Universität Hohenheim), Jana Dobritzsch, Dr. Klaus Kaiser and Prof. Robert Mikutta (Martin-Luther-Universität Halle-Wittenberg) for enabling the BET analyses. We greatfully acknowledge the contribution of the ESEM images by Dr. Christian Buchmann (Universität Koblenz-Landau). We thank Prof. Henry Strasdeit and Hannes Pleyer (Universität Hohenheim) for enabling FTIR analyses, and Detlev Frobel and Dr. Ludger Herrmann for support in XRD analyses.

Chapter 3

Interactions of dissolved organic matter and short-range ordered aluminosilicates by adsorption and co-precipitation

Coauthors: Hergen Breitzke, Gerd Buntkowsky, Christian Mikutta, Thilo Rennert

Geoderma (2022) 423:115960

https://doi.org/10.1016/j.geoderma.2022.115960

Abstract

Retention of dissolved organic matter (DOM) by short-range ordered aluminosilicates (SROAS) by adsorption and co-precipitation contributes to carbon accrual in soils and sediments. In this study, we investigated effects of SROAS composition on DOM adsorption, partitioning of carbon moieties by adsorption and co-precipitation, and the mineral structure of co-precipitates. We used four types of sorptive solutions, representing DOM collected *in situ* from topsoil and subsoil horizons of a Dystric Cambisol, and water-extracted DOM from beech and fir litter. We studied adsorption of soil DOM on three SROAS that structurally resemble proto-imogolites and silicon-rich allophanes as a function of contact time (1-168 h) at initial pH 5. Co-precipitation of soil and litter-extracted DOM was quantified as a function of the molar Al:C ratio (0.3-1.4) and at two levels of Si concentration (molar Al:Si = 1 and 2). To resolve the impact of DOM on mineral structure, we first examined time-dependent structural evolution of SROAS within 1 to 72 h and subsequently investigated the effects of DOM interference in crystallization processes. Mineral structure of SROAS and co-precipitates was resolved by infrared, solid-state ^{27}Al- and ^{29}Si-NMR spectroscopy. Chemical composition of DOM prior to reaction with SROAS and in co-precipitates was analysed by solid-state ^{13}C-NMR spectroscopy. Maximal C contents of adsorption complexes were 7.1 mg C g^{-1} for Al-rich and 20.4 mg C g^{-1} for Si-rich SROAS. We found selective adsorption of aromatic C and preferential exclusion of polysaccharide and alkyl C for both topsoil and subsoil DOM. Adsorption was larger for a Si-rich SROAS, since it exhibited a greater accessibility of aluminol groups. As a function of aromatic C content in initial DOM, 39.9 to 81% of C was retained by co-precipitation. Composition of co-precipitated organic matter was determined by C speciation in DOM supply, involving marked uptake of polysaccharides. In the absence of DOM, up to 50% of Si was present in imogolite-like configuration after 72 h, evidencing rapid development of short-range order. Complexation of Al by DOM during formation of SROAS caused partial exclusion of Si and slowed structural evolution, consequently enhancing abundance of ill-defined Si species in co-precipitates. Interactions of DOM with SROAS may cause selective accumulation of organic compounds and promote Si mobility in Andosols and Podzols.

Introduction

Successive transformation of the mineral matrix of volcanic ejecta frequently coincides with accumulation of short-range ordered aluminosilicates (SROAS) and high contents of soil organic matter (SOM; Lilienfein et al., 2003; Mikutta et al., 2009; Nieuwenhuyse et al., 2000; Torn et al., 1997). Andic soils contain a disproportionate amount of SOM compared to other mineral soils relative to their spatial distribution (Eswaran et al., 1993). A major portion of SOM in andic soils is associated with the mineral fraction (Mikutta et al., 2009; Rumpel et al., 2012; Wagai et al., 2015), particularly with SROAS (Asano et al., 2018; Basile-Doelsch et al., 2007; Wagai et al., 2020, 2018). Efficient organic matter accrual is ascribed to a high affinity of dissolved organic matter (DOM) for SROAS due to their large surface areas and reactive surface sites (Lilienfein et al., 2004; Parfitt et al., 1977; Singh et al., 2017), and encapsulation of organic substances by mineral particles (Filimonova et al., 2016; Huang et al., 2016). These processes enhance the formation of mineral-organic associations resistant to SOM degradation (Bruun et al., 2010; Fujii et al., 2019; Sanderman et al., 2014).

SROAS are nanoscale weathering products that form by polymerization of Al and Si with variable elemental composition and different degrees of crystallinity. SROAS particularly accumulate in soils developed from volcanic ejecta, but they were also detected in Podzols (Gustafsson et al., 1999; Skjemstad et al., 1992) and cambic soils (Stahr and Nakai, 1984; Tait et al., 1978) that developed from other siliceous rocks. In clay fractions isolated from weathered volcanic ejecta and subsoils, SROAS developed structurally well-defined tube-shaped particles with diameters of about 2 nm, termed imogolite, or hollow sphere-shaped particles usually referred to as allophane (Cradwick et al., 1972; Henmi and Wada, 1976; Wada and Wada, 2014). Precipitation of SROAS from monomeric Al and Si starts by condensation via olation of hydroxylated Al species that subsequently react with Si (Beardmore et al., 2016; Thill, 2016). Incorporation of Si is enhanced by Si availability, resulting in molar Al:Si ratios of 1-4 (Levard et al., 2012; Parfitt and Kimble, 1989). Depending on chemical composition and pH, precursors evolve either to form imogolite-like structural features, that is, curved dioctahedral sheets of Al with single Si tetrahedra bound to three Al in the locally defined Q^0(3Al) configuration (Barron et al., 1982; Cradwick et al., 1972), or develop a local structure more similar to tectosilicates (Farmer et al., 1979; Ildefonse et al., 1994). The latter process may occur in environments characterized by high availability of silicic acid (Gérard et al., 2007; Parfitt et al., 1983). Crystallization of SROAS was previously studied to understand the mechanism of imogolite formation or optimizing its yield. Hence, synthesis experiments were performed under acidic conditions while heating (Du et al., 2017; Farmer et al., 1977; Yucelen et al., 2011). Imogolite formation in such systems proceeded by assembly of curved fragments into ultimately sphere or tube-shaped particles within hours to days (Du et al., 2017; Yucelen et al., 2011). At ambient conditions, these processes take years (Wada, 1987). A few studies

suggest that structural ordering processes that lead to locally defined precursors are quite rapid under ambient but acidic conditions as evidenced by detection of Q^0(3Al) signals within 1 to 24 h (Du et al., 2017; Iyoda et al., 2012; Yucelen et al., 2011). How fast crystallization proceeds under moderately acid conditions typically found in soil horizons containing SROAS (pH 5-7; Parfitt and Kimble, 1989) is unknown.

Assuming two major pathways may conceptualize interaction of DOM with SROAS: DOM adsorption on existing mineral particles and co-precipitation during mineral formation (Kleber et al., 2015). Previous studies of ion adsorption on SROAS suggest that mineral surface properties governed by elemental composition and structure influence DOM adsorption. Singly coordinated aluminol groups offer positive charge and are prone to ligand exchange with organic functional groups (Parfitt et al., 1977), a mechanism driving DOM allocation to mineral surfaces (Gu et al., 1994; Kaiser et al., 1997; Mikutta et al., 2007). Greater abundance of aluminol groups may thus favour DOM adsorption on Al-rich compared to Si-rich SROAS as shown for phosphate adsorption (Clarke and McBride, 1984). Silanol groups do not form inner-sphere complexes with carboxylic acids (Pokrovski and Schott, 1998) and impart negative charge to SROAS (Su et al., 1992). Moreover, Si-rich SROAS contain Al in tedrahedral coordination (Ildefonse et al., 1994), offering permanent negative charge (Su et al., 1992), altogether causing diminished anion retention by SROAS with smaller Al:Si ratios (Clarke and McBride, 1984; Su et al., 1992).

Since dissolved organic species are ubiquitously present in soils, SROAS precipitate in the presence of DOM. Co-precipitation of SOM with SROAS in andic topsoils substantially contributes to SOM storage (Mikutta et al., 2009). Co-precipitation of DOM with poorly crystalline Fe and Al (hydr)oxides was partially more efficient than adsorption (Chen et al., 2014; Eusterhues et al., 2011; Mikutta et al., 2011). Several mechanisms may be involved in co-precipitation of Al, Si, and DOM. Charge neutralization of organic functional groups by Al or aluminosilicates may induce formation of insoluble complexes (Nierop et al., 2002), and organic species may be occluded by or adsorbed on SROAS particles (Eusterhues et al., 2008). Interference of organic substances with Fe- and Al-(hydr)oxide formation decreases particle sizes and impedes crystal growth (Chen et al., 2016; Eusterhues et al., 2008; Schwertmann et al., 2005). Similar processes may also occur during polymerization of Al and Si in the presence of DOM. In solutions exposed to heat, low-molecular-weight organic acids and organic substances extracted from soil perturbed imogolite crystallization as a function of ligand concentration and affinity for Al complexation (Inoue and Huang, 1990, 1986; Luciuk and Huang, 1974). The extent to which such processes prevent formation of imogolite-like Si configuration under natural conditions is unclear. Rouff et al. (2012) investigated Si speciation in co-precipitates formed at ambient conditions and found a slight positive effect of DOM on the quantity of Si nuclei in Q^0(3Al) coordination. Signals of Si in Q^0(3Al) were also detected in

clay fractions of soil horizons with substantial SOM accumulation (Basile-Doelsch et al., 2005; Rennert et al., 2014). Furthermore, this defined local structure was even found in secondary Al phases markedly distorted by complexation with organic functional groups (Basile-Doelsch et al., 2005; Levard et al., 2012). Hence, more information is needed on the effects of naturally occurring organic molecules on the speciation of Al and Si in co-precipitates.

Both adsorption and co-precipitation of DOM with SROAS may lead to retention of specific organic compounds. Preferential accumulation of oxidized aromatic SOM degradation products by adsorption has been detected for several types of Al and Fe (hydr)oxides (Chorover and Amistadi, 2001; Kaiser et al., 1997; Meier et al., 1999; Schneider et al., 2010), since their functional groups have a high affinity for surface sites (Gu et al., 1995; Kaiser, 2003). Such processes have also been postulated for SROAS surfaces based on studies of bulk SOM composition. Abundance of short-range ordered minerals in andic soils correlated positively with the contents of carboxyl and aromatic SOM moieties (Kramer et al., 2012), and in isolated mineral-organic associations, aromatic and carboxyl C were attributed to Al in SROAS or Al-organic complexes (Mikutta et al., 2009). Fractionation of organic moieties by favoured interaction with aromatic compounds also occurs by co-precipitation of Al and DOM (Kaiser, 1998; Scheel et al., 2008; Vilgé-Ritter et al., 1999). However, microbial exudates containing polysaccharides and proteins can also be efficiently sorbed by co-precipitation with Al (Mikutta et al., 2011). This implies that diverse DOM compounds may be able to interact with SROAS during co-precipitation. Hence, the composition of retained organic substances, that is, possible fractionation of the source DOM during co-precipitation, may depend on initial DOM composition as shown for Fe-organic-matter co-precipitates (Eusterhues et al., 2011).

The objective of this study was to investigate several aspects of interactions between SROAS and DOM. First, we aimed to elucidate how compositional heterogeneity of SROAS and DOM quantitatively and qualitatively affect DOM adsorption on pristine surfaces. We hypothesized that DOM adsorption is facilitated by the abundance of aluminol groups and increases with contact time. To represent naturally occurring organic species, we used soil solutions collected *in situ* from top- and subsoil. We expected preferential retention of aromatic lignin degradation products more pronounced from topsoil DOM than from already altered subsoil DOM. Secondly, we aimed to assess the impact of DOM composition on the amount and composition of organic matter retained by co-precipitation with SROAS. Here, we anticipated a close relationship between composition of input DOM and co-precipitated organic matter, since the coincidence of several sorption mechanisms makes the process less selective. Thirdly, we addressed the speciation of Al and Si in co-precipitates. We hypothesized that DOM hampers crystallization of SROAS with increasing DOM concentration and that crystallization depends on the chemical composition of organic matter.

Materials and methods

Origin of DOM solutions

We used four different DOM solutions. Two of them were collected from soil *in situ* at two depths, and two originated from water extracts of two different forest-floor litter layers. We are aware that DOM collected *in situ* and water extracts, even if obtained from the same horizon, do not necessarily have the same chemical composition (e.g., Rennert et al., 2007). Nonetheless, we use the common term 'DOM' for all aqueous solutions, containing dissolved organic species.

Soil solution DOM was collected at a long-term monitoring station located in the Palatinate Forest, about 15 km E of Kaiserslautern close to Hochspeyer, Germany (49° 25`54.08`` N; 7° 55`5.42`` E). The annual mean temperature is 8.7 °C, and the mean annual precipitation is 810 mm. The site is located on a slope of 3° at an absolute altitude of 385 to 400 m. Vegetation was a mixed forest stand dominated by pine and beech (*Pinus sylvestris, Fagus sylvatica*). The soil was a Dystric Cambisol with podzolisation features, developed from Lower Triassic sandstone. Two plots were sampled by zero tension lysimeters (Westpfalz-Werkstätten, Kaiserslautern, Germany) at a depth of 10 cm and ceramic suction cups (P80, Dr. Lamersdorf, Göttingen, Germany) at 60 cm depth. Selected soil properties can be found in supplementary information (Table S1). Soil solutions were collected from February to May in 2016, 2017, and 2018. Samples of one depth were pooled over the plots and sampling times, in the following referred to as top- and subsoil DOM. For water extracts ('litter DOM'), we collected litter from a mixed deciduous forest dominated by beech on the Swabian Alb 15 km E of Reutlingen (48° 29`04.6``N, 9° 18`37.0``E), and from a mixed coniferous forest stand dominated by spruce and fir in the Black Forest 20 km W of Nagold (48°33'43.2"N 8°31'01.4"E). A mass of 140 g litter was added to 700 ml deionised water and shaken for 1 h at 215 rpm on a horizontal shaker. Afterwards, it was sieved (2 mm) and centrifuged for 20 min at 1050 *g*. All solutions, in the following designated as 'DOM solutions' were pressure filtered with 0.45 µm cellulose nitrate filters (Sartorius, Göttingen, Germany) and stored at -20 °C.

Characterization of DOM solutions

Concentrations of dissolved organic C (DOC) and dissolved N (DN) were determined by combustion (multi C/N 2100s, Analytik Jena AG, Jena, Germany). Inorganic C was removed by adding 50 µl of 1 M HCl before measurement. Concentrations of Na, K, Ca, Mg, Al, Fe, and Si were measured using a microwave plasma-atomic emission spectrometer (4200 MP-AES, Agilent, Waldbronn, Germany). The pH was measured potentiometrically with a glass electrode, and electrical conductivity (EC) was measured with a conductivity sensor (Mettler Toledo, Gießen, Germany). Ionic strength was calculated from electrical conductivity according to Griffin and Jurinak (1973).

Composition of DOM was investigated by several methods. Molar absorbtivity at 254 nm (ε) is a rough indicator of aromatic moieties and C in double bonds (Weishaar et al., 2003). Absorption was measured with a UV/VIS spectrophotometer (Cary 50, Varian, Mulgrave, Australia) using a cuvette with 1 cm path length, and molar absorptivity (l mol^{-1} cm^{-1}) was calculated by dividing measured absorbance by the product of path length and DOC concentration (mol l^{-1}). Freeze-dried DOM solutions were analysed by Fourier-transform infrared spectroscopy (FTIR) in transmission mode with an accessory of a LUMOS infrared microscope (Bruker, Ettlingen, Germany). Transmission spectra were recorded from pellets prepared from a mixture of 1 mg of hand-milled sample and 200 mg of KBr with a hand press. Fifty background scans were recorded against the atmosphere, and subsequently 100 sample scans accumulated at a resolution of 4 cm^{-1}. Freeze-dried organic matter was mixed with finely ground quartz that was previously heated for 4 h to 1200 °C and analysed by solid-state ^{13}C nuclear magnetic resonance (NMR) spectroscopy. The mixture was filled into 7 mm probes and inserted into zirconia rotors. Spectra were obtained on a Bruker DSX 200 NMR spectrometer, operating at a ^{13}C resonance frequency of 50.3 MHz with the cross-polarization magic angle spinning (MAS) technique. Samples were spun at a frequency of 6.8 kHz. ^{1}H was polarized by employing a ramped pulse sequence during a contact time of 1 ms and subsequently decoupled. Spectra were recorded at an acquisition time of 0.01024 s, 1024 observation points, and a spectral width of 50 kHz, giving a resolution of 48.83 Hz. About 131,000 to 158,000 scans were accumulated using a pulse delay of 0.4 s. Resonance of tetramethylsilane was set to 0 ppm, and chemical shifts were referenced accordingly. Relative contributions of C moieties were estimated by integrating the signal intensities at a line broadening of 0 Hz in four chemical shift regions. Signals between 220 and 160 ppm were attributed to carbonyl and carboxyl C, signals between 160 and 110 to aryl C (aromatic C), between 110 and 45 to O-alkyl C, and between 45 to -10 to alkyl C (Figure 1). Spinning side bands were considered for all four C classes (Knicker et al., 2005). Integration was performed with the instrument software (TopSpin 4.0.7., Bruker).

Adsorption experiments

We studied adsorption from DOM solutions on three different SROAS. The minerals were synthesized at ambient conditions and characterized extensively for composition, structure, and physical properties (Lenhardt et al., 2021). We used one Si-rich SROAS with a molar Al:Si ratio of 1.4 and two Al-rich SROAS with molar Al:Si ratios of 2.1 and 2.6. In the following, we refer to an adsorbent by stating the molar Al:Si ratio. The Al-rich SROAS are structurally similar to proto-imogolites, and Si-rich SROAS to natural Si-rich analogues. The specific surface area (SSA) depended on composition, 296 m^2 g^{-1} for Al:Si = 1.4, and 25.6 and 0.7 m^2 g^{-1} for Al:Si = 2.1 and 2.6, respectively (Lenhardt et al., 2021). These data imply that both SROAS with Al:Si

= 1.4 and 2.1 were mesoporous (diameter 2–50 nm), and there was no evidence of micropores <2 nm (Lenhardt et al., 2021).

We conducted five sets of batch adsorption experiments per DOM solution that differed in reaction time to study adsorption kinetics over 1, 5, 24, 72, and 168 h. We adjusted the initial pH to 5 and observed no systematic shift in final pH (4.7-5.8) with DOM adsorption. A volume of 5 ml mineral suspension, containing 40 mg of mineral, and 25 ml of DOM solution was pipetted into 50 ml glass bottles with PTFE caps in duplicate. Mineral suspensions were prepared by suspending 3.4 g of freeze-dried SROAS in 425 ml deionised H_2O in 500-ml Nalgene bottles. The pH of the mineral suspension was adjusted with 0.1 M NaOH or HCl prior to the adsorption experiments. We studied adsorption at six initial DOC concentrations ranging from 0 mg l^{-1} to a maximum concentration depending on the DOC concentrations of undiluted DOM solutions (Table 1). Intermediate concentrations were adjusted with deionised water. Afterwards, pH was adjusted to 5 with 0.01 M HCl and NaOH. Ionic strength was assumed to be linearly correlated to electrical conductivity (Griffin and Jurinak, 1973) and adjusted to 38 (± 2.5) and 46 (± 1.1) µS cm^{-1} for top- and subsoil DOM solution, respectively, by dropwise addition of 0.1 M NaCl. Suspensions were shaken on a horizontal shaker at 175 rpm and subsequently filtrated through 0.22-µm polyether sulfone membrane (PES) filters (Merck Millipore, Burlington, USA). The filtrates were stored frozen prior to the measurement of pH, ε, and DOC concentration as described above. Adsorbed C was quantified by the difference between the initial and final DOC concentrations. We checked possible DOC loss by mineralisation and filtration (since we used filters with a pore size of 0.45 µm when obtaining DOM, and filters with a smaller pore size of 0.22 µm in adsorption experiments). To check DOC loss by mineralisation, we shook DOM solutions at medium and maximum DOC concentrations for 1 to 168 h similar to the adsorption experiments, but without SROAS. We quantified mineralisation as the difference between initial and final DOC concentration. To check DOC loss by filtration, we filtered (0.22 µm) half of the DOM solutions used to check mineralisation, and compared the DOC concentrations with those of the other half. We detected neither mineralisation nor loss by filtration of subsoil DOM. Loss of topsoil DOM by mineralisation was <5% and by filtration <11%. We also checked release of Al and Si from SROAS by quantifying dissolved Al and Si by MP-AES.

We recorded DRIFT spectra of freeze-dried filtrates from adsorption experiments to characterize the composition of residual DOM. In order to reach sufficient spectral sensitivity, we pooled the filtrates to increase the amount of C per sample. Consequently, we analysed two composite filtrates per contact time representing lower and higher initial DOC concentrations. Based on preliminary tests, we diluted freeze-dried samples at a C-to-KBr mass ratio of 0.02 to 0.035 to obtain absorption between 0.7 and 2 Kubelka-Munk units in the spectral range between 1800 and 1000 cm^{-1}. About 1 to 5 mg of sample was mixed with finely

ground KBr (20 to 35 mg) and gently homogenized in a mortar. The mixture was filled into stainless steel microcups, which were used as inlays in the sample cups supplied with the FTIR spectrometer. A number of 100 scans was accumulated, and 50 scans from pure KBr recorded as background.

Co-precipitation experiments

Formation of SROAS in the absence and presence of DOM solutions was studied by neutralizing aqueous $AlCl_3$ and Na_4SiO_4 at ambient temperature and pressure with an automatic titrator equipped with a glass electrode (SI Analytics GmbH, Mainz, Germany). We fixed the initial Al concentration to 1.9 mM in all samples, while the concentrations of Si and DOC were variable. All experiments in the absence and presence of DOM were run in triplicate and duplicate, respectively. Aliquots of 0.2 M $AlCl_3$ and 0.1 M Na_4SiO_4 were pipetted to a volume of 100 ml of deionised water or (diluted) DOM solution to give the desired concentrations. To proceed from initially acid conditions, 1 M HCl was added to balance base addition from Na_4SiO_4. Four moles of OH^- were assumed to be released by dissolution of 1 M Na_4SiO_4. Aqueous reactants were mixed under rapid stirring in the sequence water or DOM solution, HCl, $AlCl_3$, and Na_4SiO_4. The resulting initial pH was below 4.3. Thus, the reactants were mainly present in the form of aqueous complexes (Bi et al., 2004). Solutions were neutralized by addition of 0.1 ml of 50 mM NaOH every 15 s, corresponding to a neutralization rate of 0.1 mol OH^- mol^{-1} Al^{-1} min^{-1}. Titration was terminated when the isoelectric point was reached, which was visible by sudden turbidity and occurred at pH 6.0-8.0, depending on solution composition. For variants with DOM, pH 6.5 was sufficient to flocculate the sample irrespective of reaction time. In all cases, precipitates were left to settle for several minutes, and the supernatant was filtrated with 0.22-µm PES membranes (Merck Millipore). Molar absorbtivity and concentrations of Al, Si and Na were quantified as described before. We determined DOC concentrations by combustion using a DIMATOC 2100 (Dimatec, Essen, Germany). Molar Al:Si and Al:C ratios of precipitates and retained DOC were determined by the difference between measured initial concentrations and concentrations in the filtrates; the latter were corrected by the volume of added NaOH. Afterwards, co-precipitates were washed twice by diluting the suspensions with deionised water by a factor of approximately 2, and were then recovered by centrifugation at 1560 *g* for 15 min. The concentrated gelatinous product was then frozen (–20 °C) and freeze-dried.

Formation of SROAS in the absence of DOM was studied at seven Si concentrations, resulting in molar Al:Si ratios of 1 to 5. The procedure from initiation of neutralization to freezing the precipitate took approximately 60 min. Consequently, we refer to the respective precipitates as formed within 1 h. To study time-dependent structural rearrangement in the absence of DOC, we repeated titration experiments for variants with molar Al:Si ratios of 1, 2, and 3 with a delay time (‘reaction time’) of 5, 24 and 72 h when pH 5.2 was reached. During this period,

precipitation was not visible. The suspensions were stored in glass vessels in the dark without stirring. Finally, a volume of 100 ml of the suspensions was titrated to the isoelectric point, which increased with reaction time due to structural changes (pH 6.5-8.0 for reaction period ≥5 h). The effects of DOM on SROAS precipitation within 1 h were studied in variants with initial molar Al:Si ratios of 1 and 2 as a function of DOC concentration, the latter was adjusted to molar Al:C ratios of 0.3, 0.5, 0.8, and 1.4. Additionally, experiments with DOM solutions were repeated for Al:C molar ratios of 0.5, 0.8, and 1.4, and a delay time of 24 h. Precipitates obtained from replicates were pooled for spectroscopic analyses.

Mineral structure and composition of precipitated organic matter was characterized by FTIR spectroscopy in transmission mode with two different FTIR spectrometers. Using the transmission accessory of a LUMOS infrared microscope (4000–500 cm^{-1}), pellets were prepared by mixing 1 mg of sample with 200 mg of KBr and subsequent pressing. Fifty background spectra were recorded against the atmosphere, and subsequently 100 sample scans accumulated at a resolution of 4 cm^{-1}. To access absorption at lower wavenumbers (500–230 cm^{-1}), we additionally recorded spectra with a Vertex 80v (Bruker). Pellets were prepared at the same sample-to-KBr ratio but pressed with a hydraulic press. Sixteen background spectra were measured against vacuum (<1 hPa), and subsequently 16 scans accumulated at a resolution of 2 cm^{-1}.

Composition of co-precipitated organic matter from water-extracted DOM was analysed by solid-state ^{13}C-NMR spectroscopy. To gain sufficient amounts of sample, we repeated co-precipitation experiments (initial molar Al:Si = 2 and Al:C = 0.3, reaction period 1 h) seven times and pooled the solids. Furthermore, we investigated the chemical environments of ^{27}Al and ^{29}Si nuclei in two samples generated in the absence of DOM and reaction times of 1 (initial Al:Si <2, n.d.) and 72 h, and in three co-precipitates formed after 24 h at an initial molar Al:Si ratio of 2 and Al:C ratio of 0.5 in the presence of soil DOM and beech-litter DOM. Ten replicates were pooled per analysed sample. Solid-state NMR spectroscopy with direct-polarization (DP) and MAS was performed on a 400 MHz Bruker Avance II+ spectrometer, equipped with a 4 mm H/X MAS probe. ^{27}Al-NMR spectra were obtained at a resonance frequency of 104.3 MHz and a MAS frequency of 12 kHz while spun in 4 mm zirconia rotors. A DP pulse of 22° was applied and relaxation delay was set to 4 s. ^{1}H was decoupled with a tppm20 pulse sequence, and 64 scans were accumulated. Chemical shifts are expressed relative to an aqueous solution of $AlCl_3$. ^{29}Si-NMR spectra were recorded at a resonance frequency of 79.5 MHz and a MAS frequency of 8 kHz. Decoupling of ^{1}H was achieved with a spinal64 pulse sequence. A number of 3072 scans were acquired with DP by a 22° pulse (2 µs) and a delay time of 120 s. Chemical shifts were referenced to tetramethylsilane. All data was collected at an acquisition time of 0.04096 s, 4096 observation points and a spectral width of 50 kHz, giving a resolution of 12.02 Hz. Phase adjustment and baseline correction was conducted with TopSpin 4.0.7 (Bruker).

The quantitative contribution of Si nuclei in Q^0(3Al) coordination was derived from fitting Lorentzian functions to spectral data and calculating the proportion of integrals to the total area of the resonance signal (OriginPro 2020, OriginLab, Northampton, USA) in case a peak at -79 ppm was visible. Spectra were normalized, and the base line was set to the median of all data points. The position of the resonance signal of ^{29}Si in Q^0(3Al) coordination was fixed to the maximum of the Q^0(3Al) signal, whereas no specifications were made for other nuclei. Resonance of these ill-defined species was reproduced by four functions with no specification of peak position, height or width. We first analysed the data at a line broadening >0 Hz to identify positions of local maxima and then repeated the fit with spectra at a line broadening of 0 Hz to obtain integrals. We modelled ^{27}Al NMR spectra at a line broadening of 0 Hz with a combination of Gaussian and Lorentzian functions, whereas neither peak position nor width or height was fixed. Integrals of functions were ascribed to a coordination of Al according to the chemical shift (Hiradate, 2004) and summed.

Results and discussion

Composition of DOM

To assess the impact of DOM composition on adsorption and co-precipitation, we used four DOM solutions with diverging abundance of organic functional groups. The DOM solutions differed in concentrations of DOC, DN, composition of inorganic cations, and pH (Table 1). Potassium, Ca and Mg were more abundant in litter DOM than in soil DOM. The pH of the litter DOM solutions was circumneutral, while that of the soil solutions was acidic. Analysis of DOM composition by solid-state ^{13}C-NMR spectroscopy showed that most of signal intensity was located in the O-alkyl C region (110-45 ppm) for all samples (Figs. 1 and S1; Table 2). Particularly litter DOM was dominated by carbohydrates, since the sharp signal at 72 ppm is attributed to polysaccharides (Fig. S1, Knicker, 2011). Spectra of topsoil DOM revealed a distinct signal at 54 ppm attributed to methoxyl C, and resonance lines close to 150 ppm and 125 ppm in the aryl C region (Fig. S1; 160-110 ppm) attributed to C in syringyl and guaiacyl units (Knicker, 2011). FTIR spectra of topsoil DOM closely resembled those of aromatic acids collected from forest floor leachates (Fig. S2; Guggenberger et al., 1994). Both ^{13}C-NMR and FTIR spectra thus corroborated a major contribution of lignin oxidation products to dissolved species in topsoil DOM. Aromatic C moieties were more abundant in topsoil DOM and subsoil DOM (21%) than in litter DOM, where only 13 and 15% of signal intensity was located in the aryl region for beech- and fir-litter DOM, respectively (Table 2). Signal intensity in the aryl region corresponded well with molar absorptivity at 254 nm (Table 1). Although the contributions of aryl C in topsoil and subsoil DOC were very similar, vibrations of phenolic groups at 1265 cm^{-1} were distinctly less pronounced in FTIR spectra of the latter (Fig. S2), indicating compositional differences among aromatic compounds. In contrast to aromatic

compounds, abundance of polysaccharides was highest in litter DOM, slightly decreased in subsoil DOM, and was lowest in topsoil DOM, based on relative intensities of bond vibrations in the region from 1100 to 1000 cm^{-1} (Fig. S2; Niemeyer et al., 1992; Kacuráková et al., 2000). Spectra of litter DOM exhibited bands at 1075-1040 cm^{-1}, whereas their position was shifted to higher wavenumbers in subsoil DOM (1130-1075 cm^{-1}). This may indicate differences in the composition of polysaccharides between litter DOM and soil DOM. Aliphatic compounds contributed 21 to 24% to signal intensity in the alkyl region (45 to -10) ppm; Knicker, 2011). Given a marked resonance signal at 170 ppm in ^{13}C-NMR spectra (Fig. S1), all types of DOM contained a substantial amount of carboxyl groups (Knicker, 2011). Both top- and subsoil DOM contained carbonyl groups (aldehyde and ketone) resonating at chemical shifts from 184 to 210 ppm, which was not the case in beech-litter DOM. Altogether, the relative signal intensity of carbonyl and carboxyl C was slightly lower in litter DOM (beech 11% and fir 13%; Table 2) compared to soil DOM (topsoil 16% and subsoil 18%).

Table 1: Composition, electrical conductivity (EC), ionic strength (I), and molar absorptivity at 254 nm (ε) of dissolved organic matter (DOM) solutions. Dissolved organic C (DOC) and N (DN) correspond to species <0.45 µm.

DOM type	DOC	DN	Na	K	Ca	Mg	Al	Fe	Si	pH	EC	I	ε
	[mg l^{-1}]										[µS cm^{-1}]	[mmol l^{-1}]	[l mol^{-1} cm^{-1}]
Topsoil	53.3	1.9	1.1	2.5	0.9	0.3	0.9	0.3	0.3	4.0	55	0.72	465
Subsoil	34.8	1.0	1.5	2.4	0.5	0.6	3.0	0.6	0.3	4.1	66	0.86	397
Fir litter	70.8	8.4	1.0	20.3	7.7	2.1	0.2	0.2	0.4	7.5	117	1.52	253
Beech litter	76.3	9.1	0.9	11.7	6.1	2.3	0.3	0.2	0.5	6.4	91	1.18	169

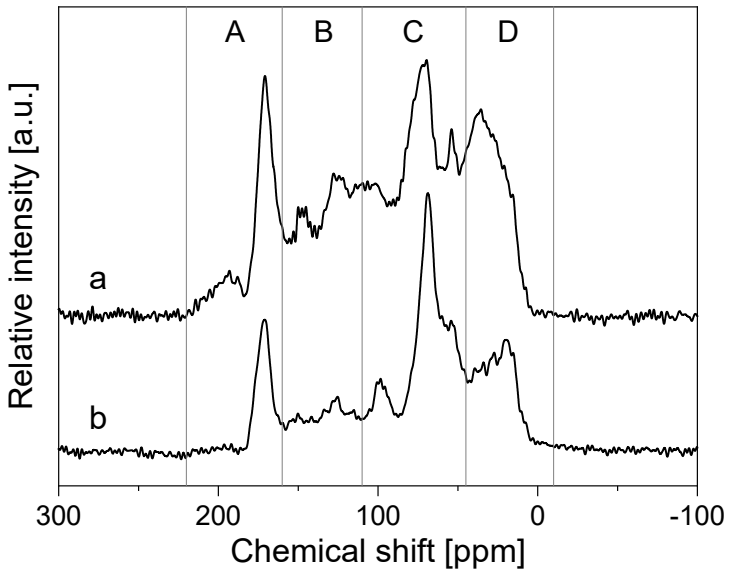

Figure 1: Solid-state ^{13}C nuclear magnetic resonance spectra of dissolved organic matter obtained from topsoil (a) and from beech litter (b) at a line broadening of 0 Hz. Spectral regions to quantify carbonyl and carboxyl C (A, 220–160 ppm), aryl C (B, 160–110 ppm), O-alkyl C (C, 110–45 ppm) and alkyl C (D, 45–(–10)) are distinguished by vertical lines.

Table 2: Composition of dissolved organic matter (DOM) and co-precipitated organic matter as derived from solid-state ^{13}C nuclear magnetic resonance spectroscopy. Chemical shift regions are delineated in Fig. 1. Analysed co-precipitates were synthesized at initial Al:Si = 2, Al:C = 0.3 and a reaction time of 1 h.

DOM type	Carbonyl / Carboxyl C	Aryl C	O-Alkyl C	Alkyl C
	[% of C]			
Initial composition				
Topsoil	15	21	41	22
Subsoil	18	21	40	21
Fir litter	13	15	48	24
Beech litter	12	13	51	24
Co-precipitated organic matter				
Fir litter	15	17	47	21
Beech litter	18	16	48	19

In summary, compositional analyses showed distinct differences between soil DOM and litter DOM. The latter contained less aromatic C, had a larger contribution of polysaccharides, and was more similar to fresh plant litter (Knicker, 2011). Topsoil DOM contained a substantial proportion of aromatic lignin degradation products. Subsoil DOM composition slightly deviated from topsoil DOM composition with respect to polysaccharide abundance and speciation of the aromatic fraction.

Time-dependent adsorption of soil DOM on SROAS

We studied adsorption of soil DOM on three SROAS with variable Al content resulting in molar Al:Si ratios of 1.4, 2.1, and 2.6. Although the Si-rich SROAS (Al:Si = 1.4) contained the least Al, its greater SSA (296 $m^2\ g^{-1}$) resulted in exceeding amounts of retained DOM compared to Al-rich SROAS (0.7-25.6 $m^2\ g^{-1}$, Lenhardt et al., 2021). Removal of topsoil DOM by an Al-rich SROAS (Al:Si = 2.6) never surpassed the amount removed in the filtration control, evidencing negligible adsorption on the mineral. With subsoil DOM, removal was only slightly higher than the filtration control after 72 h contact time, and the C content reached a maximum of 4 mg C g^{-1} after 168 h of shaking. Adsorption of topsoil DOM on the second Al-rich (Al:Si = 2.1) SROAS was detectable after 24 h, and increased with time to a maximum of 7.1 mg C g^{-1} (Fig. 2A). Maximal adsorption of subsoil DOM on this adsorbent was similar (6.2 mg g^{-1}; Fig. 2C). Only in the lower range of initial DOM concentrations, we detected an increase in C content with increasing DOC concentration, indicating that the maximum adsorption capacity for Al-rich SROAS (Al:Si = 2.1) was reached within the studied range of concentrations and contact times. In contrast, Si-rich SROAS adsorbed increasing amounts of topsoil and subsoil DOM with increasing DOC concentration at each time step (Fig. 2A, C). We observed maximal C contents of 20.4 and 16.8 mg C g^{-1} after 168 h contact time with topsoil and subsoil DOM, respectively. The rather steep increase in C contents with increasing initial DOC concentrations indicated that the observed maximal adsorption did not correspond to the

adsorption capacity of Si-rich SROAS, but adsorption was limited by DOM supply in the experiment.

The remarkably low adsorption capacity of Al-rich phases was caused by extensive aggregation during mineral synthesis (Lenhardt et al., 2021), which limited accessibility of surface sites for DOM adsorption. Carbon contents of Al-rich SROAS after DOM adsorption were in the same range as observed for Al oxides with similarly small SSA (Fleury et al., 2017). In contrast, adsorption of DOM on undried SROAS with a likely similar structure (Al:Si = 1.5) was much greater and reached C contents of up to 130 mg C g^{-1} at pH 5 (Ding et al., 2019). Complementary to data on nitrogen sorption capacity (Lenhardt et al., 2021), this shows that dehydration massively decreased the availability of surface sites capable of retaining DOM. Incorporation of Si impeded aggregation (Lenhardt et al., 2021) and consequentially facilitated DOM retention.

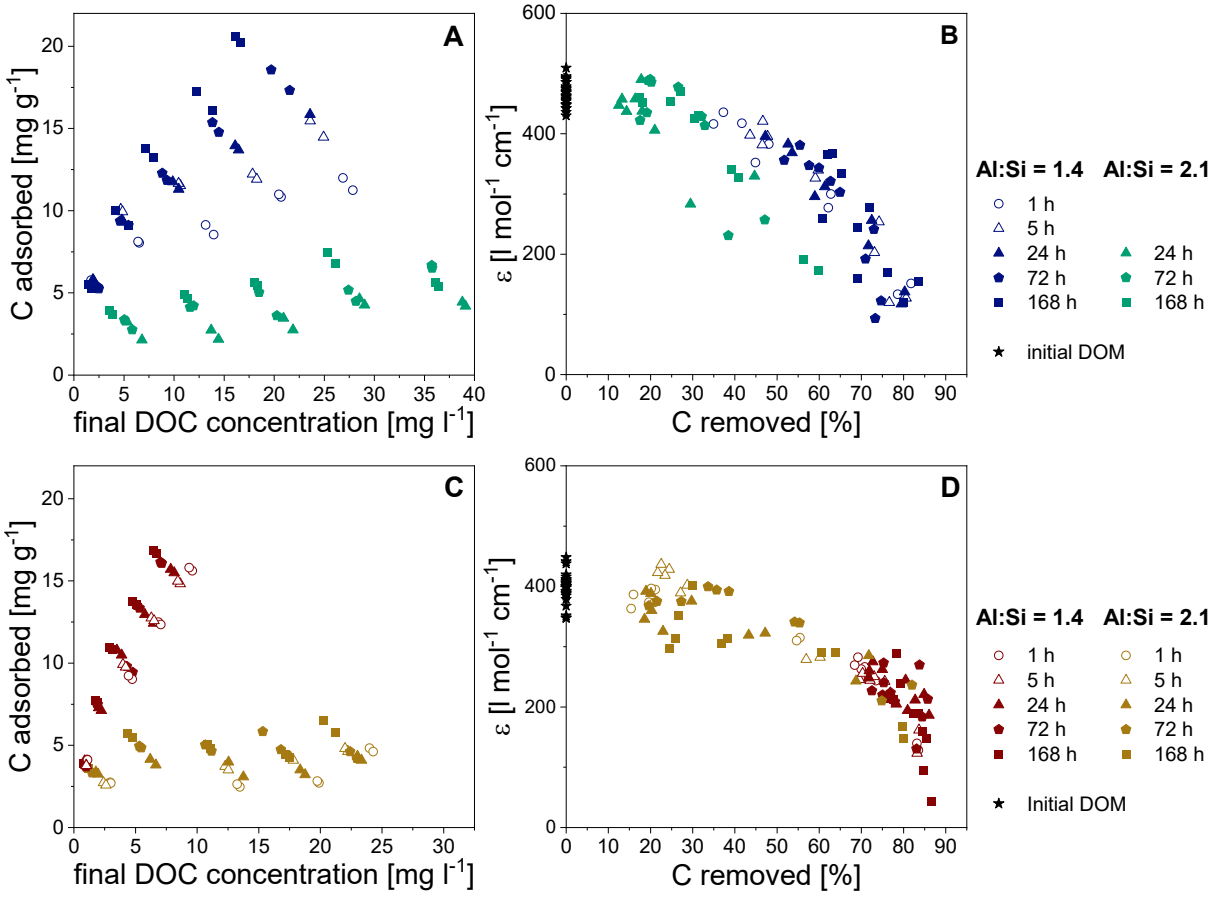

Figure 2: Time-dependent adsorption of topsoil (A) and subsoil (C) dissolved organic matter (DOM) on Si-rich (Al:Si = 1.4) and Al-rich (Al:Si = 2.1) short-range ordered aluminosilicates and corresponding molar absorbtivity at 254 nm (ε) of residual dissolved organic matter (B, D).

To assess if surface charge affected DOM adsorption, we normalized DOC adsorption by SSA. Surface loading (*S*) reached similar maximal amounts for top- and subsoil DOM on Si-rich (*S* = 5.8 and 4.7 µmol C m^{-2}) and Al-rich (*S* = 23.2 and 20.0 µmol C m^{-2}) SROAS, but Al-rich SROAS (Al:Si = 2.1) retained more C on its surface than Si-rich SROAS (Al:Si = 1.4; Table 3).

However, since we adjusted DOC concentrations in adsorption experiments to mineral mass, the initial molar excess of DOC per surface area (r_i) was much larger for Al-rich SROAS (Table 3), and may thus have caused higher surface loadings of Al-rich SROAS. Surface loadings of amorphous Al hydroxide obtained from DOM adsorption at similar r_i but lower pH (4.0-4.5) were distinctly larger (S = 42.1 µmol C m^{-2} for r_i = 63.0 µmol C m^{-2}; Kaiser and Zech, 1997; and S = 26.7-74.2 µmol C m^{-2} for r_i = 104 µmol C m^{-2}; Schneider et al., 2010). On the other hand, surface loadings of Al hydroxide obtained under similar conditions to variants with Si-rich SROAS corresponded well with the amounts determined for Si-rich SROAS in this study (S = 5.2-11 µmol C m^{-2} for r_i = 5.6-11.2 µmol C m^{-2} at pH 4; Kaiser et al., 1997). Our data is thus inconclusive with respect to surface-charge effects of Si incorporation on DOM adsorption on SROAS.

Table 3: Surface loading (S) and molar Al:C ratio after adsorption of dissolved organic matter (DOM) on short-range ordered aluminosilicates with different molar Al:Si ratios (initial pH 5). Initial conditions are specified by concentrations (c_i) and respective molar excess per unit surface area (r_i).

Topsoil DOM	**c_i [mg C l^{-1}]**	**9.3**	**17.5**	**25.5**	**34.7**	**44.0**
Al:Si = 1.4	r_i [µmol C m^{-2}]	2.0	3.7	5.4	7.3	9.3
1 h	S [µmol C m^{-2}]	1.6	2.3	2.5	3.1	3.3
	C removed [%]	80.2	62.5	46.5	41.4	36.1
	Al:C	15.8	11.0	10.1	8.2	7.7
168 h	S [µmol C m^{-2}]	1.5	2.7	3.8	4.7	5.8
	C removed [%]	81.8	72.7	70.5	63.1	62.5
	Al:C	16.5	9.4	6.6	5.4	4.4
Al:Si = 2.1	r_i [µmol C m^{-2}]	22.8	42.6	62.3	84.7	107.4
24 h	S [µmol C m^{-2}]	8.7	8.0	10.1	14.5	14.1
	C removed [%]	37.1	18.9	16.2	17.1	12.9
	Al:C	42.4	44.9	35.6	24.6	25.3
168 h	S [µmol C m^{-2}]	12.5	15.7	18.0	23.2	18.0
	C removed [%]	58.0	36.3	28.9	27.0	16.9
	Al:C	28.5	22.9	19.7	15.3	19.7
Subsoil DOM	**c_i [mg C l^{-1}]**	**6.2**	**11.9**	**17.3**	**23.2**	**29.0**
Al:Si = 1.4	r_i [µmol C m^{-2}]	1.3	2.5	3.6	4.9	6.1
1 h	S [µmol C m^{-2}]	1.2	1.6	2.6	3.5	4.4
	C removed [%]	83.4	60.0	72.6	70.4	68.8
	Al:C	21.6	16.2	9.8	7.2	5.7
168 h	S [µmol C m^{-2}]	1.1	2.2	3.1	3.9	4.7
	C removed [%]	85.7	84.9	82.9	78.8	77.2
	Al:C	23.0	11.6	8.2	6.5	5.3
Al:Si = 2.1	r_i [µmol C m^{-2}]	15.1	29.1	42.3	56.7	70.9
1 h	S [µmol C m^{-2}]	8.9	3.9	8.3	9.0	15.4
	C removed [%]	55.0	13.2	20.3	15.7	20.7
	Al:C	40.0	90.2	42.8	39.4	23.1
168 h	S [µmol C m^{-2}]	11.8	18.3	16.0	14.2	20.0
	C removed [%]	79.9	62.2	37.5	25.1	28.3
	Al:C	30.1	19.4	22.2	25.0	17.8

We observed differences in adsorption kinetics between topsoil and subsoil DOM for adsorption on Si-rich SROAS. The effect of contact time depended on initial DOC concentration. There was no difference in topsoil DOM adsorption at lower concentrations,

while at higher initial concentrations, adsorption increased with contact time (Fig. 2A). At maximum initial DOC concentration, C contents increased from 11.6 mg C g^{-1} after 1 h, to 15.8 mg C g^{-1} after 24 h, and 20.4 mg C g^{-1} after 168 h. The effect of contact time was much smaller for subsoil DOM. From 1 h to 168 h, the C content increased from 15.7 to 16.8 g C g^{-1} only at the maximum initial DOC concentration (Fig. 2C). Generally, DOM adsorption equilibrated rapidly for both types of soil DOM, since most of DOM was retained within 1 h. Similarly, adsorption of polydisperse organic species on various mineral surfaces was equilibrated within one to six hours (Shaker et al., 2012; Tomaić and Žutić, 1988; Zhou et al., 2001). Stronger time-dependency of topsoil DOM adsorption may be related to its composition. Molar absorptivity and ^{13}C-NMR spectra indicated a slightly higher content of aromatic C in topsoil DOM (Tables 1 and 2), and vibrational patterns in FTIR spectra suggested differences in polysaccharide content and composition of aromatics (Fig. S2). Variable affinity of DOM constituents for mineral surfaces can cause divergence in their adsorption kinetics (Coward et al., 2019; Ochs et al., 1994). For instance, in batch experiments with goethite, small aromatic acids rapidly adsorbed within 15 min, whereas lignin degradation products with higher molecular weight adsorbed more slowly, resulting in time-dependent fractionation (Coward et al., 2019).

To investigate fractionation of organic species upon interaction with SROAS, we examined the DOM composition in the supernatants after reaction with the minerals. Molar absorptivity of DOM decreased with increasing proportions of DOM adsorbed of both topsoil and subsoil DOM on Si-rich (Al:Si = 1.4) and Al-rich (Al:Si = 2.1) SROAS (Fig. 2B, D), indicating that aromatic fractions of DOM were preferentially retained on both minerals (Chorover and Amistadi, 2001; Meier et al., 1999). Since the proportions of added DOM removed by adsorption increased with decreasing initial DOC concentration (Table 3), fractionation of DOM was most pronounced at lowest initial concentrations (Meier et al., 1999). This pattern was also apparent in DRIFT spectra of freeze-dried supernatants, since deviation of absorption intensities from initial DOM solutions related to the proportion of C removed by adsorption. Retention of oxidized aromatic degradation products from topsoil DOM solutions by Si-rich and Al-rich SROAS was supported by decreased intensities of stretching vibrations of phenolic OH groups at 1265 cm^{-1} (Figs. 3 and S3; Niemeyer et al., 1992; Krettek and Rennert, 2021), together with lower relative absorption at 1620 cm^{-1}. Absorption at 1620 cm^{-1} is related to vibrations of aromatic C=C bonds and stretching of dissociated carboxyl groups (Niemeyer et al., 1992). Concordant with molar absorptivity (Fig. 2B), this was only visible at lower initial DOC concentrations for variants with Al-rich SROAS (Fig. S3).

A relative decrease in absorption intensity at 1720 cm^{-1} indicates retention of carboxyl groups by mineral surfaces (Kothawala et al., 2012; Krettek and Rennert, 2021). This was already

visible after 1 h of contact time, irrespective of DOC concentration and mineral phase (Figs. 3 and S3), documenting that a fraction of carboxyl groups was very rapidly adsorbed.

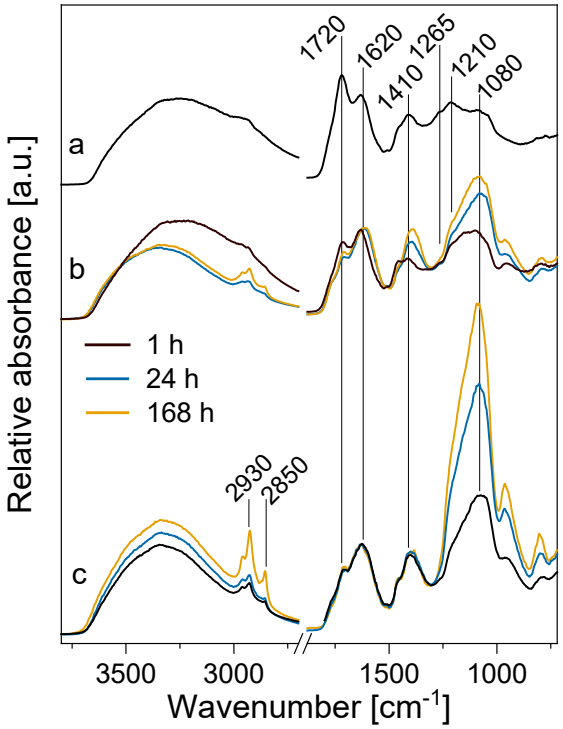

Figure 3: Diffuse reflectance infrared Fourier-transform spectra of (a) freeze-dried topsoil dissolved organic matter and supernatants obtained from variants with (b) high and (c) low initial dissolved organic C concentrations after different contact times with a short-range ordered aluminosilicate (Al:Si = 1.4). Data was normalized to absorption at 1630 cm^{-1}.

Changes in the spectral region 1300-1000 cm^{-1} further supported loss of oxygen-containing functional groups with successive adsorption of topsoil DOM. A pronounced band at 1210 cm^{-1} in freeze-dried topsoil DOM can be attributed to C-O stretching in carbonyl and carboxyl groups, together with OH-deformation vibrations in carboxyl groups (Niemeyer et al., 1992). It became less distinct with DOM removal, while absorption intensity at lower wavenumbers around 1080 cm^{-1} markedly increased in supernatants of Si-rich and Al-rich (Al:Si = 2.1) SROAS (Figs. 3 and S3), suggesting accumulation of carbohydrates in residual DOM (Kaiser and Guggenberger, 2000; Krettek and Rennert, 2021). With respect to subsoil DOM, adsorption on Si-rich SROAS caused a striking increase of absorption at 1140 cm^{-1} relative to that at 1620 cm^{-1} and 1410 cm^{-1} for all contact times (Fig. S4). This may also be related to exclusion of polysaccharides from adsorption; however, silicate species strongly absorb in the region of glyosidic bond vibrations, too (Tinti et al., 2015). Concentrations of Si were very low (≤0.6 mg l^{-1}; <1% of mineral Si). Although we cannot exclude silicate salts that may have formed during freeze-drying, we attribute infrared absorption in the respective region mainly to organic functional groups. Preferential exclusion of carbohydrates from adsorption on mineral surfaces was reported for Al-saturated montmorillonite, goethite, and amorphous Al hydroxide (Chorover and Amistadi, 2001; Kaiser et al., 1997; Kaiser and Guggenberger, 2000; Krettek

and Rennert, 2021). With respect to Al-rich SROAS (Al:Si = 2.1), we observed only marginal changes in absorption patterns of freeze-dried supernatants from experiments with subsoil DOM (Fig. S5).

Compared to initial DOM solutions, both adsorption of topsoil and subsoil DOM led to a shift in O-H stretching (approx. 3200 cm^{-1}) towards higher wavenumbers and a loss of absorption intensity between 3200 and 2500 cm^{-1}. This is likely related to the loss of organic oxygen-containing functional groups. With successive removal of DOM, sharp bands centred at 2960, 2930, and 2850 cm^{-1} from asymmetric and symmetric stretching of aliphatic C-H appeared in the spectra (Figs. 3 and S3-5), indicating preferential exclusion of alkyl C (Kaiser, 2003; Kaiser et al., 1997; Kaiser and Guggenberger, 2000).

In summary, we observed similar patterns of DOM fractionation by adsorption on both Si-rich and Al-rich SROAS, that is, preferential retention of aromatic and oxidized organic substances, and accumulation of carbohydrates and aliphatic compounds in the supernatant. This points to formation of adsorption complexes of aluminol groups with negatively charged oxygen functional groups on both minerals (Gu et al., 1994; Parfitt et al., 1977), while their accessibility quantitatively governed adsorption and thus the extent of fractionation.

Co-precipitation of Al, Si, and DOM

In addition to soil DOM, we studied uptake of litter DOM rich in polysaccharides to assess possible DOM fractionation by co-precipitation with SROAS as a function of DOM composition. In the presence of all types of DOM, precipitation of Al was almost complete (>99%) irrespective of the initial Al:C ratio. With increasing DOC concentrations, increasing total amounts of C were co-precipitated, and the solids showed decreasing Al:C ratios with increasing DOM input (Table 4). The proportion of DOM removed did not vary with initial DOC concentration, but with DOM composition only. Organic species from beech-litter DOM were removed by 39.9 to 50.8%, while removal of fir-litter DOM was slightly higher, ranging from 54.0 to 60.6% (Table 4). Precipitation from topsoil DOM was highest, ranged from 70.9 to 81.0%, while removal of subsoil DOM was lower in all variants and reached proportions of 68.2 to 77.4%. The efficacy of DOM removal was linearly related to its content of aromatic C quantified by molar absorbtivity and ^{13}C-NMR spectroscopy (Tables 1 and 2; Fig. S6). Molar absorptivity of DOM left in the supernatants decreased markedly to 78-165 l mol^{-1} cm^{-1} for soil DOM and 56-109 l mol^{-1} cm^{-1} for litter DOM compared to initial values (Fig. S7). These results support preferential enrichment of aromatic compounds by interaction with SROAS as previously evidenced for other precipitating Al forms (Kaiser, 1998; Riedel et al., 2012; Scheel et al., 2007; Vilgé-Ritter et al., 1999). Molar absorbtivity of residual DOM varied only marginally with DOC concentration and initial Al:Si ratio (Fig. S7). Hence, effects of these factors on retention of absorbing substances were negligible for the studied conditions, but may be more relevant at lower Al:C ratios and under acidic conditions (Scheel et al., 2007).

Table 4: Elemental composition of co-precipitates formed in the presence of different dissolved organic matter (DOM) types within 1 h as a function of initial Al:C and Al:Si molar ratios. Initial Al concentration was 1.9 mM in all experiments.

DOM type	**initial Al:C**	**no DOM**		**1.4**		**0.8**		**0.5**		**0.3**	
	initial Al:Si	**1**	**2**	**1**	**2**	**1**	**2**	**1**	**2**	**1**	**2**
No DOM	Al:Si	1.6	2.5								
Topsoil	Al:Si			1.8	2.7	1.8	2.8	2.0	3.2		
	Al:C			1.9	2.2	1.2	1.1	0.6	0.6		
	C removed [%]			72.8	70.9	74.2	76.4	76.9	81.0		
Subsoil	Al:Si			1.8	2.8	1.9	2.9	2.1	3.2		
	Al:C			2.0	2.2	1.1	1.2	0.8	0.7		
	C removed [%]			69.1	68.2	70.2	73.5	72.2	77.4		
Fir litter	Al:Si			1.9	2.6	1.9	2.8	2.0	2.9	2.1	3.2
	Al:C			2.7	2.2	1.7	1.5	0.9	0.8	0.5	0.6
	C removed [%]			54.0	60.6	54.7	58.8	57.0	59.8	55.9	56.9
Beech litter	Al:Si			1.8	2.7	1.9	2.7	1.9	2.9	2.1	3.2
	Al:C			2.6	2.8	1.7	1.8	1.2	0.9	0.6	0.6
	C removed [%]			49.2	50.8	48.6	50.1	39.9	49.6	45.3	48.1

We observed decreasing Si incorporation into co-precipitates (≤21%) with increasing DOC concentration for all types of DOM (Fig. 4). Moreover, there was no distinct decrease in DOM retention at higher levels of Si (Al:Si = 2 vs. 1). This indicates that DOM had a higher affinity for Al than Si and consequently impeded condensation reactions between the two elements. As a result, Al:Si ratios increased with increasing initial DOC concentration for both initial Si concentrations (Table 4). Exclusion of Si from co-precipitation with Al occurred also in the presence of low-molecular-weight organic ligands and humic acids (Inoue and Huang, 1990; Rouff et al., 2012). We did not find an effect of DOM composition on Si incorporation (Fig. 4), although previous research indicated that organic ligands suppressed condensation of Si and Al depending on their affinity towards Al (Inoue and Huang, 1986).

Major absorption bands in FTIR spectra close to 1000 cm^{-1} refer to Si-O-Al bonds (Bishop et al., 2013). Respective peak positions shifted to higher wavenumbers with increasing C contents for all types of DOM and both initial Al:Si ratios (Table S2), but the shift was particularly pronounced for litter DOM. Since organic substances caused exclusion of Si, this cannot be attributed to Si contents (Farmer et al., 1979; Montarges-Pelletier et al., 2005), but to uptake of polysaccharides (Eusterhues et al., 2011), which was confirmed by solid-state ^{13}C-NMR analyses of co-precipitates from reaction with litter DOM. Spectral features of retained organic matter were very similar to those of initial DOM with respect to peak positions and relative intensities (Fig. S1). Small increases in relative intensities of carboxyl C and aryl C (1-6%, Table 2) supported uptake of aromatic oxidized C moieties already evidenced from molar absorptivity of filtrates. In the alkyl region (45 to -10 ppm) of spectra obtained from both co-precipitates, signals of terminal methylene groups (22-20 ppm) were less pronounced

compared to initial DOM (Fig. S1; Knicker, 2011), which may indicate that lipids were excluded from co-precipitation.

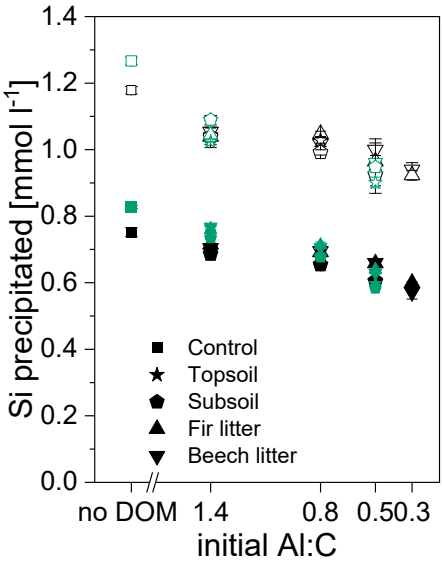

Figure 4: Amounts of Si precipitated during formation of short-range ordered aluminosilicates in the presence of four different types of dissolved organic matter (DOM) as a function of the initial molar Al:C ratio after reaction periods of 1 h (black) and 24 h (green). Full symbols indicate an initial Al:Si ratio of 2 and empty symbols of 1.

To assess differences in co-precipitated organic matter as a function of initial DOM composition, we calculated difference spectra of co-precipitates with the maximum C contents formed at an initial molar Al:Si ratio of 2 (Fig. 5) by subtracting spectra of a SROAS formed within the same reaction time and with a similar Al:Si ratio. The peak shifts caused by polysaccharide incorporation manifested in peaks centred at 1160 cm^{-1}. Intensity in this region corresponded well with polysaccharide abundance indicated from ^{13}C-NMR and FTIR analyses of parent DOM (O-alkyl C, Table 2, Fig. S2), that is, it was most pronounced for beech litter and least for topsoil DOM. A marked absorption band at 1410 cm^{-1} present in all spectra points to inner-sphere complexation of DOM with Al during co-precipitation (Kaiser et al., 1997; Parfitt et al., 1977; Scheel et al., 2008). Absorption between 1660-1600 cm^{-1} dominated the difference spectra. Absorption at 1600 cm^{-1} was relatively more pronounced with co-precipitates formed in the presence of soil DOM, while organic functional groups retained from litter DOM caused absorption maxima centred at 1660 cm^{-1} (Fig. 5). Stretching vibrations of aromatic C and deprotonated carboxyl groups cause absorption in this region (Kaiser et al., 1997; Niemeyer et al., 1992). Hence, these differences are most likely caused by variable contents of aromatic C as related to preferential uptake of aromatic compounds, and may additionally indicate ligand exchange to be more pronounced for co-precipitation of soil DOM compared to litter DOM. Formation of carboxylate by complexation with metals leads to shifts from 1625 to 1600 cm^{-1} (Kaiser et al., 1997). In difference spectra of co-precipitates formed with topsoil and fir-litter DOM, vibrations of phenolic O-H at 1265 cm^{-1} were obvious (Fig. 5; Niemeyer et al., 1992),

while respective spectra of solids formed with subsoil DOM did not exhibit a signal in this region. This indicates that the composition of retained aromatics is inherited from DOM supply.

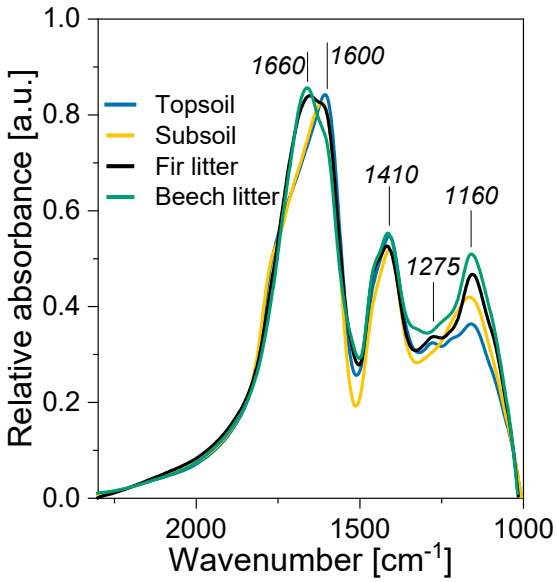

Figure 5: Difference spectra of co-precipitates formed in the presence of different types of dissolved organic matter with similar elemental composition (Al:Si = 3.2; Al:C = 0.6-0.7) obtained by transmission Fourier-transform infrared spectroscopy.

Our findings on organic matter composition in co-precipitates support its close relation to the composition of parent DOM. Abundance of aromatic products from lignin degradation enhanced uptake of DOM due to their molecular size and favoured interaction of phenolic and carboxyl groups with Al (Kaiser, 1998; Song et al., 2019). Input of DOM characterized by low contents of such compounds led to an increased proportion of polysaccharides in the co-precipitates.

Formation of SROAS in the absence of DOM

Our results on co-precipitates formed after 1 h of reaction indicated interference of DOM with SROAS formation by complexation of Al, causing displacement of Si. To identify the processes and their effects on the mineral structure of co-precipitates in detail, we first established the time-dependent chemical composition and structural evolution of SROAS in the absence of DOM. Therefore, we monitored molar Al:Si ratios and spectroscopic features of SROAS formed within 1-72 h at initial Al:Si ratios of 1-3. More than 98% of the initial Al co-precipitated irrespective of Si concentration and reaction time. Elemental composition of co-precipitates formed within 1 h was governed by increasing incorporation of Si (Fig. S8). Silicon never precipitated completely, but 3.6 to 42.2% remained in the supernatant solution. Thus, like previously reported (Lenhardt et al., 2021; Strekopytov et al., 2006), Al:Si ratios of SROAS exceeded initial Al:Si ratios of the solutes (Table S3). With increasing reaction time, Si incorporation slightly increased (Fig. S9) by up to 7.4-14.3% after 72 h. Our data corresponds well with previous findings on precipitation of SROAS within 1-100 days showing that SROAS

composition was mainly controlled by Si concentration and, to a smaller extent, by reaction time (Luciuk and Huang, 1974).

Precipitation of SROAS was initiated within 1 h by formation of Si-O-Al bonds detected from broad stretching vibrations located between 1020 and 989 cm^{-1} (Fig. 6; Fig. S10; Table S3; Bishop et al., 2013). There was no systematic shift in its position as a function of the Al:Si ratio. Decreasing Si contents only resulted in a relative increase of absorption intensity in the Al-OH bending region (ca. 590 cm^{-1}, Fig. S10; Bishop et al., 2013). The ratio of absorption bands at 690 to 590 cm^{-1} was remarkably constant for SROAS formed within 1 h (0.92 ± 0.02; Table S3), indicating a similar configuration of Al and Si irrespective of the Al:Si ratio. Solid-state ^{27}Al-NMR spectra of a SROAS with Al:Si = 2.1 revealed that Al was mainly in octahedral coordination (Al^{VI}, Hiradate, 2004). Corresponding resonances were centred at 3.6 ppm and contributed 63% to total signal intensity (Fig. 7; Table 5). Additionally, marked resonances of Al in tetrahedral (Al^{IV}; 58.2 ppm) and pentahedral (Al^{V}; 32.5 ppm) configuration point to occurrence of transient species with Al in several configurations during initial steps of SROAS polymerization, similar to Al hydroxides (Lukić et al., 2020). In solid-state ^{29}Si-NMR spectra, there was no distinct resonance line of imogolite-like Si environments (Q^0(3Al); Barron et al., 1982), but only broad resonances centred around -85 ppm (Fig. 8). The distribution of ^{29}Si resonances documents negligible condensation of Si tetrahedra, but their binding to Al (Lippmaa et al., 1980). Together with the slight upfield shift of Al^{VI} resonances compared to proto-imogolites (4-6 ppm; Levard et al., 2012), and no signals attributable to Si in Q^0(3Al), spectral features confirm the formation of amorphous species by olation of Al and Si during the first hour.

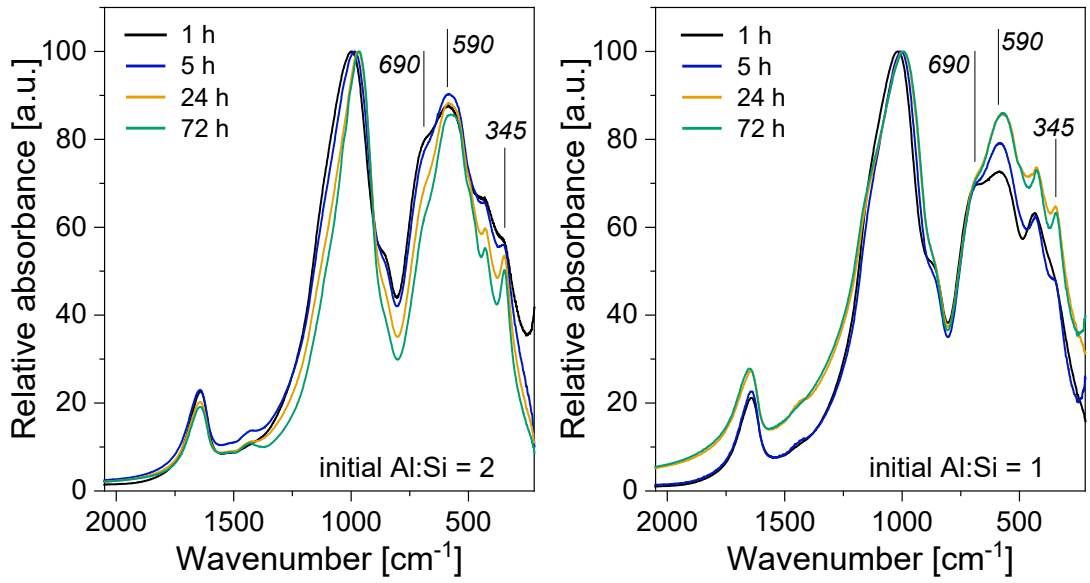

Figure 6: Structural evolution of short-range ordered aluminosilicates at an initial Al:Si ratio of 2 (left) and 1 (right) within reaction periods of 1 to 72 h at pH 5.2 as observed by transmission Fourier-transform infrared spectroscopy.

Gradually increasing the reaction time from 1 to 72 h decreased the width of the Si-O-Al band and shifted it to lower wavenumbers (Fig. 6, Table S3). Concomitantly, absorption intensities at 690 relative to 590 cm^{-1} decreased. These changes were more pronounced for initial Al:Si ratios of 2 and 3, indicating that the higher Si concentration impeded rearrangement of the chemical environment of Al (Exley, 2002; Luciuk and Huang, 1974). Vibrations of Si nuclei in Q^0(3Al) configuration close to 345 cm^{-1} (Farmer et al., 1979) emerged from a small shoulder in rapidly formed SROAS to a successively more distinct peak irrespective of the Al:Si ratio (Fig. 6). Its relative intensity was higher for SROAS formed at an initial Al:Si ratio of 2. Hence, a higher concentration of Si may also disturb formation of Si in Q^0(3Al) configuration.

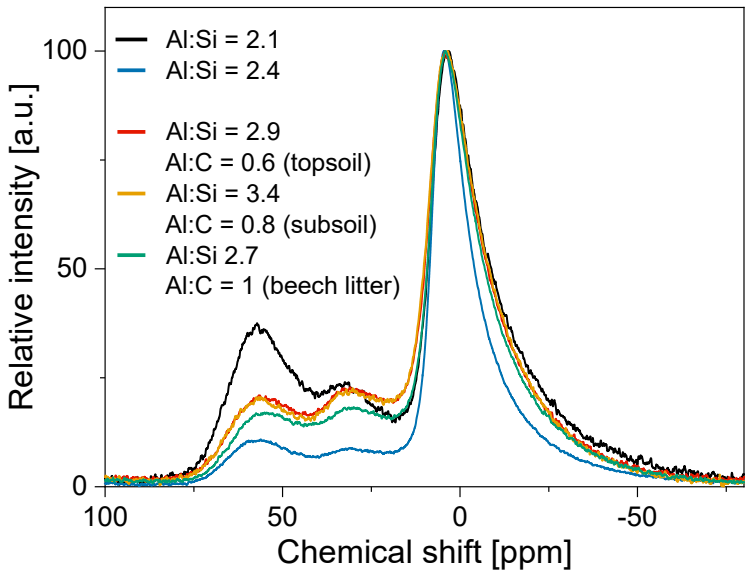

Figure 7: Solid-state ^{27}Al nuclear magnetic resonance spectra of short-range ordered aluminosilicates formed in the absence of dissolved organic matter and of co-precipitates formed in the presence of different types of dissolved organic matter at a line broadening of 25 Hz. Molar Al:Si ratios and Al:C ratios of the solids are given in the legend.

Table 5: Speciation of Al and Si in short-range ordered aluminosilicates formed in the absence and presence of dissolved organic matter (DOM). Proportions of Al nuclei in tetrahedral (Al^{IV}), pentahedral (Al^{V}) and octahedral (Al^{VI}) coordination and Si nuclei in imogolite-like configuration (Q^0(3Al)) were quantified by ^{27}Al- and ^{29}Si-NMR spectroscopy.

Initial Al:Si	Initial Al:C	DOM type	Reaction time	Al^{IV}	Al^{V}	Al^{VI}	Si in Q^0(3Al)
			[h]	[% of Al]			[% of Si]
n.d.		No DOM	1	17	20	63	
2.1		No DOM	72	7	8	85	50
2	0.5	Topsoil	24	10	20	70	18
2	0.5	Subsoil	24	9	21	69	n.d.
2	0.5	Beech litter	24	9	18	73	n.d.

We verified formation of proto-imogolite Si by solid-state ^{29}Si-NMR analysis of SROAS formed at initial Al:Si = 2 after 72 h. A sharp peak centred close to -79 ppm is attributable to Si in Q^0(3Al) (Barron et al., 1982), and contributed 50% to total signal intensity (Fig. 8, Table 5). Chemical environments of Si coincided with ^{27}Al resonances largely occurring in the Al^{VI} region

at 4.4 ppm (85%; Table 5). The slight downfield shift and decreased band width compared to amorphous precursors formed within 1 h is related to advanced polymerization of Al and its arrangement into dioctahedral sheets. We exclude significant formation of Al hydroxides since Al^{VI} nuclei in such phases resonate at higher chemical shifts (8.5 ppm; Isobe et al., 2003), and Al-hydroxide crystallites are detectable by sharp FTIR absorption bands that were lacking in spectra of all solids formed in the presence of Si (Fig. S11).

To conclude, experiments on SROAS formation in the absence of DOM showed that rapid condensation by olation governed Si incorporation into amorphous precursors. Further Si accumulation accompanied subsequent slower structural rearrangement. Locally defined imogolite-like environments (short-range order) developed within hours at moderately acidic conditions.

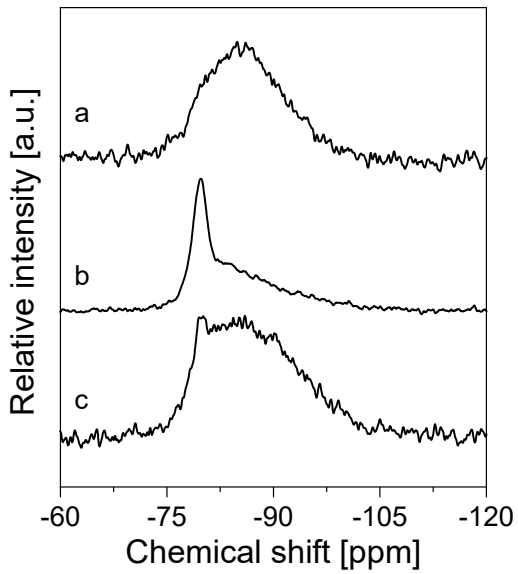

Figure 8: Solid-state ^{29}Si nuclear magnetic resonance spectra of short-range ordered aluminosilicates formed in the absence of dissolved organic matter within (a) 1 h and (b) 72 h and of (c) a co-precipitate formed in the presence of topsoil dissolved organic matter within 24 h at a line broadening of 25 Hz.

Mineral structure of co-precipitates

We compared element retention and mineral structure of two reaction times (1 and 24 h) to elucidate the effects of DOM on SROAS formation. In the previous section, we established that SROAS polymerization within 1 h was driven by olation. Consequently, interference of organic functional groups in olation reactions caused the observed Si exclusion as a function of DOM concentration. There was neither a recognizable positive effect of reaction time on the amount of co-precipitated DOM, nor an effect on molar absorptivity of residual DOM. This shows that DOM complexation rapidly equilibrated, and that organic functional groups have a higher affinity for Al compared to Si. Decreased Si incorporation caused by DOM enhanced relative absorption in the region of Al-OH bending (590 cm^{-1}, Table S2). The ratio of absorption at 690 to that at 590 cm^{-1} of co-precipitates formed within 1 h (Table S2) equalled that of SROAS

formed in the absence of DOM (reaction time = 1 h, Table S3). This indicates a similar coordination environment of OH groups bound to Al and Si nuclei irrespective of the initial DOC concentration. Hence, besides displacement of Si because of Al complexation, DOM did not seem to impose major structural changes on rapidly formed co-precipitates.

In contrast to variants without DOM addition, proceeding reaction time did not lead to further accumulation of Si (Fig. 4), indicating that DOM impeded further reactions with Si during structural rearrangement. Structural evolution of precipitates formed in the absence of DOM became evident in FTIR spectra by three indicators. First, a marked shift of the maxima position of bands attributed to Si-O-Al vibrations, second, by widening of the absorbance ratio 690:590, and third, by a progressive increase in absorption of Si in Q^0(3Al) close to 345 cm^{-1} (Fig. 6). Co-precipitates obtained after 24 h also exhibited a shift to lower wavenumbers of the Si-O-Al band irrespective of initial Al:Si and Al:C ratios, but it was more pronounced for variants with an initial Al:Si = 2 (Table S2). This implies, together with a decrease in the absorption ratio 690:590 for all co-precipitates that reacted for 24 h (Table S2), that structural reorganization occurred by further condensation of Al and Si. However, it did not proceed to the same extent as in the absence of DOM (Table S3).

We studied the absorption band related to Si in Q^0(3Al) close to 345 cm^{-1} (Farmer et al., 1979) to assess effects on the formation of this configuration. Exemplary spectra of co-precipitates formed in the presence of topsoil DOM and beech-litter DOM are shown in figure 9. These two types of DOM represent the extrema among the studied solutions regarding DOM composition (Table 2). A distinct absorption band at 345 cm^{-1} was present in all co-precipitates reacted for 24 h, irrespective of initial composition of synthesis solution, except for variants generated in the presence of topsoil DOM at maximum DOC concentration (Al:C = 0.5, Fig. 9B). For variants with initial Al:Si ratios of 2, its relative intensity decreased with increasing DOC concentration by trend for all types of DOM. This indicates that all types of DOM disturbed the formation of Q^0(3Al), but did not inhibit it completely. Effects of DOM composition were restricted to topsoil DOM, because for both initial Al:Si at maximum DOC concentration, relative absorption at 345 cm^{-1} was diminished (Fig. 9). We attribute this result to the largest amount of oxidized aromatic species in this DOM sample that are highly affine for complexing Al (Hu et al., 2008; Song et al., 2019; Xu et al., 2010).

^{27}Al-NMR spectra of co-precipitates formed within 24 h in the presence of topsoil, subsoil, and beech-litter DOM (Al:C = 0.5 and Al:Si = 2) revealed interaction of Al with all types of DOM. Compared to the precipitate formed after 72 h, all ^{27}Al spectra exhibited a greater band width of the peak caused by Al^{VI} nuclei (Fig. 7), documenting greater asymmetry in electric field gradients and thus distortion by organic functional groups. However, peak positions were centred at 4.0-4.2 ppm, that is, in a similar range as for proto-imogolites (Lenhardt et al., 2021; Levard et al., 2012). Hence, analysis of our co-precipitates points to formation of

aluminosilicate oligomers that to some degree contain Al^{VI} in dioctahedral sheets. Based on FTIR analysis, this allowed also for formation of the locally defined imogolite-like configuration. To elucidate whether formation of Si in Q^0(3Al) configuration was also possible in the presence of topsoil DOM, we analysed the corresponding sample by ^{29}Si-NMR spectroscopy. Spectra of this sample were dominated by broad resonances of ill-defined Si species centred around -85 ppm, but slightly enhanced resonances close to -79 ppm indicated formation of Si nuclei in Q^0(3Al) configuration (Fig. 8). Integration yielded a contribution of 18% to total signal intensity (Table 5). The distribution of signal intensity from ill-defined Si environments contains information on the relative contribution of bonds between Si tetrahedra and bonds between Si and Al (Lippmaa et al., 1980). Comparison with the precipitate formed within 1 h indicates that a substantial amount of Si in the co-precipitate formed in the presence of topsoil DOM has a similar coordination, but contains a fraction of Si further condensed as indicated by resonances at upfield chemical shifts (Fig. S12).

In summary, we showed that DOM hinders olation during initial steps of SROAS polymerization. Subsequently, structural evolution of mineral-organic species is partially hindered. Apparently, irrespective of chemical composition, DOM concentration was never sufficient to completely block formation of oligomeric Al and imogolite-like local configurations. All types of DOM slowed crystallization and caused the contribution of ill-defined Si species to increase. This effect was particularly pronounced for oxidized aromatic DOM.

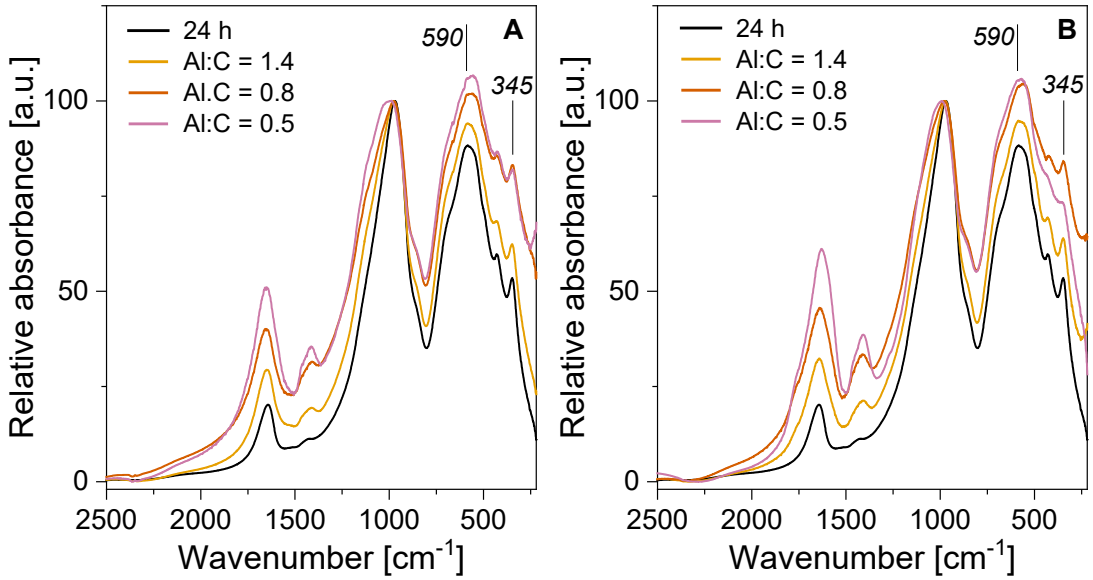

Figure 9: Transmission Fourier-transform infrared spectra of short-range ordered aluminosilicates formed in the absence of dissolved organic matter (DOM) and co-precipitates formed in the presence of beech litter (A) and topsoil DOM (B) at different initial Al:C ratios and an initial Al:Si ratio of 2.

Implications for interactions of SROAS and organic matter in the environment

In soils and sediments, SROAS are perceived as microporous solids that provide large surfaces for interaction with natural substances, but their hydrous and poorly crystalline nature

makes them very susceptible to aggregation upon dehydration (Kaufhold et al., 2010; Rousseaux and Warkentin, 1976). We ascribed low SSA of Al-rich SROAS to dense packing of small precursors of imogolite forced on the material by slow freezing (Lenhardt et al., 2021). Here, we showed that aggregation of Al-rich SROAS caused very low DOM retention. Thus, in soil environments where proto-imogolite forms in the absence of significant amounts of DOM and moisture conditions that allow pronounced dehydration (Farmer et al., 1984; Jongmans et al., 2000; Thompson et al., 1996), adsorption on Al-rich SROAS could be significantly reduced. Incorporation of Si into SROAS led to larger SSA, ultimately promoting DOM adsorption on dried mineral particles. This is very likely related to its impact on structure and surface charge, which influences aggregation mechanisms. Increased SSA of poorly crystalline metal (hydr)oxides by Si incorporation have been reported for Al (Lenhardt et al., 2021; Montarges-Pelletier et al., 2005; Pyman and Posner, 1978) and Fe (Jones et al., 2009; Schwertmann et al., 2004). Silicic acid impedes crystallization of Fe (hydr)oxides and particle growth (Cismasu et al., 2014; Doelsch et al., 2000; Tamrat et al., 2018). Consequently, dried ferrihydrite was less susceptible towards reductive dissolution by ascorbic acid than its Si-containing counterpart (Jones et al., 2009). Along with those observations, our results imply that the effects of Si on the reactivity of poorly crystalline mineral phases, especially SROAS, should be studied in more detail.

In our study, the physicochemical effect of Si incorporation on aggregation mechanisms counteracted impacts of Al contents on surface aluminol group abundance. Previous studies found a positive relation between molar Al:Si ratio of SROAS and adsorption of fluoride and phosphate that form inner-sphere complexes with aluminol groups (Clarke and McBride, 1984; Kaufhold et al., 2010). We found preferential retention of oxidized aromatic compounds and exclusion of polysaccharides and alkyl C from both topsoil and subsoil DOM solutions as previously reported for several other Al- and Fe-bearing minerals (Ding et al., 2019; Galindo and Del Nero, 2014; Kaiser et al., 1997; Krettek and Rennert, 2021; Schneider et al., 2010). This indicates that SROAS behave like other minerals with hydroxyl groups that form complexes with negatively charged oxygen groups of organic matter (Gu et al., 1994; Parfitt et al., 1977). Differences in molecular size or chemical composition among organic species with high affinity for mineral surfaces may be particularly relevant for overall adsorption kinetics. This was indicated by a more rapid adsorption of subsoil DOM compared to topsoil DOM, which may be related to differences in the available aromatic fraction (Coward et al., 2019). Mineral surfaces with abundant hydroxyl groups, like those of SROAS and poorly crystalline Al and Fe phases, induce strong fractionation. Thus, alteration of DOM composition during vertical percolation of soil may modify organic matter accrual in subsoil horizons of Andosols.

Based on molar Al:C ratios of mineral-organic associations obtained from adsorption and co-precipitation, the latter process was much more effective in DOM sorption. This was similarly

found for Al hydroxide obtained by freeze-drying (Mikutta et al., 2011), but to a lesser extent for undried poorly crystalline Fe (hydr)oxides (Chen et al., 2014; Eusterhues et al., 2011). This indicates that quantitative and qualitative differences in adsorption and co-precipitation are particularly relevant for soil environments with fluctuating water contents, since these conditions favour mineral aggregation. The composition of co-precipitated organic matter showed that compounds with low affinity for mineral surfaces such as polysaccharides may be efficiently retained by co-precipitation. This may contribute to accumulation of polysaccharides and microbial substances detected in Andosols (Asano and Wagai, 2015; Buurman et al., 2007; Nierop et al., 2005), and a Podzol (Parfitt et al., 1999).

During co-precipitation, Si was partially excluded by rapid interaction of Al with organic functional groups. Competition of Si and DOM for coordinative sites was previously reported for adsorption of both elements on Fe (hydr)oxides (Davis et al., 2001; Klotzbücher et al., 2020; Tipping, 1981). The lower affinity of Si for goethite surfaces led to its displacement in the presence of DOM when adsorption sites were limited (Klotzbücher et al., 2020). Other studies found reduced adsorption of polydisperse DOM on Fe (hydr)oxides in the presence of Si (Davis et al., 2001; Tipping, 1981). Elemental analysis of co-precipitates formed by polymerization of Fe, Al, and Si mobilized by biotite weathering in the presence of organic ligands revealed decreasing retention of Si with decreasing (Fe+Al):C ratio, indicating that competition of Si and organic functional groups also affected element speciation in this system (Tamrat et al., 2019). Several authors (Mizota and Van Reeuwijk, 1989; Shoji et al., 1993) proposed an antagonistic relationship of SOM accumulation and SROAS formation during development of andic soils, which controls the composition of pedogenic Al species. For instance, Huang (1991), Matus et al. (2006) and Shoji and Fujiwara (1984) assumed that extensive SOM input favours the formation of Al-organic complexes over SROAS. Our data show a gradual exclusion of Si from co-precipitates by organic functional groups, but DOM concentration was apparently not sufficient to block its incorporation completely. However, we show that organic substances can exclude Si from condensation with Al and subsequently hinder its accumulation during structural evolution. Moreover, interaction processes may cause the formation of an ill-defined Si fraction. This fraction is likely thermodynamically less stable than Si nuclei in Q^0(3Al) coordination (Farmer et al., 1991; Schneider et al., 2004). Corresponding processes may modify Si mobility particularly in soil environments affected by formation of metal-organic associations and mineral-organic co-precipitates.

Oxidized aromatic degradation products particularly interfered with SROAS crystallization by hampering structural ordering from aluminosilicate-olation complexes to proto-imogolite-like precursors. Consequently, alteration of DOM composition by removal of reactive functional groups by adsorption and co-precipitation may favour crystallization of SROAS in soil environments affected by the remaining, less sorptive organic compounds. Our data are

consistent with the view that interference of DOM proceeds by complexation with Al, disturbs the spatial arrangement of coordination spheres and consequently hampers the formation of Si nuclei in Q^0(3Al) configuration. Distortion of the chemical environments of Al^{VI} nuclei by organic functional groups modified resonances of Al in associations of SROAS and organic matter obtained from a buried andic horizon (Basile-Doelsch et al., 2007; Levard et al., 2012). Surprisingly, even more pronounced upfield shifts of Al^{VI} than we measured for co-precipitates coincided with Si nuclei held largely in Q^0(3Al) configuration in these natural samples. This may indicate that qualitatively different organic compounds interfered with SROAS formation under these conditions and implies that SROAS mineralogy can only be understood in relation to organic matter characteristics at a given site.

Conclusions

In soils that contain SROAS and experience large SOM input from oxidative lignin degradation, preferential retention of these organic compounds by both adsorption on and co-precipitation with SROAS likely contributes to SOM accumulation. Accessibility of aluminol groups drives DOM adsorption on SROAS. The Si content of SROAS modifies the extent of DOM adsorption, as it affects the minerals' aggregation. Fractionation upon adsorption induces a greater relative abundance of polysaccharides and aliphatic species in residual DOM, likely affecting its degradability and subsequent affinity for the mineral matrix. Co-precipitation effectively retains chemically less reactive DOM species like polysaccharides and may thus stabilize these easily degradable SOM components. Crystallization of SROAS is rapid under ambient conditions, proceeding within hours, but is particularly susceptible to disturbance by oxidized aromatic DOM. Future studies on the relationship of the mineralogical composition and the diversity of SOM may give insights into both SOM sequestration and Si mobility in soils.

Acknowledgements

Funding for this study was provided by the Deutsche Forschungsgemeinschaft (RE 2251/9-1). We thank the Forschungsanstalt für Waldökologie und Forstwirtschaft Rheinland-Pfalz, particularly Ingrid Neumann for supplying soil solutions and site data. We are thankful for technical assistance by Annerose Böttcher and Mathias Stein with MP-AES measurements. We gratefully acknowledge Isabel Prater and Jörg Prietzel (TU München) for ^{13}C-NMR analyses. We are also thankful for Claus Rüscher`s support with FTIR measurements.

References

Asano, M., Wagai, R., 2015. Distinctive organic matter pools among particle-size fractions detected by solid-state ^{13}C-NMR, δ^{13}C and δ^{15}N analyses only after strong dispersion in an allophanic Andisol. Soil Sci. Plant Nutr. 61, 242–248.

Asano, M., Wagai, R., Yamaguchi, N., Takeichi, Y., Maeda, M., Suga, H., Takahashi, Y., 2018. In search of a binding agent: nano-scale evidence of preferential carbon associations with poorly-crystalline mineral phases in physically-stable, clay-sized aggregates. Soil Syst. 2, 32.

Barron, P.F., Wilson, M.A., Campbell, A.S., Frost, R.L., 1982. Detection of imogolite in soils using solid state ^{29}Si NMR. Nature 299, 616–618.

Basile-Doelsch, I., Amundson, R., Stone, W.E.E., Borschneck, D., Bottero, J.Y., Moustier, S., Masin, F., Colin, F., 2007. Mineral control of carbon pools in a volcanic soil horizon. Geoderma 137, 477–489.

Basile-Doelsch, I., Amundson, R., Stone, W.E.E., Masiello, C.A., Bottero, J.Y., Colin, F., Masin, F., Borschneck, D., Meunier, J.D., 2005. Mineralogical control of organic carbon dynamics in a volcanic ash soil on La Réunion. Eur. J. Soil Sci. 56, 689–703.

Beardmore, J., Lopez, X., Mujika, J.I., Exley, C., 2016. What is the mechanism of formation of hydroxyaluminosilicates? Sci. Rep. 6, 30913.

Bi, S., Wang, C., Cao, Q., Zhang, C., 2004. Studies on the mechanism of hydrolysis and polymerization of aluminum salts in aqueous solution: Correlations between the “Core-links” model and “Cage-like” Keggin-Al_{13} model. Coord. Chem. Rev. 248, 441–455.

Bishop, J.L., Rampe, E.B., Bish, D.L., Abidin, Z., Baker, L.L., Matsue, N., Henmi, T., 2013. Spectral and hydration properties of allophane and imogolite. Clays Clay Miner. 61, 57–74.

Bruun, T.B., Elberling, B., Christensen, B.T., 2010. Lability of soil organic carbon in tropical soils with different clay minerals. Soil Biol. Biochem. 42, 888–895.

Buurman, P., Peterse, F., Almendros Martin, G., 2007. Soil organic matter chemistry in allophanic soils: A pyrolysis-GC/MS study of a Costa Rican Andosol catena. Eur. J. Soil Sci. 58, 1330–1347.

Chen, C., Dynes, J.J., Wang, J., Sparks, D.L., 2014. Properties of Fe-organic matter associations via coprecipitation versus adsorption. Environ. Sci. Technol. 48, 13751–13759.

Chen, K.-Y., Chen, T.-Y., Chan, Y.-T., Cheng, C.-Y., Tzou, Y.-M., Liu, Y.-T., Teah, H.-Y., 2016. Stabilization of natural organic matter by short-range-order Iron hydroxides. Environ. Sci. Technol. 50, 12612–12620.

Chorover, J., Amistadi, M.K., 2001. Reaction of forest floor organic matter at goethite, birnessite and smectite surfaces. Geochim. Cosmochim. Acta 65, 95–109.

Cismasu, A.C., Michel, F.M., Tcaciuc, A.P., Brown, G.E., 2014. Properties of impurity-bearing ferrihydrite III. Effects of Si on the structure of 2-line ferrihydrite. Geochim. Cosmochim. Acta 133, 168–185.

Clarke, C.J., McBride, M.B., 1984. Cation and anion retention by natural and synthetic allophane and imogolite. Clays Clay Miner. 32, 291–299.

Coward, E.K., Ohno, T., Sparks, D.L., 2019. Direct Evidence for Temporal Molecular Fractionation of Dissolved Organic Matter at the Iron Oxyhydroxide Interface. Environ. Sci. Technol. 53, 642–650.

Cradwick, P.D.G., Farmer, V.C., Russell, J.D., Masson, C.R., Wada, K., Yoshinaga, N., 1972. Imogolite, a hydrated aluminum silicate of tubular structure. Nat. Phys. Sci. 240, 187–189.

Davis, C.C., Knocke, W.R., Edwards, M., 2001. Implications of aqueous silica sorption to iron hydroxide: Mobilization of iron colloids and interference with sorption of arsenate and humic substances. Environ. Sci. Technol. 35, 3158–3162.

Ding, Y., Lu, Y., Liao, P., Peng, S., Liang, Y., Lin, Z., Dang, Z., Shi, Z., 2019. Molecular fractionation and sub-nanoscale distribution of dissolved organic matter on allophane. Environ. Sci. Nano 6, 2037–2048.

Doelsch, E., Rose, J., Masion, A., Bottero, J.Y., Nahon, D., Bertsch, P.M., 2000. Speciation and crystal chemistry of iron(III) chloride hydrolyzed in the presence of SiO_4 ligands. 1. An Fe K-edge EXAFS study. Langmuir 16, 4726–4731.

Du, P., Yuan, P., Thill, A., Annabi-Bergaya, F., Liu, D., Wang, S., 2017. Insights into the formation mechanism of imogolite from a full-range observation of its sol-gel growth. Appl. Clay Sci. 150, 115–124.

Eswaran, H., Van Den Berg, E., Reich, P., 1993. Organic carbon in soils of the world. Soil Sci. Soc. Am. J. 57, 192–194.

Eusterhues, K., Rennert, T., Knicker, H., Kögel-Knabner, I., Totsche, K.U., Schwertmann, U., 2011. Fractionation of organic matter due to reaction with ferrihydrite: Coprecipitation versus adsorption. Environ. Sci. Technol. 45, 527–533.

Eusterhues, K., Wagner, F.E., Häusler, W., Hanzlik, M., Knicker, H., Totsche, K.U., Kögel-Knabner, I., Schwertmann, U., 2008. Characterization of ferrihydrite-soil organic matter coprecipitates by X-ray diffraction and Mössbauer spectroscopy. Environ. Sci. Technol. 42, 7891–7897.

Exley, C., Schneider, C., Doucet, F., 2002. The reaction of aluminium with silicic acid in acidic solution: an important mechanism in controlling the biological availability of aluminium? Coord. Chem. Rev. 228, 127–135.

Farmer, V.C., Fraser, A.R., Robertson, L., Sleeman, J.R., 1984. Proto-imogolite allophane in podzol concretions in Australia: Possible relationship to aluminous ferrallitic (lateritic) cementation. J. Soil Sci. 35, 333–340.

Farmer, V.C., Fraser, A.R., Tait, J.M., 1979. Characterization of the chemical structures of natural and synthetic aluminosilicate gels and sols by infrared spectroscopy. Geochim. Cosmochim. Acta 43, 1417–1420.

Farmer, V.C., Fraser, A.R., Tait, J.M., 1977. Synthesis of imogolite: A tubular aluminium silicate polymer. J. Chem. Soc. Chem. Commun. 13, 462–463.

Farmer, V.C., McHardy, W.J., Palmieri, F., Violante, A., Violante, P., 1991. Synthetic allophanes formed in calcareous environments: Nature, conditions of formation, and transformations. Soil Sci. Soc. Am. J. 55, 1162–1166.

Filimonova, S., Kaufhold, S., Wagner, F.E., Häusler, W., Kögel-Knabner, I., 2016. The role of allophane nano-structure and Fe oxide speciation for hosting soil organic matter in an allophanic Andosol. Geochim. Cosmochim. Acta 180, 284–302.

Fleury, G., Del Nero, M., Barillon, R., 2017. Effect of mineral surface properties (alumina, kaolinite) on the sorptive fractionation mechanisms of soil fulvic acids: Molecular-scale ESI-MS studies. Geochim. Cosmochim. Acta 196, 1–17.

Fujii, K., Hayakawa, C., Inagaki, Y., Ono, K., 2019. Sorption reduces the biodegradation rates of multivalent organic acids in volcanic soils rich in short-range order minerals. Geoderma 333, 188–199.

Galindo, C., Del Nero, M., 2014. Molecular level description of the sorptive fractionation of a fulvic acid on aluminum oxide using electrospray ionization Fourier transform mass spectrometry. Environ. Sci. Technol. 48, 7401–7408.

Gérard, M., Caquineau, S., Pinheiro, J., Stoops, G., 2007. Weathering and allophane neoformation in soils developed on volcanic ash in the Azores. Eur. J. Soil Sci. 58, 496–515.

Griffin, B.A., Jurinak, J.J., 1973. Estimation of activity coefficients from the electrical conductivity of natural aquatic systems and soil extracts. Soil Sci. 116, 26–30.

Gu, B., Schmitt, J., Chen, Z., Liang, L., McCarthy, J.F., 1995. Adsorption and desorption of different organic matter fractions on iron oxide. Geochim. Cosmochim. Acta 59, 219–229.

Gu, B., Schmitt, J., Chen, Z., Liang, L., McCarthy, J.F., 1994. Adsorption and desorption of natural organic matter on iron oxide: Mechanisms and models. Environ. Sci. Technol. 28, 38–46.

Guggenberger, G., Zech, W., Schulten, H.-R., 1994. Formation and mobilization pathways of dissolved organic matter: Evidence from chemical structural studies of organic matter fractions in acid forest floor solutions. Org. Geochem. 21, 51–66.

Gustafsson, J.P., Bhattacharya, P., Karltun, E., 1999. Mineralogy of poorly crystalline aluminium phases in the B horizon of Podzols in southern Sweden. Appl. Geochem. 14, 707–718.

Henmi, T., Wada, K., 1976. Morphology and composition of allophane. Am. Mineral. 61, 379–390.

Hiradate, S., 2004. Speciation of aluminum in soil environments: Application of NMR technique. Soil Sci. Plant Nutr. 50, 303–314.

Hu, Y.F., Xu, R.K., Dynes, J.J., Blyth, R.I.R., Yu, G., Kozak, L.M., Huang, P.M., 2008. Coordination nature of aluminum (oxy)hydroxides formed under the influence of tannic acid studied by X-ray absorption spectroscopy. Geochim. Cosmochim. Acta 72, 1959–1969.

Huang, P.M., 1991. Ionic factors affecting the formation of short-range ordered aluminosilicates. Soil Sci. Soc. Am. J. 55, 1172–1180.

Huang, Y.-T., Lowe, D.J., Churchman, G.J., Schipper, L.A., Cursons, R., Zhang, H., Chen, T.-Y., Cooper, A., 2016. DNA adsorption by nanocrystalline allophane spherules and nanoaggregates, and implications for carbon sequestration in Andisols. Appl. Clay Sci. 120, 40–50.

Ildefonse, P., Kirkpatrick, R.J., Montez, B., Calas, G., Flank, A.M., Lagarde, P., 1994. ^{27}Al MAS NMR and Aluminum X-ray absorption near edge structure study of imogolite and allophanes. Clays Clay Miner. 42, 276–287.

Inoue, K., Huang, P.M., 1990. Perturbation of imogolite formation by humic substances. Soil Sci. Soc. Am. J. 54, 1490-1497.

Inoue, K., Huang, P.M., 1986. Influence of selected organic ligands on the formation of allophane and imogolite. Soil Sci. Soc. Am. J. 50, 1623–1633.

Isobe, T., Watanabe, T., D'Espinose De La Caillerie, J.B., Legrand, A.P., Massiot, D., 2003. Solid-state ^{1}H and ^{27}Al NMR studies of amorphous aluminum hydroxides. J. Colloid Interface Sci. 261, 320–324.

Iyoda, F., Hayashi, S., Arakawa, S., John, B., Okamoto, M., Hayashi, H., Yuan, G., 2012. Synthesis and adsorption characteristics of hollow spherical allophane nano-particles. Appl. Clay Sci. 56, 77–83.

Jones, A.M., Collins, R.N., Rose, J., Waite, T.D., 2009. The effect of silica and natural organic matter on the Fe(II)-catalysed transformation and reactivity of Fe(III) minerals. Geochim. Cosmochim. Acta 73, 4409–4422.

Jongmans, A.G., Denaix, L., Van Oort, F., Nieuwenhuyse, A., 2000. Induration of C horizons by allophane and imogolite in Costa Rican volcanic soils. Soil Sci. Soc. Am. J. 64, 254–262.

Kacuráková, M., Capek, P., Sasinková, V., Wellner, N., Ebringerová, A., 2000. FT-IR study of plant cell wall model compounds: Pectic polysaccharides and hemicelluloses. Carbohydr. Polym. 43, 195–203.

Kaiser, K., 2003. Sorption of natural organic matter fractions to goethite (α-FeOOH): Effect of chemical composition as revealed by liquid-state ^{13}C NMR and wet-chemical analysis. Org. Geochem. 34, 1569–1579.

Kaiser, K., 1998. Fractionation of dissolved organic matter affected by polyvalent metal cations. Org. Geochem. 28, 849–854.

Kaiser, K., Guggenberger, G., 2000. The role of DOM sorption to mineral surfaces in the preservation of organic matter in soils. Org. Geochem. 31, 711–725.

Kaiser, K., Guggenberger, G., Haumaier, L., Zech, W., 1997. Dissolved organic matter sorption on subsoils and minerals studied by ^{13}C-NMR and DRIFT spectroscopy. Eur. J. Soil Sci. 48, 301–310.

Kaiser, K., Zech, W., 1997. Competitive sorption of dissolved organic matter fractions to soils and related mineral phases. Soil Sci. Soc. Am. J. 61, 64–69.

Kaufhold, S., Dohrmann, R., Abidin, Z., Henmi, T., Matsue, N., Eichinger, L., Kaufhold, A., Jahn, R., 2010. Allophane compared with other sorbent minerals for the removal of fluoride from water with particular focus on a mineable Ecuadorian allophane. Appl. Clay Sci. 50, 25–33.

Kleber, M., Eusterhues, K., Keiluweit, M., Mikutta, C., Mikutta, R., Nico, P.S., 2015. Mineral-organic associations: Formation, properties, and relevance in soil environments. Adv. Agron. 130, 1–140.

Klotzbücher, T., Treptow, C., Kaiser, K., Klotzbücher, A., Mikutta, R., 2020. Sorption competition with natural organic matter as mechanism controlling silicon mobility in soil. Sci. Rep. 10, 11225.

Knicker, H., 2011. Solid state CPMAS ^{13}C and ^{15}N NMR spectroscopy in organic geochemistry and how spin dynamics can either aggravate or improve spectra interpretation. Org. Geochem. 42, 867–890.

Knicker, H., González-Vila, F.J., Polvillo, O., González, J.A., Almendros, G., 2005. Fire-induced transformation of C- and N-forms in different organic soil fractions from a Dystric Cambisol under a Mediterranean pine forest (*Pinus pinaster*). Soil Biol. Biochem. 37, 701–718.

Kothawala, D.N., Roehm, C., Blodau, C., Moore, T.R., 2012. Selective adsorption of dissolved organic matter to mineral soils. Geoderma 189–190, 334–342.

Kramer, M.G., Sanderman, J., Chadwick, O.A., Chorover, J., Vitousek, P.M., 2012. Long-term carbon storage through retention of dissolved aromatic acids by reactive particles in soil. Glob. Change Biol. 18, 2594–2605.

Krettek, A., Rennert, T., 2021. Mobilisation of Al, Fe, and DOM from topsoil during simulated early Podzol development and subsequent DOM adsorption on model minerals. Sci. Rep. 11, 19741.

Lenhardt, K.R., Breitzke, H., Buntkowsky, G., Reimhult, E., Willinger, M., Rennert, T., 2021. Synthesis of short-range ordered aluminosilicates at ambient conditions. Sci. Rep. 11, 4207.

Levard, C., Doelsch, E., Basile-Doelsch, I., Abidin, Z., Miche, H., Masion, A., Rose, J., Borschneck, D., Bottero, J.-Y., 2012. Structure and distribution of allophanes, imogolite and proto-imogolite in volcanic soils. Geoderma 183–184, 100–108.

Lilienfein, J., Qualls, R.G., Uselman, S.M., Bridgham, S.D., 2004. Adsorption of dissolved organic carbon and nitrogen in soils of a weathering chronosequence. Soil Sci. Soc. Am. J. 68, 292.

Lilienfein, J., Qualls, R.G., Uselman, S.M., Bridgham, S.D., 2003. Soil formation and organic matter accretion in a young andesitic chronosequence at Mt. Shasta, California. Geoderma 116, 249–264.

Lippmaa, E., Magi, M., Samoson, A., Engelhardt, G., Grimmer, A.-R., 1980. Structural studies of silicates by solid-state high-resolution ^{29}Si NMR. J. Am. Chem. Soc. 102, 4889–4893.

Luciuk, G.M., Huang, P.M., 1974. Effect of monosilicic acid on hydrolytic reactions of aluminum. Soil Sci. Soc. Am. Proc. 38, 235–244.

Lukić, M.J., Wiedenbeck, E., Reiner, H., Gebauer, D., 2020. Chemical trigger toward phase separation in the aqueous Al(III) system revealed. Sci. Adv. 6, eaba6878.

Matus, F., Amigo, X., Kristiansen, S.M., 2006. Aluminium stabilization controls organic carbon levels in Chilean volcanic soils. Geoderma 132, 158–168.

Meier, M., Namjesnik-Dejanovic, K., Maurice, P.A., Chin, Y.-P., Aiken, G.R., 1999. Fractionation of aquatic natural organic matter upon sorption to goethite and kaolinite. Chem. Geol. 157, 275–284.

Mikutta, R., Mikutta, C., Kalbitz, K., Scheel, T., Kaiser, K., Jahn, R., 2007. Biodegradation of forest floor organic matter bound to minerals via different binding mechanisms. Geochim. Cosmochim. Acta 71, 2569–2590.

Mikutta, R., Schaumann, G.E., Gildemeister, D., Bonneville, S., Kramer, M.G., Chorover, J., Chadwick, O.A., Guggenberger, G., 2009. Biogeochemistry of mineral-organic associations across a long-term mineralogical soil gradient (0.3-4100 kyr), Hawaiian Islands. Geochim. Cosmochim. Acta 73, 2034–2060.

Mikutta, R., Zang, U., Chorover, J., Haumaier, L., Kalbitz, K., 2011. Stabilization of extracellular polymeric substances (Bacillus subtilis) by adsorption to and coprecipitation with Al forms. Geochim. Cosmochim. Acta 75, 3135–3154.

Mizota, C., Van Reeuwijk, L.P., 1989. Clay Mineralogy and Chemistry of Soils Formed in Volcanic Material in Diverse Climatic Regions. ISRIC, Wageningen.

Montarges-Pelletier, E., Bogenez, S., Pelletier, M., Razafitianamaharavo, A., Ghanbaja, J., Lartiges, B., Michot, L., 2005. Synthetic allophane-like particles: Textural properties. Coll. Surf. A 255, 1–10.

Niemeyer, J., Chen, Y., Bollag, J.-M., 1992. Characterization of humic acids, composts, and peat by diffuse reflectance Fourier-transform infrared spectroscopy. Soil Sci. Soc. Am. J. 56, 135–140.

Nierop, K.G.J., Jansen, B., Verstraten, J.M., 2002. Dissolved organic matter, aluminium and iron interactions: Precipitation induced by metal/carbon ratio, pH and competition. Sci. Tot. Environ. 300, 201–211.

Nierop, K.G.J., Van Bergen, P.F., Buurman, P., Van Lagen, B., 2005. NaOH and $Na_4P_2O_7$ extractable organic matter in two allophanic volcanic ash soils of the Azores Islands - A pyrolysis GC/MS study. Geoderma 127, 36–51.

Nieuwenhuyse, A., Verburg, P.S.J., Jongmans, A.G., 2000. Mineralogy of a soil chronosequence on andesitic lava in humid tropical Costa Rica. Geoderma 98, 61–82.

Ochs, M., Ćosović, B., Stumm, W., 1994. Coordinative and hydrophobic interaction of humic substances with hydrophilic Al_2O_3 and hydrophobic mercury surfaces. Geochim. Cosmochim. Acta 58, 639–650.

Parfitt, R.L., Fraser, A.R., Farmer, V.C., 1977. Adsorption on hydrous oxides. 3. Fulvic-acid and humic-acid on goethite, gibbsite and imogolite. J. Soil Sci. 28, 289–296.

Parfitt, R.L., Kimble, J.M., 1989. Conditions for formation of allophane in soils. Soil Sci. Soc. Am. J. 53, 971–977.

Parfitt, R.L., Russell, M., Orbell, G.E., 1983. Weathering sequence of soils from volcanic ash involving allophane and halloysite, New Zealand. Geoderma 29, 41–57.

Parfitt, R.L., Yuan, G., Theng, B.K.G., 1999. A ^{13}C-NMR study of the interactions of soil organic matter with aluminium and allophane in podzols. Eur. J. Soil Sci. 50, 695–700.

Pokrovski, G.S., Schott, J., 1998. Experimental study of the complexation of silicon and germanium with aqueous organic species: Implications for germanium and silicon transport and Ge/Si ratio in natural waters. Geochim. Cosmochim. Acta 62, 3413–3428.

Pyman, M.A.F., Posner, A.M., 1978. The surface areas of amorphous mixed oxides and their relation to potentiometric titration. J. Colloid Interface Sci. 66, 85–94.

Rennert, T., Gockel, K.F., Mansfeldt, T., 2007. Extraction of water-soluble organic matter from mineral horizons of forest soils. J. Plant Nutr. Soil Sci. 170, 514–521.

Rennert, T., Eusterhues, K., Hiradate, S., Breitzke, H., Buntkowsky, G., Totsche, K.U., Mansfeldt, T., 2014. Characterisation of Andosols from Laacher See tephra by wet-chemical and spectroscopic techniques (FTIR, ^{27}Al-, ^{29}Si-NMR). Chem. Geol. 363, 13–21.

Riedel, T., Biester, H., Dittmar, T., 2012. Molecular fractionation of dissolved organic matter with metal salts. Environ. Sci. Technol. 46, 4419–4426.

Rouff, A.A., Phillips, B.L., Cochiara, S.G., Nagy, K.L., 2012. The effect of dissolved humic acids on aluminosilicate formation and associated carbon sequestration. Appl. Environ. Soil Sci. 430354.

Rousseaux, J.M., Warkentin, B.P., 1976. Surface properties and forces holding water in allophane soils. Soil Sci. Soc. Am. J. 40, 446–451.

Rumpel, C., Rodríguez-Rodríguez, A., González-Pérez, J.A., Arbelo, C., Chabbi, A., Nunan, N., González-Vila, F.J., 2012. Contrasting composition of free and mineral-bound organic matter in top- and subsoil horizons of Andosols. Biol. Fertil. Soils 48, 401–411.

Sanderman, J., Maddern, T., Baldock, J., 2014. Similar composition but differential stability of mineral retained organic matter across four classes of clay minerals. Biogeochemistry 121, 409–424.

Scheel, T., Dörfler, C., Kalbitz, K., 2007. Precipitation of dissolved organic matter by aluminum stabilizes carbon in acidic forest soils. Soil Sci. Soc. Am. J. 71, 64–74.

Scheel, T., Haumaier, L., Ellerbrock, R.H., Rühlmann, J., Kalbitz, K., 2008. Properties of organic matter precipitated from acidic forest soil solutions. Org. Geochem. 39, 1439–1453.

Schneider, C., Doucet, F., Strekopytov, S., Exley, C., 2004. The solubility of an hydroxyaluminosilicate. Polyhedron 23, 3185–3191.

Schneider, M.P.W., Scheel, T., Mikutta, R., van Hees, P., Kaiser, K., Kalbitz, K., 2010. Sorptive stabilization of organic matter by amorphous Al hydroxide. Geochim. Cosmochim. Acta 74, 1606–1619.

Schwertmann, U., Friedl, J., Kyek, A., 2004. Formation and properties of a continuous crystallinity series of synthetic ferrihydrites (2- to 6-line) and their relation to FeOOH forms. Clays Clay Miner. 52, 221–226.

Schwertmann, U., Wagner, F., Knicker, H., 2005. Ferrihydrite-humic associations: Magnetic hyperfine interactions. Soil Sci. Soc. Am. J. 69, 1009–1015.

Shaker, A.M., Komy, Z.R., Heggy, S.E.M., El-Sayed, M.E.A., 2012. Kinetic study for adsorption humic acid on soil minerals. J. Phys. Chem. A 116, 10889–10896.

Shoji, S., Fujiwara, Y., 1984. Active aluminum and iron in the humus horizons of andosols from northeastern japan: Their forms, properties, and significance in clay weathering. Soil Sci. 137, 216–226.

Shoji, S., Nanzyo, M., Dahlgren, R.A., 1993. Volcanic ash soils: genesis, properties and utilization. Dev. Soil Sci. 21. Elsevier, Amsterdam.

Singh, M., Sarkar, B., Hussain, S., Ok, Y.S., Bolan, N.S., Churchman, G.J., 2017. Influence of physico-chemical properties of soil clay fractions on the retention of dissolved organic carbon. Environ. Geochem. Hlth. 39, 1–16.

Skjemstad, J.O., Fitzpatrick, R.W., Zarcinas, B.A., Thompson, C.H., 1992. Genesis of podzols on coastal dunes in Southern Queensland. II. Geochemistry and forms of elements as deduced from various soil extraction procedures. Aust. J. Soil Res. 30, 615–644.

Song, J., Jin, X., Wang, X.C., Jin, P., 2019. Preferential binding properties of carboxyl and hydroxyl groups with aluminium salts for humic acid removal. Chemosphere 234, 478–487.

Stahr, K., Nakai, M., 1984. Der Nachweis von Imogulit in sauren Braunerden und Podsolen des Südschwarzwaldes und seine Bedeutung für die Bodenentwicklung. Mitt. Dtsch. Bodenkd. Ges. 39, 53–58.

Strekopytov, S., Jarry, E., Exley, C., 2006. Further insight into the mechanism of formation of hydroxyaluminosilicates. Polyhedron 25, 3399–3404.

Su, C., Harsh, J.B., Bertsch, P.M., 1992. Sodium and chloride sorption by imogolite and allophanes. Clays Clay Miner. 40, 280–286.

Tait, J.M., Yoshinaga, N., Mitchell, B.D., 1978. The occurrence of imogolite in some Scottish soils. Soil Sci. Plant Nutr. 24, 145–151.

Tamrat, W.Z., Rose, J., Grauby, O., Doelsch, E., Levard, C., Chaurand, P., Basile-Doelsch, I., 2019. Soil organo-mineral associations formed by co-precipitation of Fe, Si and Al in presence of organic ligands. Geochim. Cosmochim. Acta 260, 15–28.

Tamrat, W.Z., Rose, J., Grauby, O., Doelsch, E., Levard, C., Chaurand, P., Basile-Doelsch, I., 2018. Composition and molecular scale structure of nanophases formed by precipitation of biotite weathering products. Geochim. Cosmochim. Acta 229, 53–64.

Thill, A., 2016. From molecular precursor to imogolite nanotubes. Dev. Clay Sci. 7, 429–457.

Thompson, C.H., Bridges, E.M., Jenkins, D.A., 1996. Pans in humus podzols (Humods and Aquods) in coastal Southern Queensland. Aust. J. Soil Res. 34, 161–182.

Tinti, A., Tugnoli, V., Bonora, S., Francioso, O., 2015. Recent applications of vibrational mid-infrared (IR) spectroscopy for studying soil components: A review. J. Cent. Eur. Agric. 16, 1–22.

Tipping, E., 1981. The adsorption of aquatic humic substances by iron oxides. Geochim. Cosmochim. Acta 45, 191–199.

Tomaić, J., Žutić, V., 1988. Humic material polydispersity in adsorption at hydrous alumina/seawater interface. J. Colloid Interface Sci. 126, 482–492.

Torn, M.S., Trumbore, S.E., Chadwick, O.A., Vitousek, P.M., Hendricks, D.M., 1997. Mineral control of soil organic carbon storage and turnover. Nature 389, 170–173.

Vilgé-Ritter, A., Masion, A., Boulangé, T., Rybacki, D., Bottero, J.-Y., 1999. Removal of natural organic matter by coagulation-flocculation: A Pyrolysis-GC-MS study. Environ. Sci. Technol. 33, 3027–3032.

Wada, S., 1987. Imogolite synthesis at 25°C. Clays Clay Miner. 35, 379–384.

Wada, S.-I., Wada, K., 2014. Visualization of the hollowness in unit particles of allophane and imogolite. J. Fac. Agric. Kyushu Univ. 59, 369–372.

Wagai, R., Kajiura, M., Asano, M., 2020. Iron and aluminum association with microbially processed organic matter via meso-density aggregate formation across soils: Organo-metallic glue hypothesis. SOIL 6, 597–627.

Wagai, R., Kajiura, M., Asano, M., Hiradate, S., 2015. Nature of soil organo-mineral assemblage examined by sequential density fractionation with and without sonication: Is allophanic soil different? Geoderma 241–242, 295–305.

Wagai, R., Kajiura, M., Uchida, M., Asano, M., 2018. Distinctive roles of two aggregate binding agents in allophanic andisols: Young carbon and poorly-crystalline metal phases with old carbon. Soil Syst. 2, 1–23.

Weishaar, J.L., Aiken, G.R., Bergamaschi, B.A., Fram, M.S., Fujii, R., Mopper, K., 2003. Evaluation of specific ultraviolet absorbance as an indicator of the chemical composition and reactivity of dissolved organic carbon. Environ. Sci. Technol. 37, 4702–4708.

Xu, R.K., Hu, Y.F., Dynes, J.J., Zhao, A.Z., Blyth, R.I.R., Kozak, L.M., Huang, P.M., 2010. Coordination nature of aluminum (oxy)hydroxides formed under the influence of low molecular weight organic acids and a soil humic acid studied by X-ray absorption spectroscopy. Geochim. Cosmochim. Acta 74, 6422–6435.

Yucelen, G.I., Choudhury, R.P., Vyalikh, A., Scheler, U., Beckham, H.W., Nair, S., 2011. Formation of single-walled aluminosilicate nanotubes from molecular precursors and curved nanoscale intermediates. J. Am. Chem. Soc. 133, 5397–5412.

Zhou, Q., Maurice, P.A., Cabaniss, S.E., 2001. Size fractionation upon adsorption of fulvic acid on goethite: Equilibrium and kinetic studies. Geochim. Cosmochim. Acta 65, 803–812.

Chapter 4

Silicon incorporation reduces the reactivity of short-range ordered aluminosilicates toward organic acids

Coauthors: Mathias Stein, Thilo Rennert

Clays and Clay Minerals (2023) 71, 416–429

https://doi.org/10.1007/s42860-023-00248-2

Abstract

The structure and composition of short-range ordered aluminosilicates (SROAS) may control their affinity for organic acids with potential effects on soil organic matter stabilization. Adsorption mechanisms of model organic acids were studied to resolve the effect of Si incorporation. Adsorption of oxalic, salicylic, and octanoic acid on Al-rich (Al:Si = 3.7) and Si-rich (Al:Si = 1.4) SROAS was quantified by analyses of dissolved organic carbon using catalytic high temperature combustion. The initial pH of 5 and 6.5 increased up to 6.3–8.2 during adsorption of oxalic and salicylic acid, demonstrating hydroxyl release by ligand exchange. Minor changes in pH indicated weak interactions of octanoic acid with both SROAS. Adsorbates were characterized by Fourier-transform infrared spectroscopy. Asymmetric stretching of carboxylate groups at 1720 and 1700 cm^{-1}, and symmetric stretching at 1430 cm^{-1} evinced the formation of chelate complexes for oxalic acid. An absorption band centered at 1545 cm^{-1} indicated partial inner-sphere binding of salicylic acid on both SROAS. Silicon-rich SROAS adsorbed 80–90% less than Al-rich SROAS, suggesting that adsorption of oxalic and salicylic acid was controlled by surface aluminol groups. Fast kinetics of oxalate adsorption on Al sites was studied by a conductivity-based stopped-flow technique. Ligand exchange proceeded at a rate constant of 3.5 s^{-1} (25°C), similar to solute Al complexation, with an activation energy of up to 34.1 kJ mol^{-1}. A slow process with a rate constant of 0.13 s^{-1} (25°C) was attributed to diffusion of oxalate at the surface or into SROAS particles. As supported by structural characterization of Si-rich SROAS, the much lower susceptibility of Si-rich SROAS to ligand exchange relates to Al speciation. The formation of tetrahedral Al precludes its complexation by carboxyl groups.

Introduction

Short-range ordered aluminosilicates (SROAS) are hydrous minerals that form frequently in the course of weathering of volcanic ejecta (Levard & Basile-Doelsch, 2016; Parfitt, 2009). At the nanoscale, these phases exhibit variable degrees of spatial order, including structurally defined tube-shaped imogolite (Cradwick et al., 1972). Moreover, primary particles may occur as hollow spheres and corresponding fragments with variable chemical composition, frequently referred to as allophane (Levard & Basile-Doelsch, 2016). Adsorption of dissolved organic matter (DOM) on SROAS is presumed to be a major pathway of soil organic matter (SOM) accrual because SROAS surfaces have a high affinity for DOM (Lilienfein et al., 2004; Singh et al., 2017). Carboxylic aromatic acids, derived from lignin degradation, are retained preferentially on SROAS (Ding et al., 2019; Lenhardt et al., 2022), forming stable bonds by displacing hydroxyls (OH^-) from the surface (Parfitt et al., 1977). Consequently, they are protected from microbial degradation, contributing to deceleration of SOM turnover in andic soils (Basile-Doelsch et al., 2005; Kramer et al., 2012; Torn et al., 1997).

Surface affinity of SROAS for carboxylic acids probably depends on chemical composition, which is governed by formation conditions. Aluminum-rich SROAS have molar Al:Si ratios of 2–4 and were detected in andic and podzolic soils (e.g. Gustafsson et al., 1999; Parfitt et al., 1980). In particular, Al-rich SROAS exhibit short-range order, namely, imogolite-like structural features (Cradwick et al., 1972; Goodman et al., 1985). A pronounced abundance of silicic acid facilitates Si incorporation into SROAS, and phases with Al:Si ratios close to 1 form. Such conditions may prevail in the early stages of tephra weathering (Gérard et al., 2007), when water availability restrains Si leaching (Parfitt et al., 1983), or during precipitation of stream deposits (Childs et al., 1990). Together with smaller Al contents, Si incorporation is accompanied by the formation of tetrahedral Al and condensation of Si tetrahedra, resulting in structural features similar to tectosilicates in Si-rich SROAS (Farmer et al., 1979; Ildefonse et al., 1994). Positive correlations of Al:Si ratios and amounts of adsorbed anions with high affinity for inner-sphere complexation (oxalate, fluoride, phosphate; Clarke & McBride, 1984; Hanudin et al., 2002; Kaufhold et al., 2010) suggest that Si incorporation diminishes SROAS reactivity toward carboxyl groups. This may be related to a lesser abundance of aluminol groups, as silanol groups do not participate in ligand exchange with organic functional groups (Pokrovski & Schott, 1998). On the other hand, silicic acid disturbs Al oxolation (Exley et al., 2002; Lenhardt et al., 2022), which may actually foster aluminol abundance. The formation of tetrahedral Al imparts negative charge on SROAS particles (Su et al., 1992). This may cause repulsion of oxidized DOM components, but facilitates hydrogen bonding or electrostatic interactions with amino groups. Sugars, nitrogenous compounds, and benzene derivatives adsorbed on SROAS by forces weaker than chemical binding (Hashizume & Theng, 2007; Nishikiori et al., 2009). Polymerized Si species provide variable charge to SROAS (Clarke &

McBride, 1984; Su et al., 1992), and may thus contribute to electrostatic retention of organic substances. Hence, mechanistic studies are needed to resolve the effect of SROAS structure and composition on DOM binding.

Fourier-transform infrared (FTIR) spectroscopy was used to characterize the chemical environment of adsorbed functional groups on SROAS (e.g. Nishikiori et al., 2009; Parfitt et al., 1977). This technique allows for a differentiation of outer-sphere and inner-sphere complexes on Al-containing minerals (e.g. Parfitt et al., 1977; Axe & Persson, 2001). Evaluation of adsorption kinetics provides information on the rate-controlling processes and respective activation energies (Sparks, 1985; Guan et al., 2006) and is, thus, a tool to study the affinity of organic substances for SROAS surfaces in more detail. However, a suitable kinetic method must consider rapid reactions, because adsorption of organic molecules on Al-containing minerals equilibrates in the range of seconds to minutes (Borah et al., 2007; Das et al., 2004). This task may be accomplished by a conductivity-based stopped-flow technique that has been used frequently to study solute Al complexation and ion adsorption on minerals (e.g. Ikeda et al., 1984; Pohlmeier & Knoche, 1996).

The objective of the current study was to assess the impact of Si incorporation on SROAS surface reactivity toward different organic acids as models of natural DOM. For the first time, interaction mechanisms were elucidated by spectroscopic characterization of adsorbates together with the evaluation of fast adsorption kinetics using structurally characterized SROAS. Synthesis of SROAS was performed at ambient conditions to mimic surface properties of natural, poorly ordered phases (Lenhardt et al., 2021). Oxalic, salicylic, and octanoic acid were used as models of functional moieties present in soil DOM. Oxalic and salicylic acid are introduced to soil solution by organic matter degradation and root exudation (Strobel, 2001). Oxalic acid, in particular, is able to displace OH^- from surface Al sites that may react with carboxyl groups in DOM (Hanudin et al., 2002; Parfitt et al., 1977). Salicylic acid contains phenolic groups presumably involved in binding of aromatic acids. Octanoic acid resembles hydrophobic aliphatic components from plant residues (Buurman et al., 2007). This study is based on the hypothesis that Si incorporation reduces the amount of surface sites susceptible to ligand exchange and, thus, the affinity of SROAS for organic acids.

Materials and methods

Synthesis and characterization of SROAS

Two SROAS were synthesized at ambient conditions according to Lenhardt et al. (2021) by neutralizing Al-chloride hexahydrate ($AlCl_3$; AppliChem GmbH, Darmstadt, Germany) with sodium orthosilicate (Na_4SiO_4; abcr GmbH, Karlsruhe, Germany). The suspensions were dialyzed with a cellulose membrane (molecular weight cut-off 6–8 kD; Spectra Por 7, Repligen, Waltham, Massachusetts, USA) until the electrical conductivity of the permeate was

<10 µS cm^{-1} for 24 h. Suspensions were subsequently stored at ambient temperature prior to use in batch experiments. The suspension concentration was determined gravimetrically after drying 5 mL of suspension at 105°C in triplicate. The element contents (Al, Si) of SROAS were determined by dissolving SROAS in 0.2 M HCl and subsequent quantification of Al and Si by microwave plasma-atomic emission spectrometry (MP-AES; 4200 MP-AES, Agilent, Waldbronn, Germany). The synthesized SROAS contained 199 and 262 mg Al g^{-1}, and 140 and 73 mg Si g^{-1}, resulting in molar Al:Si ratios of 1.4 and 3.7, respectively. Aliquots of suspensions were freeze-dried and ground in a mortar for mineral characterization by X-ray diffractometry (XRD) and FTIR spectroscopy. Samples were exposed to CoKα radiation (λ = 0.179 nm) and diffractograms recorded at a step size of 0.02°2θ and a counting time of 97.5 s with a Bruker D2 Phaser (Bruker, Ettlingen, Germany). Transmission FTIR spectra in the mid-infrared range were obtained with an external accessory of a LUMOS infrared microscope with a mercury-cadmium-telluride detector (Bruker) using pellets prepared with a hand press from a mixture of 1 mg of sample and 200 mg of KBr. Fifty background scans were recorded against the atmosphere, and subsequently 100 sample scans accumulated at a resolution of 4 cm^{-1}. A Vertex 70 spectrometer equipped with a deuterated D-alanine-doped triglycine sulfate detector (Bruker) was used to obtain spectra in the far-infrared range at a resolution of 2 cm^{-1}. Pellets were prepared with a hydraulic press from a mixture of 1 mg of sample and 200 mg of KBr. Background scans were measured against the atmosphere before sample scans were recorded (64 scans each). The electrophoretic mobility of SROAS particles was measured in dilute suspensions (500 mg L^{-1}) at pH 5 and 6.5, and two concentrations of sodium chloride (NaCl, Chemsolute, Renningen, Germany; no addition of NaCl and 50 mmol L^{-1} NaCl). The electrophoretic mobility was analyzed by phase analysis light scattering using a Zetasizer Nano ZSP (Malvern Panalytical, Herrenberg, Germany) equipped with a helium-neon laser (λ = 633 nm) and a non-invasive backscatter detector at a fixed angle of 173°. Zeta potential was obtained by conversion of electrophoretic-mobility data using the Smoluchowski approximation.

Batch-adsorption experiments

Adsorption of oxalic, salicylic, and octanoic acid was studied at initial pH 5 and 6.5, and 5 h contact time at room temperature. Batch experiments were performed in duplicate with a mass of 200 mg of adsorbent in 40 mL of background electrolyte solution (50 mmol L^{-1} NaCl) in 50 mL glass bottles with polytetrafluoroethylene caps. Total Al and Si concentrations in batch experiments were 995–1310 and 365–700 mg L^{-1}, respectively. Adsorption was quantified as a function of initial concentration (0–7.5 mmol L^{-1} for oxalic and salicylic acid, and 0–1.2 mmol L^{-1} for octanoic acid given its lower aqueous solubility). Stock solutions were prepared from oxalic acid di-hydrate (25 mmol L^{-1}, AppliChem GmbH), sodium salicylate (25 mmol L^{-1}, Merck KGaA, Darmstadt, Germany), and octanoic acid (3.5 mmol L^{-1}, Arcos

Organics, Geel, Belgium). Stock solutions of octanoic acid were neutralized by dropwise addition of diluted NaOH (Chemsolute) to increase its solubility (Bell, 1973). The mass of SROAS, background electrolyte, and initial concentration of adsorptives were adjusted by mixing aliquots of stock solutions and SROAS suspensions previously adjusted to pH 5 or 6.5 with diluted HCl and NaOH (Chemsolute). Batches were shaken horizontally at 125 rpm, and phase separation was subsequently achieved by vacuum filtration with 0.22-µm polyether sulfone membranes (Merck Milipore, Burlington, Massachusetts, USA). The filtrates were analyzed for pH using a potentiometric electrode (Mettler Toledo, Gießen, Germany), and the concentrations of the remaining organic acids were quantified as dissolved organic carbon by catalytic high-temperature combustion using a DIMATOC 2100 (Dimatec, Essen, Germany). Filtrate Al and Si concentrations were quantified by MP-AES to detect possible SROAS dissolution.

Changes in pH during the first 30 min of contact between SROAS and adsorptives (c = 1.2 mmol L^{-1} each) were monitored at a resolution of 5 s in separate experiments (Seven Excellence S475, Mettler Toledo). Aliquots of stock solutions (NaCl, adsorptive) were pipetted into glass beakers, and the pH adjusted to 5 or 6.5. Detection of pH was initiated, and the SRAOS suspension (pH adjusted to 5 or 6.5) added after ~15 s under stirring to monitor rapid changes occurring as soon as SROAS were exposed to the adsorptives. The final volume was 20 mL. The mineral-to-solution ratio and the background electrolyte concentration equaled that in batches shaken for 5 h.

Adsorbed organic species were analyzed using air-dried filters from batches shaken for 5 h by diffuse reflectance infrared Fourier-transform (DRIFT) spectroscopy in the mid-infrared range again with the accessory of a LUMOS infrared microscope. Pestled samples (10 mg) were mixed with 150 mg KBr. Fifty background scans were recorded from pure KBr, and 50 scans of each sample were accumulated. Spectra were normalized to the absorption maximum of Si–O–Al stretching vibrations (1020–970 cm^{-1}; Farmer et al., 1979). Difference spectra were calculated by subtracting spectra of pure SROAS (batch experiments with no organic acid added) from those of the adsorption variants. Reference DRIFT spectra of oxalic acid di-hydrate, sodium oxalate (Fluka Chemie AG, Buchs, Switzerland), salicylic acid (AppliChem GmbH), and sodium salicylate were obtained from mixtures of 3–10 mg of the compound with 100 mg of KBr.

Fast adsorption kinetics

Fast adsorption kinetics were investigated by monitoring the decline of electrical conductivity in SROAS suspensions immediately after addition of organic acids. Experiments were performed with a stopped-flow apparatus that allows for detection of conductivity changes <0.1% at a resolution of milliseconds (Hi-Tech CSF-21, TkG Scientific United, Wiltshire, United Kingdom). A dilute SROAS suspension and a solution containing an organic acid were stored

in two parallel syringes and pressed simultaneously into a mixing cell. The cell had a volume of 21 µL, and mixing was complete after <30 ms. Electrical conductivity was traced ten times for 30 s at five temperatures (5, 10, 15, 20, 25°C) in individual experiments and averaged. Mineral suspensions had a mass concentration of 1 or 2 g L^{-1} and organic-acid concentration was 1 mmol L^{-1}, both were adjusted to pH 5. The background electrolyte was not adjusted to a specific concentration, but the electrical conductivity to the same level for suspension and adsorptive solution by dropwise addition of NaCl.

The approach yields information on reactions far from equilibrium, i.e. on forward reactions; backward reactions can be ignored (Sparks et al., 1996). Based on batch-adsorption experiments, reactant concentrations were adjusted to establish an excess of organic acid relative to surface sites to guarantee pseudo-first order conditions. Then, adsorption kinetics can be described by exponential functions to obtain rate constants of adsorption processes (Rennert et al., 2005; Sparks et al., 1996). Analysis of conductivity data indicated two relaxation effects with different rate constants (Supplementary Material, Fig. S1). Thus, the time(*t*)-dependent conductivity decay was fitted to a bi-exponential function:

$$\Delta K(t) = \Delta K_1 \exp(-k_1 t) + \Delta K_2 \exp(-k_2 t) + b \qquad (1)$$

where $\Delta K(t)$ represents the cumulative time-dependent decay of conductivity, ΔK_1 and ΔK_2 the relative contribution of the two processes, k_1 and k_2 the respective rate constants, and *b* the equilibrium conductivity of the system at a given temperature.

Evaluation of data obtained at different temperatures (5–25°C) yielded rate constants as a function of temperature. According to the Arrhenius equation, the temperature (*T*) dependency of rate constants is given by:

$$k = A \exp\left(-\frac{E_\mathrm{A}}{\mathrm{R}T}\right) \qquad (2)$$

with the activation energy (E_A), the gas constant (R), and a pre-exponential factor (*A*). In logarithmic form (ln(*k*)), *k* is a linear function of 1/*T* with the slope $-E_A/\mathrm{R}$. The activation energies of the two processes were calculated from a linear fit of measured ln(k_i). Data analysis was performed using OriginPro 2020 (OriginLab, Northampton, Massachusetts, USA).

Results

Characterization of adsorbents

X-ray diffractograms of SROAS showed very broad reflections indicative of a poorly ordered structure and confirmed that no crystalline Al hydroxides had formed (Fig. S2). Stretching Si–O–Al vibrations caused a band centered at 1015 cm^{-1}, typical of Si-rich SROAS (Fig. S3a; Farmer et al., 1979). The band shifted to a lower wavenumber in Al-rich SROAS (970 cm^{-1}, Fig. S3b), as observed previously for natural proto-imogolites (Gustafsson et al., 1999; Parfitt et al., 1980). The presence of Si in imogolite-like configuration was confirmed by an absorption

band close to 345 cm^{-1} (Fig. S4; Farmer et al., 1979). Infrared spectra of adsorbents were similar to those of SROAS previously characterized by ^{27}Al nuclear magnetic resonance (NMR) spectroscopy (Fig. S3; Lenhardt et al., 2021). High intensity of Al–OH bending vibrations close to 590 cm^{-1} evinced mainly octahedral coordination of Al in Al-rich SROAS. This band was less pronounced in spectra of Si-rich SROAS, and a shoulder related to OH bending centered at 690 cm^{-1} appeared, indicating tetrahedral Al and ill-defined Si species (Farmer et al., 1979; Lenhardt et al., 2021).

Zeta potentials confirmed differences in surface charge as expected from structural characterization. Irrespective of pH and NaCl concentration, the zeta potential of Al-rich SROAS exceeded that of Si-rich SROAS, indicating a more positive charge (Fig. S5). It decreased from 52.4 to 43.7 mV with increasing pH from 5 to 6.5 for Al-rich SROAS and more strongly for Si-rich SROAS, as it fell from 35.5 to –8.2 mV. Consistent with the greater Si content, this result confirmed the contribution of permanent negative charge by tetrahedral Al in Si-rich SROAS (Su et al., 1992).

Adsorption of organic acids

Release of Al and Si from SROAS during batch-adsorption experiments was negligible (Fig. S6). Aluminum-rich and Si-rich SROAS differed strongly in their affinity for oxalic and salicylic acid at both initial pH. However, the adsorbed amounts of both acids were similar for a given SROAS (Fig. 1). Dissolved organic acids were mostly in anionic form in the studied pH range, oxalic acid largely as oxalate (pK_{a1} = 1.25, pK_{a2} = 3.81 at 25°C), and the carboxyl group of salicylic acid was dissociated (pK_a (COOH) = 2.98 at 20°C). At initial pH 5, maximal adsorption of oxalic and salicylic acid on Al-rich SROAS reached 0.83–0.84 mmol g^{-1} and decreased to 0.51–0.63 mmol g^{-1} at initial pH 6.5. Maximal adsorption of both acids on Si-rich SROAS was reduced by 80–90%, relative to Al-rich SROAS. At initial pH 5, maximal adsorption of oxalic and salicylic acid on Si-rich SROAS was 0.09–0.17 mmol g^{-1} and decreased marginally to 0.06–0.09 mmol g^{-1} at initial pH 6.5. Because Al surface sites presumably control interactions with carboxylic acids (Parfitt et al., 1977), the amounts adsorbed were normalized to the adsorbents' Al contents (Table 1). The maximal amounts ranged from 1.95 to 3.17 mmol g^{-1} Al^{-1} for Al-rich SROAS and were 74–87% less for Si-rich SROAS (Table 1). Considering the marginal increase in adsorption on Si-rich SROAS at final concentrations >1.5 mmol L^{-1} (Fig. 1), measured maximal adsorption probably corresponded to the adsorption capacity of Si-rich SROAS.

The adsorption of oxalic and salicylic acid on SROAS raised the pH as a function of adsorbate quantity after 5 h (Fig. S7), indicating ligand exchange. According to time-dependent pH measurements, oxalic- and salicylic-acid adsorption equilibrated rapidly, as OH^- release occurred mostly within the first minute (Figs 3; S8). The increase in pH was greater for oxalic

acid (0.8–1.9 units) evidencing more ligand exchange than for salicylic acid (0.3–0.9 units), as maximal adsorption of both oxalic and salicylic acid on a given SROAS was similar.

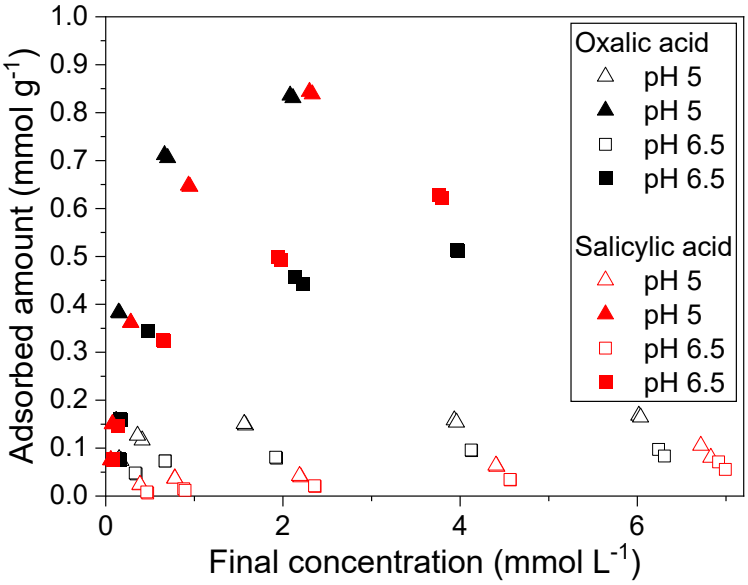

Fig. 1. Adsorption of oxalic acid and salicylic acid on short-range ordered aluminosilicates with molar Al:Si ratios of 1.4 (open symbols) and 3.7 (full symbols) at two initial pH

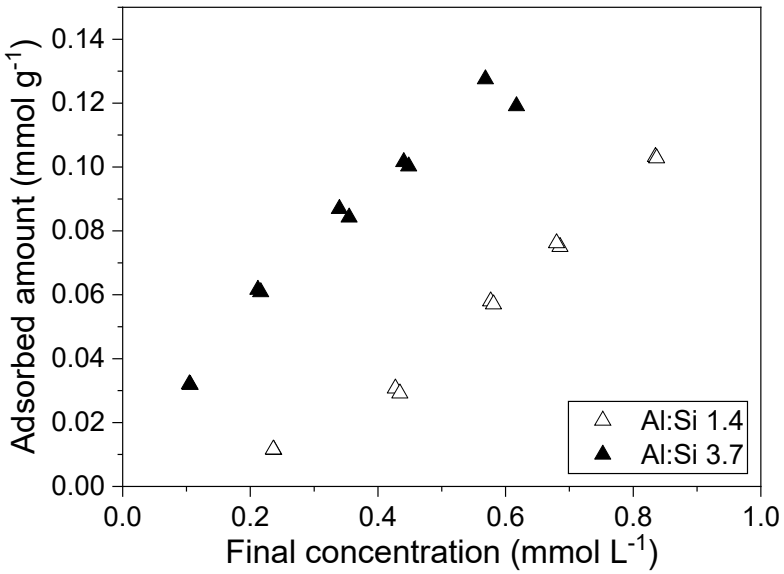

Fig. 2. Adsorption of octanoic acid on two short-range ordered aluminosilicates at initial pH 5

Adsorption of octanoic acid increased linearly with concentration at initial pH 5 for both Al- and Si-rich SROAS (Fig. 2). No adsorption was detected at initial pH 6.5. Octanoic acid has a greater pK_a (4.89 at 25°C) than oxalic and salicylic acid, indicating a greater proportion in undissociated form. Aluminum-rich and Si-rich SROAS differed only slightly in their affinity for octanoic acid. Maximal octanoic-acid adsorption was 0.12 mmol g^{-1} for Al-rich, and 0.1 mmol g^{-1} for Si-rich SROAS. Normalized to Al content, this also corresponded to similar amounts adsorbed (0.47–0.53 mmol g^{-1} Al^{-1}; Table 1). Due to solubility constraints, octanoic

acid concentrations were probably not sufficient to reach adsorption capacity. No distinct OH^- release by octanoic-acid adsorption was observed within 30 min (Fig. 3).

Table 1. Maximum adsorption (*S*) of organic acids on two short-range ordered aluminosilicates normalized by Al content (*S* given in mmol g^{-1} Al^{-1}) as a function of initial pH, and molar adsorbate-to-Al ratios (Ratio). No octanoic acid was adsorbed at initial pH 6.5

Adsorbent (molar Al:Si ratio)		**1.4**		**3.7**	
initial pH		**5**	**6.5**	**5**	**6.5**
Adsorbate					
Oxalic acid ($C_2H_2O_4$)	*S*	0.84	0.45	3.17	1.95
	Ratio	0.023	0.012	0.086	0.053
Salicylic acid ($C_7H_6O_3$)	*S*	0.47	0.32	3.2	2.38
	Ratio	0.013	0.009	0.087	0.064
Octanoic acid ($C_8H_{16}O_2$)	*S*	0.52	–	0.47	–
	Ratio	0.014	–	0.013	–

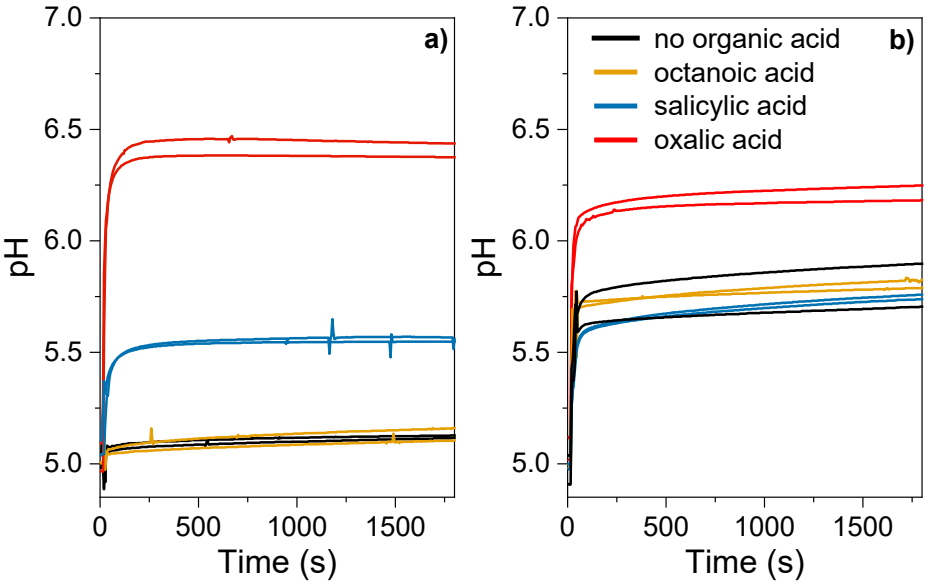

Fig. 3. Time-dependent pH change during adsorption of organic acids (1.2 mmol L^{-1}) on short-range ordered aluminosilicates with molar Al:Si ratios of **a** 1.4 and **b** 3.7 at initial pH 5

Fast adsorption kinetics

Changes in electrical conductivity within 30 s were used to retrace adsorption reactions. Absolute changes in conductivity (ΔK) were poorly reproducible and <1 µS without addition of organic acids. Adsorption of octanoic and salicylic acid did not lead to greater ΔK values (≤0.6 and ≤1.1 µS, respectively). Although adsorption was most pronounced for oxalic acid on Al-rich SROAS at initial pH 5, ΔK at *c*(SROAS) = 0.5 g L^{-1} was 0.5–1.4 µS and did not increase with SROAS concentration (1 g L^{-1}; ΔK = 0.6–1.3 µS), indicating that conductivity was poorly related to decreasing oxalic-acid concentration. Adsorption of oxalic acid on Si-rich SROAS decreased conductivity by 1–1.7 µS at 0.5 g L^{-1} and 1.5–2.4 µS at 1 g L^{-1}.

Altogether, ΔK cohered with pH changes in time-dependent analyses (Fig. 3). The release of OH^- consumes H_3O^+ ions, which have a distinctly larger molar conductivity than the anions of the organic acids under study (Table S1). At low concentrations, the molar conductivity of ions is approximately equal to limiting molar conductivities, i.e. 404 S cm^2 mol^{-1} for H_3O^+ and 74.9 S cm^2 mol^{-1} for oxalate (Kinart, 2021). This implies that conductivity is particularly sensitive to ligand exchange. The effect of oxalic-acid adsorption on Al-rich SROAS on conductivity was small due to neutralization of OH^- in direct vicinity of the mineral surface, as supported by zeta potentials and time-dependent pH data. An increase in pH decreased the zeta potential only slightly, and the increase in pH was small relative to oxalic-acid adsorption (Fig. 3). Both indicate greater buffering by Al-rich SROAS. This is probably related to the greater affinity of aluminol groups for protons compared to silanol groups. Oxygen in aluminol groups is more polarized than oxygen in silanol groups, as the electronegativity differs between Al and Si (Essington, 2004).

Given the pronounced buffering of Al-rich SROAS, evaluation of the time-dependent decay in conductivity was limited to oxalic-acid adsorption on Si-rich SROAS. Two exponential terms were necessary to reconstruct conductivity decay (Figs 4, S1), indicating at least two processes. The pre-exponential factors ΔK_1 and ΔK_2 (Table 2) were similar, suggesting equal contribution of both processes to cumulative conductivity decay. The rate constants of the two processes (k_1, k_2) differed (Table 2). Rate constants of the fast process (k_1) increased with temperature from 1.4 to 3.5 s^{-1}, while those of the slow process (k_2) increased from 0.11 to 0.13 s^{-1} at c(SROAS) = 0.5 g L^{-1}. Neither rate constant responded to an increase in SROAS concentration, which confirms that pseudo-first order conditions were established (Sparks et al., 1996). Activation energies according to the Arrhenius equation (Eq. 2; inset in Fig. 4) were 5.5 and 9.5 kJ mol^{-1} for the slow process at SROAS concentrations of 0.5 and 1 g L^{-1}, respectively (Table 2). Both the rate constants and the magnitude of activation energies are similar to a relaxation effect detected for fast adsorption of ferrocyanide on birnessite (Rennert et al., 2005). The slow process is presumably diffusion controlled because of the low activation energy (Sparks, 1985). The activation energies of the fast process were greater and ranged from 33.4 to 34.1 kJ mol^{-1} (Table 2). Activation energies of partial inner-sphere complexation of small aromatic acids on aluminum (hydr)oxides were 31.3–47.9 kJ mol^{-1} (Das et al., 2004; Guan et al., 2006). Furthermore, the rate constant of the fast process was similar to rate constants (25°C) of ligand exchange between monomeric Al and chloroacetate (1.1 s^{-1}), fluoride (4 s^{-1}), and formate (10 s^{-1}; Pohlmeier et al., 1993). The fast process is, therefore, attributed to ligand exchange by oxalate with surface aluminol groups. Rates of proton dissociation or association are too fast to be detected in the applied approach (Pohlmeier & Knoche, 1996). Hence, the slow relaxation effect may be related to diffusive transport of oxalate at the surface (‘film diffusion’) or into SROAS particles (‘intraparticle diffusion’).

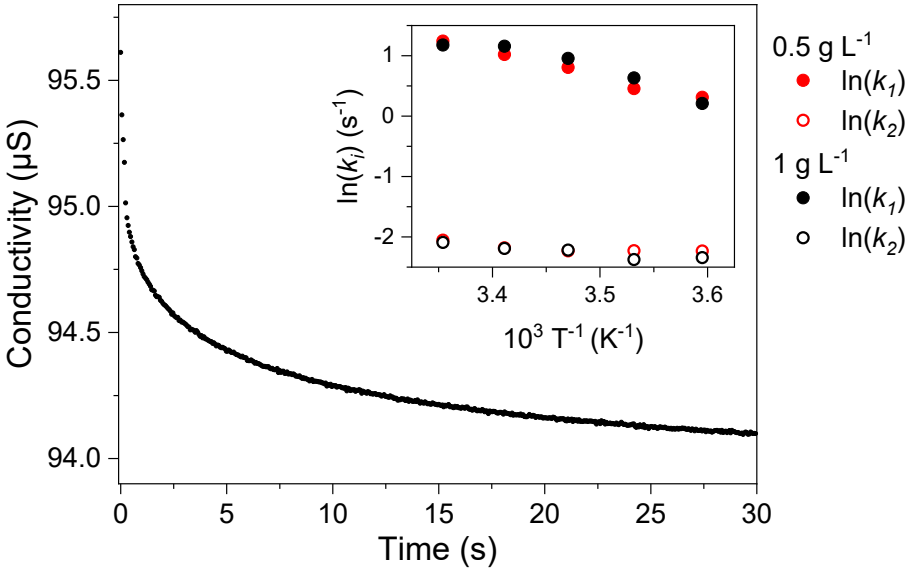

Fig. 4. Time-dependent conductivity decay due to adsorption of oxalic acid (0.5 mmol L^{-1}) on short-range ordered aluminosilicates (SROAS, Al:Si = 1.4; 1 g L^{-1}) at 25°C. The inset shows the Arrhenius plots for k_1 and k_2 at SROAS concentrations of 0.5 and 1 g L^{-1}

Table 2. Parameters obtained from fitting a bi-exponential function (Eq. 1) to conductivity decay observed in stopped-flow experiments. ΔK_1 and ΔK_2 represent relative changes in conductivity, k_1 and k_2 = rate constants, b = equilibrium conductivity, and R^2 is the coefficient of determination. Activation energies (E_A) were calculated from a linear fit of ln(k) using the Arrhenius equation (Eq. 2). R^2 and level of significance are given in parentheses

T **(°C)**	**ΔK_1 (µS)**	**k_1 (s^{-1})**	**ΔK_2 (µS)**	**k_2 (s^{-1})**	***b*** **(µS)**	***R²***
Al:Si 1.4 (0.5 g L^{-1}), oxalic acid (0.5 mmol L^{-1}; initial pH 5)						
5	0.76	1.4	0.76	0.11	35.5	0.998
10	0.69	1.6	0.64	0.11	38.8	0.997
15	0.57	2.2	0.40	0.11	42.6	0.996
20	0.56	2.8	0.37	0.11	46.3	0.996
25	0.41	3.5	0.57	0.13	50.0	0.996
E_A (kJ mol^{-1})		33.4 ± 2.2 (R^2 = 0.98; p<0.05)		5.5 ± 2.2 (R^2 = 0.58; p<0.1)		
Al:Si 1.4 (1 g L^{-1}), oxalic acid (0.5 mmol L^{-1}; initial pH 5)						
5	0.89	1.2	1.3	0.1	65.5	0.998
10	0.71	1.9	0.82	0.09	72.5	0.996
15	0.68	2.6	0.62	0.11	79.3	0.995
20	0.71	3.2	0.55	0.11	86.6	0.995
25	0.78	3.2	0.64	0.12	94.1	0.995
E_A (kJ mol^{-1})		34.1 ± 5.9 (R^2 = 0.89; p<0.05)		9.5 ± 2.1 (R^2 = 0.83; p<0.05)		

FTIR analyses of adsorbed organic acids

Adsorbed organic acids were analyzed by FTIR spectroscopy to verify adsorption modes. Generally, the intensity of vibrations from organic functional groups was proportional to the amount of organic acid adsorbed (Fig. 5). Absorption of functional groups of octanoic acid

adsorbed on SROAS was too low for interpretation. Band positions and the relative intensities of oxalic and salicylic acid did not vary between Al- and Si-rich SROAS, pH, or organic-acid concentrations.

The high molecular symmetry of aqueous oxalate results in two defined absorption bands in infrared spectra caused by asymmetric and symmetric C–O stretching vibrations (1570 and 1280 cm^{-1}; Axe & Persson, 2001). Interactions with mineral surfaces modify the electronic structure of carboxylate groups, and cause band shifts and additional peaks. Marked absorption at 1720, 1700, 1430, and 1300 cm^{-1} in difference spectra of adsorbed oxalic acid (Fig. 5a) indicate the formation of bidentate inner-sphere complexes, as asymmetric stretching vibrations were shifted to higher wavenumbers (1720, 1700 cm^{-1}), and symmetric stretching of C–O bonds appeared at 1430 cm^{-1} (Axe & Persson, 2001). This is confirmed by reference spectra of oxalic acid di-hydrate and Na oxalate with marked absorption by asymmetric C–O stretching at smaller wavenumbers (1570–1680 cm^{-1}, Fig. S9). Oxalic acid weakly bound to SROAS surfaces would also cause absorption close to 1570 cm^{-1} (Axe & Persson, 2001; Rosenqvist et al., 2003; Yoon et al., 2004), which was lacking in the spectra obtained in the current study. A distinct split of asymmetric C–O stretching (>60 cm^{-1}; Axe & Persson, 2001) would indicate monodentate binding of oxalic acid, which, however, was not the case. Intensity distribution is very similar to spectra of dissolved oxalate-Al complexes (Fujita et al., 1962), which supports the formation of mononuclear chelates.

Interactions of salicylate with Al hydroxides, monomeric Al and Fe caused absorption close to 1530 cm^{-1}, resulting from a shift in asymmetric stretching of carboxylate C–O due to complexation (Yost et al., 1990; Biber & Stumm, 1994; Guan et al., 2007). Hence, the band centered at 1545 cm^{-1} in difference spectra of adsorbed salicylic acid (Fig. 5b) indicated partial inner-sphere complexation of carboxyl groups. This was confirmed by its absence from reference spectra of Na salicylate (Fig. S10). The band at 1580 cm^{-1} (Fig. 5b) was attributed to both aromatic C–C and asymmetric C–O carboxylate stretching (Yost et al., 1990). This band disappeared following salicylate adsorption on illite (Kubicki et al., 1997). Hence, two bands related to asymmetric C–O stretching, and broad symmetric C–O stretching vibrations at 1385 cm^{-1} (Yost et al., 1990), indicated several interaction modes between salicylic acid and SROAS. Stretching vibrations of phenolic C–OH were centered at 1265 cm^{-1} with a shoulder close to 1245 cm^{-1} (Fig. 5b). Their positions depended on dissociation and surface interactions (Biber & Stumm, 1994; Yost et al., 1990). Phenolic C–OH stretching shifted downward to 1241 cm^{-1} and upward to 1266–1259 cm^{-1} upon adsorption on goethite and aluminum oxides, respectively (Biber & Stumm, 1994; Das et al., 2004; Yost et al., 1990). Biber and Stumm (1994) explained these shifts with hydrogen bonds on aluminum oxide, but inner-sphere complexation on goethite, as protonation of phenolic groups also caused blue shifts.

Accordingly, the intensity pattern in difference spectra of adsorbed salicylic acid (Fig. 5b) indicated interactions of phenolic groups with SROAS surfaces by electrostatic forces.

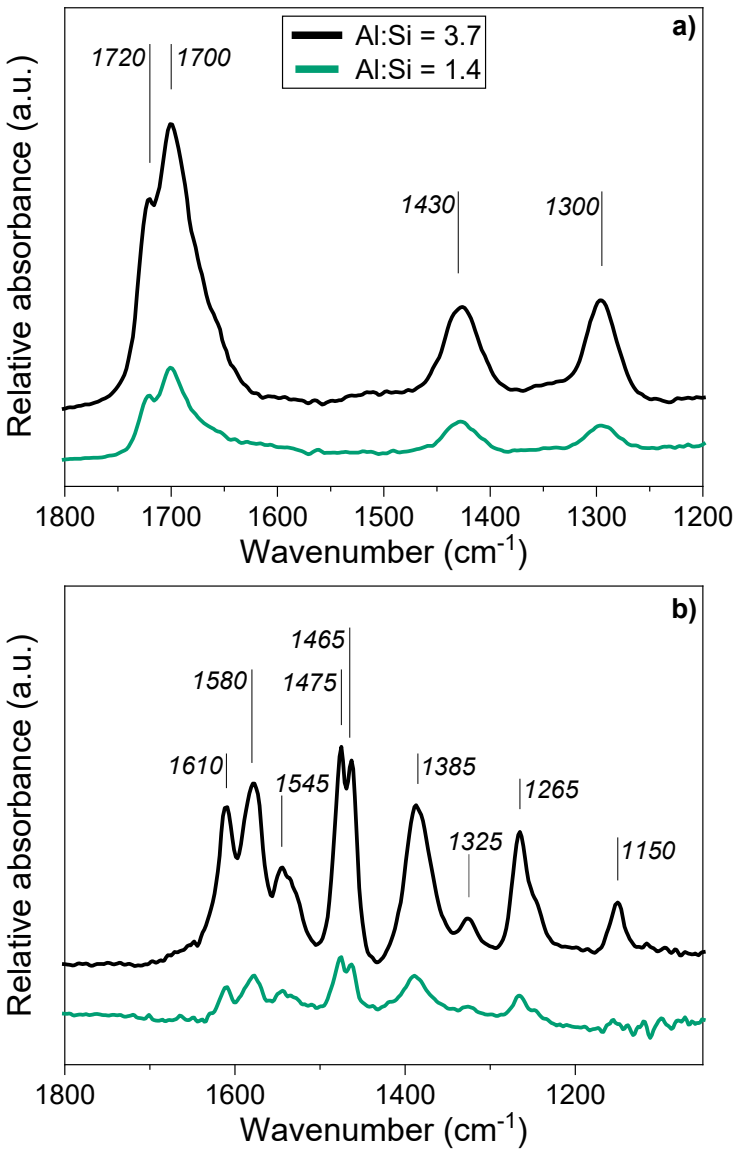

Fig. 5. Difference spectra of adsorption complexes formed by interaction of **a** oxalic and **b** salicylic acid with short-range ordered aluminosilicates at initial pH 5 obtained by diffuse reflectance infrared Fourier-transform spectroscopy. Absorbance is given in arbitrary units (a.u.) relative to absorption bands of Si–O–Al stretching vibrations (1020–970 cm^{-1}) in SROAS

Discussion

Characterization of SROAS

Spectral features of synthesized SROAS supported their structural similarity to natural Al-rich and Si-rich phases. The synthesized SROAS may be perceived as polynuclear species that contain Si in imogolite-like configuration locally, Al-rich SROAS in particular; or have features of Si-rich phases, because the extension of ordered sheets was very small (Lenhardt et al., 2021). The conditions of synthesis (concentrations, ambient temperature) hindered the

assembly of proto-imogolite-like fragments to tube- or sphere-shaped particles (Thill, 2016; Lenhardt et al., 2021). Proto-imogolites with Al:Si ratios >2 may form in soil with enhanced Al availability as shown for Podzols (Gustafsson et al., 1999; Young et al., 1980). As evinced from the pattern of O–H bending vibrations, Al was mainly in octahedral coordination in Al-rich SROAS, while Si-rich SROAS had ~30% of Al in tetrahedral coordination (Lenhardt et al., 2021). Negative zeta potentials at pH 6.5, which indicate a lower point of zero charge, supported the presence of tetrahedral Al in Si-rich SROAS (Su et al., 1992). Tetrahedral Al in SROAS forms either by condensation of aluminate ($Al(OH)_4^-$) with silicic acid at neutral to alkaline pH (Wada & Wada, 1981), or during incorporation of Si into Al olation complexes (Beardmore et al., 2016; Doucet et al., 2001). Both pathways may apply, as precipitation was rapid (Lenhardt et al., 2021). The chemical environment of tetrahedral Al in Si-rich SROAS is similar to tectosilicates (Ildefonse et al., 1994), i.e. Al is connected to four Si tetrahedra by corner-sharing.

Mechanisms of organic-acid adsorption on SROAS

The three organic acids under study interacted with SROAS surfaces by different mechanisms. Oxalic acid formed inner-sphere complexes with both carboxyl groups involved, i.e. mononuclear chelates with surface Al sites. There was no evidence of molecules retained by electrostatic forces only, so that interactions of oxalic acid with silanol groups were negligible. Less OH^- per adsorbed organic molecule was released by salicylic acid than by oxalic acid. Infrared spectra indicated that carboxyl groups of salicylic acid participated only partially in ligand exchange, and phenolic groups interacted through electrostatic forces with SROAS surfaces, forming outer-sphere complexes. As the amounts of oxalic and salicylic acid adsorbed coincided for Al- and Si-rich SROAS at both initial pH, salicylate adsorption is also related to the abundance of aluminol groups, while weak interactions with Si sites seem to be insignificant. Outer-sphere complexation is probably caused by a lower affinity of salicylate for ligand exchange than oxalate. Consistently, adsorption enthalpies of dicarboxylic acids are more exothermic than those of salicylic acid (Benoit et al., 1993).

Weaker interactions than ligand exchange controlled adsorption of octanoic acid, as no OH^- was released by adsorption. Octanoic-acid adsorption was favored by a decrease in pH, indicating that dissociated carboxyl groups interacted electrostatically with positively charged surface sites. Concordantly, retention of fatty acids by Al and Fe oxides involved carboxyl groups while the hydrophobic end did not interact with the surface (Chernyshova et al., 2011; McBride, 1980).

Effect of SROAS structure on organic-acid adsorption

Quantitative adsorption data indicated that the effect of mineral structure on adsorption depended on the adsorption mechanism. Maximum adsorption of all organic acids on Si-rich

SROAS was similar, while adsorption of oxalic and salicylic acid on Al-rich SROAS exceeded significantly that of octanoic acid. Thus, electrostatic adsorption on positively charged surface sites seems less affected by the composition of SROAS than inner-sphere complexation. Adsorption of octanoic acid on SROAS was greater than on Al oxide (0.06 mmol g^{-1}; Benoit et al., 1993), indicating more surface sites per mass for both poorly crystalline SROAS.

In contrast, the amounts of oxalic and salicylic acid adsorbed on Si-rich SROAS resembled those detected for crystalline Al (hydr)oxides (boehmite, 0.14 mmol oxalate g^{-1}; Axe & Persson, 2001; gibbsite, 0.22 mmol salicylate g^{-1}; Molis et al., 2000; Al oxide, 0.11 mmol salicylate g^{-1}; Ainsworth et al., 1998). However, adsorption was significantly greater on Al-rich SROAS, surpassing the amounts detected for natural SROAS with lower Al:Si ratios (1–1.5, 0.6–0.8 mmol oxalate g^{-1}; initial pH 6; Hanudin et al., 2002). Ligand exchange of oxalic and salicylic acid with aluminol sites confirms that octahedral Al surface sites control SROAS reactivity toward carboxylic acids. Outer-sphere complexation of oxalate with doubly coordinated hydroxyl groups as found for crystalline Al hydroxides (Axe & Persson, 2001) did not occur because of the low crystallinity of Al-rich SROAS. The lower reactivity of Si-rich SRAOS toward carboxylic acids is mainly caused by a larger abundance of tetrahedral Al, as the difference between SROAS in maximal adsorption normalized to Al content was large (74–87%). Incorporation of Si adds unreactive functional groups coordinated to Si to the surface; however, Al speciation controls the extent of inner-sphere complexation with carboxyl groups. Silicon-rich SROAS may form preferentially during weathering of alkaline tephra, when silicic acid and Al are highly available (Schaller et al., 2021). Then, a significant amount of Al may precipitate in tetrahedral coordination (Farmer et al., 1979) so that fewer sites are available for ligand exchange with DOM, and less SOM is protected against microbial degradation by chemical bonds with mineral surfaces (Mikutta et al., 2007).

Kinetics of organic-acid adsorption on SROAS

Adsorption of oxalic and salicylic acid on SROAS equilibrated within seconds to minutes, as derived from OH^- release and conductivity decay. Resolving the adsorption kinetics for <1 min allowed for a differentiation of rate-controlling processes of surface interactions. In experiments with oxalic acid and Si-rich SROAS, two relaxation effects with different rates indicated diffusive transport of oxalic acid and ligand exchange with surface Al sites. Pseudo-first order rate constants of the ligand-exchange reaction were similar to those of complexation of monomeric Al and organic anions (salicylate, benzoate, formate, acetate) determined by stopped-flow conductivity measurements at 25°C (0.17 to 30 s^{-1}; Pohlmeier et al., 1993; Secco & Venturini, 1975). The rate constants decreased with the ligand's acidity, which may be related to a greater affinity of organic anions for protons of coordinated water with increasing dissociation constant (Pohlmeier et al., 1993). Likewise, the chemical properties of organic acids may affect the rate of ligand exchange with Al surface sites of SROAS. However, rate

constants of inner-sphere complexation by organic acids on SROAS surfaces seem to be similar to rate constants of solute Al complexation.

Outer-sphere complexation in solution is very rapid, and exchange of water or OH^- from the inner hydration shell of Al is the rate-limiting step (Eigen & Wilkins, 1965; Pohlmeier & Knoche, 1996). Ligand exchange of oxalic acid at SROAS surfaces was followed by a slower, diffusion-controlled process, indicating that the rate of mass transfer through the Stern layer or into the particles affect overall adsorption kinetics, as suggested for molybdate adsorption on goethite (Lang et al., 2000). Similarly, phosphate adsorption on natural SROAS proceeded by initially rapid ligand exchange and slower subsequent phosphate uptake (Parfitt, 1989) that may relate to reactions at imperfections or diffusion into pores (Strauss et al., 1997). Diffusion of adsorptives into interstices of crystallites, resulting in slow equilibration, is particularly applicable for poorly crystalline minerals.

Conclusion

Uptake of Si accompanied by formation of tetrahedral Al results in a decreased affinity of SROAS for carboxylic acids because fewer aluminol sites are available for ligand exchange. However, Si-rich SROAS have a greater capacity for adsorption by electrostatic interactions than crystalline Al hydroxides. Partial inner-sphere complexation of salicylic acid and oxalic acid on SROAS, as detected by FTIR spectroscopy, was confirmed by the fast kinetics of oxalic-acid adsorption on Si-rich SROAS. Slow diffusive transport of oxalate along the SROAS surface or into the particles may follow adsorption. The rate of OH^- exchange at the SROAS surface resembles that of Al complexation with organic ligands in solution. The diminished formation of chemical bonds between Si-rich SROAS and organic acids may affect SOM accrual and stabilization during initial soil formation in volcanic ejecta.

Acknowledgments

Funding of this study was received from the Deutsche Forschungsgemeinschaft (RE 2251/9-1). The authors gratefully acknowledge help with mineral syntheses and adsorption experiments from Johannes Herre, the technical assistance of Annerose Böttcher with MP-AES measurements, and support from Detlev Frobel and Ludger Herrmann with XRD analyses. Far-infrared spectroscopy was conducted at the Institute of Applied Physics, University of Tübingen. Alexander Gerlach, Frank Schreiber, and Maximilian Senft are thanked for access to and support of the equipment.

References

Ainsworth, C.C., Friedrich, D.M., Gassman, P.L., Wang, Z., & Joly, A.G. (1998). Characterization of salicylate-alumina surface complexes by polarized fluorescence spectroscopy. *Geochimica et Cosmochimica Acta*, *62*, 595–612.

Axe, K. & Persson, P. (2001). Time-dependent surface speciation of oxalate at the water-boehmite (γ-AlOOH) interface: Implications for dissolution. *Geochimica et Cosmochimica Acta*, *65*, 4481–4492.

Basile-Doelsch, I., Amundson, R., Stone, W.E.E., Masiello, C.A., Bottero, J.Y., Colin, F., et al. (2005). Mineralogical control of organic carbon dynamics in a volcanic ash soil on La Réunion. *European Journal of Soil Science*, *56*, 689–703.

Beardmore, J., Lopez, X., Mujika, J.I., & Exley, C. (2016). What is the mechanism of formation of hydroxyaluminosilicates? *Scientific Reports*, *6*, 30913.

Bell, G.H. (1973). Solubilities of normal aliphatic acids, alcohols and alkanes in water. *Chemistry and Physics of Lipids*, *10*, 1–10.

Benoit, P., Hering, J.G., & Stumm, W. (1993). Comparative study of the adsorption of organic ligands on aluminum oxide by titration calorimetry. *Applied Geochemistry*, *8*, 127–139.

Biber, M.V. & Stumm, W. (1994). An in-situ ATR-FTIR Study: The surface coordination of salicylic acid on aluminum and iron(III) oxides. *Environmental Science and Technology*, *28*, 763–768.

Borah, J.M., Das, M.R., & Mahiuddin, S. (2007). Influence of anions on the adsorption kinetics of salicylate onto α-alumina in aqueous medium. *Journal of Colloid and Interface Science*, *316*, 260–267.

Buurman, P, Peterse, F., & Almendros Martin, G. (2007). Soil organic chemistry in allophanic soils: a pyrolysis-GC/MS study of a Costa Rican Andosol catena. *European Journal of Soil Science*, *58*, 1330-1347.

Chernyshova, I.V., Ponnurangam, S., & Somasundaran, P. (2011). Adsorption of fatty acids on iron (hydr)oxides from aqueous solutions. *Langmuir*, *27*, 10007–10018.

Childs, C.W., Parfitt, R.L., & Newman, R.H. (1990). Structural studies of Silica Springs allophane. *Clay Minerals*, *25*, 329–341.

Clarke, C.J. & McBride, M.B. (1984). Cation and anion retention by natural and synthetic allophane and imogolite. *Clays and Clay Minerals*, *32*, 291–299.

Cradwick, P.D.G., Farmer, V.C., Russell, J.D., Masson, C.R., Wada, K., & Yoshinaga, N. (1972). Imogolite, a hydrated aluminum silicate of tubular structure. *Nature Physical Science*, *240*, 187–189.

Das, M.R., Sahu, O.P., Borthakur, P.C., & Mahiuddin, S. (2004). Kinetics and adsorption behaviour of salicylate on α-alumina in aqueous medium. *Colloids and Surfaces A: Physicochemical and Engineering Aspects*, *237*, 23–31.

Ding, Y., Lu, Y., Liao, P., Peng, S., Liang, Y., Lin, Z., et al. (2019). Molecular fractionation and sub-nanoscale distribution of dissolved organic matter on allophane. *Environmental Science: Nano*, *6*, 2037–2048.

Doucet, F.J., Schneider, C., Bones, S.J., Kretchmer, A., Moss, I., Tekely, P., et al. (2001). The formation of hydroxyaluminosilicates of geochemical and biological significance. *Geochimica et Cosmochimica Acta*, *65*, 2461–2467.

Eigen, M. & Wilkins, R.G. (1965). The kinetics and mechanism of formation of metal complexes. *Advances in Chemistry*, *49*, 55–67.

Essington, M.E. (2004). Soil and Water Chemistry: An Integrative Approach. CRC Press, Boca Raton, Florida, USA.

Exley, C., Schneider, C., & Doucet, F.J. (2002). The reaction of aluminium with silicic acid in acidic solution: An important mechanism in controlling the biological availability of aluminium? *Coordination Chemistry Reviews*, *228*, 127–135.

Farmer, V.C., Fraser, A.R., & Tait, J.M. (1979). Characterization of the chemical structures of natural and synthetic aluminosilicate gels and sols by infrared spectroscopy. *Geochimica et Cosmochimica Acta*, *43*, 1417–1420.

Fujita, J., Martell, A.E., & Nakamoto, K. (1962). Infrared spectra of metal chelate compounds. VI. A normal coordinate treatment of oxalato metal complexes. *The Journal of Chemical Physics*, *36*, 324–331.

Gérard, M., Caquineau, S., Pinheiro, J., & Stoops, G. (2007). Weathering and allophane neoformation in soils developed on volcanic ash in the Azores. *European Journal of Soil Science*, *58*, 496–515.

Goodman, B.A., Russell, J.D., Montez, B., Oldfield, E., & Kirkpatrick, R.J. (1985). Structural studies of imogolite and allophanes by aluminum-27 and silicon-29 nuclear magnetic resonance spectroscopy. *Physics and Chemistry of Minerals*, *12*, 342–346.

Guan, X.-H., Chen, G.-H., & Shang, C. (2006). Combining kinetic investigation with surface spectroscopic examination to study the role of aromatic carboxyl groups in NOM adsorption by aluminum hydroxide. *Journal of Colloid and Interface Science*, *301*, 419–427.

Guan, X.-H., Chen, G.-H., & Shang, C. (2007). ATR-FTIR and XPS study on the structure of complexes formed upon the adsorption of simple organic acids on aluminum hydroxide. *Journal of Environmental Sciences*, *19*, 438–443.

Gustafsson, J.P., Bhattacharya, P., & Karltun, E. (1999). Mineralogy of poorly crystalline aluminium phases in the B horizon of Podzols in southern Sweden. *Applied Geochemistry*, *14*, 707–718.

Hanudin, E., Matsue, N., & Henmi, T. (2002). Reactions of some short-range ordered aluminosilicates with selected organic ligands. *Developments in Soil Science*, *28*, 319–332.

Hashizume, H. & Theng, B.K.G. (2007). Adenine, adenosine, ribose and 5`-AMP adsorption to allophane. *Clays and Clay Minerals*, *55*, 599–605.

Ikeda, T., Nakahara, J., Sasaki, M., & Yasunaga, T. (1984). Kinetic behavior of alkali metal ion on zeolite 4A surface using the stopped-flow method. *Journal of Colloid and Interface Science*, *97*, 278–283.

Ildefonse, P., Kirkpatrick, R.J., Montez, B., Calas, G., Flank, A.M., & Lagarde, P. (1994). ^{27}Al MAS NMR and aluminum X-ray absorption near edge structure study of imogolite and allophanes. *Clays and Clay Minerals*, *42*, 276–287.

Kaufhold, S., Dohrmann, R., Abidin, Z., Henmi, T., Matsue, N., Eichinger, L., et al. (2010). Allophane compared with other sorbent minerals for the removal of fluoride from water with particular focus on a mineable Ecuadorian allophane. *Applied Clay Science*, *50*, 25–33.

Kinart, Z. (2021). Conductance studies of sodium salts of selected dicarboxylic acids in water at temperatures of 283.15 K to 313.15 K. *Journal of Molecular Liquids*, *337*, 116262.

Kramer, M.G., Sanderman, J., Chadwick, O.A., Chorover, J., & Vitousek, P.M. (2012). Long-term carbon storage through retention of dissolved aromatic acids by reactive particles in soil. *Global Change Biology*, *18*, 2594–2605.

Kubicki, J.D., Itoh, M.J., Schroeter, L.M., & Apitz, S.E. (1997). Bonding mechanisms of salicylic acid adsorbed onto illite clay: An ATR- FTIR and molecular orbital study. *Environmental Science and Technology*, *31*, 1151–1156.

Lang, F., Pohlmeier, A., & Kaupenjohann, M. (2000). Mechanism of molybdenum sorption to iron oxides using pressure-jump relaxation. *Journal of Plant Nutrition and Soil Science*, *163*, 571-575.

Lenhardt, K.R., Breitzke, H., Buntkowsky, G., Reimhult, E., Willinger, M., & Rennert, T. (2021). Synthesis of short-range ordered aluminosilicates at ambient conditions. *Scientific Reports*, *11*, 4207.

Lenhardt, K.R., Breitzke, H., Buntkowsky, G., Mikutta, C., & Rennert, T. (2022). Interactions of dissolved organic matter with short-range ordered aluminosilicates by adsorption and co-precipitation. *Geoderma*, *423*, 115960.

Levard, C. & Basile-Doelsch, I. (2016). Geology and mineralogy of imogolite-type materials. *Developments in Clay Science*, *7*, 49–65.

Lilienfein, J., Qualls, R.G., Uselman, S.M., & Bridgham, S.D. (2004). Adsorption of dissolved organic carbon and nitrogen in soils of a weathering chronosequence. *Soil Science Society of America Journal*, *68*, 292-305.

McBride, M.B. (1980). Adsorption of fatty acid spin probes on amorphous alumina. *Journal of Colloid and Interface Science*, *76*, 393-398.

Mikutta, R., Mikutta, C., Kalbitz, K., Scheel, T., Kaiser, K., & Jahn, R. (2007). Biodegradation of forest floor organic matter bound to minerals via different binding mechanisms. *Geochimica et Cosmochimica Acta*, *71*, 2569–2590.

Molis, E., Barrès, O., Marchand, H., Sauzéat, E., Humbert, B., & Thomas, F. (2000). Initial steps of ligand-promoted dissolution of gibbsite. *Colloids and Surfaces A: Physicochemical and Engineering Aspects*, *163*, 283–292.

Nishikiori, H., Shindoh, J., Takahashi, N., Takagi, T., Tanaka, N., & Fujii, T. (2009). Adsorption of benzene derivatives on allophane. *Applied Clay Science*, *43*, 160–163.

Parfitt, R.L. (1989). Phosphate reactions with natural allophane, ferrihydrite and goethite. *Journal of Soil Science*, *40*, 359–369.

Parfitt, R.L. (2009). Allophane and imogolite: Role in soil biogeochemical processes. *Clay Minerals*, *44*, 135–155.

Parfitt, R.L., Fraser, A.R., Russell, J.D., & Farmer, V.C. (1977). Adsorption on hydrous oxides II. Oxalate, benzoate and phosphate on gibbsite. *Journal of Soil Science*, *28*, 40-47.

Parfitt, R.L., Furkert, R.J., & Henmi, T. (1980). Identification and structure of two types of allophane from volcanic ash soils and tephra. *Clays and Clay Minerals*, *28*, 328–334.

Parfitt, R.L., Russell, M., & Orbell, G.E. (1983). Weathering sequence of soils from volcanic ash involving allophane and halloysite, New Zealand. *Geoderma*, *29*, 41–57.

Pohlmeier, A. & Knoche, W. (1996). Kinetics of the complexation of Al^{3+} with aminoacids, IDA and NTA. *International Journal of Chemical Kinetics*, *28*, 125–136.

Pohlmeier, A., Thesing, U., & Knoche, W. (1993). Formation of aluminium(III)-monocarboxylates in aqueous solution. *Berichte der Bunsengesellschaft für Physikalische Chemie*, *97*, 10–15.

Pokrovski, G.S. & Schott, J. (1998). Experimental study of the complexation of silicon and germanium with aqueous organic species: Implications for germanium and silicon transport and Ge/Si ratio in natural waters. *Geochimica et Cosmochimica Acta*, *62*, 3413–3428.

Rennert, T., Pohlmeier, A., & Mansfeldt, T. (2005). Oxidation of ferrocyanide by birnessite. *Environmental Science and Technology*, *39*, 821–825.

Rosenqvist, J., Axe, K., Sjöberg, S., & Persson, P. (2003). Adsorption of dicarboxylates on nano-sized gibbsite particles: Effects of ligand structure on bonding mechanisms. *Colloids and Surfaces A: Physicochemical and Engineering Aspects*, *220*, 91–104.

Schaller, J., Puppe, D., Kaczorek, D., Ellerbrock, R., & Sommer, M. (2021). Silicon cycling in soils revisited. *Plants*, *10*, 295.

Secco, F. & Venturini, M. (1975). Mechanism of complex formation. Reaction between aluminum and salicylate ions. *Inorganic Chemistry*, *14*, 1978–1981.

Singh, M., Sarkar, B., Hussain, S., Ok, Y.S., Bolan, N.S., & Churchman, G.J. (2017). Influence of physico-chemical properties of soil clay fractions on the retention of dissolved organic carbon. *Environmental Geochemistry and Health*, *39*, 1335–1350.

Sparks, D.L. (1985). Kinetics of ionic reactions in clay minerals and soils. *Advances in Agronomy*, *38*, 231-265.

Sparks, D.L., Fendorf, S.E., Toner, C.V., & Carski, T.H. (1996). Kinetic methods and measurements. In D.L. Sparks (Ed.), *Methods of Soil Analysis, Part 3: Chemical Methods* (pp. 1275-1307). Madison: Soil Science Society of America Inc.

Strauss, R., Brümmer, G.W., & Barrow, N.J. (1997). Effects of crystallinity of goethite: II. Rates of sorption and desorption of phosphate. *European Journal of Soil Science*, *48*, 101-114.

Strobel, B.W. (2001). Influence of vegetation on low-molecular-weight carboxylic acids in soil solution – a review. *Geoderma*, *99*, 169-198.

Su, C., Harsh, J.B., & Bertsch, P.M. (1992). Sodium and chloride sorption by imogolite and allophanes. *Clays and Clay Minerals*, *40*, 280–286.

Thill, A. (2016). From molecular precursor to imogolite nanotubes. *Developments in Clay Science*, *7*, 429–457.

Torn, M.S., Trumbore, S.E., Chadwick, O.A., Vitousek, P.M., & Hendricks, D.M. (1997). Mineral control of soil organic carbon storage and turnover. *Nature*, *389*, 170–173.

Wada, S.-I. & Wada, K. (1981). Reactions between aluminate ions and orthosilicic acid in dilute, alkaline to neutral solutions. *Soil Science*, *132*, 267–273.

Yoon, T.H., Johnson, S.B., Musgrave, C.B. & Brown, G.E. (2004). Adsorption of organic matter at mineral/water interfaces: I. ATR-FTIR spectroscopic and quantum chemical study of oxalate

adsorbed at boehmite/water and corundum/water interfaces. *Geochimica et Cosmochimica Acta*, *48*, 4505–4518.

Yost, E.C., Tejedor-Tejedor, M.I., & Anderson, M.A. (1990). In situ CIR-FTIR characterization of salicylate complexes at the goethite/aqueous solution interface. *Environmental Science and Technology*, *24*, 822–828.

Young, A.W., Campbell, A.S., & Walker, T.W. (1980). Allophane isolated from a podsol developed on a non-vitric parent material. *Nature*, *284*, 46–48.

Chapter 5

Release of glucose from dissolved and mineral-bound organic matter by enzymatic hydrolysis

Coauthors: Luise Brandt, Christian Poll, Thilo Rennert, Ellen Kandeler

European Journal of Soil Science (2023) 74:e13421

https://doi.org/10.1111/ejss.13421

Abstract

Sorption of dissolved organic matter (DOM) by poorly crystalline minerals during their formation may protect large amounts of carbon in soils from mineralization. We investigated the bioavailability of carbohydrates in DOM and after co-precipitation with short-range ordered aluminosilicates. Carbohydrates originated from soil solutions collected *in situ* at two depths of a Dystric Cambisol, and from litter extracts. Quantification of substrate-specific degradability was achieved by the addition of β-glucosidase at an optimal concentration and subsequent determination of glucose release. Depending on DOM composition, 0.6–41.4 mg g^{-1} C^{-1} of glucose was enzymatically released from dissolved carbohydrates. Co-precipitated carbohydrates were partially accessible, resulting in a glucose release of 0.7–5.2 mg g^{-1} C^{-1}. Restricted enzymatic depolymerisation due to co-precipitation may contribute to accumulation of easily degradable substrates in soils.

Introduction

Association of organic matter (OM) with minerals plays a pivotal role in soil carbon sequestration. Particularly poorly crystalline Al- and Fe-bearing minerals efficiently contribute to OM accrual by incorporation of dissolved OM (DOM) during mineral formation (Kleber et al., 2015; Mikutta et al., 2009). Together with adsorption of OM on mineral surfaces, co-precipitation of OM thus results in mineral-bound OM. Occlusion likely diminishes microbial access to co-precipitated OM by extracellular enzymes (Zimmerman et al., 2004), the primary agents of microbial substrate mobilization. However, it is yet unclear, to what extent enzymatic mobilization of co-precipitated OM is limited.

Carbohydrates are a preferred substrate for microorganisms and rapidly decomposed in solution by enzymatic depolymerization (Kalbitz et al., 2003). The availability of carbohydrates for microbial utilization is controlled by two factors. First, content and structural diversity of soil carbohydrates vary as they originate from several sources, such as plant litter, root exudates, and neoformation by soil organisms (Gunina and Kuzyakov, 2015). Second, mineral-OM interactions result in differentiation between DOM and mineral-associated OM. Recently, we have shown that co-precipitation of DOM with short-range ordered aluminosilicates (SROAS) allows for substantial sorption of carbohydrates (Lenhardt et al., 2022). The formation of SROAS is facilitated in soil environments with pronounced release of Al and Si from primary minerals and stabilizes large amounts of OM (Basile-Doelsch et al., 2007). About 1 up to 57% of C in carbohydrate-rich OM from plant and microbial residues, respectively, was mineralized despite of its co-precipitation with poorly crystalline Fe and Al hydroxides (Eusterhues et al., 2014; Mikutta et al., 2011). The considerable variability of mineralization indicates that enzymatic mobilization of co-precipitated carbohydrates depends on OM composition. In addition, it suggests that co-precipitated carbohydrates may be partially accessible to extracellular enzymes and thus utilized by microorganisms.

The aim of this study was to assess the bioavailability of carbohydrates co-precipitated with SROAS and how qualitative differences in the initial DOM affect the bioavailability. Therefore, we prepared co-precipitates of SROAS with DOM from top- and subsoil solutions and from fir- and beech-litter extracts (Lenhardt et al., 2022). We determined the bioavailability of carbohydrates in initial DOM (iDOM) prior to co-precipitation, co-precipitated OM (cOM), and DOM remaining in solution (‘excluded DOM’, eDOM) to account for compositional changes of OM during co-precipitation (Lenhardt et al., 2022). We hypothesized partial mobilization of co-precipitated carbohydrates and more pronounced degradability of eDOM, as aromatic compounds preferentially co-precipitate with SROAS (Lenhardt et al., 2022).

Materials and methods

In principle, we analysed enzymatic OM mobilization as a proxy for bioavailability by adding a specific enzyme in excess, inducing substrate limitation of the enzymatic reaction, and subsequent quantification of reaction products (Bünemann, 2008). Previously, several studies evaluated the availability of different organic phosphorus compounds in soil by addition of phosphatases (Bünemann, 2008; Hallama et al., 2022) and the degradability of soil OM by addition of hydrolytic enzymes (Nadeau et al., 2007; Tateno, 1988). As mainly plant-derived carbohydrates co-precipitated with SROAS (Lenhardt et al., 2022), we used β-glucosidase to catalyse cleavage of terminal glycosidic bonds (Seidle et al., 2004) and quantified glucose release. Figure S1 shows a scheme of the experimental setup and the work sequence.

We prepared iDOM solutions from top- and subsoil solutions obtained *in situ* from a Dystric Cambisol at a mixed forest site, and from fir- and beech-litter extracts (Lenhardt et al., 2022). Soil solutions and extracts were concentrated by freeze-drying, the pH neutralized, and filtered to 0.45 µm. We analysed concentrations of DOC, Al, Si, Fe, Na, K, Ca, and Mg in iDOM solutions (Table S1), and characterized iDOM by its molar absorptivity at 254 nm (ε; Cary 50, Varian, Mulgrave, Australia) and diffuse reflectance Fourier-transform infrared spectroscopy (DRIFT; Lenhardt et al., 2022). About 5 mg of sample was mixed with finely ground KBr (35 mg) and filled into stainless steel microcups. The mixture was analysed with a DRIFT accessory of a LUMOS infrared microscope (Bruker, Ettlingen, Germany). Fifty scans from pure KBr were accumulated as background, and 100 scans from the sample. Co-precipitates were prepared by neutralization of an $AlCl_3$ solution (10 mmol L^{-1}) in the presence of dissolved Na_4SiO_4 and iDOM within 1 h reaction time at an initial molar Al:Si ratio of 2.2 and an initial Al:C ratio of 0.6 (Lenhardt et al., 2022). Co-precipitates were recovered by centrifugation for 3 min at 2000 *g* and re-dispersed in de-ionized water before incubation. Supernatants were filtered (0.45 µm) and analysed for DOC, Al, Si, and composition of eDOM (ε, DRIFT). The composition of co-precipitates was examined by calculating the difference between initial and final Al, Si and DOC concentrations (Table S2), together with difference spectra of cOM by transmission Fourier-transform infrared spectroscopy (FTIR; transmission accessory, LUMOS, Bruker). Pellets were prepared from 1 mg of sample and 200 mg KBr with a hand press. Fifty background scans were recorded against the atmosphere, and 100 sample scans accumulated at a resolution of 4 cm^{-1}. Difference spectra of cOM were calculated by subtracting spectra of SROAS with similar Al:Si ratios (Lenhardt et al., 2022) from spectra of co-precipitates. Excluded DOM in the filtrates was concentrated by freeze-drying, the pH neutralized and filtered (0.45 µm) before incubation.

We applied three treatments to each substrate (iDOM, cOM, eDOM) in incubation experiments (Fig. S1). All variants were incubated in MES-buffer (2-(N-morpholino)ethanesulfonic acid, 0.1 mol L^{-1}, pH 6.1, Sigma-Aldrich, Steinheim, Germany) at a final volume of 6 mL under

stirring at room temperature. The input of organic C was adjusted to similar amounts for iDOM and cOM (Table S3). To minimize the microbial uptake of glucose, penicillin potassium salt (70 mg L^{-1}, Sigma-Aldrich) and amphotericine (2.5 mg L^{-1}, Sigma-Aldrich) were added to DOM and buffer solutions. Variants with enzyme addition were incubated with β-glucosidase at a concentration of 1 g L^{-1} (*Aspergillus niger*; Sigma-Aldrich). According to the manufacturer, catalytic activity towards *p*-nitrophenyl-β-*D*-glucopyranoside was ≥750 U g^{-1} at pH 4, and the isolate potentially also contained α-glucosidase. In another variant, we incubated each substrate solely to quantify background glucose levels ('negative controls', Table S3). Moreover, we incubated the substrates separately with the addition of glucose (25 mg L^{-1}) and antibiotics to quantify glucose loss by mineralization or sorption ('positive controls', Table S3). Each incubation treatment was prepared in triplicate. We measured glucose concentrations after 2 h for DOM and after 4 h for co-precipitates using a spectrophotometric assay based on chemical conversion of glucose to gluconate-6-phosphate together with the formation of NADPH (R-Biopharm AG, Darmstadt, Germany). The amount of NADPH is equivalent to the amount of glucose and was quantified by absorption at 340 nm. Samples with cOM were filtered (0.45 µm) before photometric quantification with syringe filters (LLG Labware, Meckenheim, Germany). The amounts of enzymatically released glucose from DOM and co-precipitates were corrected for background glucose and for glucose loss, and normalized to DOC concentration. Glucose loss was 79% for fir-litter iDOM, likely caused by microbial uptake, and <31% for the other substrates (Table S3). We detected <2% glucose loss in the presence of co-precipitates indicating negligible antibiotic inhibition by SROAS. As aromatic compounds and SROAS may inhibit β-glucosidase activity (Allison, 2006), we previously tested the effect of topsoil iDOM and co-precipitates (beech-litter cOM) on cleavage of cellobiose (30 mg L^{-1}, Sigma-Aldrich). However, we found no enzyme inhibition. Analyses of variance across the means of enzymatic glucose release were performed in R (Version 4.3.0; R Core Team, 2023) using the function aov with subsequent Tukey post-hoc tests using the function TukeyHSD from the R package stats (R Core Team, 2023). Normal distribution of residuals was checked visually, while homogeneity of variance was validated using the leveneTest function from the R package car (Fox and Weisberg, 2019).

Results and discussion

Characterization of iDOM revealed marked differences in carbohydrate concentrations. Absorption of glycosidic bonds and C-OH side groups in carbohydrates at 1200–1000 cm^{-1} (Kacuráková et al., 2000) was distinctly more pronounced for beech- and fir-litter DOM (Fig. 1a), thus indicating a greater proportion of polysaccharides compared with soil DOM (Inbar et al., 1989). In soil DOM, aromatic compounds mobilized by oxidative lignin degradation were more abundant as shown by greater ε (Table 1, Lenhardt et al., 2022). Compared with topsoil

and litter-derived iDOM, absorbance in the carbohydrate region of subsoil iDOM was at higher wavenumbers (Fig. 1a), indicating a different origin of carbohydrates, that is, microbial residues (Guggenberger and Zech, 1994). Negative controls of incubation experiments showed negligible glucose contribution to dissolved carbohydrates in iDOM. For soil and fir-litter iDOM, glucose concentrations were below the detection limit (0.4 mg L^{-1}), while beech-litter iDOM contained small amounts (2 mg L^{-1}, Table S3).

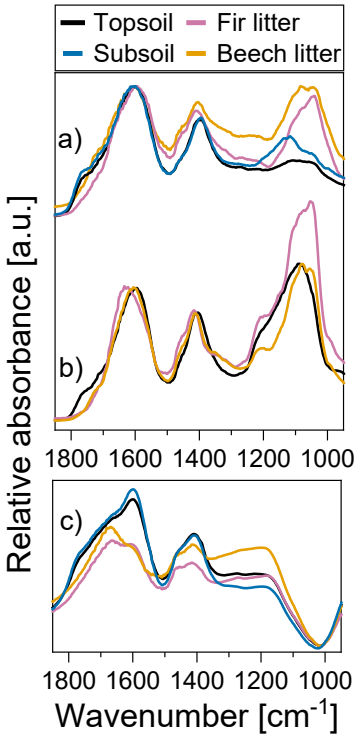

Figure 1: Infrared spectra of (a) initial DOM, (b) excluded DOM (DRIFT mode, normalized to absorption maxima at 1630–1600 cm^{-1}), and (c) difference spectra of co-precipitates (transmission mode).

After 2 h of incubation, we detected glucose release by β-glucosidase addition ranging from 1.4 to 5.1 mg g^{-1} C^{-1} for topsoil and subsoil iDOM. Compared with soil iDOM, enzymatic glucose release from beech-litter iDOM was significantly higher (18 mg g^{-1} C^{-1}, Table 1, Fig. S2). The amounts relate to carbohydrate abundance in iDOM obtained by DRIFT spectroscopy (Table 1, Fig. 1). Enzymatic glucose release from soil and beech-litter iDOM corresponds to <0.1%–0.7% of C (Table 1). Increasing the incubation duration to 4 h changed glucose release only for topsoil iDOM (13.8 mg g^{-1} C^{-1}; 0.6% of C). Deduced from β-glucosidase activity given by the manufacturer, the experimental enzyme concentration corresponds to a maximal potential glucose release of 16 g L^{-1}, which exceeds the measured glucose concentrations by three orders of magnitude. Hence, glucose release was not limited by enzyme activity, but substrate properties such as carbohydrate concentration and composition.

Accessibility of dissolved carbohydrates in iDOM may vary. Particularly topsoil iDOM may contain carbohydrates associated with lignin (Guggenberger and Zech, 1994), which impedes

their microbial degradation (Moran and Hodson, 1989). Mobilization of this carbohydrate fraction requires oxidative enzymes (Nadeau et al., 2007). The low aromaticity of beech-litter iDOM (ε, Table 1) points to minor protection of carbohydrates by lignin. Based on ^{13}C-NMR analyses, about 51% of C in beech-litter iDOM is attributable to carbohydrates (O-Alkyl C; Lenhardt et al., 2022). Hence, glucose release corresponds to 1.4% of carbohydrate-C. Therefore, the low carbohydrate turnover by β-glucosidase relates to the enzyme`s specificity for β-glycosidic bonds at non-reducing chain ends (Seidle et al., 2004). Carbohydrates present in DOM also contain other types of linkages between monomers (Gunina and Kuzyakov, 2015).

Table 1: Chemical characteristics of organic matter and release of glucose by enzymatic hydrolysis for initial DOM (iDOM), co-precipitated organic matter (cOM) and excluded DOM (eDOM).

DOM type	**iDOM**	**cOM**	**eDOM**
	Molar absorptivity ε [L mol^{-1} cm^{-1}]		
Topsoil	359		270
Subsoil	457		182
Fir litter	228		74
Beech litter	125		67
	Relative absorption of carbohydrates [–]*		
Topsoil	0.43	0.48	0.97
Subsoil	0.50	0.37	–**
Fir litter	0.92	0.69	1.77
Beech litter	0.99	0.99	1.13
	*Release of glucose [mg g^{-1} C^{-1}]***		
Topsoil	1.4$^{a, a}$	0$^{a, a}$	4.0$^{a, a}$
Subsoil	5.1$^{a, a}$	0$^{a, a}$	0.6$^{a, a}$
Fir litter	–***	0.7$^{a, a}$	22.1$^{b, b}$
Beech litter	18.0$^{a, b}$	5.2$^{b, a}$	41.4$^{c, c}$
	Release of glucose [% of C]		
Topsoil	<0.1	0	0.2
Subsoil	0.2	0	<0.1
Fir litter	–***	<0.1	0.9
Beech litter	0.7	0.2	1.7

*Ratio of absorption intensity at 1050 cm^{-1} (iDOM, eDOM) or 1180 cm^{-1} (cOM) and 1600 cm^{-1}.
**Excluded from interpretation due to excessive absorption of Si bonds in the carbohydrate region, interpreted from a low molar C:Si ratio in the supernatant (Table S2).
***Not quantifiable due to microbial activity.
****The same letters indicate no statistical difference at p<0.05. The first letter refers to comparisons of means in rows, the second letter refers to comparisons of means in columns.

Preferential removal of oxidized aromatic compounds during co-precipitation with SROAS reduced ε irrespective of DOM origin (eDOM, Table 1). Relative absorption at 1200–1000 cm^{-1} increased for eDOM (Fig. 1b), together with the emergence of alkyl bands at 2950 cm^{-1} in spectra of topsoil eDOM (not shown), evincing accumulation of aliphatic C, particularly

carbohydrates, in eDOM. Consequently, glucose release from topsoil and litter eDOM was higher compared with iDOM, ranging from 4 mg g^{-1} C^{-1} for topsoil eDOM to 22.1–41.3 mg g^{-1} C^{-1} for litter eDOM (Table 1, Fig. S2). Minor amounts of glucose were released from subsoil eDOM, which points to co-precipitation of hydrolysable carbohydrates present in subsoil iDOM (Table 1). We found significant differences between iDOM and eDOM for litter substrates only, likely due to higher carbohydrate concentrations (Table 1, Fig. S2).

For fir- and beech-litter eDOM, we detected 12.4–33.0 mg L^{-1} glucose in negative controls (Table S3). This is caused by acid hydrolysis of carbohydrates during the initial stage of co-precipitation, when pH was <2. Acid hydrolysis of carbohydrates is more efficient than enzymatic hydrolysis due to the smaller size of protons, enabling them to penetrate macromolecules as opposed to enzymes (Marsden et al., 1985). Taking the proportion of C removed by co-precipitation into account (Table S2), enzymatic glucose release from beech-litter eDOM was disproportionately higher than expected by assuming complete exclusion of carbohydrates, indicating either fractionation of carbohydrates by interaction with SROAS (Eusterhues et al., 2011), or pH effects on subsequent degradability of eDOM for β-glucosidase.

The prevalence of aromatic and oxidized C moieties in co-precipitates from soil DOM is reflected by absorption bands of carboxyl, carbonyl, and aromatic functional groups in FTIR spectra (cOM, 1600 and 1410 cm^{-1}; Fig. 1c). Co-precipitates formed with fir- and beech-litter-derived DOM contained more carbohydrates, as evidenced by stronger absorbance at 1180 cm^{-1} (Fig. 1c) and previously verified by ^{13}C-NMR analyses (Lenhardt et al., 2022). Concordantly, we detected glucose release by β-glucosidase addition only for cOM of fir- and beech-litter. Its amount for beech-litter cOM (5.2 mg g^{-1} C^{-1}) exceeded that of fir-litter cOM (0.7 mg g^{-1} C^{-1}). Glucose release from litter-derived cOM was significantly lower compared with respective iDOM and eDOM (Table 1, Fig. S2). Glucose release from beech-litter cOM corresponded to a carbohydrate-C turnover of at most 0.4%, which was lower than that of dissolved carbohydrates (1.4%). Overall, glucose release from dissolved carbohydrates ranged from 1.4 to 41.4 mg g^{-1} C^{-1} while only 0.7–5.2 mg g^{-1} C^{-1} glucose was enzymatically mobilized from co-precipitates (Table 1). These results confirm restricted substrate accessibility for extracellular enzymes by incorporation into SROAS.

Conclusion

In conclusion, the formation of SROAS in the presence of DOM results in partial OM occlusion and alters the composition of excluded DOM (Fig. 2). Physical and chemical changes of OM were reflected in its degradability by β-glucosidase, suggesting effects of co-precipitation on the fate of carbohydrates. Protection of co-precipitated carbohydrates from enzymatic depolymerization may contribute to their accumulation in soils (Nierop et al., 2005; Parfitt et

al., 1999) because carbohydrate degradation was reduced even at optimal enzyme concentrations. A small portion, likely at the exterior of mineral-organic particles (Fig. 2), may be utilized by microorganisms, as indicated by rapid mobilization via enzymatic hydrolysis. The quantity of this portion related to the amount of co-precipitated carbohydrates, indicating that the stability of co-precipitated OM is partially inherited from initial DOM. The alteration of mineral-organic particles by dissolution seems necessary for further exposition of co-precipitated OM to microbial degradation, underlining the importance of co-precipitation as an OM-stabilization mechanism.

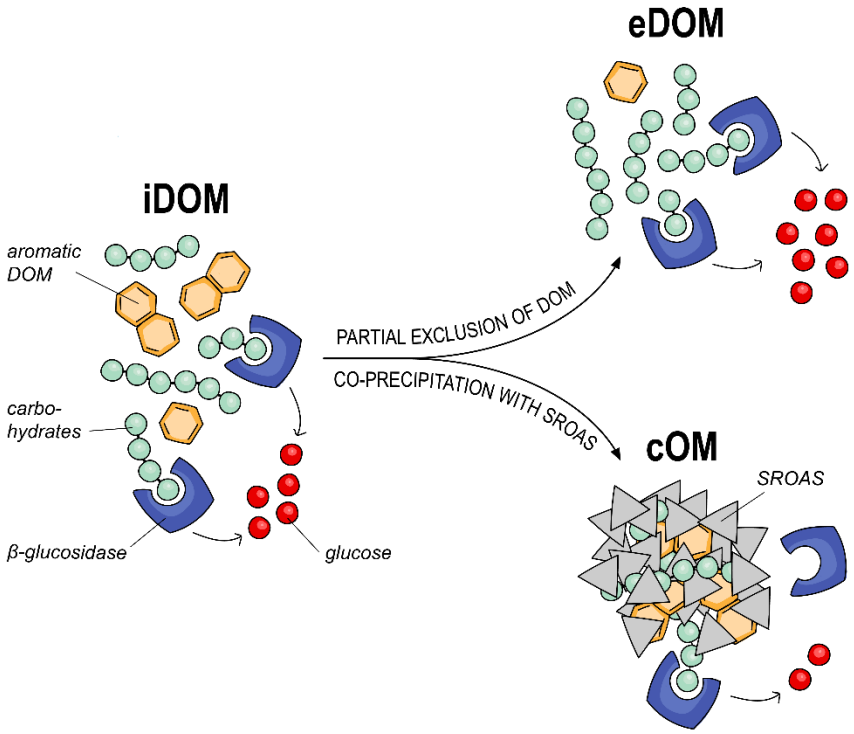

Figure 2: Schematic representation of short-range ordered aluminosilicate (SROAS) formation in the presence of dissolved organic matter (DOM) and its consequences for accessibility of carbohydrates by microbial extracellular enzymes.

Acknowledgements

We gratefully acknowledge the help of Julian Ruggaber during method development and technical assistance by Gabriela Grassadonia and Annerose Böttcher with MP-AES measurements.

References

Allison, S.D., 2006. Soil minerals and humic acids alter enzyme stability: Implications for ecosystem processes. *Biogeochemistry 81*, 361–373. https://doi.org/10.1007/s10533-006-9046-2

Basile-Doelsch, I., Amundson, R., Stone, W.E.E., Borschneck, D., Bottero, J.Y., Moustier, S., Masin, F., Colin, F., 2007. Mineral control of carbon pools in a volcanic soil horizon. *Geoderma 137*, 477–489. https://doi.org/10.1016/j.geoderma.2006.10.006

Bünemann, E.K., 2008. Enzyme additions as a tool to assess the potential bioavailability of organically bound nutrients. *Soil Biology and Biochemistry 40*, 2116–2129. https://doi.org/10.1016/j.soilbio.2008.03.001

Eusterhues, K., Neidhardt, J., Hädrich, A., Küsel, K., Totsche, K.U., 2014. Biodegradation of ferrihydrite-associated organic matter. *Biogeochemistry 119*, 45–50. https://doi.org/10.1007/s10533-013-9943-0

Eusterhues, K., Rennert, T., Knicker, H., Kögel-Knabner, I., Totsche, K.U., Schwertmann, U., 2011. Fractionation of organic matter due to reaction with ferrihydrite: Coprecipitation versus adsorption. *Environmental Science & Technology 45*, 527–533. https://doi.org/10.1021/es1023898

Fox, J., Weisberg, S., 2019. *An R companion to applied regression* (Third ed.). Sage.

Guggenberger, G., Zech, W., 1994. Composition and dynamics of dissolved carbohydrates and lignin-degradation products in two coniferous forests, N.E. Bavaria, Germany. *Soil Biology and Biochemistry 26*, 19–27. https://doi.org/10.1016/0038-0717(94)90191-0

Gunina, A., Kuzyakov, Y., 2015. Sugars in soil and sweets for microorganisms: Review of origin, content, composition and fate. *Soil Biology and Biochemistry 90*, 87–100. https://doi.org/10.1016/j.soilbio.2015.07.021

Hallama, M., Pekrun, C., Mayer-Gruner, P., Uksa, M., Abdullaeva, Y., Pilz, S., Schloter, M., Lambers, H., Kandeler, E., 2022. The role of microbes in the increase of organic phosphorus availability in the rhizosheath of cover crops. *Plant and Soil 476*, 353–373. https://doi.org/10.1007/s11104-022-05340-5

Inbar, Y., Chen, Y., Hadar, Y., 1989. Solid-state carbon-13 nuclear magnetic resonance and infrared spectroscopy of composted organic matter. *Soil Science Society of America Journal 53*, 1695–1701. https://doi.org/10.2136/sssaj1989.03615995005300060014x

Kacuráková, M., Capek, P., Sasinková, V., Wellner, N., Ebringerová, A., 2000. FT-IR study of plant cell wall model compounds: Pectic polysaccharides and hemicelluloses. *Carbohydrate Polymers 43*, 195–203. https://doi.org/10.1016/S0144-8617(00)00151-X

Kalbitz, K., Schwesig, D., Schmerwitz, J., Kaiser, K., Haumaier, L., Glaser, B., Ellerbrock, R., Leinweber, P., 2003. Changes in properties of soil-derived dissolved organic matter induced by biodegradation. *Soil Biology and Biochemistry 35*, 1129–1142. https://doi.org/10.1016/S0038-0717(03)00165-2

Kleber, M., Eusterhues, K., Keiluweit, M., Mikutta, C., Mikutta, R., Nico, P.S., 2015. Mineral-organic associations: Formation, properties, and relevance in soil environments. *Advances in Agronomy 130*, 1–140. https://doi.org/10.1016/bs.agron.2014.10.005

Lenhardt, K.R., Breitzke, H., Buntkowsky, G., Mikutta, C., Rennert, T., 2022. Interactions of dissolved organic matter with short-range ordered aluminosilicates by adsorption and co-precipitation. *Geoderma 423*, 115960. https://doi.org/10.1016/j.geoderma.2022.115960

Marsden, W.L., Gray, P.P., Mandels, M., 1985. Enzymatic hydrolysis of cellulose in lignocellulosic materials. *Critical Reviews in Biotechnology 3*, 235–276.

Mikutta, R., Schaumann, G.E., Gildemeister, D., Bonneville, S., Kramer, M.G., Chorover, J., Chadwick, O.A., Guggenberger, G., 2009. Biogeochemistry of mineral-organic associations across a long-

term mineralogical soil gradient (0.3-4100 kyr), Hawaiian Islands. *Geochimica et. Cosmochimica Acta 73*, 2034–2060. https://doi.org/10.1016/j.gca.2008.12.028

Mikutta, R., Zang, U., Chorover, J., Haumaier, L., Kalbitz, K., 2011. Stabilization of extracellular polymeric substances (Bacillus subtilis) by adsorption to and coprecipitation with Al forms. *Geochimica et. Cosmochimica Acta 75*, 3135–3154. https://doi.org/10.1016/j.gca.2011.03.006

Moran, M.A., Hodson, R.E., 1989. Formation and bacterial utilization of dissolved organic carbon derived from detrital lignocellulose. *Limnology and Oceanography. 36*, 1034–1047. https://doi.org/10.4319/lo.1989.34.6.1034

Nadeau, J.A., Qualls, R.G., Nowak, R.S., Blank, R.R., 2007. The potential bioavailability of organic C, N, and P through enzyme hydrolysis in soils of the Mojave Desert. *Biogeochemistry 82*, 305–320. https://doi.org/10.1007/s10533-007-9077-3

Nierop, K.G.J., Van Bergen, P.F., Buurman, P., Van Lagen, B., 2005. NaOH and $Na4P_2O_7$ extractable organic matter in two allophanic volcanic ash soils of the Azores Islands - a pyrolysis GC/MS study. *Geoderma 127*, 36–51. https://doi.org/10.1016/j.geoderma.2004.11.003

Parfitt, R.L., Yuan, G., Theng, B.K.G., 1999. A ^{13}C-NMR study of the interactions of soil organic matter with aluminium and allophane in podzols. *European Journal of Soil Science 50*, 695–700. https://doi.org/10.1046/j.1365-2389.1999.00274.x

R Core Team, 2023. R: *A language and environment for statistical computing*. R Foundation for Statistical Computing.

Seidle, H.F., Marten, I., Shoseyov, O., Huber, R.E., 2004. Physical and kinetic properties of the family 3 β-glucosidase from *Aspergillus niger* which is important for cellulose breakdown. *The Protein Journal 23*, 11–23. https://doi.org/10.1023/B:JOPC.0000016254.58189.2a

Tateno, M., 1988. Limitations of available substrates for the expression of cellulase and protease activities in soil. *Soil Biology and Biochemistry 20*, 117–118. https://doi.org/10.1016/0038-0717(88)90136-8

Zimmerman, A.R., Chorover, J., Goyne, K.W., Brantley, S.L., 2004. Protection of mesopore-adsorbed organic matter from enzymatic degradation. *Environmental Science & Technology 38*, 4542–4548. https://doi.org/10.1021/es035340+

Chapter 6

Epilogue

The findings of this thesis

The preceding chapters present novel findings on the formation of SROAS and their interactions with organic matter by adsorption and co-precipitation, advancing the understanding of SOM accrual and stabilization. Contrary to the widespread belief that SROAS generally have a large surface area, it was shown that the poor crystallinity of Al-rich SROAS permits strong aggregation, resulting in limited surface accessibility. The incorporation of Si seems to alter aggregation mechanisms as evinced by restricted aggregation of Si-rich SROAS, demonstrating that dehydration influences the physical properties of SROAS as a function of structure. The adsorption of DOM on SROAS relies on surface accessibility and involves interactions between oxidized aromatic DOM and surface aluminol groups, inducing accumulation of aliphatic DOM in the solution. Incorporation of Si reduces the susceptibility of SROAS surfaces for ligand exchange with carboxyl groups as it coincides with formation of tetrahedral Al, indicating a strong impact of Al speciation on chemical binding of SOM to SROAS. Co-precipitation may contribute more effectively to SOM accrual than adsorption as associations formed by co-precipitation contained more organic matter than adsorption complexes. Moreover, co-precipitation retains substances with low affinity for mineral surfaces such as carbohydrates. Only a small fraction of SOM located at the exterior of co-precipitates is accessible for microbial enzymes, showing that co-precipitation stabilizes SOM that would otherwise be easily degradable. Preferential association of lignin degradation products with SROAS alters the degradability and reactivity of DOM during soil percolation, potentially affecting subsequent mineral-organic interactions. Interference of DOM in SROAS formation causes partial exclusion of Si and enhances the formation of ill-defined Si in the co-precipitates. Aromatic DOM, in particular, disturbs crystallization of the Al sheet, implying that the structure of SROAS relates to DOM characteristics prevalent during precipitation. In summary, this thesis showed how mutual interactions of SROAS and organic matter may shape the speciation of SOM and Si in soils.

Formation of SROAS and Al-(Si)-SOM co-precipitates

Execution of synthesis experiments under controlled conditions and subsequent spectroscopic characterization of the newly formed phases allowed to track the initial reactions of SROAS formation and the effect of organic matter on these reactions (chapter 3). Condensation of silicic acid and Al^{3+} proceeds rapidly when the pH permits hydrolysis and polymerization of Al. The amorphous species formed by olation develop short-range order within several hours at moderately acidic pH. Both processes are hampered by organic matter and thus the contents of Al and ill-defined Si in the co-precipitates gradually increase as a function of DOM concentration and composition. However, in young volcanic deposits with neutral to alkaline pH, Al is presumably present in the soil solution as aluminate ($Al(OH)_4^-$) and the silicic acid

concentration may exceed Al concentrations (Duan and Gregory, 2003; Wolff-Boenisch et al., 2004). Hence, the co-precipitation experiments performed in the current study may not be representative for initial stages of soil formation as they mimic SROAS formation from Al^{3+} or Al^{3+}-organic complexes. When SROAS form by polymerization of aluminate and silicic acid (Wada and Wada, 1981), repulsive forces may impede complexation of aluminate by oxidized functional groups, potentially influencing the quantity and quality of SOM sorbed by co-precipitation. Moreover, precipitation of Si-rich SROAS with a high content of tetrahedral Al may reduce the affinity of SROAS particles for SOM (chapter 4). Hence, co-precipitation of SROAS and SOM by reactions of aluminate, silicic acid and organic matter should be investigated.

Structural evolution from amorphous precursors to short-range ordered SROAS was susceptible to disturbance by oxidized aromatic DOM, promoting ill-defined Si species in the co-precipitates. Thus, it seems unlikely that morphologically defined SROAS particles form in the presence of DOM. Nevertheless, Si in Q^0(3Al) configuration was detected in all co-precipitates obtained in the current study, confirming that short-range ordered co-precipitates can form in spite of SOM interference (Levard et al., 2012). Silicon release from SROAS related to the contents of ill-defined Si (Farmer et al., 1991b; Schneider et al., 2004; Lenhardt et al., 2023a: Fig. S6), indicating that the poorly ordered Si fraction is thermodynamically less stable than Si in Q^0(3Al) configuration. The formation of co-precipitates may thus enhance Si mobility in soils; however, the current study is inconclusive regarding the fate of Si in co-precipitates. A fraction of Si tetrahedra in co-precipitates formed in the presence of topsoil DOM was apparently further condensed compared with olation products according to ^{29}Si-NMR spectra (Lenhardt et al., 2022: Fig. S12). This points to effects of incorporated organic molecules on Si polymerization in co-precipitates at Si concentrations below the solubility limit of silica (dissolved Si in the filtrate after co-precipitation: ~0.3 mmol L^{-1}). Naturally formed co-precipitates did not contain a major portion of ill-defined Si (Basile-Doelsch et al., 2005). However, it may contribute to oxalate-extractable Si exceeding the quantities of Si nuclei in Q^0(3Al) configuration in clay fractions of andic soils (Rennert et al., 2014). Co-precipitates may evolve further towards proto-imogolite, increasing Si in Q^0(3Al) configuration, or a fraction of condensed Si may form, or the ill-defined Si fraction may dissolve. These processes presumably depend on the solution composition, in particular, on the concentration of silicic acid. Further studies analysing the structural evolution and the stability of co-precipitates at reaction times exceeding several days may give valuable insights into the transformation of these phases.

Based on correlations of soil pH and oxalate-extractable Al and Si, it is assumed that SROAS naturally form at pH 5–7 (Parfitt and Kimble, 1989). However, this assumption is contrasted by the low Al availability at pH 5–7, suggesting that SROAS are rather stable under these

conditions and may have formed at earlier stages of soil development (Schaller et al., 2021). In principle, SROAS may form by reactions of dissolved species in the bulk solution or by reactions at the weathering interface, that is, in alteration layers at the surfaces of primary minerals. Weathering of glasses may lead to surficial enrichment of Si and Al by coupled dissolution and sorption processes (Hellmann et al., 2015; Okhrimenko et al., 2020). Locally high Si concentrations and a circumneutral pH may lead to formation of Si-rich SROAS with high contents of tedrahedral Al (Farmer et al., 1979; Strekopytov et al., 2006); however, natural Si-rich SROAS previously characterized contained more octahedral Al than tetrahedral Al (Ildefonse et al., 1994). Hiradate and Wada (2005) suggested that Al released from glasses is rapidly transformed into octahedral Al as they detected proto-imogolite in weathered pumice while no Si-rich SROAS was present. Overall, the alteration processes of volcanic parent material leading to the formation of SROAS are poorly understood, particularly the structure of the newly formed phases. Given the strong effect of Al speciation on the surface properties of SROAS documented in the current study (chapter 4), the controls of Al-rich vs. Si-rich SROAS formation should be studied in detail.

The presence of organic matter during formation of SROAS hampers condensation and crystallisation by complexation of Al^{3+}, resulting in a gradual decrease of Si contents in the co-precipitates and distortion of the chemical environment of octahedral Al as a function of the initial molar Al:C ratio and DOM composition (chapter 3). The chemical environment of octahedral Al in naturally formed proto-imogolite-SOM co-precipitates was more strongly distorted compared with the synthetic phases prepared in the current study, indicating that formation of short-range ordered co-precipitates is possible in the presence of more strongly complexing organic compounds (Basile-Doelsch et al., 2005; Levard et al., 2012). Complementary to previous studies of interactions between Al, Si and organic matter, the gradual changes of Si content and structure suggest a high diversity of reaction products. When condensation of Al and Si is hampered by low Si concentrations, low pH, or strong Al complexation, Al-SOM co-precipitates containing negligible Si may form. At low molar Al:C ratios, flocculation of dominantly organic phases containing little Al is possible (Nierop et al., 2002; Jansen et al., 2003). Depending on the affinity of DOM for complexation of Al^{3+} and the initial molar Al:C ratio, these co-precipitates may be composed of monomeric Al complexes and polymerized Al forms with a variable number of Al atoms and degree of spatial order (Masion et al., 1994, 2000). Synthetic reaction products of Al^{3+} and organic substances contained majorly octahedral Al, while poorly crystalline co-precipitates of Al aged at circumneutral pH contained also tetrahedral Al (Hu et al., 2008; Xu et al., 2010). Progressive acidification and desilication of andic soils are presumed to result in formation of Al-SOM co-precipitates instead of SROAS (Takahashi and Dahlgren, 2016). However, the fundamental processes are poorly understood as pedogenic Al species in andic soils have been

insufficiently characterized so far (Rennert, 2019). Elemental analyses at the submicron scale show that pedogenic factors such as climate induce differentiation of pedogenic Al species (Inagaki et al., 2020). Since poorly ordered soil components cannot be completely separated from soil without damage, spectroscopic characterization of bulk samples would be desirable. Differentiation of poorly ordered secondary Al phases by solid-state ^{27}Al-NMR spectroscopy is complicated by the quadrupolar moment of ^{27}Al nuclei broadening the line width and by the rather low sensitivity of the resonance shifts for the local environment of octahedral Al (0–8.5 ppm, Masion et al., 2000; Isobe et al., 2003; Levard et al., 2012). When the structural characteristics of crystalline clay-sized minerals are known, deconvolution of ^{27}Al-NMR spectra may allow for characterisation and quantification of poorly ordered Al provided that the variability of these species is limited (Bardy et al., 2007). Recently, Prietzel et al. (2023) investigated Al speciation of organic and mineral soil horizons by X-ray absorption spectroscopy at the Al K-edge, suggesting possible identification and estimation of Al in 1:1 clay minerals, 2:1 clay minerals, feldspars and organically bound Al. It would be highly interesting to investigate whether this technique also allows for discrimination of volcanic glasses, SROAS, SROAS-SOM co-precipitates and Al-SOM co-precipitates. If so, a sophisticated combination of X-ray diffraction, X-ray absorption and infrared spectroscopy may give a detailed insight into the speciation of Al-bearing phases and thus SOM stabilization mechanisms in andic soils.

Aggregation of SROAS and Al-(Si)-SOM co-precipitates

Strong aggregation of SROAS is an important mechanism decelerating SOM degradation (chapter 1). The current study revealed a structure-dependent effect on aggregation of SROAS, indicating that interfacial processes actuated by local concentration of SROAS are influenced by particle composition. The pore space may be reduced to variable extent by assembly of primary particles, involving several types of interactions between particles such as van der Waals forces, electrostatic interactions or condensation reactions (Wells and Theng, 1988). Hence, differences in particle shape, surface functional group abundance, and interaction mechanisms may have caused the diverging aggregation behaviour of Al-rich and Si-rich SROAS observed in the current study. The marked reduction of accessible surface of Al-rich SROAS was ascribed to dense assembly of proto-imogolite particles <4 nm during freezing (chapter 2). Remarkably, the specific surface area (SSA) of Al-rich SROAS was low irrespective of the freezing rate, contrasting to the behaviour of ferrihydrite (Hofmann et al., 2004). Aluminium-rich SROAS submerged in liquid nitrogen had a SSA <6 $m^2\ g^{-1}$, although rapid freezing reduced aggregate sizes (data not shown). This corroborates that severe aggregation is specific for poorly crystalline Al-rich SROAS. When the freeze-dried SROAS were suspended in deionised water during preparation of adsorption experiments, Al-rich

SROAS released protons and Si-rich SROAS hydroxyls as detected by pH measurements, showing that condensation reactions of particles differed. Acidification by reactions of aluminol groups may have occurred in Al-rich SROAS, similar to drying-induced acidification of Al-saturated smectite (Clarke et al., 2011). Surficial pH changes may affect binding of SOM to SROAS. Conversion of outer-sphere complexes into inner-sphere complexes by release of protons during dehydration promoted chemical binding of organic matter to mineral surfaces (Kang and Xing, 2007; Kang et al., 2008), highlighting the need for a detailed understanding of interfacial processes during aggregation of SROAS.

Strong aggregation of Al-rich SROAS contributes to induration of subsoils (Farmer et al., 1984; Thompson et al., 1996; Jongmans et al., 2000); however, compositional changes may modify aggregation mechanisms. Adsorption of anions, phosphate in particular, balances surface charge of SROAS (Li and Kobayashi, 2021; Li et al., 2022) and sorption of SOM by SROAS reduces the point of zero charge by introduction of negatively charged functional groups or masking of aluminol groups (Hanudin et al., 2000). Moreover, condensation of aluminol groups may be impeded by chemically bound SOM and adsorbed molecules may hinder particle approach by steric effects. Interference of organic matter in formation of ferrihydrite and Al hydroxides altered the physical properties and surface reactivity of the co-precipitates (Yu et al., 2006; Mikutta and Kretzschmar, 2008; Mikutta et al., 2014; Zhu et al., 2022), suggesting that the physical properties of SROAS-SOM co-precipitates also differ from pure SROAS. Al-SOM co-precipitates are resistant to biodegradation (Scheel et al., 2007) and act as a cementing agent in subsoils of some Podzols (Kaczorek et al., 2004); however, little is known about their reactivity and physical properties. The structure and composition of pedogenic poorly crystalline Al species, including SROAS and co-precipitates, may impose differences in the microstructural stability of andic soils (Baumgarten et al., 2013). Shrinkage and aggregation was more pronounced in andic subsoils compared with topsoils (Kubota, 1972; Bartoli et al., 2007). Hence, interfacial processes during aggregation of variably composed poorly crystalline Al species should be investigated in detail to assess their response to alternating water contents.

Interactions of SROAS and Fe

Incorporation of Fe is a possibly overlooked process affecting SROAS structure and reactivity. Natural SROAS formed in andic soils contained ferric Fe (Fe^{III}) in isomorphic substitution for octahedral Al (~1% of Al), adsorbed Fe^{3+} and Fe^{III} polymers (Baker et al., 2014; Filimonova et al., 2016). Synthesis experiments at ≥95 °C suggest that more Fe^{III} substitution at octahedral sites than previously observed in nature is structurally possible (≤20%; Du et al., 2020) with Si-rich SROAS containing less neighbouring Fe atoms than Al-rich SROAS (Jeute et al., 2021). Polymerization of Fe hampered crystallisation of Al-rich SROAS and caused formation of a

separate Fe^{III} phase (>95 °C; McBride et al., 1984; Du et al., 2020). The synthesis conditions probably facilitated precipitation of Fe polymers because hydrolysis and polymerization of Fe^{3+} occur at lower pH than respective reactions of Al^{3+} (Duan and Gregory, 2003) and are promoted by temperatures >60 °C (Jolivet et al., 2006). In soils, mobilisation of monomeric Fe^{3+} is linked to pronounced acidification, that is, conditions that promote SROAS dissolution. However, Fe can be mobilized at pH>3 by low-molecular-weight organic substances and reductive formation of ferrous Fe (Fe^{II}; Colombo et al., 2014). Ferrous Fe reacts with silicic acid at circumneutral pH (Francisco et al., 2020) and may co-precipitate with SROAS (Farmer et al., 1991a; Jeute et al., 2021). Shortly after contact with air, Fe^{II} in SROAS is partially oxidized (Farmer et al., 1991a; Jeute et al., 2021). Structural features of Si-rich SROAS may slow the oxidation of Fe^{II} compared with Al-rich SROAS (Farmer et al., 1991a). Interestingly, several studies report that Fe^{2+} enhances crystallisation of Si-rich SROAS to phyllosilicates at neutral to alkaline pH. Precipitation of Si-rich SROAS in the presence of Fe^{2+} enabled formation of poorly crystalline halloysite (initial Al:Si ratio = 1) and poorly ordered aluminous nontronite (initial Al:Si<1) within 12 weeks at room temperature (Farmer et al., 1991a). Alternating redox potentials enhanced the crystallinity of nontronite at 90 °C (Farmer et al., 1994). Harder (1976) synthesized 2:1 phyllosilicate within days at 3–20 °C under constantly reducing conditions and suggested that Fe^{II} favours the formation of the octahedral sheet as a template for binding of Si tetrahedra, provided that Si is present in monomeric form (Harder, 1976, 1978). Spectroscopic analyses of Fe speciation in these SROAS and intermediate phases are lacking. A fraction of Fe^{II} may be stabilized against oxidation in the octahedral sheet as a function of its crystallinity (Mizutani et al., 1991; Jeute et al., 2021). Occupancy of tetrahedral sites by Fe^{II} is unlikely due to size constraints (Neumann et al., 2011) while tetrahedral Fe^{III} was observed in smectites (Baron et al., 2016). Fluctuating redox conditions, for instance caused by paddy management of andic soils, may enhance transformation of SROAS into phyllosilicates (Winkler et al., 2018). Incorporated Fe may affect SROAS surface properties and participate in electron transfer reactions in soil. Studies on redox reactions mediated by clay minerals focussed on Fe-rich 2:1 phyllosilicate (Yu et al., 2023) while Fe in SROAS has not been addressed yet. Organic matter may influence Fe availability and speciation (Colombo et al., 2014; Possinger et al., 2021); however, little is known about interactions of Fe and SROAS in the presence of SOM. Association of Fe and Al with SOM at the submicron scale in andic soils evinces possible co-precipitation of these compounds (Inagaki et al., 2020). Moreover, organically bound Fe may interact with SROAS in illuvial horizons of Podzols.

Assessing labile mineral-bound SOM by enzyme addition

The current study used a novel approach for testing the accessibility of mineral-associated organic matter for microorganisms, that is, the addition of an extracellular enzyme and

subsequent quantification of the reaction product (chapter 5). The chemical composition and accessibility of both dissolved DOM and co-precipitated organic matter were reflected in the quantity of glucose released by hydrolysis of carbohydrates, suggesting that enzyme-addition assays are a promising tool for quantification and characterization of labile SOM in mineral-organic associations more broadly. Due to the specificity of β-glucosidase, the degradation of carbohydrates was incomplete; however, addition of enzymes that are capable to cleave polysaccharide chains internally may increase the yield of reaction products. Future studies could also investigate the composition of the released species, as the composition of sugar monomers could give information whether the cleaved carbohydrates originate from plants or microorganisms (Gunina and Kuzyakov, 2015).

Given the preferential sorption of oxidized aromatic compounds by adsorption and co-precipitation with SROAS, addition of an oxidative enzyme was considered during method development. As oxidation products of aromatic SOM are unspecific, quantification of oxygen consumption was envisaged. Oxidative cleavage of aromatic DOM mobilised from forest topsoil (Krettek et al., 2022) by a fungal laccase induced oxygen consumption (data not shown); however, the low rates impeded application to mineral-organic associations. Deployment of devices that allow for detection of oxygen concentrations in small sample volumes could avoid this problem (Zimmerman et al., 2004). Generally, a combination of several enzymes, including hydrolytic and oxidative enzymes, may mimic the capability of a diverse microbial community for substrate mobilisation.

Application of enzyme-addition assays for testing the degradability of mineral-associated SOM enables targeting of a specific substrate in a mixture of organic matter. In conventional mineralization experiments, that is, incubation of mineral-organic associations with microorganisms and quantification of respiration, this is only possible by isotopic labelling. Moreover, alteration of mineral-organic associations by phosphate addition as a fertilizer to support microbial growth is avoided (Spohn and Schleuss, 2019), provided that an appropriate buffer is used. The current study revealed that a fraction of SOM in co-precipitates is accessible for microbial enzymes. Moreover, organic matter adsorbed to minerals or held by organic-organic interactions (Kleber et al., 2007) may protrude from mineral surfaces and thus be cleavable for enzymes. For instance, ectomycorrhizal fungi can degrade mineral-bound proteins by formation of a surficial enzyme-substrate complex (Wang et al., 2020; 2021). Hydrolysis of pesticides intercalated within montmorillonite was suggested to proceed by enzymes entering the interlayer space (Singh et al., 2003); however, the degradability of sorbed pesticide may also be explained by surface depletion driving outward diffusion of the pesticide (Pignatello and Nason, 2020). When assessing the accessibility of mineral-bound SOM, it should be noted that many oxidative depolymerisation reactions do not proceed by formation of enzyme-substrate complexes, but involve electron transfer by low-molecular-

weight mediators (Datta et al., 2017). The mobility of such species is much higher compared with enzymes, possibly enabling penetration of co-precipitates or adsorbed molecules.

Interactions of microorganisms, SROAS and SOM

Several aspects of interactions between SROAS and microorganisms remain to be elucidated in the future to fully comprehend SOM stabilization mechanisms actuated by SROAS. Inactivation of extracellular enzymes was suggested to decelerate SOM decay based on studies showing a lowered catalytic potential of adsorbed enzymes (e.g., Kobayashi and Aomine, 1967; Shindo et al., 2002). However, adsorbed enzymes remained active to some degree and can be protected from protease attack at SROAS surfaces (Menezes-Blackburn et al., 2011). In soil, enzymes are released together with other substances that may reduce enzyme adsorption and enhance their resistance against proteolysis, altogether promoting enzyme activity at mineral surfaces (Flemming and Wingender, 2010; Olsson et al., 2012; Wang et al., 2020). As microorganisms invest energy and nutrients in enzyme exudation, there is an incentive for synthesis of extracellular enzymes that are stable in soil. Thus, interactions of enzymes with the soil matrix may actually support the persistence of enzymatic activity for weeks (Schimel et al., 2017). Hence, the relevance of enzyme inactivation by SROAS for SOM stabilization is not clear.

Association of microbial residues with the mineral matrix of andic soils contributes to SOM accrual (Buurman et al., 2007; Hernández et al., 2012; Asano and Wagai, 2015). In the presence of SROAS, mineralization of freshly added substrates was low relative to microbial biomass, indicating that organic matter was effectively converted into stable forms or microbial biomass (Saggar et al., 1994; Yang et al., 2023). The formation of mineral-organic associations may be regulated by the efficiency of microorganisms to allocate assimilated organic matter into their biomass or reactive metabolites (Kallenbach et al., 2016; Wang et al., 2017). Sorption of P forms by SROAS may induce a low P availability and alter the composition of the colonizing microbial community (Heckman et al., 2013; Brandt et al., 2023). Short-range ordered minerals were shown to restrict the growth of bacteria, presumably because bacterial species were less capable to cope with low nutrient availability (Finley et al., 2022). Microorganisms employ several strategies to respond to low P availability, for instance, increased exudation of P cleaving enzymes and low-molecular-weight compounds that promote P mobilization (Mooshammer et al., 2014). These compounds may liberate SOM from mineral-organic associations either by displacement of mineral-bound SOM or by stimulation of microbial activity (Keiluweit et al., 2015; Jilling et al., 2021). Hence, a low P availability may induce SOM destabilization instead of limiting its degradation. Addition of simple organic substrates enhanced decomposition of native SOM more strongly in soils rich in short-range ordered minerals compared with soil containing crystalline clay-sized minerals (Finley et al.,

2018), suggesting that co-precipitates may be susceptible to dissolution in the rhizosphere or other microbial hotspots. Besides native SOM, exudates may also rapidly mobilize Al from poorly crystalline species (Dahlgren and Saigusa, 1994; Takahashi et al., 1995). Organic Al-complexes are less toxic than monomeric Al^{3+} (Gensemer and Playle, 1999) and microorganisms may adapt to Al toxicity (Jorquera et al., 2010). Overall, is not clear how mutual interactions of microorganisms and SROAS affect the quantity of mineral-associated SOM as accrual and destabilization may occur in variable proportions as a function of microbial composition and SROAS structure. The importance of interactions between microorganisms and SROAS is presumably further regulated by microbial abundance on mineral surfaces or per soil volume (Sokol et al., 2018). In forest ecosystems, direct sorption of plant-derived compounds to soil minerals contributes to greater extent to SOM accrual, while favourable conditions for microbial proliferation in cultivated soils and grasslands increase the contribution of microbial residues to SOM (Liang et al., 2019; Mikutta et al., 2019; Angst et al., 2021). Hence, the composition of mineral-organic associations formed by interactions of SROAS and organic matter supposably varies with environmental factors as they form in different soil types.

References

Angst G., Mueller K. E., Nierop K. G. J. and Simpson M. J. (2021) Plant- or microbial-derived? A review on the molecular composition of stabilized soil organic matter. Soil Biol. Biochem. 156, 108189.

Asano M. and Wagai R. (2015) Distinctive organic matter pools among particle-size fractions detected by solid-state ^{13}C-NMR, δ^{13}C and δ^{15}N analyses only after strong dispersion in an allophanic Andisol. Soil Sci. Plant Nutr. 61, 242–248.

Baker L. L., Nickerson R. D. and Strawn D. G. (2014) XAFS study of Fe-substituted allophane and imogolite. Clays Clay Miner. 62, 20–34.

Bardy M., Bonhomme C., Fritsch E., Maquet J., Hajjar R., Allard T., Derenne S. and Calas G. (2007) Al speciation in tropical podzols of the upper Amazon Basin: A solid-state ^{27}Al MAS and MQMAS NMR study. Geochim. Cosmochim. Acta 71, 3211–3222.

Baron F., Petit S., Tertre E. and Decarreau A. (2016) Influence of aqueous Si and Fe speciation on tetrahedral Fe(III) substitutions in nontronites: A clay synthesis approach. Clays Clay Miner. 64, 230–244.

Bartoli F., Poulenard A. J. and Schouller B. E. (2007) Influence of allophane and organic matter contents on surface properties of Andosols. Eur. J. Soil Sci. 58, 450–464.

Basile-Doelsch I., Amundson R., Stone W. E. E., Masiello C. A., Bottero J. Y., Colin F., Masin F., Borschneck D. and Meunier J. D. (2005) Mineralogical control of organic carbon dynamics in a volcanic ash soil on La Réunion. Eur. J. Soil Sci. 56, 689–703.

Baumgarten W., Dörner J. and Horn R. (2013) Microstructural development in volcanic ash soils from South Chile. Soil Tillage Res. 129, 48–60.

Brandt L., Stache F., Poll C., Bramble D. S., Schöning I., Schrumpf M., Ulrich S., Kaiser K., Mikutta R., Mikutta C., Oelmann Y., Konrad A., Siemens J. and Kandeler E. (2023) Mineral type and land-

use intensity control composition and functions of microorganisms colonizing pristine minerals in grassland soils. Soil Biol. Biochem. 182, 109037.

Buurman P., Peterse F. and Almendros Martin G. (2007) Soil organic matter chemistry in allophanic soils: A pyrolysis-GC/MS study of a Costa Rican Andosol catena. Eur. J. Soil Sci. 58, 1330–1347.

Clarke C. E., Aguilar-Carrillo J. and Roychoudhury A. N. (2011) Quantification of drying induced acidity at the mineral–water interface using ATR-FTIR spectroscopy. Geochim. Cosmochim. Acta 75, 4846–4856.

Colombo C., Palumbo G., He J.-Z., Pinton R. and Cesco S. (2014) Review on iron availability in soil: Interaction of Fe minerals, plants, and microbes. J. Soils Sediments 14, 538-548-538–548.

Dahlgren R. A. and Saigusa M. (1994) Aluminum release rates from allophanic and nonallophanic Andosols. Soil Sci. Plant Nutr. 40, 125–136.

Datta R., Kelkar A., Baraniya D., Molaei A., Moulick A., Meena R. S. and Formanek P. (2017) Enzymatic degradation of lignin in soil: A review. Sustainability 9, 1163.

Du P., Yuan P., Liu J., Yang Y., Bu H., Wang S., Zhou J., Song H., Liu D., Michalski J. R. and Liu C. (2020) Effects of environmental Fe concentrations on formation and evolution of allophane in Al-Si-Fe systems: Implications for both earth and Mars. J. Geophys. Res. Planets 125, e2020JE006590.

Duan J. and Gregory J. (2003) Coagulation by hydrolysing metal salts. Adv. Colloid Interface Sci. 100–102, 475–502.

Farmer V. C., Fraser A. R., Robertson L. and Sleeman J. R. (1984) Proto-imogolite allophane in Podzol concretions in Australia: Possible relationship to aluminous ferrallitic (lateritic) cementation. J. Soil Sci. 35, 333–340.

Farmer V. C., Fraser A. R. and Tait J. M. (1979) Characterization of the chemical structures of natural and synthetic aluminosilicate gels and sols by infrared spectroscopy. Geochim. Cosmochim. Acta 43, 1417–1420.

Farmer V. C., Krishnamurti G. S. R. and Huang P. M. (1991a) Synthetic allophane and layer-silicate formation in SiO_2-Al_2O_3-FeO-Fe_2O_3-MgO-H_2O systems at 23°C and 89°C in a calcareous environment. Clays Clay Miner. 39, 561–570.

Farmer V. C., McHardy W. J., Elsass F. and Robert M. (1994) *hk*-Ordering in aluminous nontronite and saponite synthesized near 90°C: Effects of synthesis conditions on nontronite composition and ordering. Clays Clay Miner. 42, 180–186.

Farmer V.C., McHardy W. J., Palmieri F., Violante A. and Violante P. (1991b) Synthetic allophanes formed in calcareous environments: Nature, conditions of formation, and transformations. Soil Sci. Soc. Am. J. 55, 1162–1166.

Filimonova S., Kaufhold S., Wagner F. E., Häusler W. and Kögel-Knabner I. (2016) The role of allophane nano-structure and Fe oxide speciation for hosting soil organic matter in an allophanic Andosol. Geochim. Cosmochim. Acta 180, 284–302.

Finley B. K., Dijkstra P., Rasmussen C., Schwartz E., Mau R. L., Liu X.-J. A., Gestel N. van and Hungate B. A. (2018) Soil mineral assemblage and substrate quality effects on microbial priming. Geoderma 322, 38–47.

Finley B. K., Mau R. L., Hayer M., Stone B. W., Morrissey E. M., Koch B. J., Rasmussen C., Dijkstra P., Schwartz E. and Hungate B. A. (2022) Soil minerals affect taxon-specific bacterial growth. ISME J. 16, 1318–1326.

Flemming H.-C. and Wingender J. (2010) The biofilm matrix. Nat. Rev. Microbiol. 8, 623–633.

Francisco P. C. M., Mitsui S., Ishidera T., Tachi Y., Doi R. and Shiwaku H. (2020) Interaction of Fe^{II} and Si under anoxic and reducing conditions: Structural characteristics of ferrous silicate co-precipitates. Geochim. Cosmochim. Acta 270, 1–20.

Gensemer R. W. and Playle R. C. (1999) The bioavailability and toxicity of aluminum in aquatic environments. Crit. Rev. Environ. Sci. Technol. 29, 315–450.

Gunina A. and Kuzyakov Y. (2015) Sugars in soil and sweets for microorganisms: Review of origin, content, composition and fate. Soil Biol. Biochem. 90, 87–100.

Hanudin E., Matsue N. and Henmi T. (2000) Change in charge characteristics of allophane with adsorption of low molecular weight organic acids. Clay Sci. 11, 243–255.

Harder H. (1976) Nontronite synthesis at low temperatures. Chem. Geol. 18, 169–180.

Harder H. (1978) Synthesis of iron layer silicate minerals under natural conditions. Clays Clay Miner. 26, 65–72.

Heckman K., Welty-Bernard A., Vazquez-Ortega A., Schwartz E., Chorover J. and Rasmussen C. (2013) The influence of goethite and gibbsite on soluble nutrient dynamics and microbial community composition. Biogeochemistry 112, 179–195.

Hellmann R., Cotte S., Cadel E., Malladi S., Karlsson L. S., Lozano-Perez S., Cabié M. and Seyeux A. (2015) Nanometre-scale evidence for interfacial dissolution-reprecipitation control of silicate glass corrosion. Nat. Mater. 14, 307–311.

Hernández Z., Almendros G., Carral P., Álvarez A., Knicker H. and Pérez-Trujillo J. P. (2012) Influence of non-crystalline minerals in the total amount, resilience and molecular composition of the organic matter in volcanic ash soils (Tenerife Island, Spain). Eur. J. Soil Sci. 63, 603–615.

Hiradate S. and Wada S.-I. (2005) Weathering process of volcanic glass to allophane determined by ^{27}Al and ^{29}Si solid-state NMR. Clays Clay Miner. 53, 401–408.

Hofmann A., Pelletier M., Michot L., Stradner A., Schurtenberger P. and Kretzschmar R. (2004) Characterization of the pores in hydrous ferric oxide aggregates formed by freezing and thawing. J. Colloid Interface Sci. 271, 163–173.

Hu Y. F., Xu R. K., Dynes J. J., Blyth R. I. R., Yu G., Kozak L. M. and Huang P. M. (2008) Coordination nature of aluminum (oxy)hydroxides formed under the influence of tannic acid studied by X-ray absorption spectroscopy. Geochim. Cosmochim. Acta 72, 1959–1969.

Ildefonse P., Kirkpatrick R. J., Montez B., Calas G., Flank A. M. and Lagarde P. (1994) ^{27}Al MAS NMR and Aluminum X-ray absorption near edge structure study of imogolite and allophanes. Clays Clay Miner. 42, 276–287.

Inagaki T. M., Possinger A. R., Grant K. E., Schweizer S. A., Mueller C. W., Derry L. A., Lehmann J. and Kögel-Knabner I. (2020) Subsoil organo-mineral associations under contrasting climate conditions. Geochim. Cosmochim. Acta 270, 244–263.

Isobe T., Watanabe T., D'Espinose De La Caillerie J. B., Legrand A. P. and Massiot D. (2003) Solid-state ^{1}H and ^{27}Al NMR studies of amorphous aluminum hydroxides. J. Colloid Interface Sci. 261, 320–324.

Jansen B., Nierop K. G. J. and Verstraten J. M. (2003) Mobility of Fe(II), Fe(III) and Al in acidic forest soils mediated by dissolved organic matter: Influence of solution pH and metal/organic carbon ratios. Geoderma 113, 323–340.

Jeute T., Baker L. L., Bishop J. L., Abidin Z. and Rampe E. B. (2021) Spectroscopic analysis of allophane and imogolite samples with variable Fe abundance for characterizing the poorly crystalline components on Mars. Am. Mineral. 106, 527–540.

Jilling A., Keiluweit M., Gutknecht J. L. M. and Grandy A. S. (2021) Priming mechanisms providing plants and microbes access to mineral-associated organic matter. Soil Biol. Biochem. 158.

Jolivet J.-P., Tronc E. and Chanéac C. (2006) Iron oxides: From molecular clusters to solid. A nice example of chemical versatility. Comptes Rendus - Geosci. 338, 488–497.

Jongmans A. G., Denaix L., Van Oort F. and Nieuwenhuyse A. (2000) Induration of C horizons by allophane and imogolite in Costa Rican volcanic soils. Soil Sci. Soc. Am. J. 64, 254–262.

Jorquera M. A., Hernández M., Martínez O., Marschner P. and Mora M. de la L. (2010) Detection of aluminium tolerance plasmids and microbial diversity in the rhizosphere of plants grown in acidic volcanic soil. Eur. J. Soil Biol. 46, 255–263.

Kaczorek D., Sommer M., Andruschkewitsch I., Oktaba L., Czerwinski Z. and Stahr K. (2004) A comparative micromorphological and chemical study of "Raseneisenstein" (bog iron ore) and "Ortstein." Geoderma 121, 83–94.

Kallenbach C. M., Frey S. D. and Grandy A. S. (2016) Direct evidence for microbial-derived soil organic matter formation and its ecophysiological controls. Nat. Commun. 7, 13630.

Kang S., Amarasiriwardena D. and Xing B. (2008) Effect of dehydration on dicarboxylic acid coordination at goethite/water interface. Colloids Surf. Physicochem. Eng. Asp. 318, 275–284.

Kang S. and Xing B. (2007) Adsorption of dicarboxylic acids by clay minerals as examined by *in situ* ATR-FTIR and *ex situ* DRIFT. Langmuir 23, 7024–7031.

Keiluweit M., Bougoure J. J., Nico P. S., Pett-Ridge J., Weber P. K. and Kleber M. (2015) Mineral protection of soil carbon counteracted by root exudates. Nat. Clim. Change 5, 588–595.

Kleber M., Sollins P. and Sutton R. (2007) A conceptual model of organo-mineral interactions in soils: Self-assembly of organic molecular fragments into zonal structures on mineral surfaces. Biogeochemistry 85, 9–24.

Kobayashi Y. and Aomine S. (1967) Mechanism of inhibitory effect of allophane and montmorillonite on some enzymes. Soil Sci. Plant Nutr. 13, 189–194.

Krettek A., Stein M. and Rennert T. (2022) Distribution of Al, Fe, Si, and DOC between size fractions mobilised from topsoil horizons with progressing degree of podzolisation. Sci. Rep. 12, 8384.

Kubota T. (1972) Aggregate-formation of allophanic soils: Effect of drying on the dispersion of the soils. Soil Sci. Plant Nutr. 18, 79–97.

Lenhardt K. R., Breitzke H., Buntkowsky G., Mikutta C. and Rennert T. (2022) Interactions of dissolved organic matter with short-range ordered aluminosilicates by adsorption and co-precipitation. Geoderma 423, 115960.

Lenhardt K. R., Stein M. and Rennert T. (2023a) Silicon incorporation reduces the reactivity of short-range ordered aluminosilicates toward organic acids. Clays Clay Miner. 71, 416–429.

Levard C., Doelsch E., Basile-Doelsch I., Abidin Z., Miche H., Masion A., Rose J., Borschneck D. and Bottero J.-Y. (2012) Structure and distribution of allophanes, imogolite and proto-imogolite in volcanic soils. Geoderma 183–184, 100–108.

Li M. and Kobayashi M. (2021) The aggregation and charging of natural clay allophane: Critical coagulation ionic strength in the presence of multivalent counter-ions. Colloids Surf. Physicochem. Eng. Asp. 626, 127021.

Li M., Sugimoto T., Yamashita Y. and Kobayashi M. (2022) Aggregation and charging of natural allophane particles in the presence of oxyanions. Colloids Surf. Physicochem. Eng. Asp. 649, 129431.

Liang C., Amelung W., Lehmann J. and Kästner M. (2019) Quantitative assessment of microbial necromass contribution to soil organic matter. Glob. Change Biol. 25, 3579–3590.

Masion A., Thomas F., Bottero J.-Y., Tchoubar D. and Tekely P. (1994) Formation of amorphous precipitates from aluminum-organic ligands solutions: Macroscopic and molecular study. J. Non-Cryst. Solids 171, 191–200.

Masion A., Vilgé-Ritter A., Rose J., Stone W. E. E., Teppen B. J., Rybacki D. and Bottero J.-Y. (2000) Coagulation-flocculation of natural organic matter with Al salts: Speciation and structure of the aggregates. Environ. Sci. Technol. 34, 3242–3246.

McBride M., Farmer V. C., Russell J. D., Tait J. M. and Goodman B. A. (1984) Iron substitution in aluminosilicate sols synthesized at low pH. Clay Miner. 19, 1–8.

Menezes-Blackburn D., Jorquera M., Gianfreda L., Rao M., Greiner R., Garrido E. and de la Luz Mora M. (2011) Activity stabilization of *Aspergillus niger* and *Escherichia coli* phytases immobilized on allophanic synthetic compounds and montmorillonite nanoclays. Bioresour. Technol. 102, 9360–9367.

Mikutta C. and Kretzschmar R. (2008) Synthetic coprecipitates of exopolysaccharides and ferrihydrite. Part II: Siderophore-promoted dissolution. Geochim. Cosmochim. Acta 72, 1128–1142.

Mikutta R., Lorenz D., Guggenberger G., Haumaier L. and Freund A. (2014) Properties and reactivity of Fe-organic matter associations formed by coprecipitation versus adsorption: Clues from arsenate batch adsorption. Geochim. Cosmochim. Acta 144, 258–276.

Mikutta R., Turner S., Schippers A., Gentsch N., Meyer-Stüve S., Condron L. M., Peltzer D. A., Richardson S. J., Eger A., Hempel G., Kaiser K., Klotzbücher T. and Guggenberger G. (2019) Microbial and abiotic controls on mineral-associated organic matter in soil profiles along an ecosystem gradient. Sci. Rep. 9, 10294.

Mizutani T., Fukushima Y., Okada A., Kamigaito O. and Kobayashi T. (1991) Synthesis of 1:1 and 2:1 iron phyllosilicates and characterization of their iron state by Mössbauer spectroscopy. Clays Clay Miner. 39, 381–386.

Mooshammer M., Wanek W., Zechmeister-Boltenstern S. and Richter A. (2014) Stoichiometric imbalances between terrestrial decomposer communities and their resources: Mechanisms and implications of microbial adaptations to their resources. Front. Microbiol. 5, 22.

Neumann A., Sander M. and Hofstetter T. B. (2011) Redox properties of structural Fe in smectite clay minerals. ACS Symp. Ser. 1071, 361–379.

Nierop K. G. J., Jansen B. and Verstraten J. M. (2002) Dissolved organic matter, aluminium and iron interactions: Precipitation induced by metal/carbon ratio, pH and competition. Sci. Total Environ. 300, 201–211.

Okhrimenko D. V., Nielsen C. F., Lakshtanov L. Z., Dalby K. N., Johansson D. B., Solvang M., Deubener J. and Stipp S. L. S. (2020) Surface reactivity and dissolution properties of alumina-silica glasses and fibers. ACS Appl. Mater. Interfaces 12, 36740–36754.

Olsson R., Giesler R., Loring J. S. and Persson P. (2012) Enzymatic hydrolysis of organic phosphates adsorbed on mineral surfaces. Env. Sci Technol 46, 285–291.

Parfitt R. L. and Kimble J. M. (1989) Conditions for formation of allophane in soils. Soil Sci. Soc. Am. J. 53, 971–977.

Pignatello J. J. and Nason S. L. (2020) Importance of Soil Properties and Processes on Bioavailability of Organic Compounds. Handb. Environ. Chem. 100, 7–41.

Possinger A. R., Zachman M. J., Dynes J. J., Regier T. Z., Kourkoutis L. F. and Lehmann J. (2021) Co-precipitation induces changes to iron and carbon chemistry and spatial distribution at the nanometer scale. Geochim. Cosmochim. Acta 314, 1–15.

Prietzel J., Ayala G. V., Häusler W., Eusterhues K., Mahakot S. and Klysubun W. (2023) Aluminum speciation in forest soils and forest floor density fractions using synchrotron-based XANES spectroscopy. Geoderma 431, 116373.

Rennert T. (2019) Wet-chemical extractions to characterise pedogenic Al and Fe species - a critical review. Soil Res 57, 1–16.

Rennert T., Eusterhues K., Hiradate S., Breitzke H., Buntkowsky G., Totsche K. U. and Mansfeldt T. (2014) Characterisation of Andosols from Laacher See tephra by wet-chemical and spectroscopic techniques (FTIR, ^{27}Al-, ^{29}Si-NMR). Chem. Geol. 363, 13–21.

Saggar S., Tate K. R., Feltham C. W., Childs C. W. and Parshotam A. (1994) Carbon turnover in a range of allophanic soils amended with ^{14}C-labelled glucose. Soil Biol. Biochem. 26, 1263–1271.

Schaller J., Puppe D., Kaczorek D., Ellerbrock R. and Sommer M. (2021) Silicon cycling in soils revisited. Plants 10, 1–36.

Scheel T., Dörfl C., Kalbitz K., Dörfler C. and Kalbitz K. (2007) Precipitation of dissolved organic matter by aluminum stabilizes carbon in acidic forest soils. Soil Sci. Soc. Am. J. 71, 64–74.

Schimel J., Becerra C. A. and Blankinship J. (2017) Estimating decay dynamics for enzyme activities in soils from different ecosystems. Soil Biol. Biochem. 114, 5–11.

Schneider C., Doucet F., Strekopytov S. and Exley C. (2004) The solubility of an hydroxyaluminosilicate. Polyhedron 23, 3185–3191.

Shindo H., Watanabe D., Onaga T., Urakawa M., Nakahara O. and Huang Q. (2002) Adsorption, activity, and kinetics of acid phosphatase as influenced by selected oxides and clay minerals. Soil Sci. Plant Nutr. 48, 763–767.

Singh N., Megharaj M., Gates W. P., Churchman G. J., Anderson J., Kookana R. S., Naidu R., Chen Z., Slade P. G. and Sethunathan N. (2003) Bioavailability of an organophosphorus pesticide, fenamiphos, sorbed on an organo clay. J. Agric. Food Chem. 51, 2653–2658.

Sokol N. W., Sanderman J. and Bradford M. A. (2018) Pathways of mineral-associated soil organic matter formation: integrating the role of plant carbon source, chemistry, and point-of-entry. Glob. Change Biol., 1–13.

Spohn M. and Schleuss P.-M. (2019) Addition of inorganic phosphorus to soil leads to desorption of organic compounds and thus to increased soil respiration. Soil Biol. Biochem. 130, 220–226.

Strekopytov S., Jarry E. and Exley C. (2006) Further insight into the mechanism of formation of hydroxyaluminosilicates. Polyhedron 25, 3399–3404.

Takahashi T. and Dahlgren R. A. (2016) Nature, properties and function of aluminum-humus complexes in volcanic soils. Geoderma 263, 110–121.

Takahashi T., Fukuoka T. and Dahlgren R. A. (1995) Aluminum solubility and release rates from soil horizons dominated by aluminum-humes complexes. Soil Sci. Plant Nutr. 41, 119–131.

Thompson C. H., Bridges E. M. and Jenkins D. A. (1996) Pans in humus podzols (Humods and Aquods) in coastal southern Queensland. Aust. J. Soil Res. 34, 161–182.

Wada S.-I. and Wada K. (1981) Reactions between aluminate ions and orthosilicic acid in dilute, alkaline to neutral solutions. Soil Sci. 132, 267–273.

Wang T., Persson P. and Tunlid A. (2021) A widespread mechanism in ectomycorrhizal fungi to access nitrogen from mineral-associated proteins. Environ. Microbiol. 23, 5837–5849.

Wang T., Tian Z., Bengtson P., Tunlid A. and Persson P. (2017) Mineral surface-reactive metabolites secreted during fungal decomposition contribute to the formation of soil organic matter. Environ. Microbiol. 19, 5117–5129.

Wang T., Tian Z., Tunlid A. and Persson P. (2020) Nitrogen acquisition from mineral-associated proteins by an ectomycorrhizal fungus. New Phytol. 228, 697–711.

Wells N. and Theng B. K. G. (1988) The cracking behaviour of allophane- and ferrihydrite-rich materials; Effect of pretreatment and material amendments. Appl. Clay Sci. 3, 237–252.

Winkler P., Kaiser K., Thompson A., Kalbitz K., Fiedler S. and Jahn R. (2018) Contrasting evolution of iron phase composition in soils exposed to redox fluctuations. Geochim. Cosmochim. Acta 235, 89–102.

Wolff-Boenisch D., Gislason S. R., Oelkers E. H. and Putnis C. V. (2004) The dissolution rates of natural glasses as a function of their composition at pH 4 and 10.6, and temperatures from 25 to 74°C. Geochim. Cosmochim. Acta 68, 4843–4858.

Xu R. K., Hu Y. F., Dynes J. J., Zhao A. Z., Blyth R. I. R., Kozak L. M. and Huang P. M. (2010) Coordination nature of aluminum (oxy)hydroxides formed under the influence of low molecular weight organic acids and a soil humic acid studied by X-ray absorption spectroscopy. Geochim. Cosmochim. Acta 74, 6422–6435.

Yang H. I., Baek N., Kwak J.-H., Lim S.-S., Lee Y.-H., Lee S.-M. and Choi W.-J. (2023) Microbial contribution to organic carbon accumulation in volcanic ash soils. J. Soils Sediments 23, 866–879.

Yu C., Qian A., Lu Y., Liao W., Zhang P., Tong M., Dong H., Zeng Q. and Yuan S. (2023) Electron transfer processes associated with structural Fe in clay minerals. Crit. Rev. Environ. Sci. Technol. 00, 1–26.

Yu G., Saha U. K., Kozak L. M. and Huang P. M. (2006) Kinetics of cadmium adsorption on aluminum precipitation products formed under the influence of tannate. Geochim. Cosmochim. Acta 70, 5134–5145.

Zhu X., Wang P., Jiang J., Wang R., Xu R. and Yu Y. (2022) Effect of incorporation of pectin on the adsorption of phosphate by Al (oxy)hydroxides. Pol. J. Environ. Stud. 31, 4975–4983.

Zimmerman A. R., Chorover J., Goyne K. W. and Brantley S. L. (2004) Protection of mesopore-adsorbed organic matter from enzymatic degradation. Environ. Sci. Technol. 38, 4542–4548.

Appendix

Supplementary material to Lenhardt et al. (2021) *Sci. Rep.* 11:4207

Table S1: Specific surface area (SSA) of short-range ordered aluminosilicates quantified by linear regression with the Brunauer-Emmett-Teller (BET) equation (see method section). Table S1 presents parameters used to calculate monolayer capacity (nmon), C and SSA. Sample mass (m) corresponds to sample mass after outgassing.

Al:Si	Sample treatment	m [g]	Intercept	Std error	Slope	Std error	R^2	n_{mon} [mol g^{-1}]	C	SSA [m^2 g^{-1}]
1.4	unground	0.6985	2.35	0.22	327.83	1.22	0.99	0.00303	140.6	295.5
	cryomilled	0.2498	3.45	0.12	352.33	0.81	0.99	0.00281	103	274.2
2.1	unground	1.4499	34.61	0.72	3783.61	4.28	0.99	2.62×10^{-4}	110.3	25.6
	cryomilled	0.2802	91.72	5.68	2168.29	25.71	0.99	4.42×10^{-4}	24.6	43.2
2.6	unground	1.382	18923.33	1207.58	128222.97	5796.30	0.96	6.80×10^{-6}	7.8	0.7
	decanted, unground	1.3848	12060.39	231.07	39465.19	1184.27	0.99	1.94×10^{-5}	4.3	1.9
	cryomilled	0.3057	48.97	2.81	14092.77	52.17	0.99	7.07×10^{-5}	288.8	6.9

Figure S1: Samples with a mass of 1 g each of freeze-dried short-range ordered aluminosilicates.

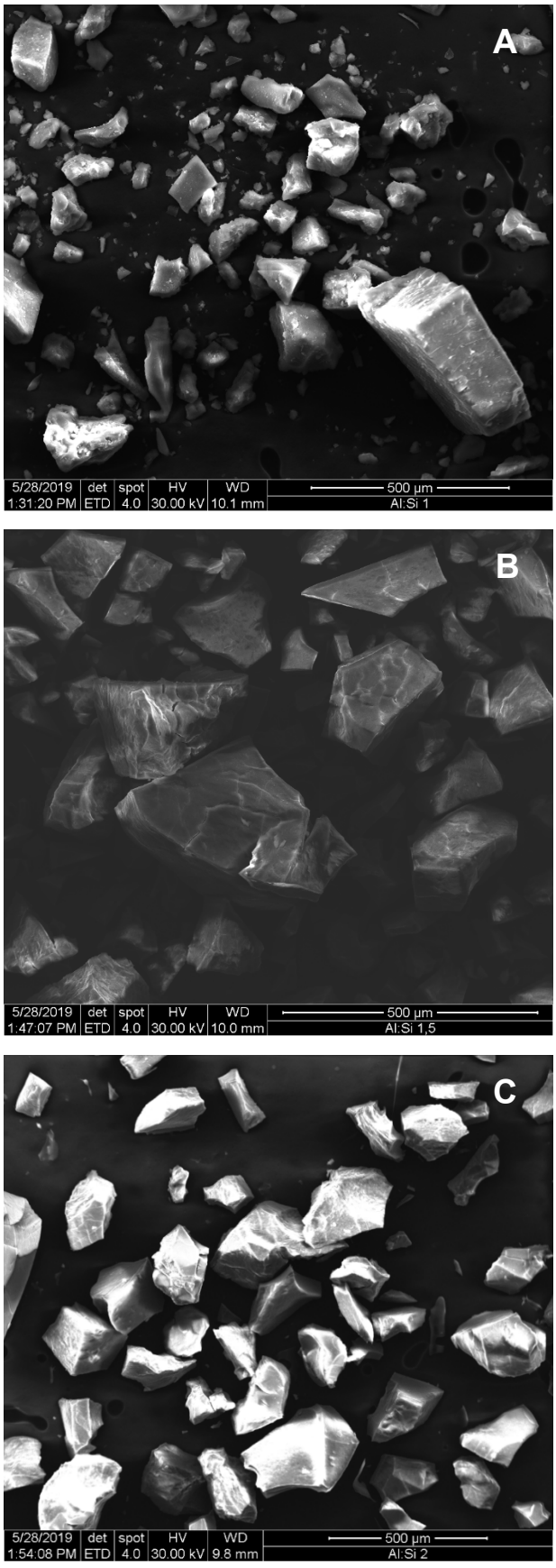

Figure S2: Morphology of aggregates of short-range ordered aluminosilicates with Al:Si ratios of 1.4 (A), 2.1 (B) and 2.6 (C) visualized by environmental scanning electron microscopy. The images were taken by Christian Buchmann.

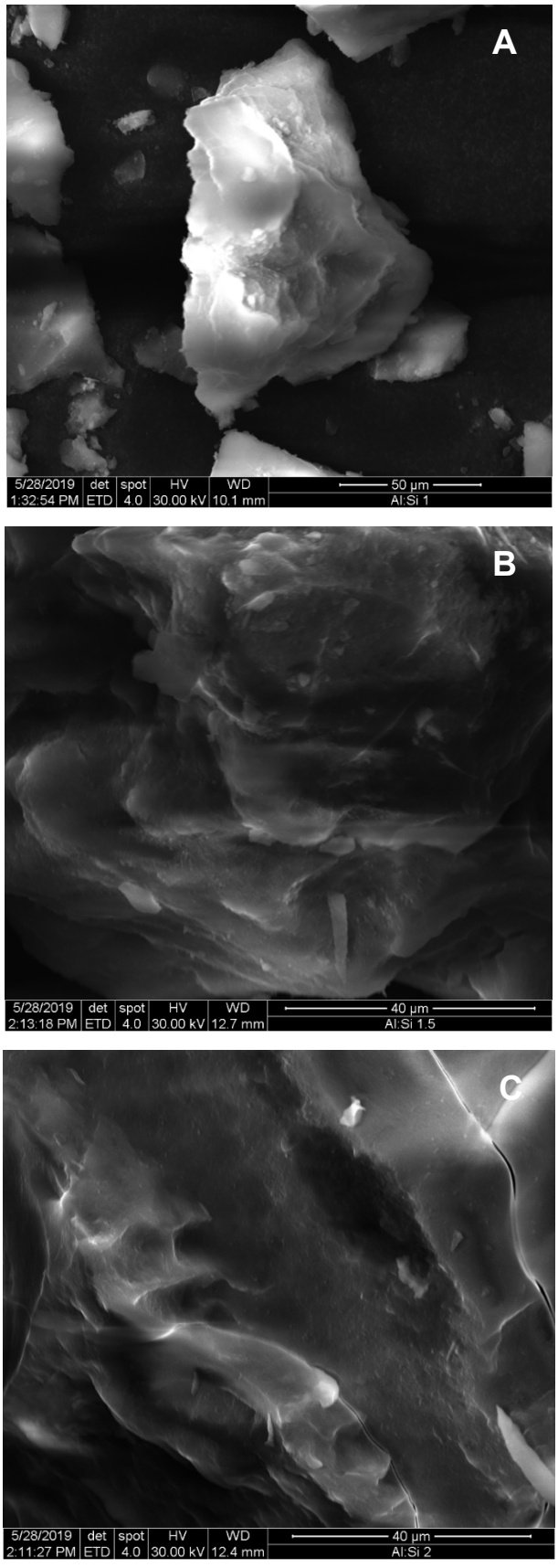

Figure S3: Aggregate surfaces of short-range ordered aluminosilicates with Al:Si ratios of 1.4 (A), 2.1 (B) and 2.6 (C) visualized by environmental scanning electron microscopy. The images were taken by Christian Buchmann.

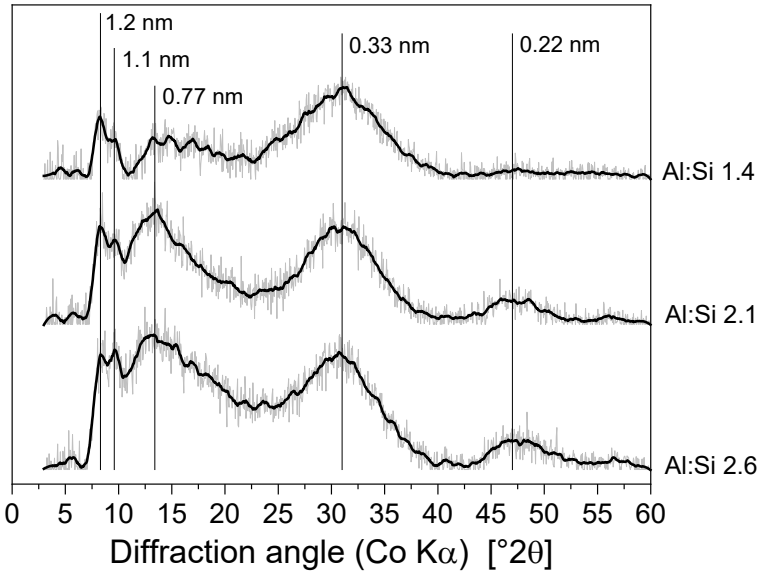

Figure S4: Baseline corrected X-ray diffractograms of short-range ordered aluminosilicates (SROAS). Data is shifted along the y-axis for clarity and given in arbitrary units. Black lines correspond to smoothed datasets. Several local maxima corresponded well with previously published analyses of natural and synthetic SROAS and respective *d*-values are thus delineated.

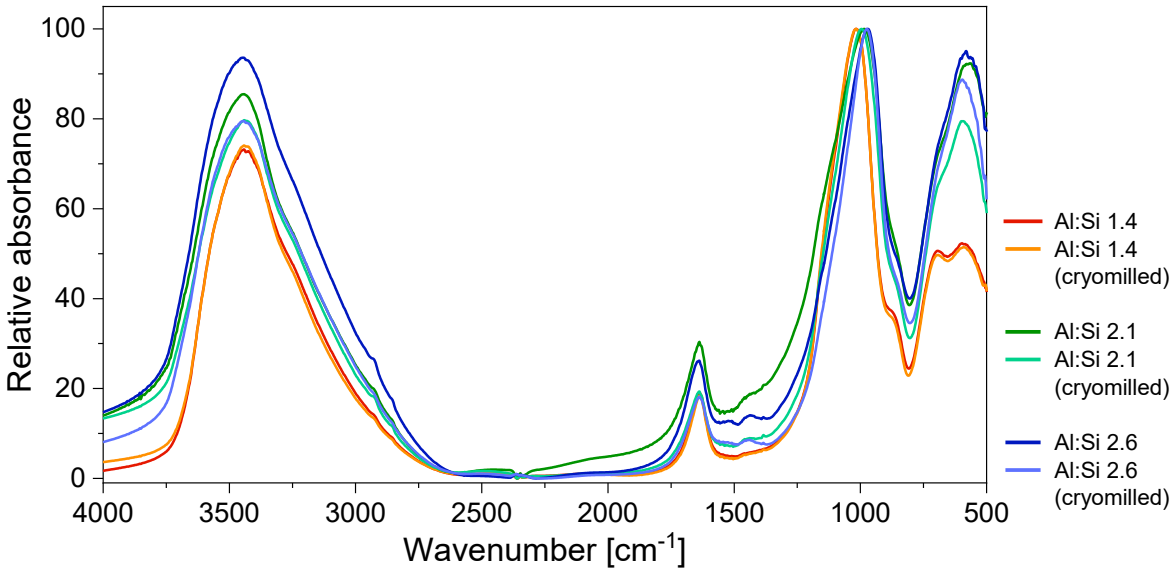

Figure S5: Fourier-transform infrared spectra of short-range ordered aluminosilicates recorded in transmission mode.

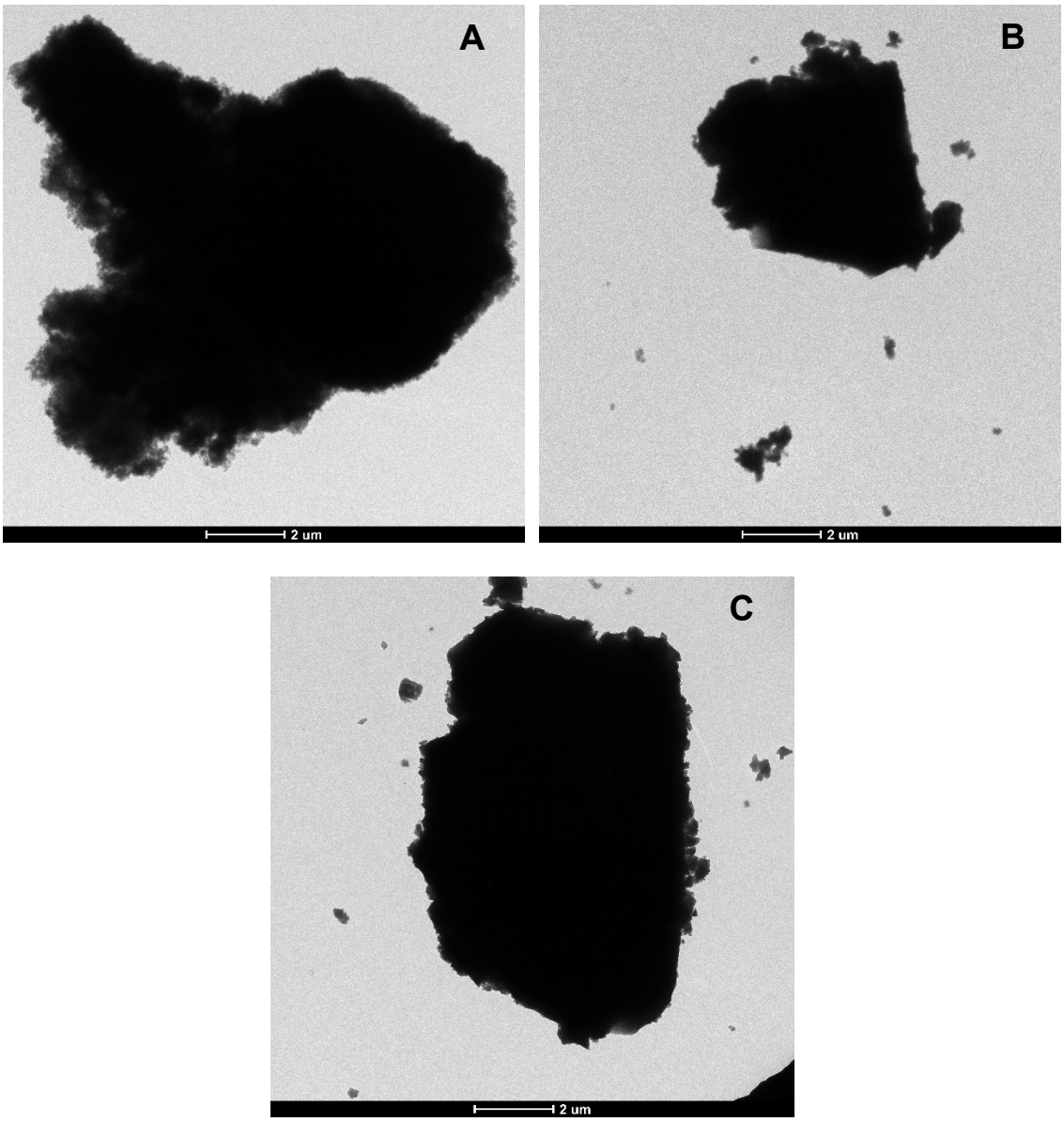

Figure S6: Largest single particles of cryomilled short-range ordered aluminosilicates with Al:Si ratios of 1.4 (A), 2.1 (B) and 2.6 (C) visualized by transmission electron microscopy.

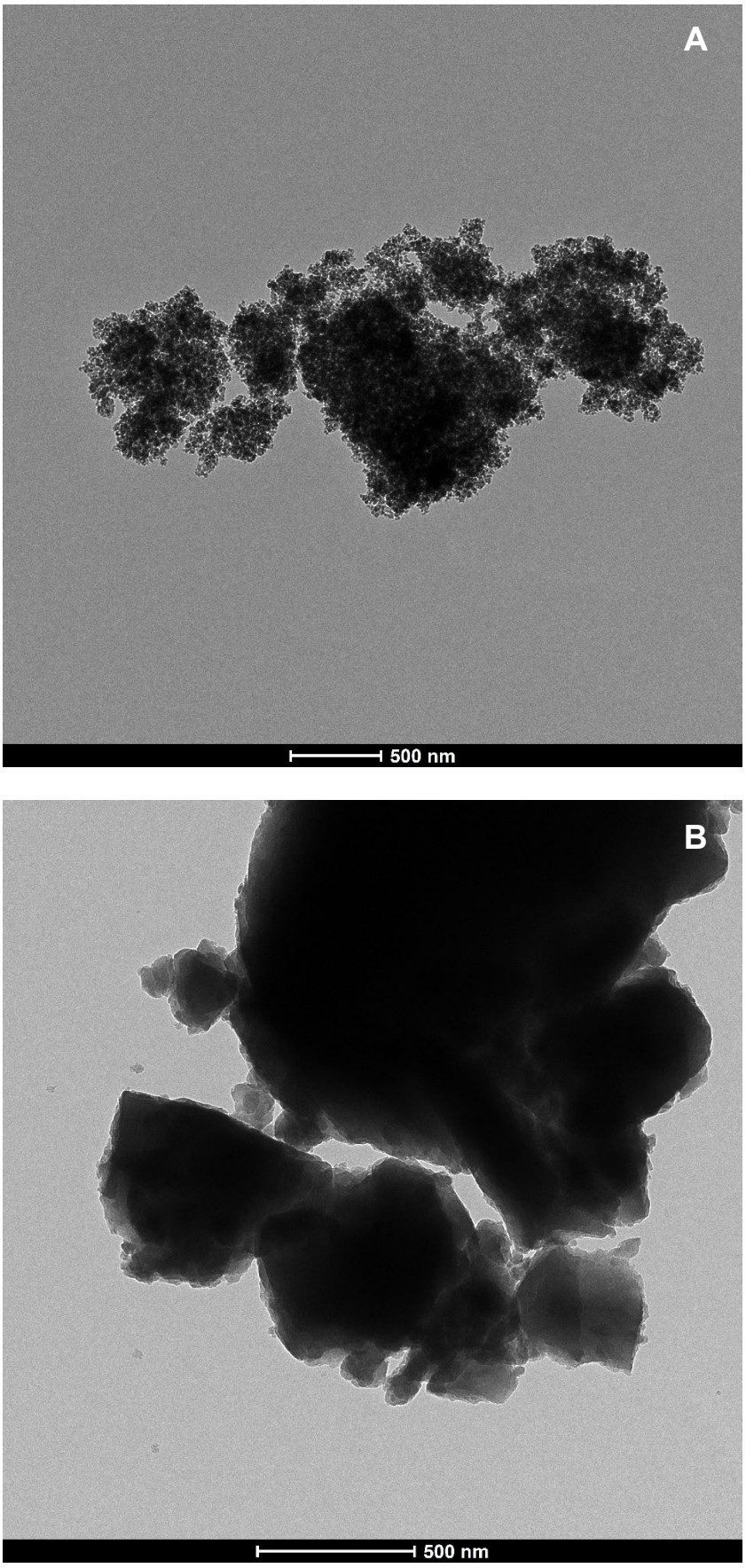

Figure S7: Particle clusters of cryomilled short-range ordered aluminosilicates with Al:Si ratios of 1.4 (A), 2.6 (B) visualized by transmission electron microscopy.

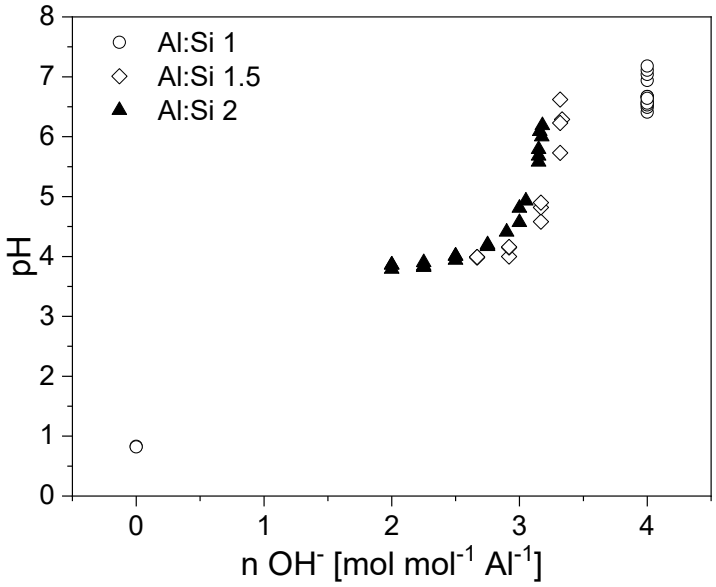

Figure S8: Course of neutralization during synthesis of short-range ordered aluminosilicates (SROAS) as a function of hydroxide added to synthesis batches with different molar ratios of Al and Si concentration. The amount of hydroxide is expressed as a molar ratio of OH:Al, with both aqueous Na_4SiO_4 and NaOH included. The latter was used only for precipitation of Al-rich SROAS (Al:Si 1.5 and 2, see method section). An amount of 4 mol hydroxide was assumed to be released by dissolution of 1 mol Na_4SiO_4. Note that the rate of addition differed between variants and Al supplying solution was acidified by 0.35 mol H mol^{-1} Al^{-1} in the case of Si-rich SROAS.

Peak Analysis

Data Set:[AlSi2lb0basel]AlSi2_lb0_baselinecorr!C
BaseLine:Constant
Chi^2=1.08168E+01 Adj. R-Square=7.82955E-01 # of Data Points=32767
SS=3.54346E+05 Degrees of Freedom=32759

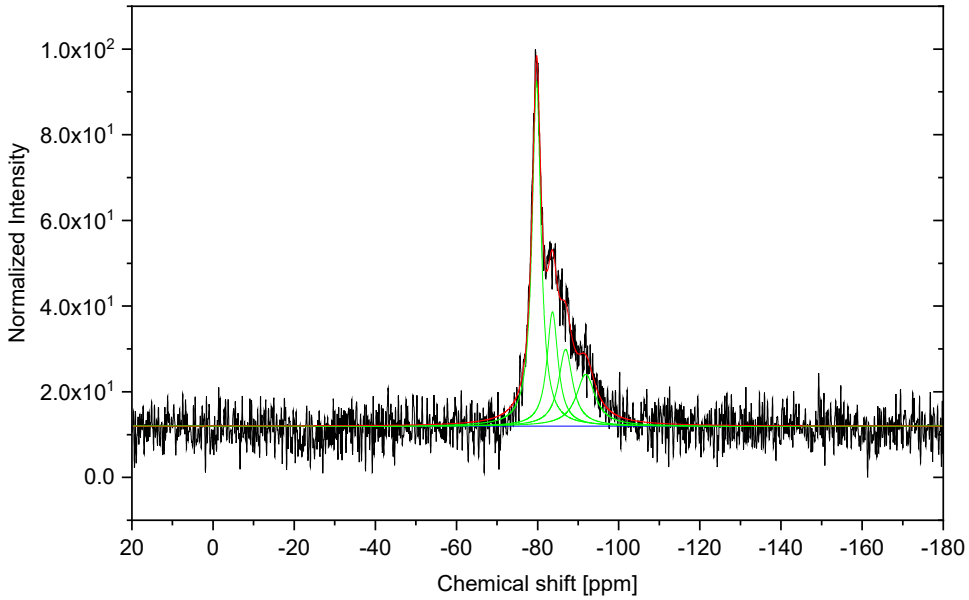

Fitting Results

Peak Index	Peak Type	Area Intg	Area IntgP	Center Grvty	Max Height	FWHM
1	Lorentz	-106.61877	-15.5254	-91.87301	12.11999	5.63265
2	Lorentz	-116.52321	-16.96764	-86.89956	17.93139	4.15449
3	Lorentz	-136.23558	-19.83808	-83.67155	26.67225	3.26252
4	Lorentz	-327.36032	-47.66889	-79.74923	80.51822	2.59512

Figure S9: Peak analysis report of solid-state ^{29}Si nuclear magnetic resonance spectra of short-range aluminosilicates with Al:Si ratio of 2.6. Proportion of Si in Q^0(3Al) (peak centred at -79.7 ppm) was derived from integral contribution ("Area IntgP" [%]; see method section).

Peak Analysis

Data Set:[AlSi2]Al_AlSI2_lb0_baselinecorr!C
BaseLine:Constant
Chi^2=3.99924E-01 Adj. R-Square=9.97711E-01 # of Data Points=32767
SS=1.30983E+04 Degrees of Freedom=32752

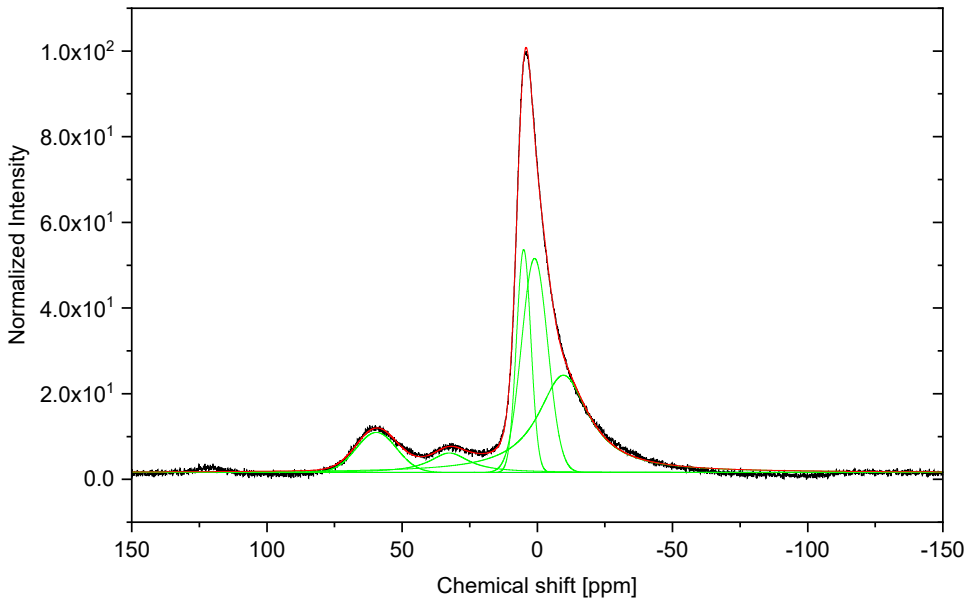

Fitting Results

Peak Index	Peak Type	Area Intg	Area IntgP	Center Grvty	Max Height	FWHM
1	Lorentz	-787.75223	-38.69028	-9.66499	22.71992	22.77551
2	Gauss	-605.20997	-29.72476	0.99142	50.00236	11.37063
3	Gauss	-344.99331	-16.94427	5.02881	52.06778	6.22459
4	Lorentz	-123.20389	-6.05113	32.50543	4.55315	17.63969
5	Gauss	-174.88744	-8.58956	59.50739	9.36922	17.53574

Figure S10: Peak analysis report of solid-state ^{27}Al nuclear magnetic resonance spectra of short-range aluminosilicates with Al:Si ratio of 2.6. Proportion of Al in tetrahedral, pentahedral and octahedral coordination was derived from respective integrals. Content of octahedral Al was calculated from the sum of integrals centred at <6 ppm (“Area IntgP” [%]; see method section).

Calculation of a hypothetical diameter of primary particles of Al-rich (2.6) SROAS

Calculation of a hypothetical particle diameter based on cubic close packing was done to rationalize the observation of poorly crystalline SROAS assembling to aggregates that are impermeable towards nitrogen diffusion. Hofmann et al. (2004) characterized aggregates formed by freezing suspensions of Fe (hydr)oxide particles at conditions similar to our procedure. Measured porosity and pore sizes corresponded well with values calculated on the basis of cubic close packing of primary particles (Ø 2 nm, determined by TEM). The face diagonal of this arrangement`s unit cell is $4r$ with sphere radius r. Application of Pythagorean law results in an edge length of $2\sqrt{2}r$. The diameter of the void between spheres is $2\sqrt{2}r - 2r$. Based on the assumption that nitrogen diffusion is restricted by pore sizes in Al-rich (2.6) SROAS, we set the void diameter to 2 nm and calculated the respective sphere radius and diameter ($r = 2.4$ nm, Ø = 4.8 nm). We are aware that the assumptions for this calculation are an ideal approximation of the conditions in Al-rich SROAS, which are in reality modified by, for instance, deviation from monodispersity and particle shape. Nonetheless, the calculations indicate that polynuclear aluminosilicate species with local imogolite-like structure (Si in Q^0(3Al)) have to be small (< 4 nm) to hinder diffusion of nitrogen to interparticle spaces and that surface accessibility is very sensitive to interparticle distances (i.e. effective r), which is determined by the width of the hydration layer and thus the binding mechanism.

Supplementary material to Lenhardt et al. (2022) *Geoderma* 423:115960

Table S1: Selected properties of bulk soil material at sampling depths of soil solutions.

Horizon	**Sampling depth** [cm]	**Coarse fragments** (>2 mm) [%]	**Clay**	**Silt** [%]	**Sand**	**C_{org}**	**N**	**C:N**	**pH ($CaCl_2$)**
						[g kg^{-1}]			
Oi						438.5	14.2	30.9	3.0
AE	10	5	12	29	59	72.8	2.7	27.8	2.9
Cw	60	65	8	20	72	6.5	0.3	20.2	3.9

Table S2: Elemental composition and features of transmission Fourier-transform infrared spectra of co-precipitates formed at different initial molar Al:Si, Al:C and reaction times. Initial Al concentration was 1.9 mM in all experiments.

DOM type	initial Al:C	Al:C		initial Al:Si	Al:Si		*v* (Si-O-Al)[1]		590:(Si-O-Al)[2]		690:590[3]	
Reaction time		**1 h**	**24 h**		**1 h**	**24 h**	**1 h**	**24 h**	**1 h**	**24 h**	**1 h**	**24 h**
Topsoil	1.4	1.88	1.94	1	1.76	2.00	1014	1000	0.83	0.94	0.94	0.87
		2.16	2.05	2	2.75	2.46	1014	972	0.98	0.99	0.91	0.83
	0.8	1.19	n.d.	1	1.81	n.d.	1014	n.d.	0.86	n.d.	0.93	n.d.
		1.13	1.17	2	2.75	2.65	1014	978	0.99	1.04	0.9	0.86
	0.5	0.63	0.57	1	1.97	2.22	1018	1014	0.88	1.01	0.92	0.88
		0.61	0.57	2	3.25	2.99	1022	988	1.1	1.09	0.89	0.88
Subsoil	1.4	1.97	2.2	1	1.83	1.94	1026	1000	0.87	0.97	0.92	0.86
		2.20	1.98	2	2.84	2.56	1010	972	0.99	1.04	0.91	0.85
	0.8	1.15	n.d.	1	1.91	n.d.	1018	n.d.	0.87	n.d.	0.92	n.d.
		1.15	1.17	2	2.88	2.82	1006	982	1.03	1.07	0.90	0.86
	0.5	0.78	0.83	1	2.10	2.30	1018	1004	0.97	1.17	0.91	0.88
		0.73	0.74	2	3.22	3.23	1020	986	1.16	1.17	0.87	0.88
Fir litter	1.4	2.67	2.4	1	1.88	1.93	1016	1002	0.8	0.99	0.94	0.87
		2.23	3.1	2	2.63	2.46	1010	980	0.91	1.04	0.91	0.84
	0.8	1.66		1	1.90	n.d.	1020	n.d.	0.79	n.d.	0.95	n.d.
		1.45	1.59	2	2.80	2.59	1018	978	0.92	1	0.91	0.86
	0.5	0.86	0.68	1	2.02	2.20	1026	1002	0.9	1.05	0.90	0.87
		0.83	0.9	2	2.92	2.84	1030	984	0.98	1.08	0.89	0.87
	0.3	0.54	n.d.	1	2.13	n.d.	1032	n.d.	0.94	n.d.	0.88	n.d.
		0.56	n.d.	2	3.20	n.d.	1034	n.d.	1.06	n.d.	0.86	n.d.

Beech litter	1.4	2.60	2.81	1	1.82	1.88	1018	1000	0.82	0.94	0.94	0.88
		2.80	2.84	2	2.69	2.46	1012	976	0.97	0.99	0.92	0.84
	0.8	1.69	n.d.	1	1.89	n.d.	1022	n.d.	0.86	1.05	0.92	0.84
		1.75	1.81	2	2.74	2.55	1022	978	0.93	n.d.	0.91	n.d.
	0.5	1.20	0.9	1	1.93	2.09	1026	1014	0.79	n.d.	0.91	n.d.
		0.91	0.87	2	2.86	2.87	1032	988	0.93	1.1	0.90	0.87
	0.3	0.64	n.d.	1	2.06	n.d.	1038	n.d.	0.89	n.d.	0.88	n.d.
		0.57	n.d.	2	3.25	n.d.	1034	n.d.	1.02	n.d.	0.88	n.d.

[1] Peak position of stretching vibrations of Si-O-Al bonds (Bishop et al., 2013).

[2] Ratio of absorption intensity at 590 cm^{-1} to absorption intensity at peak positions of stretching vibrations of Si-O-Al bonds.

[3] Ratio of absorption intensities at 690 cm^{-1} to 590 cm^{-1}.

Table S3: Elemental composition and features of transmission Fourier-transform infrared spectra of short-range ordered aluminosilicates formed at different initial molar Al:Si ratios and reaction times. Initial Al concentration was 1.9 mM in all experiments.

Reaction time [h]	**initial Al:Si**	**Al:Si**	***v* (Si-O-Al)[1]**	**590:(Si-O-Al)[2]**	**690:590[3]**
1	1	1.64	1020	0.79	0.93
1	1.3	2.19	1020	0.82	0.92
1	2	2.45	997	0.92	0.9
1	2.5	3.11	1016	0.89	0.92
1	3	3.27	989	0.98	0.9
1	4.5	4.65	1014	1.01	0.91
1	5	5.09	1008	1.18	0.89
1	1	1.64	1020	0.79	0.93
5	1	1.64	1006	0.79	0.9
24	1	1.5	995	0.86	0.83
72	1	1.46	995	0.9	0.84
1	2	2.45	997	0.92	0.9
5	2	2.6	985	0.95	0.85
24	2	2.41	969	0.89	0.77
72	2	2.2	965	0.87	0.74
1	3	3.27	989	0.98	0.9
5	3	3.23	979	0.97	0.86
24	3	2.91	965	0.99	0.78
72	3	3.05	963	0.94	0.73

[1] Peak position of stretching vibrations of Si-O-Al bonds (Bishop et al., 2013).

[2] Ratio of absorption intensity at 590 cm^{-1} to absorption intensity at peak positions of stretching vibrations of Si-O-Al bonds.

[3] Ratio of absorption intensities at 690 cm^{-1} to 590 cm^{-1}.

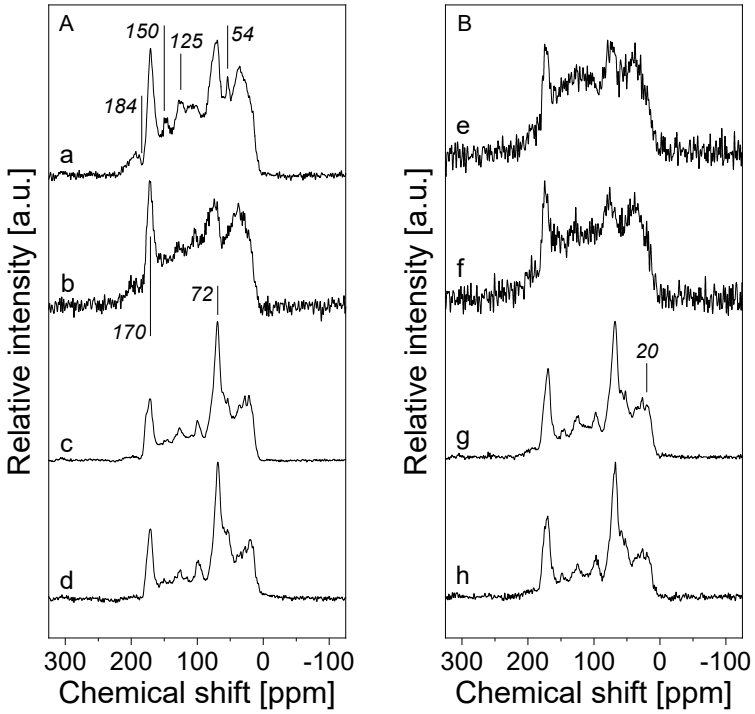

Figure S1: Solid-state ^{13}C nuclear magnetic resonance spectra of dissolved organic matter (DOM) obtained from (a) topsoil and (b) subsoil and from (c) fir and beech (d) litter are presented in panel A (left). Solid-state ^{13}C nuclear magnetic resonance spectra of organic matter associated to SROAS from respective DOM solutions are given in panel B (right). Spectra of organic matter in adsorption complexes of Si-rich SROAS after a contact time of 24 h with (e) topsoil and (f) subsoil DOM (variants with maximum C contents) and spectra of co-precipitated organic matter at an initial Al:Si of 2 and Al:C of 0.3 in the presence of DOM from (g) fir and (h) beech litter. Spectra of adsorption complexes are not discussed due to poor spectral resolution. All spectra are given at a line broadening of 0 Hz.

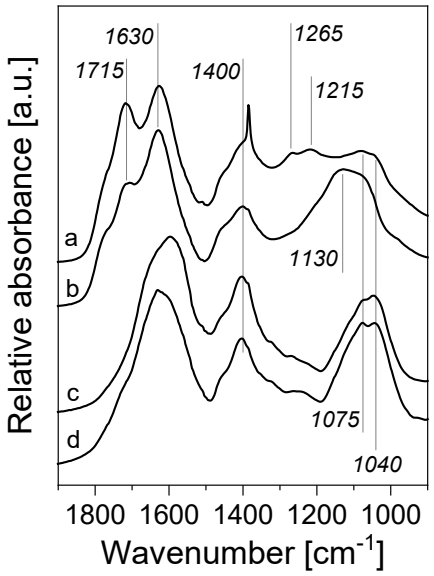

Figure S2: Transmission Fourier-transform infrared spectra of dissolved organic matter collected from (a) topsoil and (b) subsoil and extracted from (c) fir and (d) beech litter. Data was normalized to absorption maxima at 1630–1600 cm^{-1}. The sharp band at 1385 cm^{-1} in topsoil DOM spectra is caused by nitrate.

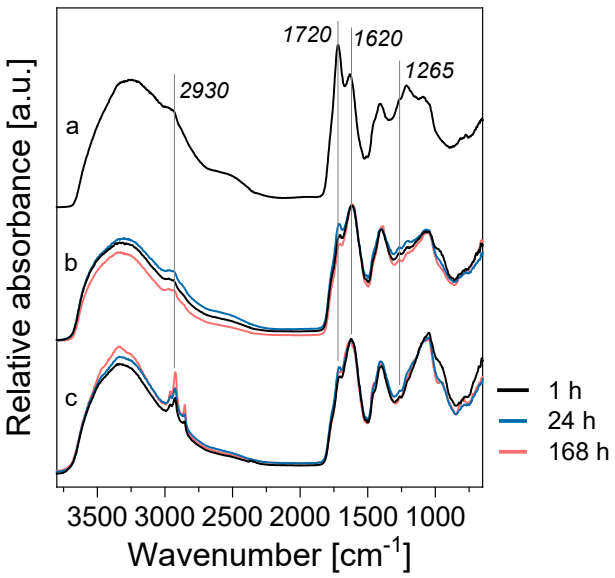

Figure S3: Diffuse reflectance infrared Fourier-transform spectra of freeze-dried (a) topsoil DOM and supernatants obtained from variants with (b) high and (c) low initial DOC concentrations after different contact times with a short-range ordered aluminosilicate with Al:Si = 2.1. Data was normalized to absorption at 1630 cm^{-1}.

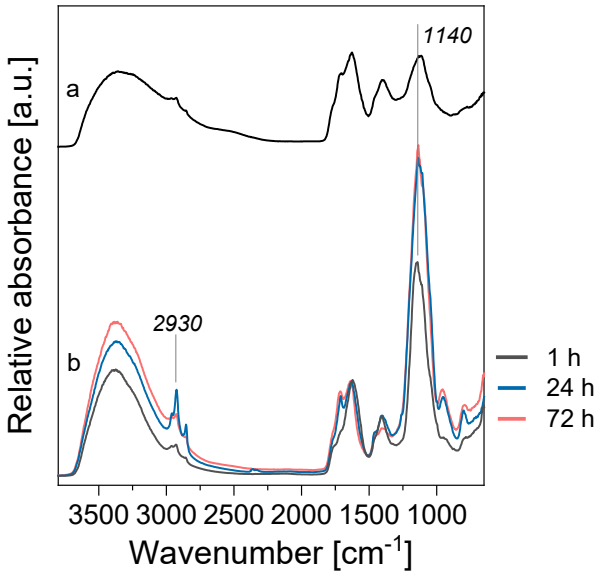

Figure S4: Diffuse reflectance infrared Fourier-transform spectra of freeze-dried (a) subsoil DOM solutions and (b) supernatants obtained after different contact times with a short-range ordered aluminosilicate with Al:Si = 1.4. Low DOC concentrations after reaction with the mineral restricted the analyses to one level of initial DOC concentration. Data was normalized to absorption at 1630 cm^{-1}.

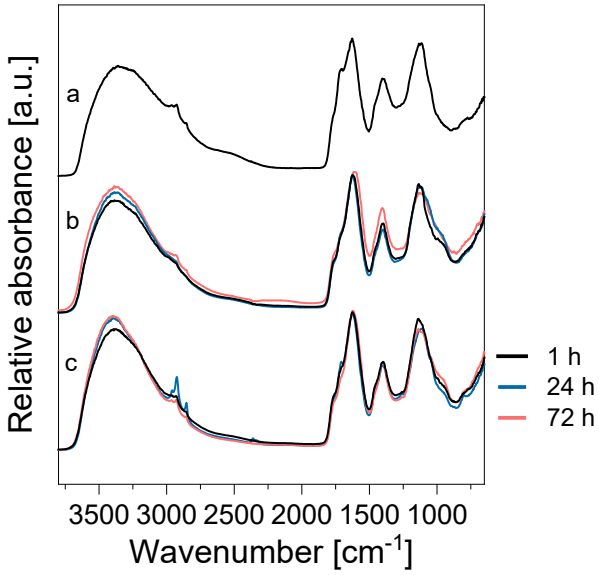

Figure S5: Diffuse reflectance infrared Fourier-transform spectra of freeze-dried (a) subsoil DOM solutions and supernatants obtained from variants with (b) high and (c) low initial DOC concentrations after different contact times with a short-range ordered aluminosilicate with Al:Si = 2.1. Data was normalized to absorption at 1630 cm^{-1}.

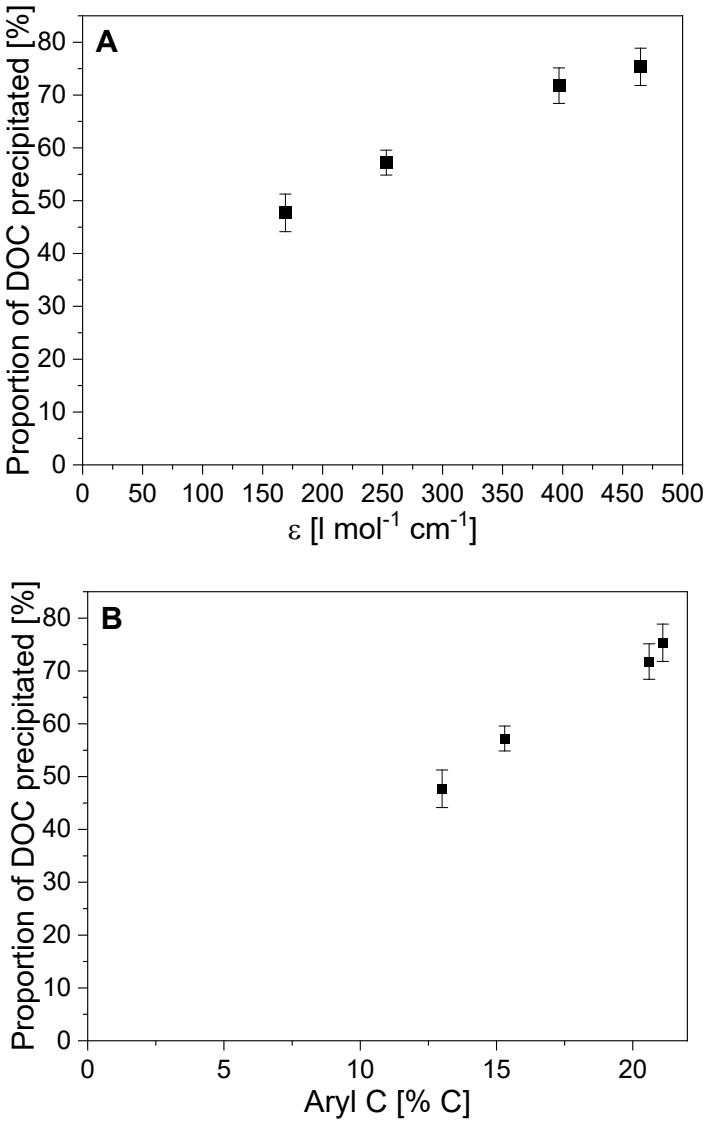

Figure S6: Proportions of DOC retained by co-precipitation with short-range ordered aluminosilicates against molar absorptivity at 254 nm (ε) of initial DOM solutions (A) and respective contents of aryl C quantified by ^{13}C nuclear magnetic resonance spectroscopy (B). Proportions are given as means of variants with different initial Al:C ratios, together with standard deviations.

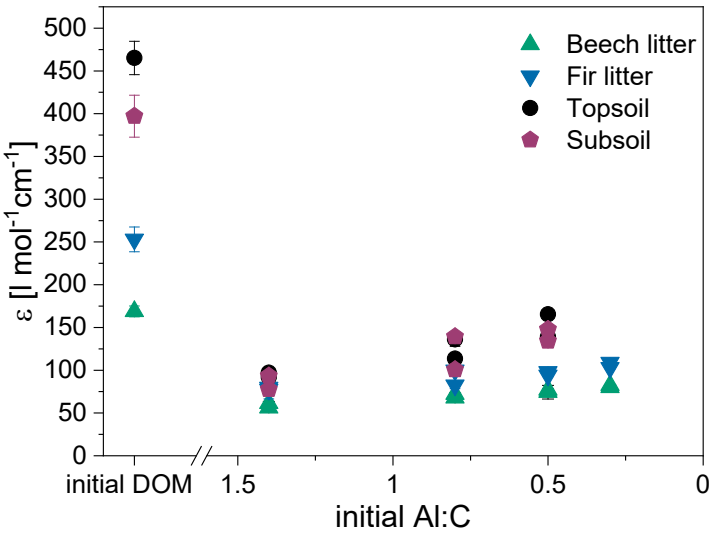

Figure S7: Molar absorbtivity at 254 nm (ε) of DOM solutions and supernatants obtained from co-precipitation experiments at different initial DOC concentrations (designated as Al:C ratio).

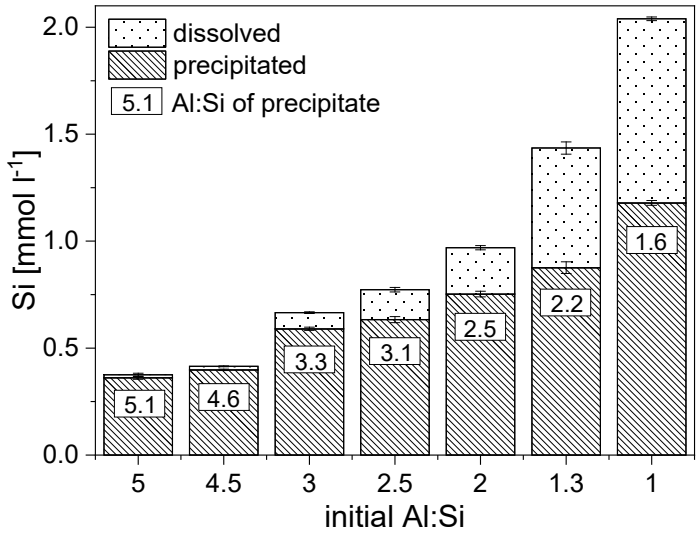

Figure S8: Amounts of Si precipitated during formation of short-range ordered aluminosilicates at different initial Si concentrations within 1 h.

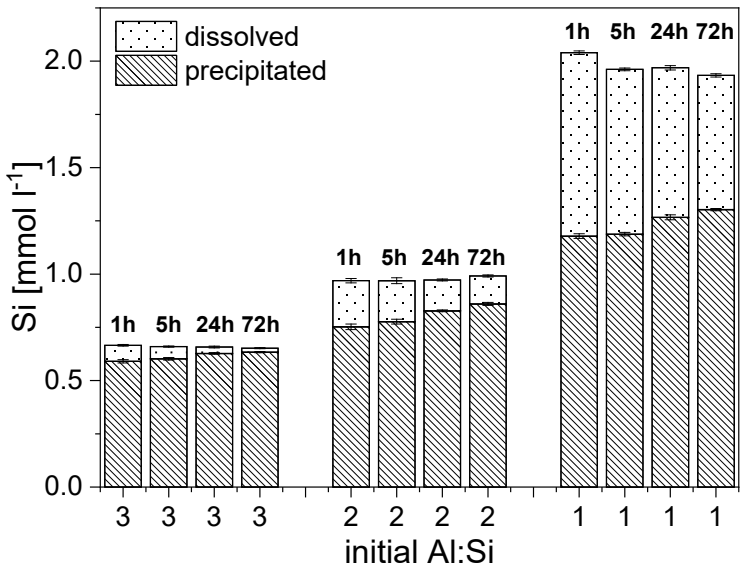

Figure S9: Amounts of Si precipitated during formation of short-range ordered aluminosilicates as a function of reaction time (1-72 h) at three different initial Si concentrations (designated as Al:Si ratio).

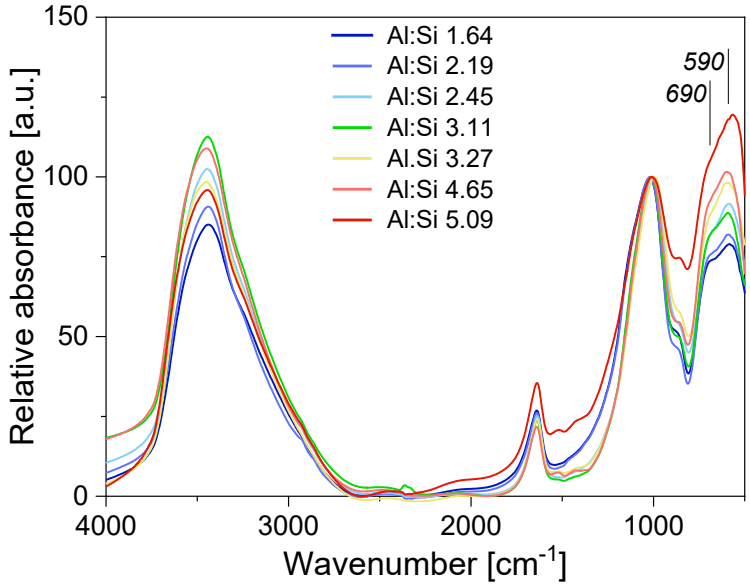

Figure S10: Transmission Fourier transform infrared spectra of short-range ordered aluminosilicates formed within 1 h at variable initial Al:Si ratios. Final Al:Si ratios of precipitates are given in the figure. Data was normalized to absorption maxima at 1020-985 cm^{-1}.

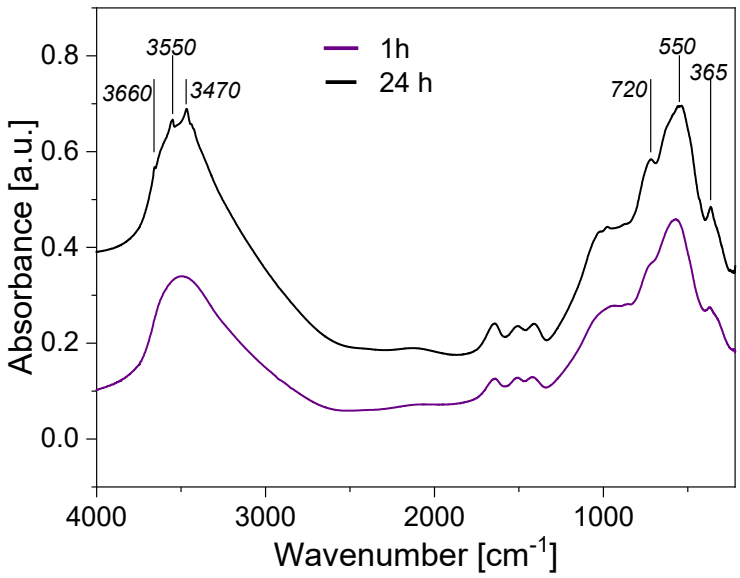

Figure S11: Transmission Fourier-transform infrared spectra of Al hydroxides formed in the absence of Si within reaction times of 1 and 24 h.

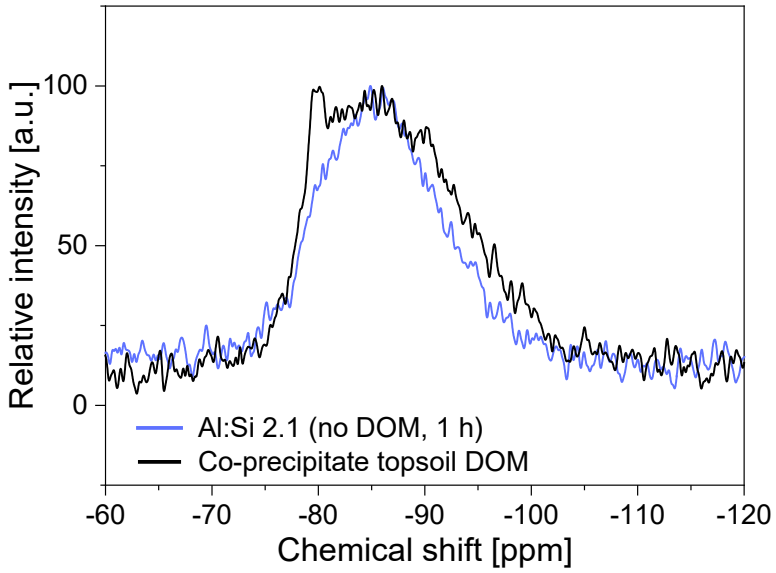

Figure S12: Solid-state ^{29}Si nuclear magnetic resonance spectra of short-range ordered aluminosilicates formed in the absence of dissolved organic matter (DOM) within 1 h and of a co-precipitate formed in the presence of topsoil DOM within 24 h at a line broadening of 25 Hz.

References

Bishop, J.L., Rampe, E.B., Bish, D.L., Abidin, Z., Baker, L.L., Matsue, N., Henmi, T., 2013. Spectral and hydration properties of allophane and imogolite. Clays Clay Miner. 61, 57–74.

Supplementary material to Lenhardt et al. (2023a) *Clays Clay Miner.* 71, 416–429

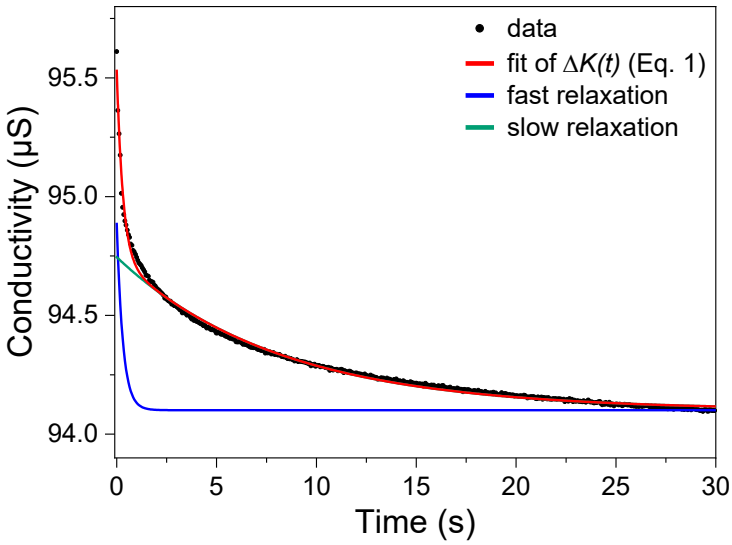

Fig. S1 Exemplary data analysis of stopped-flow conductivity measurements. The red curve results from fitting a bi-exponential function (Eq. 1) to data obtained at 25 °C from experiments with a short-range ordered aluminosilicate (Al:Si = 1.4; 1 g L^{-1}) and oxalic acid (0.5 mmol L^{-1}) at initial pH 5. The red curve is the sum of the two exponential functions representing a fast (blue) and a slow process (green)

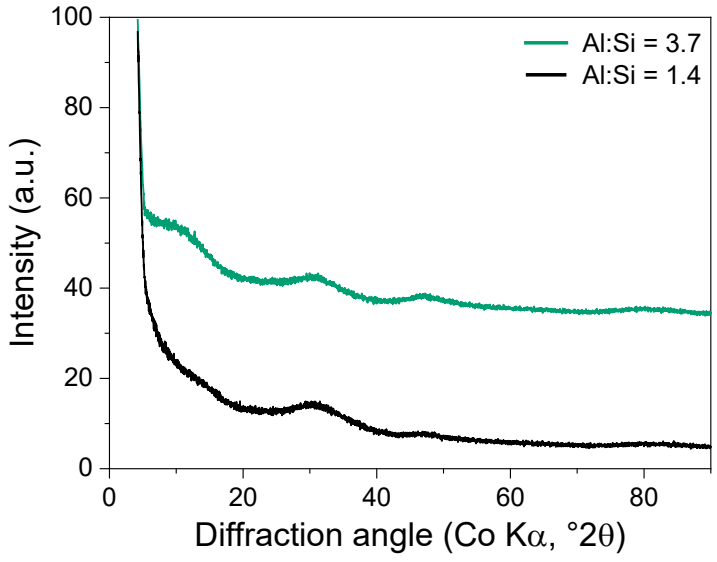

Fig. S2 X-ray diffractograms of short-range ordered aluminosilicates used as adsorbents. Data are shifted along the y-axis for clarity

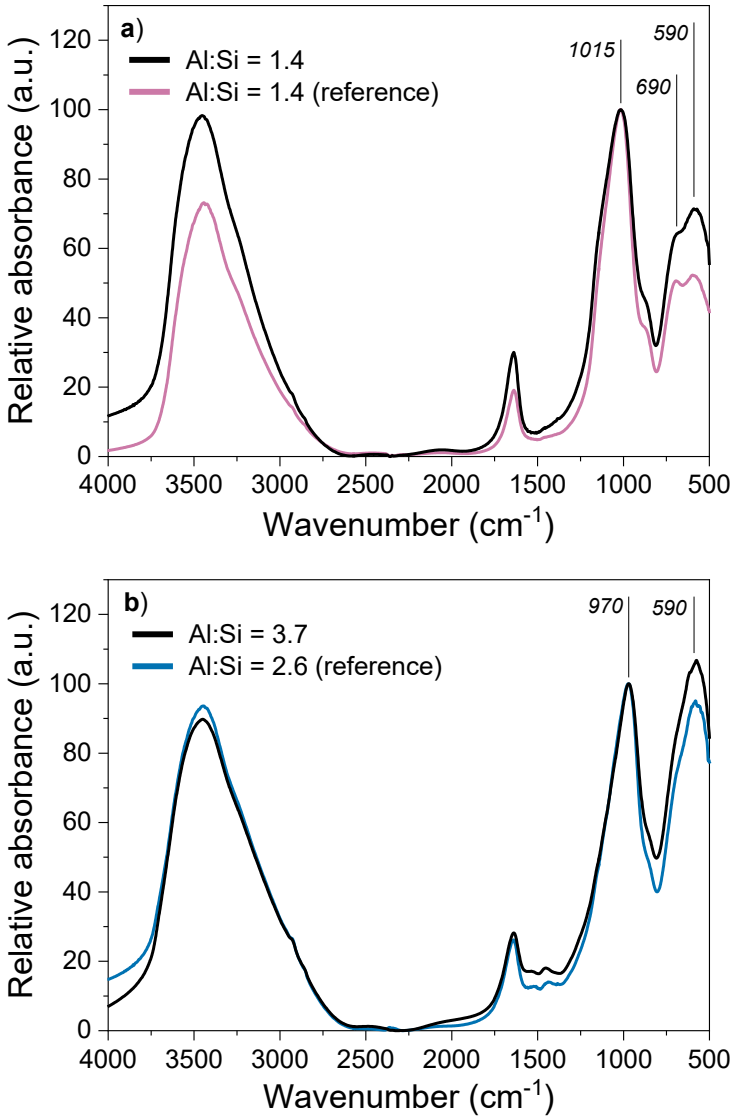

Fig. S3 Transmission Fourier-transform infrared spectra of short-range ordered aluminosilicates (SROAS) with an Al:Si ratio of 1.4 (a) and 3.7 (b) used as adsorbents. Spectra of SROAS previously characterized by ^{27}Al and ^{29}Si nuclear magnetic resonance spectroscopy (Lenhardt et al., 2021) are given as reference. Data were normalized to absorption maxima at 1015–970 cm^{-1}

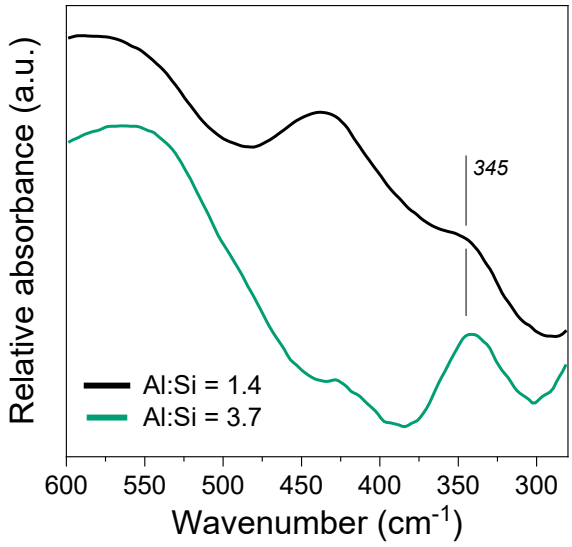

Fig. S4 Transmission Fourier-transform infrared spectra of short-range ordered aluminosilicates used as adsorbents. Data were normalized to absorption maxima at 590–565 cm^{-1} and shifted along the y-axis for clarity

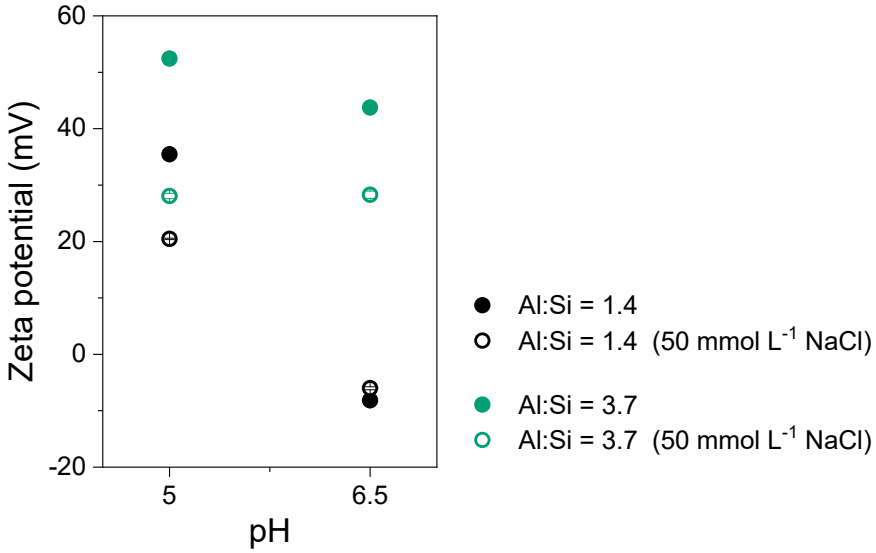

Fig. S5 Zeta potential of short-range ordered aluminosilicate particles measured in water and 50 mmol L^{-1} NaCl solution at pH 5 and 6.5

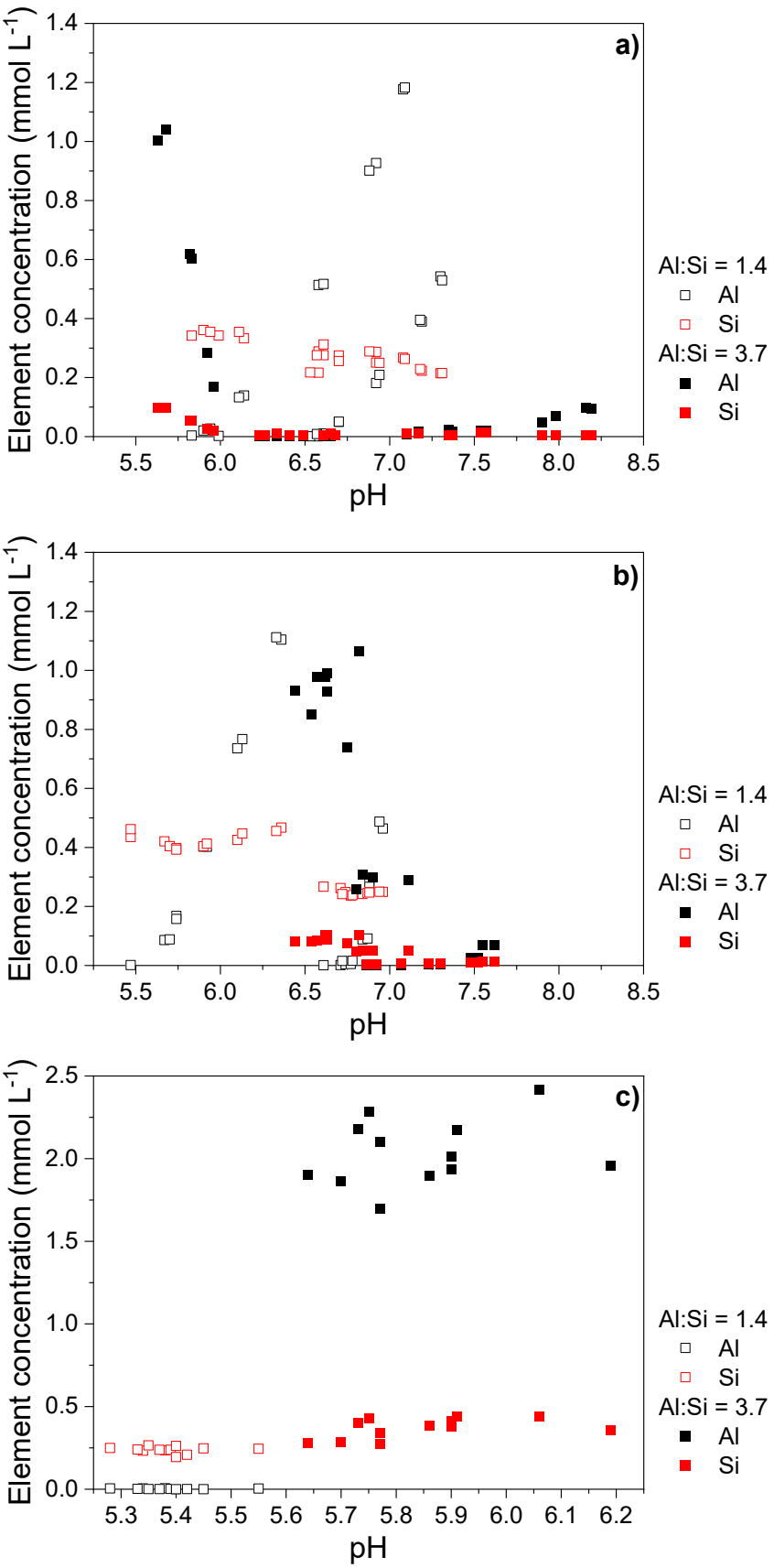

Fig. S6 Aluminum and silicon concentrations in filtrates of batch-adsorption experiments with short-range ordered aluminosilicates (molar Al:Si ratio 1.4 and 3.7) and oxalic acid (a), salicylic acid (b), and octanoic acid (c) plotted against pH

Release of Al and Si from SROAS during batch-adsorption experiments

Figure S6 gives Al and Si concentrations in filtrates of batch-adsorption experiments with organic acids after 5 h reaction time. Maximal relative amounts of Al and Si released were 4.3% and 2%, respectively. Therefore, the processes discussed in the following do not affect the conclusions in the main article on adsorption phenomena.

We plotted the concentrations against pH, since dissolution of SROAS and the processes that may have led to incomplete phase separation depend on pH. However, since adsorption of organic acids caused OH^- release as a function of their concentration, the final pH was proportional to organic-acid concentration, particularly for oxalic and salicylic acid.

The pH of the filtrates ranged from 5.2 to 8.2. The presence of Al and Si in filtrates with pH <7 from experiments with Al-rich SROAS cannot be explained by dissolution, since the concentrations surpassed the solubility of proto-imogolite (Lumsdon & Farmer, 1995; 1997). Hence, especially at lower pH, net positive surface charge likely favored disaggregation and thus incomplete phase separation. Molar Al:Si ratios in filtrates were slightly higher than those of the adsorbent (4.9–6.8; adsorbent: 3.7). A slight increase in Al concentrations at pH >7 that was reached only in the presence of oxalic and salicylic acid, may be caused by dissolution of Al-rich SROAS or mobilization of Al by organic acids.

Incomplete phase separation was negligible in batches with Si-rich SROAS. In filtrates from experiments with octanoic acid (Fig. S6c) and from variants without organic-acid addition (lowest pH, Fig. S6), Al concentrations were very low. A lower point of zero charge of Si-rich SROAS likely thwarted disaggregation (Su et al., 1992). With increasing concentrations of oxalic and salicylic acid, Al concentrations increased (Figs. S6a, b), while Si concentrations were unaffected. This indicates that organic acids formed soluble complexes with Al. Surprisingly, this process was negligible in batches with Al-rich SROAS, although oxalic and salicylic acid had a much higher affinity for Al-rich SROAS (see main article). Concentrations of Si markedly surpassed Al concentrations in most samples and were generally independent of final pH. This indicates preferential release of Si by depolymerization of ill-defined SROAS (Farmer et al., 1991; Strekopytov et al., 2006). Particularly Si-rich SROAS contain ill-defined and thus less stable Si species (Farmer et al., 1991; Strekopytov et al., 2006; Lenhardt et al., 2021).

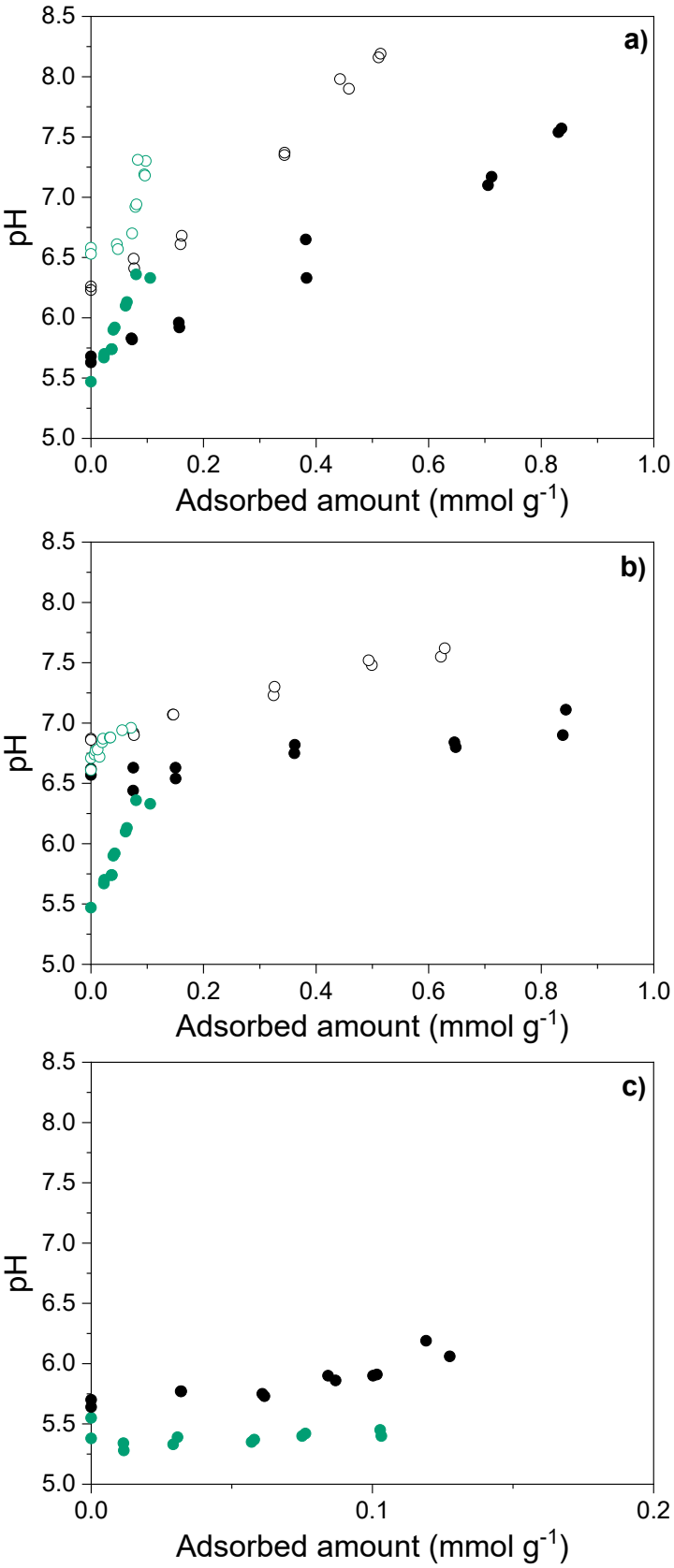

Fig. S7 Filtrate pH as a function of oxalic-acid (a), salicylic-acid (b) and octanoic-acid (c) adsorption on two short-range ordered aluminosilicates (Al:Si = 1.4 and 3.7, green and black symbols, respectively) after a contact time of 5 h. Initial pH was adjusted to 5 and 6.5 (full and open symbols, respectively) in mineral suspensions and adsorptive solutions. There was no adsorption of octanoic acid at initial pH 6.5

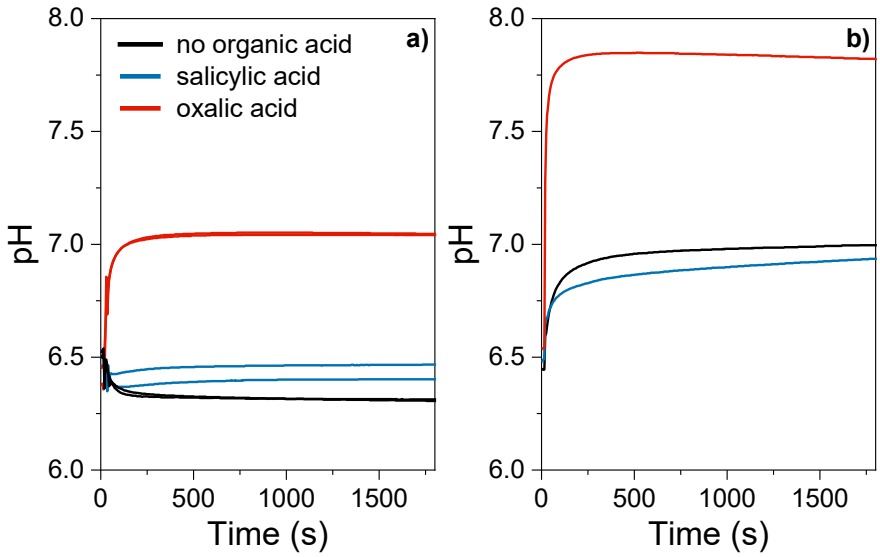

Fig. S8 Time-dependent pH change during adsorption of salicylic and oxalic acid (1.2 mmol L^{-1}) on short-range ordered aluminosilicates with molar Al:Si ratio of 1.4 (a) and 3.7 (b) at initial pH 6.5

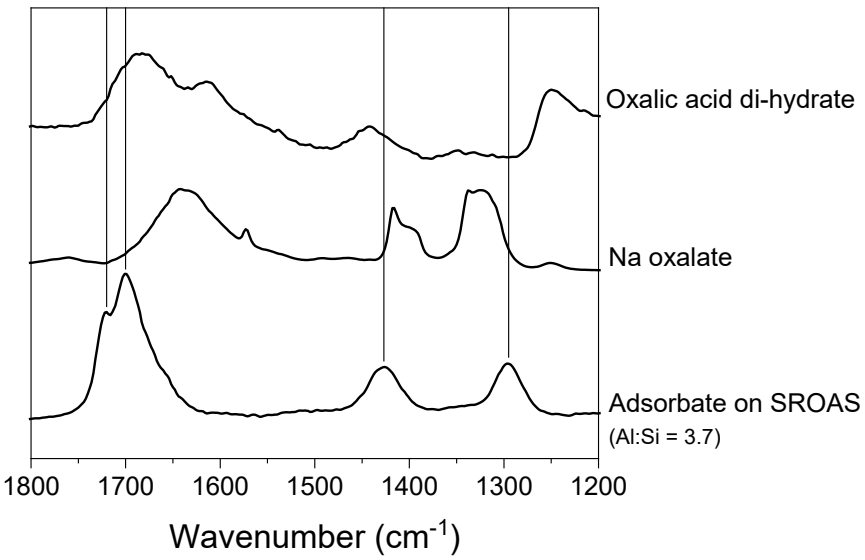

Fig. S9 DRIFT spectra of reference compounds and difference spectra of adsorption complexes formed by interaction of oxalic acid and a short-range ordered aluminosilicate (SROAS; Al:Si = 3.7) at initial pH 5. Bands of C–O stretching in adsorption complexes are marked by vertical lines

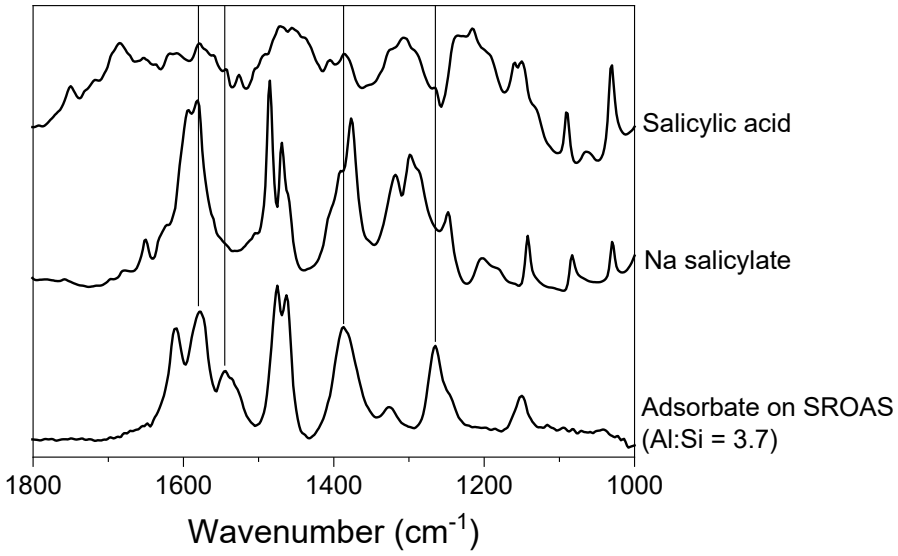

Fig. S10 DRIFT spectra of reference compounds and difference spectra of adsorption complexes formed by interaction of salicylic acid and a short-range ordered aluminosilicate (SROAS; Al:Si = 3.7) at initial pH 5. Bands of C–O stretching in adsorption complexes are marked by vertical lines

Table S1 Limiting molar conductivities (S cm^2 mol^{-1}) of ions used in stopped-flow experiments. At low adsorptive concentration (0.5 mmol L^{-1}), the limiting molar conductivity is an appropriate indicator for the contribution of the various ions to specific conductivity.

Ion	10 °C	15 °C	20 °C	25 °C	Reference
H_3O^+	314	344	375	404	Kinart (2019)
Octanoate	15.6	18.8	21.9	25.0	Kinart (2017)
Oxalate	51.0	58.7	66.4	74.9	Kinart (2021)
Salicylate		26.9	30.4	34.2	Stańczyk et al. (2019)

References

Farmer, V.C., McHardy, W.J., Palmieri, F., Violante, A., & Violante, P. (1991). Synthetic allophanes formed in calcareous environments: Nature, conditions of formation, and transformations. *Soil Science Society of America Journal*, *55*, 1162–1166.

Kinart, Z. (2017). Conductance studies of sodium salts of some aliphatic carboxylic acids in water at different temperatures. *Journal of Molecular Liquids*, *248*, 1059–1064.

Kinart, Z. (2019). Conductometric studies of dissociation constants of selected monocarboxylic acids a wide range of temperatures. *Journal of Molecular Liquids*, *292*, 111405.

Kinart, Z. (2021). Conductance studies of sodium salts of selected dicarboxylic acids in water at temperatures of 283.15 K to 313.15 K. *Journal of Molecular Liquids*, *337*, 116262.

Lenhardt, K.R., Breitzke, H., Buntkowsky, G., Reimhult, E., Willinger, M., & Rennert, T. (2021). Synthesis of short-range ordered aluminosilicates at ambient conditions. *Scientific Reports*, *11*, 4207.

Lumsdon, D.G. & Farmer, V.C. (1995). Solubility characteristics of proto-imogolite sols: How silicic acid can de-toxify aluminium solutions. *European Journal of Soil Science*, *46*, 179–186.

Lumsdon, D.G. & Farmer, V.C. (1997). Solubility of a proto-imogolite sol in oxalate solutions. *European Journal of Soil Science*, *48*, 115–120.

Stańczyk, M., Boruń, A., & Jóźwiak, M. (2019). Conductance studies of aqueous solutions of sodium salts of selected benzoic acid derivatives at temperatures from (288.15 to 318.15) K. *Journal of Molecular Liquids*, *278*, 247–252.

Strekopytov, S., Jarry, E., & Exley, C. (2006). Further insight into the mechanism of formation of hydroxyaluminosilicates. *Polyhedron*, *25*, 3399–3404.

Su, C., Harsh, J.B., & Bertsch, P.M. (1992). Sodium and chloride sorption by imogolite and allophanes. *Clays and Clay Minerals*, *40*, 280–286.

Supplementary material to Lenhardt et al. (2023b) *Eur. J. Soil Sci. 74:e13421*

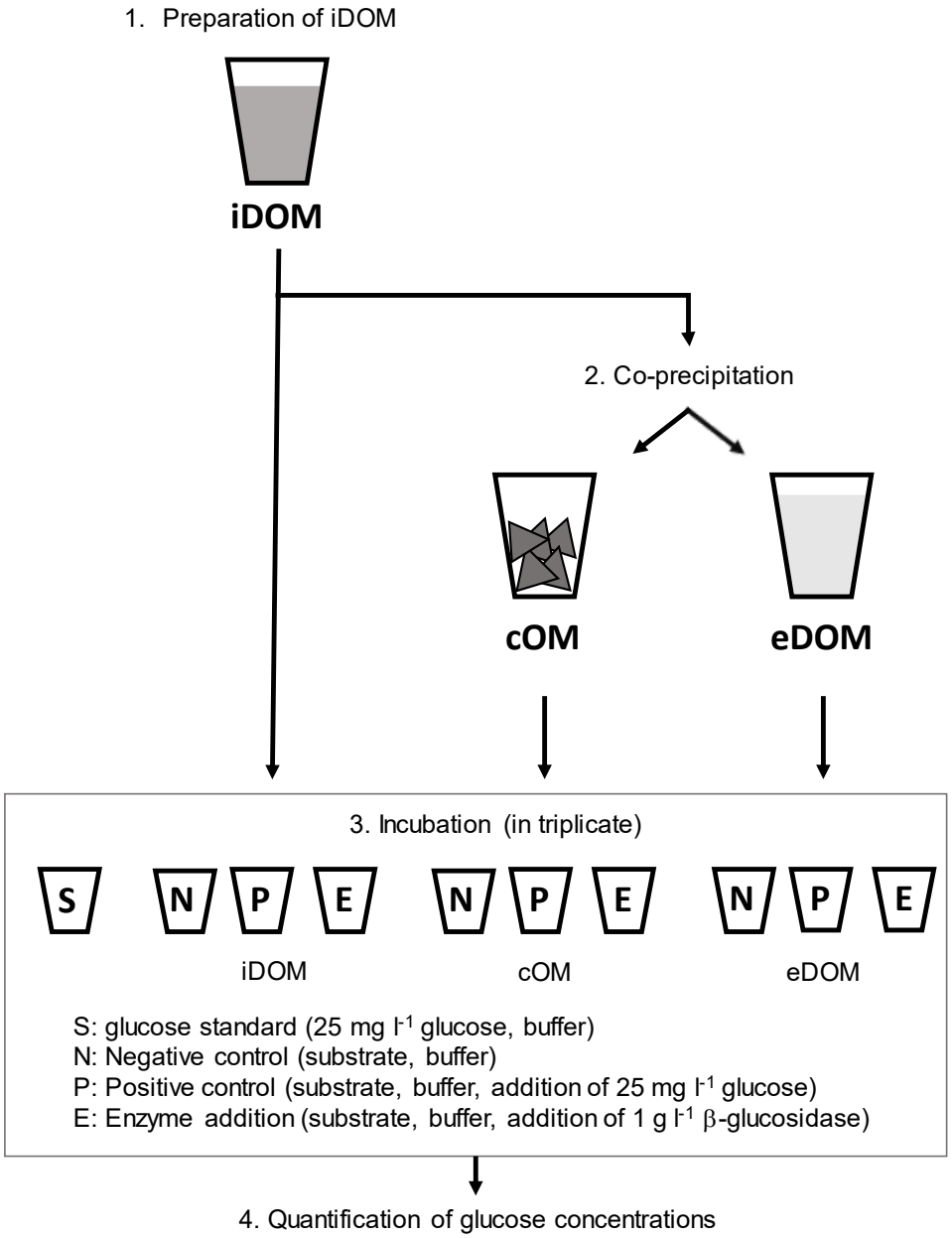

Figure S1: Scheme of experimental setup and work sequence. We prepared one stock solution per origin (topsoil, subsoil, fir litter, beech litter) containing initially dissolved organic matter (iDOM). We generated co-precipitated organic matter (cOM) and excluded DOM (eDOM) using iDOM solutions. cOM and eDOM were pooled after preparation, resulting in three substrates (iDOM, cOM, eDOM) per origin. Each substrate was incubated in buffer (negative control (N)), with addition of 25 mg l^{-1} glucose (positive control (P)), and with addition of enzyme (E) in triplicate. Background glucose concentrations in substrates were inferred from negative controls. Glucose loss by mineralization or sorption was calculated from the difference of glucose concentrations between positive controls and a glucose standard. Enzymatic glucose release was corrected for background glucose concentrations and glucose loss.

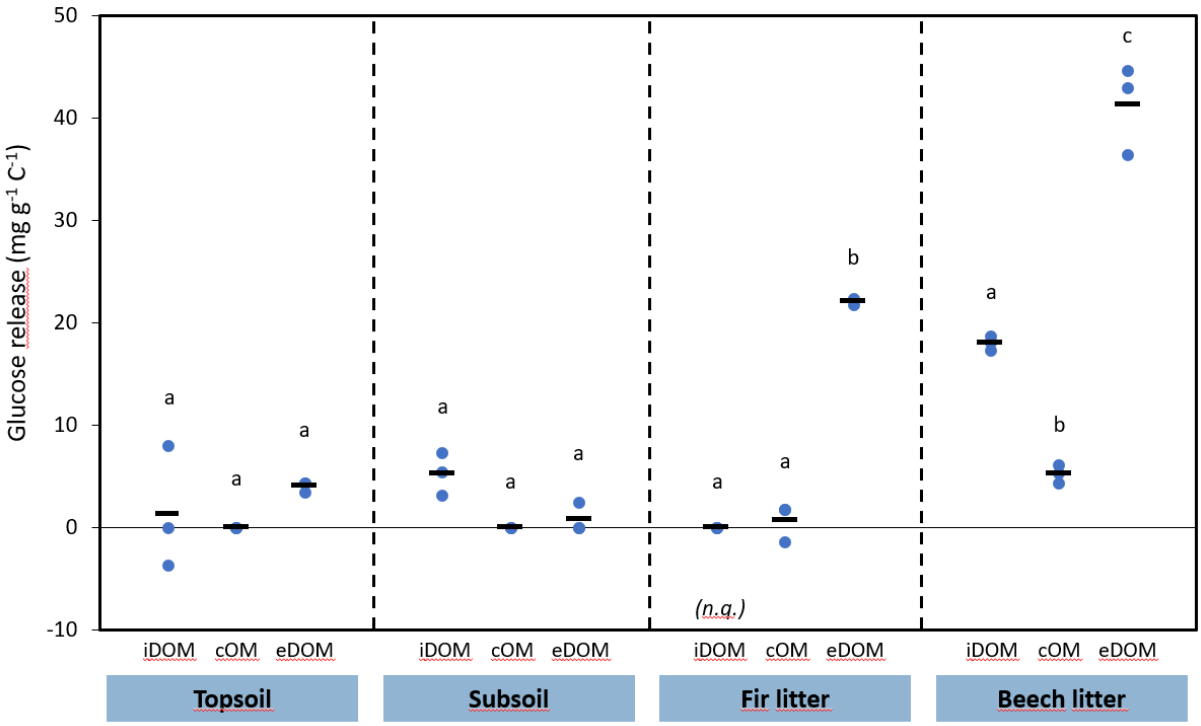

Figure S2: Enzymatic glucose release from initial DOM (iDOM), co-precipitated OM (cOM), and excluded DOM from topsoil, subsoil, fir litter and beech litter. Blue points represent individual values, while black lines indicate their mean. Glucose release from fir litter was not quantifiable (n.q.) due to excessive mineralization (Table S3). Different letters indicate significant differences (p<0.05) according to analysis of variance (ANOVA).

Table S1: Composition of iDOM solutions.

DOM type	DOC	Al	Fe	Si	Na	K	Mg	Ca
				[mg l^{-1}]				
Topsoil	444	17.0	3.6	2.4	77.8	16.3	14.2	15.8
Subsoil	340	23.6	4.6	1.4	91.1	28.4	4.1	3.8
Fir litter	575	1.0	0.7	3.2	24.5	124	14.4	63.5
Beech litter	552	1.5	1.1	3.1	20.0	60.8	10.6	35.0

Table S2: Conditions of co-precipitation, composition of co-precipitates before incubation, the proportions of elements removed by co-precipitation, and the resulting molar C:Si ratio in the filtrates.

DOM type	*Conditions of co-precipitation*					*Co-precipitates*		*Elements precipitated*			*Filtrate*
	DOC	**Al**	**Si**	**Al:C**	**Al:Si**	**Al:C**	**Al:Si**	**Al**	**Si**	**C**	**C:Si**
	[mg l^{-1}]	[mmol l^{-1}]	[mmol l^{-1}]					[%]			
Topsoil	201	10.4	4.6	0.62	2.25	0.99	2.70	99.9	83.4	62.9	14.2
Subsoil	180	10.1	4.7	0.67	2.12	0.90	3.12	100	68.1	74.6	4.37
Fir litter	215	10.1	4.7	0.56	2.16	1.56	2.77	100	77.8	36.4	19.6
Beech litter	204	10.0	4.5	0.59	2.21	3.35	2.69	99.9	82.2	17.7	30.0

Table S3: Organic matter input to incubation experiments, background glucose concentrations, and release of glucose by enzymatic hydrolysis for initial DOM (iDOM), co-precipitated organic matter (cOM) and excluded DOM (eDOM).

DOM type	iDOM	cOM	eDOM
	Organic matter input [mg DOC l^{-1}]		
Topsoil	296	316	269
Subsoil	255	329	168
Fir litter	287	311	468
Beech litter	295	310	517
	Background glucose concentration [mg l^{-1}][a]		
Topsoil	0	0	0
Subsoil	0	0	0
Fir litter	0	1	12.4
Beech litter	2	2.6	33.0
	Release of glucose [mg l^{-1}]		
Topsoil	0.4	0	1.1
Subsoil	1.3	0	0.1
Fir litter	-[b]	0.2	10.3
Beech litter	5.3	1.6	21.4
	Glucose loss [%][c]		
Topsoil	5	0	3
Subsoil	13	0	2
Fir litter	79	0	3
Beech litter	19	2	31

[a] Glucose concentrations in negative controls.
[b] Not quantifiable due to microbial activity.
[c] Relative decrease of glucose concentrations in positive controls compared to glucose standards (25 mg l^{-1}).

Acknowledgements

Many people contributed to the success of this dissertation. First of all, I would like to thank my advisor Thilo Rennert for his support, his constructive criticism, and valuable discussions.

Ellen Kandeler is highly appreciated for her advice and support during the development of my studies of the degradability of mineral-bound organic matter.

Hergen Breitzke and Gerd Buntkowsky are thanked for their support with solid-state ^{27}Al- and ^{29}Si-NMR measurements, advice on interpretation of the data, and interest in my studies.

I would like to thank my coauthors Max Willinger and Erik Reimhult for their contributions to the characterisation of the synthesized SROAS. Moreover, application of the enzyme addition assay would not have been possible without previous work and conceptualization by Luise Brandt and Christian Poll. Mathias Stein is thanked for support with analyses, experimental work and for revising the introduction and epilogue of my thesis.

All members of the Department of Soil Chemistry and Pedology are thanked for accompanying me in my dissertation project. I am beyond grateful for the solidarity from my colleagues Agnes Krettek, Verena Zöphel, Mathias Stein and Selina Tenzer. Annerose Böttcher, Gabriela Grassadonia and Detlev Frobel are thanked for their technical support with countless analyses. I am very thankful for the support and advice of Ludger Herrmann. Nadine Brunsmann is thanked for her kindness and for administrative support.

Christian Mikutta is thanked for his contributions as coauthor and for rewiewing my dissertation.

I am grateful to Wolf-Anno Bischoff for his encouragement.

Many more people contributed to this work, namely Dörte Diehl, Gabriele Schaumann, Jana Dobritzsch, Klaus Kaiser, Robert Mikutta, Christian Buchmann, Henry Stasdeit, Hannes Pleyer, Ingrid Neumann, Isabel Prater, Jörg Prietzel, Claus Rüscher, Johannes Herre, Alexander Gerlach, Frank Schreiber, Maximilian Senft, and Julian Ruggaber. The details of their contributions can be found in the acknowledgements of the publications.

Funding of my studies was provided by the Deutsche Forschungsgemeinschaft.